CRANFIELD UNIVERSITY


E. REZIG


# INFLUENCE OF CORROSION DAMAGE ON THE INITIATION OF FATIGUE CRACKS IN HIGH STRENGTH STAINLESS STEELS


SCHOOL OF APPLIED SCIENCES


M.Phil Thesis

Academic years: 2006-2011


Supervisors: Prof. P.E. Irving and Dr. M.J. Robinson

April 2011

# CRANFIELD UNIVERSITY

SCHOOL OF APPLIED SCIENCES

MPhil THESIS

Academic Years: 2006-2011

## E. REZIG

# Influence of corrosion damage on the initiation of fatigue cracks in high strength stainless steels

Supervisors: Prof. P.E. Irving and Dr. M.J. Robinson

April 2011

This thesis is submitted in partial fulfilment of the requirements for the degree of Master of Philosophy

# ABSTRACT

This research project investigates the influence of corrosion flaws on the initiation of fatigue cracks in high strength stainless steels, and more particularly in 15-5 precipitation hardening high strength stainless steel.

Susceptibility of 15-5PH to localised corrosion was examined and pit-like corrosion flaws produced by pitting and crevice corrosion were introduced in fatigue specimens in order to measure the influence of these surface flaws on fatigue crack initiation. From the results and observations made during the experiments, models of crevice corrosion propagation and initial stage of fatigue were developed.

Experimental testing revealed that 15-5 precipitation hardening stainless steel is more prone to crevice corrosion than pitting, and that crevice corrosion is thought to be the most likely cause of any pit-like flaws in this material. The first results of the modelling of the propagation of crevice corrosion in 15-5PH stainless steel showed that the initial growth across the metal surface was proportional $t^{3/8}$. It follows that the depth growth rate in that initial stage was proportional $t^{5/8}$.

All pre-corroded fatigue specimens failed from fatigue cracks which initiated from crevice corrosion flaws during fatigue testing. After failure the shape and size of corrosion flaws where the cracks initiated were measured and their largest Kt values determined by finite element analysis. No general pattern linking total fatigue life and stress concentration factor value was found. However, it was shown that stress concentration factor Kt has an influence on the initiation and early crack growth behaviour, but has no effect on the life of longer cracks. In addition, it appeared that not considering the small excursions found at the bottom of corrosion flaws in the assessment of the stress concentration factor Kt underestimates the values of Kt.

**Key words**: 15-5PH, stainless steel, crevice corrosion, fatigue, stress concentration factor

# ACKNOWLEDGEMENTS

# TABLE OF CONTENT

# LIST OF FIGURES

viii

# LIST OF TABLES

# 1 INTRODUCTION

The aim of this research project was to investigate the influence of corrosion damage on the initiation of fatigue cracks in high strength stainless steels. Indeed, passive metals such as stainless steels suffer from localised corrosion when in contact with corrosive environments like chloride solutions. When coupled with fatigue, localised corrosion damage acts as a stress raiser and moves the endurance of the metal from crack initiation domination to a life consumed by crack propagation.

15-5 precipitation hardening stainless steel was mainly examined in this research since it is considered as an alternative to 300M for the construction of aircraft landing gear. Whereas the influence of corrosion damage in fatigue life of 300M has previously been investigated in detail and its loss of performance in corrosion fatigue is well known, the behaviour of high strength corrosion resistant alloys, including 15-5PH has received less attention. Unlike 300M where corrosion tends to result in widespread but shallow corrosion damage, the corrosion resisting alloys are prone to forms of corrosion that produce deep and localised flaws, while the majority if the surface remains unaffected. These flaws are expected to be much more significant stress raisers when the component is subjected to cyclic stresses. For this reason, this project has concentrated on the development of such corrosion damage produced by pitting and crevice corrosion, and their role in fatigue crack initiation.

The emphasis of the work has been to use experimentally generated data to develop models both for the growth of corrosion generated flaws and for predicting the influence of these flaws on fatigue life. Tests performed on small scale fatigue specimens have been used to examine the influence of damaging flaws of differing size and shape and gain experience in interpreting and anticipating their effects. Finally, larger scale fatigue tests, using two specimens closer to the dimensions of an actual landing gear component, has been tested to confirm that the methodology and predictions used in the small scale tests are equally applicable in the more general case.

The aims of the research can be summarized as follows:

1. Investigate the susceptibility to localized corrosion of 15-5PH high strength stainless steel.

## 1. INTRODUCTION

2. Measure the influence of surface flaws generated by corrosion on fatigue crack initiation, and determine whether corrosion fatigue is more or less of a problem in 15-5PH high strength stainless steel.

3. Model the processes of corrosion and the initial stages of fatigue to establish the critical flaw size to initiated a fatigue crack and use this as a criterion for selecting preferred materials.

# 2   LITERATURE REVIEW

## 2.1   Corrosion

Corrosion is commonly defined as the natural deterioration of a metal and its properties due to electrochemical reaction with the surrounding environment. Besides being an undesirable process causing early and unexpected failure of structures, corrosion is also very costly. Indeed, a study initiated by NACE International estimated the total annual direct cost of corrosion in the U.S at $276 billion, which represented around 3% of the gross domestic product of the country [1]. It is therefore important to understand the process of corrosion in order to choose the more appropriate designs and materials, and thus prevent or slow down its occurrence.

The aim of this section is to provide the reader with an overview of the basic concepts of corrosion. Detailed explanations of corrosion processes are available in several reference text books [2-4].

### 2.1.1   Principles

Corrosion is an electrochemical process which can be represented by an electrochemical cell composed of two electrodes (the anode and the cathode) and the electrolyte, as illustrated in Figure 2-1. In the case of a single metal in contact with a solution, the anode and cathode are both on the metal, but their respective location varies depending on the immersion conditions of the metal (semi or fully immersed) [3]. When two metals are in contact with a solution, the term galvanic coupling is employed, and the anode is the metal with the more active (electronegative) potential. In both cases, an oxidation (or anodic reaction) takes place at the anode, and a reduction (or cathodic reaction) occurs at the cathode. The anodic reaction is the dissolution of the metal with a production of electrons. These electrons are consumed simultaneously and at the same rate by the cathodic reaction. There are different types of reductions depending on the composition of the electrolyte, as listed in Table 2-1, the most encountered being the hydrogen evolution and the oxygen reduction [2].
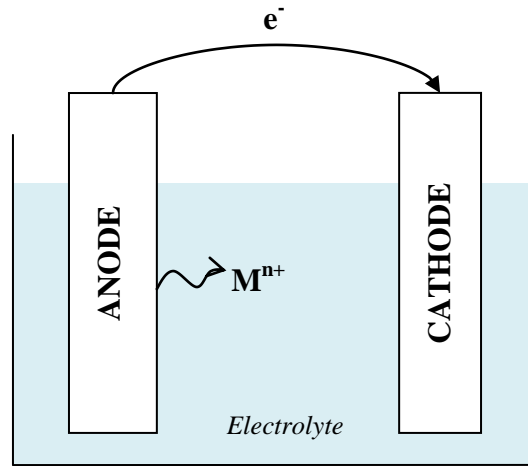
**Figure 2-1: Electrochemical cell**

| Oxygen reduction (neutral or basic solution) | $O_2 + 2H_2O + 4e^- \rightarrow 4OH^-$ |
|---|---|
| Oxygen reduction (acid solution) | $O_2 + 4H^+ + 4e^- \rightarrow 2H_2O$ |
| Hydrogen evolution | $2H^+ + 2e^- \rightarrow H_2$ |
| Metal ion reduction | $M^{3+} + e^- \rightarrow M^{2+}$ |
| Metal ion deposition | $M^+ + e^- \rightarrow M$ |

**Table 2-1: Common cathodic reactions occurring in metallic corrosion** [2]

## 2.1.2 Corrosion rate and polarisation

During the corrosion process, the difference of potential between the metal and the solution, called the metal potential $E_{M^{n+}/M}$, reaches a value, defined as the corrosion potential $E_{corr}$, such that the rate of oxidation equals the rate of reduction. Indeed at that potential $E_{corr}$, the number of electrons produced by the dissolution of the metal is equal to the number of electrons consumed by the reduction. That particular number of exchanged electrons corresponds to a particular electric current inside the corrosion cell, called $i_{corr}$. The rate of the corrosion process is therefore dependent of the metal potential, which defines the number of exchanged electrons, that is to say the electric current, $i$, of the corrosion cell.

The rate of corrosion can be controlled by modifying the potential or the current of the corrosion cell. This process is called polarisation and there are three different types of polarisation:

      a. Activation polarisation or anodic polarisation: the rate of the corrosion process is controlled by the rate of the anodic reaction.

b. Concentration polarisation: the corrosion rate is limited by the transport (diffusion, convection) of the species consumed during the cathodic reaction (eg. hydrogen bubbles or dissolved oxygen) from the electrolyte to the metal surface.

c. Resistance polarisation: the corrosion rate depends of the conductivity of the electrolyte experimentally.

Curves, called polarisation curves, representing the behaviour of the potential as a function of the logarithm of the current density can be used to predict the corrosion rate. For a given corrosion cell, the polarisation curves for the anodic and cathodic reactions are schematically plotted in the same diagram, called an Evans diagram, to assess the corrosion rate and the influence of a change in the corrosion potential or the corrosion current on the corrosion rate, as illustrated in Figure 2-2.
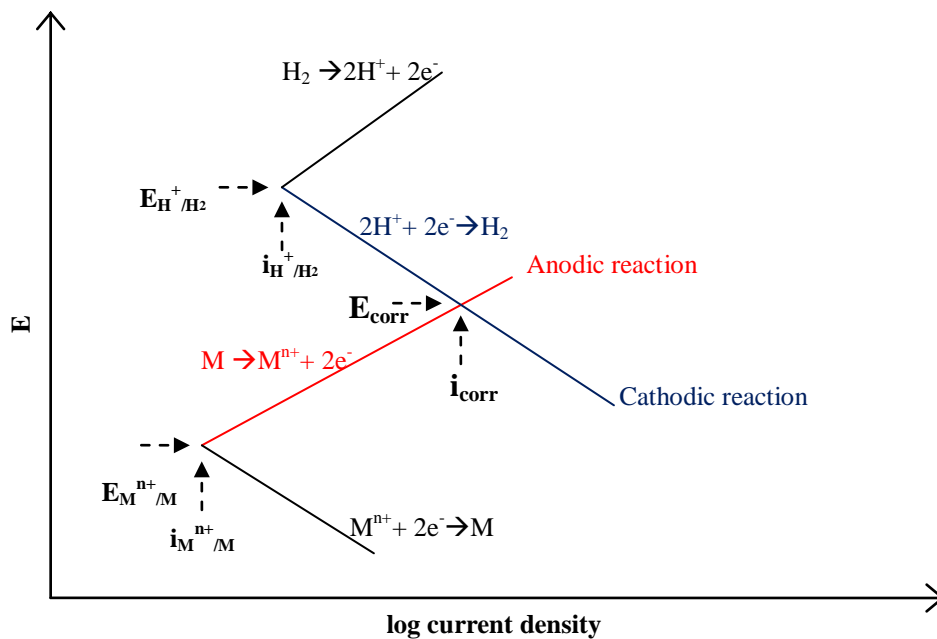


**Figure 2-2: Evans diagram for a metal corroding in acid solution**

## 2.1.3 Passivity

The potential of an active metal increases linearly with log of current density, as illustrated in Figure 2-3. The potential curve is said to exhibit linear Tafel region.
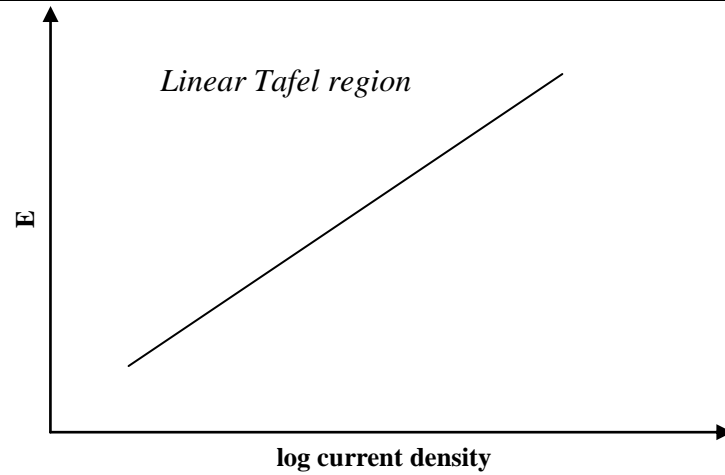
**Figure 2-3: Polarisation curve for an active metal**
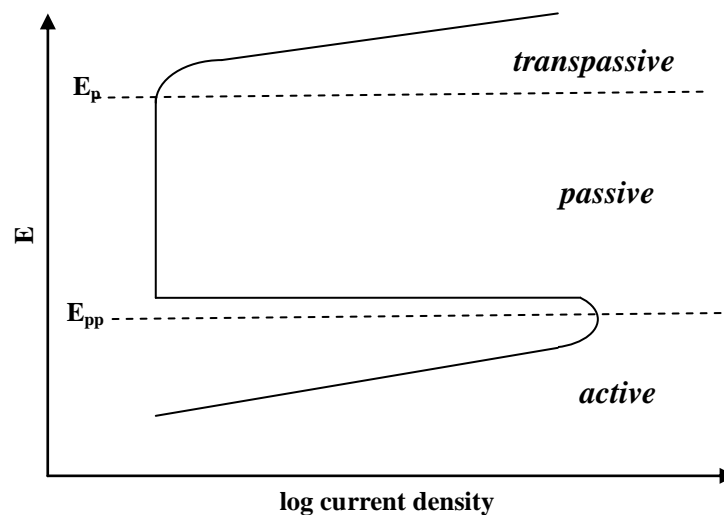


**Figure 2-4: Polarisation curve for a passive metal**

For some metals, a sudden decrease in the current density is observed after the potential reached a particular critical value, called passivation potential $E_{pp}$, in the Tafel region, as shown in Figure 2-4. At that potential, an oxide film is formed on the surface of the metal which protects the metal from being corroded. This phenomenon is called passivation and is observed in metals such as stainless steels and aluminium alloys. In that region, the current density stays at a low value despite the increase in potential. The current density increased again once the potential reaches the critical pitting potential $E_p$. At that potential, localised breakdowns of the passive film occur, which leads to localised corrosion called pitting. That third zone zone is called transpassive.

## 2.1.4  Types of corrosion

There are various forms of corrosion, and several types of corrosion can be found on a same metallic component. The common classification, established by Fontana [2] according to the aspect of the corroded metal, differentiates height forms of corrosion, as detailed in the following list.

a.  Uniform or general corrosion: the most common form of corrosion which takes place at a uniform rate over the whole exposed surface of the metal.

b.  Galvanic corrosion: occurs when dissimilar materials are in contact in a solution.

c.  Crevice corrosion: develops in crevices or shielded areas of materials.

d.  Pitting corrosion: corrosion occurs at localised area and produced small holes.

e.  Intergranular corrosion: corrosion occurs at grain boundaries.

f.  Selective leaching: extraction by corrosion of one particular element in an alloy.

g.  Erosion corrosion: accelerate form of corrosion due to the movement between a corrosive solution and the component.

h.  Stress corrosion: occurs when tensile stresses are applied to a component in a corrosive environment.

In this research project, pitting and crevice corrosion have been examined. The following section aims to provide the reader with an overview of these particular forms of localised corrosion.

## 2.2  Pitting and crevice corrosion

Passive metals in aggressive environment are prone to localised breakdown of their protective film [9]. Some parts of the metal surface are then exposed to the environment and start to dissolve. This phenomenon is called localised corrosion and the rate at which the metal dissolution occurs in localised corrosion is usually faster than in uniform corrosion [11]. When localised corrosion happens in shielded areas, the term crevice corrosion is employed, whereas pitting corrosion is used to describe localised corrosion on a free surface.

## 2.2.1 Pitting

The local dissolution of the metal in pitting corrosion leads to the formation of holes or cavities at the metal surface, called pits. The surface diameter of the pits is generally small and they are very often covered by corrosion product [2], which makes their detection very difficult. In addition, pits can have a wide variety of shapes, as illustrated in Table 2-2, depending on many factors such as the material composition or the surface orientation [11]. Each shape has a different degree of severity, which adds more difficulties to assessing the damage. For instance, an undercutting pit may seem small and not very deep from the surface, but actually spreads on a large area under the surface.
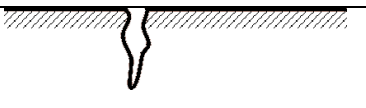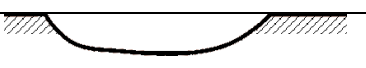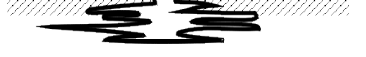
| | | |
|---|---|---|
| **Trough pits** | Narrow and deep | |
| | Elliptical | |
| | Vertical grain attack | |
| | Shallow and wide | |
| **Sideway pits** | Subsurface | |
| | Undercutting | |
| | Horizontal grain attack | |

**Table 2-2: Illustrations of the different pit shapes [7]**

Therefore, pitting corrosion is considered as one of the most dangerous form of corrosion due to the difficulty to detect it and also due to the fact that failure of a structure happens with only a small percentage of weight loss [2].

The initiation of pits occurs at heterogeneities on the surface of the metal according to Szklarska-Smialowska [14]. Several authors [2,8,9,10,15] considered that non metallic inclusions, and notably sulphide inclusions in stainless steels, are the most common site. The initiation of pits depends on many factors and is not clearly understood yet, which lead to a variety of model for the initiation process [11]. For instance, there is a particular temperature, called the critical pitting temperature

8

(CPT), under which no pitting corrosion will develop. This temperature depends on the environment (anions concentration, pH, etc.) and the metal. A critical potential, the pitting potential $E_p$, have also been identified. This potential was first defined as the potential threshold above which pitting corrosion will occur [14], but Burstein et al. [10] showed that pits do initiate and grow at potentials below Ep. In fact, the pitting potential does not represent the boundary between pitting and no pitting but between metastable and stable pits [9]. Indeed, it has been observed that pits initiating below $E_p$, called metastable pits, grow for a short period before repassivating, whereas pits having initiated at potential higher than $E_p$ are stable and keep propagating. Although a long time is usually required to initiate pits, their propagation happens at a rate which increases with time. The mechanism of propagation in pitting corrosion is similar to the propagation of crevice corrosion [2,11] and is detailed in section 2.2.3.

## 2.2.2 Crevice corrosion

Crevice corrosion occurs when a metal is locally obstructed by another component because of the design or by some deposit, such as dirt or corrosion product for instance. A crevice is defined by its depth and gap, as illustrated in Figure 2-5, the depth of the crevice being half the width of the crevice former, and the gap being the distance between the surface of the metal and the surface of the crevice former. Both the depth and the gap of the crevice have a significant effect on the initiation of crevice corrosion. For instance, crevice corrosion needs stagnant conditions to nucleate, therefore the crevice gap should be wide enough to let the electrolyte enter the crevice but narrow enough to keep the solution in place [2,5]. Kain [13] predicted the time to initiate crevice corrosion as a function of the crevice gap using the mathematical model developed by Oldfield and Sutton [12]. He showed that, for a given crevice depth, the predicted time to initiate crevice corrosion increased when the crevice gap increased and that there was a critical gap value above which no crevice corrosion nucleated. Likewise, he showed that for a fixed crevice gap, the predicted time to initiate crevice corrosion decreased with the increase in crevice depth, and that a for a particular crevice gap corresponded a minimum crevice depth under which no breakdown of the passive film occurs. Although, the crevice gap and depth have a significant effect on the initiation of crevice corrosion, they are not the only factors having an influence. Oldfield and Sutton [12] listed these factors, as detailed in Figure 2-6, and explained the difficulty to predict crevice corrosion by this

multitude of parameters which should, but cannot, be all included in models for an accurate model.
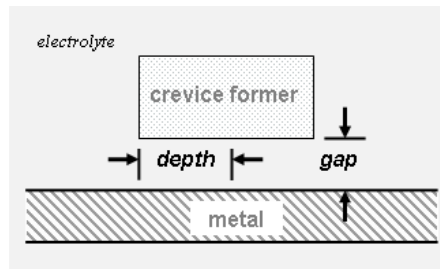


**Figure 2-5: Illustration of the depth and gap of a crevice [13]**
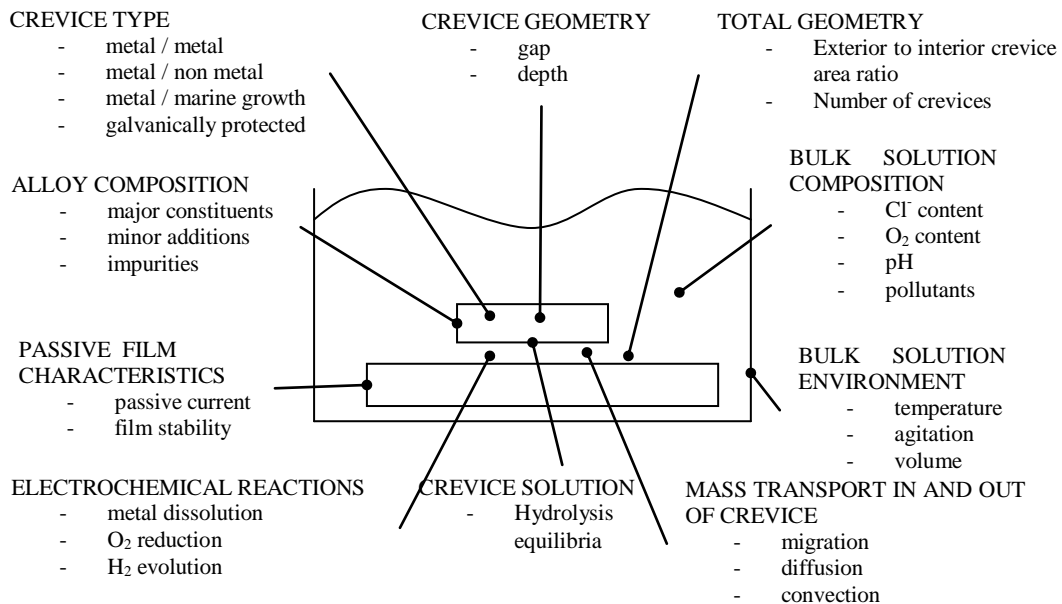


**Figure 2-6: Factors affecting crevice corrosion [12]**

Like pitting corrosion, the period of time before any breakdown of the passive film in crevice corrosion is long, whereas the propagation of the corrosion happens at an accelerating rate. Karlsberg and Wranglen [5] showed that a large potential difference between the "free" metal surface and the shielded metal surface was not necessary for the initiation of crevice corrosion. The initiation is due to a chemical change in the crevice solution, involving very often the depletion of oxygen within the crevice [16]. The mechanism of crevice corrosion is detailed in section II-2.2.3.

## 2.2.3 Mechanism

Pitting and crevice corrosion are two forms of localized corrosion with many links and similarities. It is said that pitting corrosion cannot initiate unless a "crevice-

like cavity has been created" [15], whereas Fontana [2] said that "pitting is a self initiating form of crevice corrosion which does not require a crevice". It has also been observed that crevice corrosion on stainless steels begins as small pits [5]. Both forms of localised corrosion exhibited a long initiation period, of which the process is not clearly understood, followed by a propagation phase which is autocatalytic and accelerates with time. Once initiated, either due to an inclusion (pitting) or due to the depletion of oxygen in the shielded area (crevice), the mechanisms of pitting and crevice corrosion both involve the dissolution of the metal (anodic reaction) and the reduction of oxygen (cathodic reaction). The anodic reaction occurs within the pit or crevice, whereas the cathodic reaction happens on the surface adjacent to the pit or crevice. The dissolution of the metal produces positive ions, $M^+$, inside the pit or crevice at a fast rate. These metal ions $M^+$ in contact with the water of the solution produce hydrogen ions $H^+$ by hydrolysis. In addition, anions present in the solution, usually chloride ions $Cl^-$, diffuse into the pit or crevice to maintain the electro neutrality of the solution. Therefore, in the solution the concentration of $Cl^-$ increases, as well as the concentration of $H^+$, this means that the pH decreases. These aggressive conditions promote more metal dissolution and the autocatalytic process accelerates.

## 2.3 Fatigue

Fatigue occurs when a structure undergoes repetitive periods of loading and unloading. These cyclic stresses develop structural damage within the material taking form of cracks which reduce the mechanical properties of the material and its service life. When cracks reach the critical length, the structure fails at stresses lower than the ultimate tensile strength of the material. If the crack is not detected, it can lead to unexpected premature and catastrophic failures, such as crash of aircrafts [17, 18], it is therefore important to be able to assess the time to propagate fatigue cracks to a critical stage or design structures to hinder their apparition.

The aim of this section is to provide the reader with an overview of the basic concepts of fatigue and fracture mechanics. Detailed explanations are available in several reference text books [19-21].

### 2.3.1 Fatigue life

Fatigue life is made of three different phases. These are the crack initiation, the crack propagation and the final failure. The proportion of each stage in the fatigue life

of a component varies. Indeed, in some component, most of the fatigue life is occupied by the initiation stage, whereas in other structures this is the crack growth life which prevails. However, in every case, the final failure happens fast, hence represents little in the fatigue life of a component.

The passage from the initiation stage to the propagation stage is arbitrary [24], since it depends mainly on the considered definition of the initiation stage. Indeed, in fracture mechanics, the initiation is considered as soon as the crack tip has moved from its original position [22], but it is more generally described as the period of time, or number of loading cycles, needed to detect the crack. However, the initiation/propagation boundary is even more difficult to accurately define since the detection of the crack is also dependent of the means of detection. Indeed, generally used non destructive test (NDT) methods, such as Eddy current can detect 1 or 2mm long crack, whereas laboratory tools, like replica techniques might detect crack of few microns in length. Regarding the definition of the crack propagation stage, it remains unchanged whatever the situation. It is the period of time needed for an initiated crack to grow to a critical size causing the failure of the component.

## 2.3.2  Crack initiation

The mechanism of fatigue crack initiation differs for pristine specimen and damaged specimens.

The process of fatigue crack initiation in pristine ductile material was identified by Wood in 1958 [19]. Wood theory stated that the cyclic loading, that undergoes a material, leads to movements of slip bands. After a while, the slip bands reach the surface, where the irreversible deformations due to slip movements of different amplitude appear. These deformations forms hills and valleys at the surface of the material, more commonly called extrusions and intrusions. Stress concentrations at the roots of the intrusions result in more slip movements. Slip movements also lead to vacancy movements, hence the amount of vacancies increases in the slip band, and by a diffusion process, the vacancies reach the surface causing the fatigue crack initiation.

In non pristine components, the damage acts as stress raisers, and a plastic zone ahead of the damage tip is created. The fatigue crack initiation is due to plastic deformations in a direction normal to the direction of the applied load.

### 2.3.3  Crack growth

Fatigue crack growth, like crack initiation at stress raisers, is due to localised deformations within a plastic zone ahead of the crack tip. Two stages of crack growth were described by Forsyth in 1962 [12]. In stage I, the crack and the plastic zone have the size of a few grain diameters; the crack propagates by single shear following the direction of the primary slip system forming a zig-zag crack, as illustrated in Figure 2-7. In stage II, the size of the crack and the plastic zone now represents several grains; a duplex slip mechanism occurs implying two slip bands, and the crack propagates in a direction normal to the direction of the applied load, as shown in Figure 2-8.
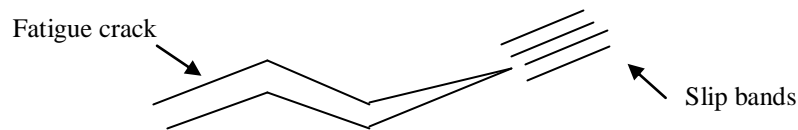


**Figure 2-7: Sketch of stage I crack growth [12]**
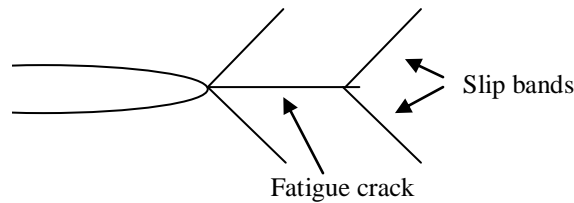


**Figure 2-8: Sketch of stage II crack growth [12]**

### 2.3.4  Crack growth rate

Paris et al. showed experimentally that the fatigue crack growth rate for constant loading ratio could be correlated by linear elastic fracture mechanics (LEFM) for cracks whose length in all direction is in the order of the millimetres [19,20]. Indeed, by plotting the crack growth rate da/dN as a function of the stress intensity factor range $\Delta K$ in a log-log scale, they obtained for most of the materials a sigmoid curve, as illustrated in Figure 2-9.

The crack growth rate da/dN is obtained by differentiation from the crack length a measured at different number of cycles N during fatigue testing. The stress intensity factor range $\Delta K$ is the difference between the stress intensity factors maximum $K_{max}$ and minimum $K_{min}$ during a fatigue cycle, as detailed in Eq. 2-1. The stress intensity factor K, qualifies the stress field at the crack tip due to the remote applied stress, and

it depends on that applied stress, the crack length and the geometry, as detailed in Eq. 2-2. The stress intensity factor also allows "quantifying the intrinsic resistance of the material to fatigue growth" [19]. The stress intensity factor range is dependent on the amplitude ratio, R, since R is the ratio of the minimum stress over the maximum stress during a fatigue cycle, as detailed in Eq. 2-3, hence a same specimen would have different da/dN vs ΔK curves for tests at different R ratios.

The plot of the fatigue crack growth rate as a function of the stress intensity factor range, shown in Figure 2-9, exhibits three different regimes of crack growth rate. In the regime A area, the crack growth rate is very slow, and there is a threshold value, $\Delta K_{th}$, under which no crack propagation occurs. Experimentally, this threshold is the stress intensity factor range corresponding to a maximum crack growth rate of $10^{-8}$ mm/cycle. In the regime C zone, the crack growth rate increases rapidly leading to catastrophic failure. In the regime B, the crack growth rate relationship with the stress intensity factor is linear. That section of the curve is described by the Paris law, as detailed in Eq. 2-4, and allows calculating the fatigue life to grow a crack from a size $a_0$ to a size $a_f$ by integrating the Paris Law, as shown in Eq. 2-5.

Eq. 2-1
$$\Delta K = K_{max} - K_{min}$$

Eq. 2-2
$$K = \beta \sigma \sqrt{\pi a}$$

*Where β is a geometrical factor, σ the applied load and **a** the crack length*

Eq. 2-3
$$R = \frac{\sigma_{min}}{\sigma_{max}} = \frac{K_{min}}{K_{max}}$$

Eq. 2-4
$$\frac{da}{dN} = C(\Delta K)^m$$

*Where C and m are material constants*

Eq. 2-5
$$N = \frac{2}{(m-2)C\beta^m (\Delta\sigma)^m \pi^{m/2}} \left( \frac{1}{a_0^{(m-2)/2}} - \frac{1}{a_f^{(m-2)/2}} \right) \text{ for } m \neq 2$$
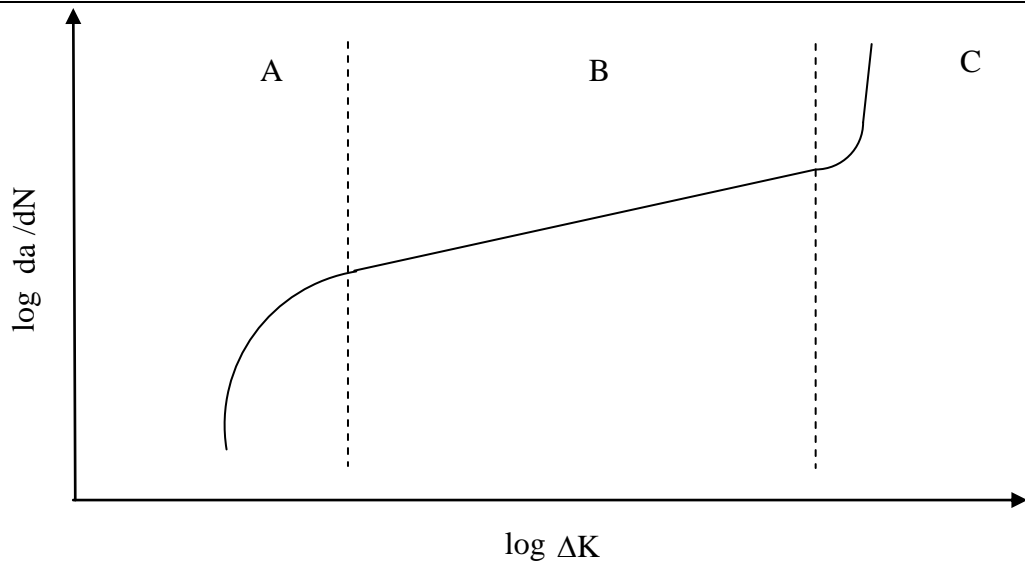
**Figure 2-9: Schematic plot of the fatigue crack growth rate as a function of the stress intensity factor range**

## 2.3.5 Design concepts

### 2.3.5.1 Safe-life approach

The safe-life approach consists of calculating the component lifetime during which no failure will occur. When the calculated life is reached, the component is removed from service whether fatigue signs are present or not.

As the service life of a component is relative of the stresses it will undergo, the load spectrum over the whole service time needs to be known. Then, laboratory tests are performed on coupons subjected to that load spectrum and an average fatigue life during which no fatigue damage has initiated is assessed. A safety factor is then affected to that average fatigue life, so that the period during which no fatigue cracks will occur in that component could be reliably given.

The safety factors, which are generally high, are used to compensate the factors which are not considered in that approach, such as a change in the load spectrum or the presence of an initial damage in the material for instance. Indeed, these factors have an influence on the fatigue life of the component, and could reduce it. However, the live affected with the safety factor might be too conservative, that is to say, the fatigue live of the material might be too largely underestimated. Therefore the component would be replaced too early, which means that the use of the material would not be optimum, hence an economic loss for the company.

In addition, the major drawback of the safe-life approach is that if a fatigue crack initiated during the calculated service life, it would not be detected and would lead to a premature failure with potentially catastrophic consequences.

### *2.3.5.2  Fail-safe approach*

Unlikely to the safe-life concept, the fail-safe approach was developed considering that fatigue cracks will occur during the component service life, but will not propagate to a critical state before the cracks be detected. Fail-safe designs might be structures with cracks arresters, for instance, which would slow down or even stop the crack from propagating. They can also be structures, called multiple load path (MLP), with redundant parts to allow a redistribution of the load in the intact components in case of failure of one of them.

Indeed, the concept of fail-safe lies on regular scheduled inspections, which allow the component to maintain a structural integrity sufficient enough to keep operating if a fatigue crack had developed between two inspections. However, the difficulty to detect the crack with non-destructive testing (NDT) methods, such as minimum detectable crack sizes or difficult access to the inspected component, makes that concept not applicable to every structure.

### *2.3.5.3  Damage tolerant approach*

Like the fail-safe approach, the damage tolerant concept considered the presence of fatigue cracks during the service life of a structure. The difference is that before its entry into service, the component is already considered as having an initial damage. During service life, the damage will developed into a crack, which will grow until reaching a particular size making the crack detectable by NDT methods. The time at which the flaw has reached the minimum detectable size is called first inspection threshold. Then using fracture mechanics concepts and materials properties, such as the toughness, the time to propagate the crack from the inspection threshold size to a critical size leading to the failure of the component is calculated. Knowing this interval of time, regular scheduled inspections are carried out to assess the progression of the crack and when the crack length is closed to its critical size, the structure is retired from service.

## 2.4 Corrosion fatigue

### 2.4.1 Principles

As seen in section 2.2, localised corrosion led to corrosion flaws generally in the shape of pits at the surface of the metal. These pits act as stress raisers, and when the metal is subjected to cyclic loading, fatigue cracks initiated from these defects, as explained in section 2.3.2. The combination of cyclic stresses and corrosive environment is defined as corrosion fatigue.

Fatigue crack initiation and propagation are very sensitive to the environment. Congleton and Craig [26] explained that the combined action of corrosion and fatigue generally decreased the fatigue life of a component since it has been observed that the fatigue crack initiation occurs earlier in a corrosive environment compare with an inert atmosphere and that the crack propagation rate is also increased in these conditions. However, in some particular cases, some aggressive environments coupled with high stresses, retard the fatigue crack nucleation. Nevertheless, the total fatigue life of the structure is not improved compare to the fatigue life in an inert environment.

Experiments on fatigue crack growth had highlighted three different ways of representing the crack propagation behaviour in corrosion fatigue [27,19], as detailed in Figure 2-10:

  a. True corrosion fatigue

In the true corrosion fatigue plot (a), where the action of cyclic loading is combined with an aggressive environment, it can be seen that the shape of the crack growth rate curve is similar to the crack growth rate curve in an inert environment. However the aggressive environment curve is higher, meaning that for a same value of stress intensity factor range, the crack growth rate in the corrosive environment is higher than in the inert environment. Therefore, as previously said, crack propagation is faster in a corrosive environment compare to an inert environment.

  b. Stress corrosion fatigue

In the stress corrosion fatigue plot (b), the crack growth rate curve in an inert environment is compared with the crack growth rate curve of combined fatigue and stress corrosion cracking. It is observed that the influence of stress corrosion cracking appears only when the stress intensity factor range reaches the value of the static stress intensity factor relating to stress corrosion cracking (SCC) in mode I, $K_{ISCC}$.

Below $K_{ISCC}$ the crack growth rate behaves like in the inert environment, whereas above $K_{ISS}$ the propagation rate steeply increased until failure of the material.

  c.   Mixed corrosion

In the mixed corrosion plot (c), the two previous behaviours are combined. For stress intensity factor ranges below $K_{ISCC}$, the true corrosion crack growth rate behaviour prevails, whereas above $K_{ISCC}$ the crack growth rate followed the stress corrosion fatigue trend.
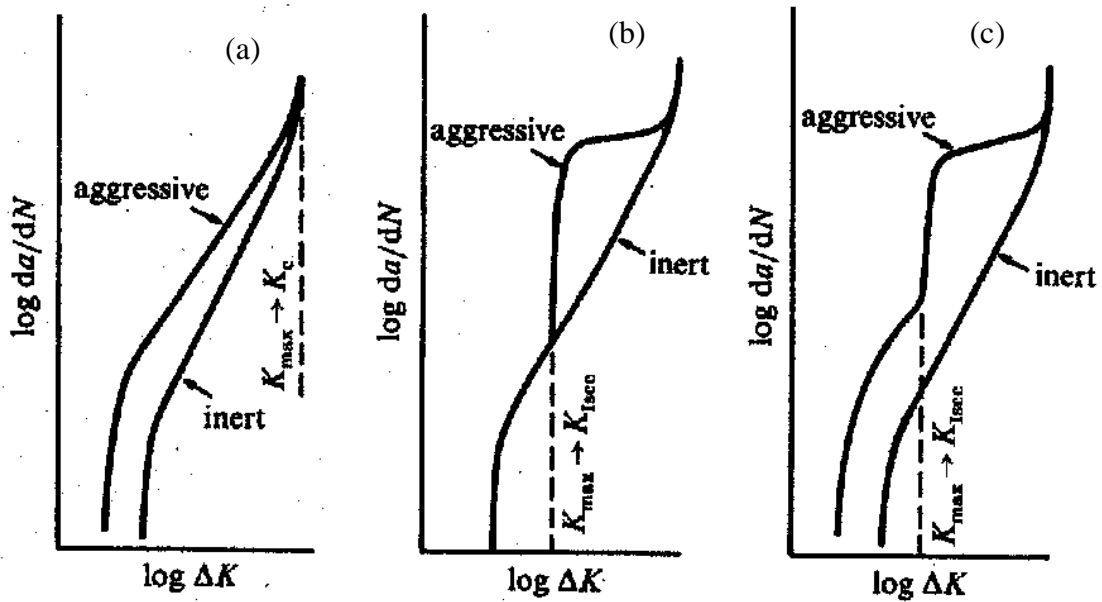


**Figure 2-10: Crack growth behaviour for true corrosion fatigue (a), stress corrosion fatigue (b) and mixed corrosion fatigue (c) [19]**

From these crack propagation behaviours, a superposition model was developed to estimate the crack growth rate considering the mechanical fatigue (mf), that is to say the phenomenon of fatigue in an inert environment, the corrosion fatigue (cf) and the stress corrosion cracking (scc), as detailed in Eq. 2-6.

**Eq. 2-6**
$$\left(\frac{da}{dN}\right)_{tot} = \left(\frac{da}{dN}\right)_{mf} + \left(\frac{da}{dN}\right)_{cf} + \left(\frac{da}{dN}\right)_{scc}$$

The main advantage of this superposition model is that it is easy to use, however it can only estimate the crack growth rate and not provide the actual growth rate. Indeed, the propagation rate depends on many parameters, such as the material, the composition of the environment, the cyclic stresses, etc..., which are not considered in

this model. Due to the complexity of such models, numerous studies have been conducted to developed models allowing the prediction of corrosion fatigue life of structures.

## 2.4.2 Models

A review of the literature regarding fatigue corrosion modelling has been carried out. Models have been developed for two different testing conditions: the first is the case where the specimen undergoes fatigue and corrosion simultaneously. In the second testing condition, the specimen is pre-corroded and then tested in fatigue.

Numerous models of corrosion fatigue are present in the literature [28-41].The aim of this section was to provide the reader with a selection of different models and criteria used to describe the phenomenon of corrosion fatigue.

### 2.4.2.1 Models for corrosion and fatigue simultaneously

In these particular conditions, two main theories have been proposed by Müller [28] and Kondo [29]. From these theories two criteria have arisen. Other authors have found these two criteria are not sufficient and have had added a third criterion, as described below.

#### 2.4.2.1.1 Critical pit size criterion

Müller [28] stated that a corrosion fatigue crack will initiate from a pit only if the pit reaches a critical size, which corresponds to Eq. 2-7. The critical pit size is calculated using elastic-plastic fracture mechanics based on the Dugdale model, as shown in Eq. 2-8. Considering that the growth kinetics of corrosion pits follows a power law, as detailed in Eq. 2-9, Müller expressed the time to reach the critical pit size, that is to say the time to initiate a fatigue crack from a pit, as shown in Eq. 2-10.

**Eq. 2-7**
$$d_L(t) = d_{CL}$$

*where $d_L$ is the pit depth and $d_{CL}$ the critical pit depth*

**Eq. 2-8**
$$d_{CL} = \frac{\cos\left(\dfrac{\pi\Delta\sigma_0}{4\sigma_{FC}}\right) \cdot \pi\Delta K_0^2}{32G^2\sigma_{FC}^2\left[1 - \cos\left(\dfrac{\pi\Delta\sigma_0}{4\sigma_{FC}}\right)\right]}$$

*where $\Delta\sigma_0$ is the applied stress range, $\Delta K_0$ the fatigue crack growth threshold, $\sigma_{FC}$ the cyclic yield strength and G a geometrical factor*

## 2. LITERATURE REVIEW

**Eq. 2-9**
$$d_L(t) = C_2(t - t_0)^\beta \qquad , t > t_0$$

*where $d_L$ is the pit depth, $t_0$ the incubation time for pit nucleation and $C_2$ a constant*

**Eq. 2-10**
$$t = \left(\frac{d_{CL}}{C_2}\right)^{1/\beta} + t_0$$

### 2.4.2.1.2 Critical growth rate

The second theory produced by Kondo [29] states that a fatigue crack will initiate from a pit, if the fatigue crack growth rate exceeds the pit growth rate, which corresponds to Eq. 2-11. Kondo considered the volume growth rate of the pit to be unchanged during the growth, which led to a pit growth law proportional to the time at the power one third, as detailed in Eq. 2-12. Then he expressed the time as a function of the number of cycles and frequency according to Eq. 2-13, to have a number of cycles based pit growth law (shown in Eq. 2-14). So by deriving the number of cycles based pit growth law, Kondo obtained the number of cycles based pit growth rate, as shown in Eq. 2-15, which can be comparable with the crack growth rate.

**Eq. 2-11**
$$\frac{da}{dN} \geq \frac{dc}{dN}$$

*where $\frac{da}{dN}$ is the crack growth rate and $\frac{dc}{dN}$ is the pit growth rate*

**Eq. 2-12**
$$c = C_p t^{1/3}$$

*where c is the pit size, t the time and $C_p$ a constant*

**Eq. 2-13**
$$N = f \cdot t$$

*where $N$ is the number of cycles, $f$ the frequency and $t$ the time*

**Eq. 2-14**
$$c = C_p \left(\frac{N}{f}\right)^{1/3}$$

**Eq. 2-15**
$$\frac{dc}{dN} = \frac{1}{3} C_p f^{-1/3} N^{-2/3}$$

**Eq. 2-16**
$$\Delta K = 2.24\sigma_a \sqrt{c \frac{\alpha\pi}{Q}}$$

*where $\Delta K$ is the stress intensity factor range, $\sigma_a$ the stress amplitude, $c$ the pit size, $\alpha$ the aspect ratio of the pit and $Q$ a shape factor*

**Eq. 2-17**
$$\frac{dc}{dt} = \frac{1}{3} \frac{C_p^3 \pi^2 \alpha^2 (2.24\sigma_a)^4}{Q} \Delta K^{-4}$$

Then, Kondo expressed the time as a function of the pit size according to Eq. 2-12 and substituted the time by this expression. Afterwards, Kondo used the stress intensity factor range, as detailed in Eq. 2-16, to express the pit size, c, and substitute it into the crack growth rate. This process led to an equation of the pit growth rate as a function of the stress intensity range, as shown in Eq. 2-17. Therefore, the pit growth rate and the crack growth rate can be easily compared as the fatigue growth rate is expressed as a function of the stress intensity range (Paris' law). Finally, Kondo identified the critical point condition, $(\Delta K)_p$, where the two growth rates are equal, and that the pit initiate a fatigue crack.

### 2.4.2.1.3 *Stress intensity threshold criterion*

Harlow and Wei [30] have developed a model for the prediction of corrosion-fatigue life which is divided into three regimes:

 i. "Time required for a nucleated pit to grow and for a surface crack to initiate from it: $t_{ci}$"

 ii. "Time required for the surface crack to grow into a through crack: $t_{tc}$"

 iii. "Time for a through crack to grow to a prescribed critical length, given as part of a failure criterion: $t_{cg}$"

In this research, only the expression of $t_{ci}$ is examined.

To express $t_{ci}$, Harlow and Wei have based their model on Kondo's [29]. Indeed, they considered that the pit remains hemispherical in shape and grows at constant volumetric rate. The difference with Kondo is in the expression of the volume rate that Harlow and Wei have developed and expressed following thermodynamic data, as shown in Eq. 2-18. By integrating the right hand side of Eq. 2-19 between $t_0$, the time at which a nucleated pit is considered, and $t_{ci}$, the time at which this considered nucleated pit had initiated a surface crack, then the expression of $t_{ci}$ is obtained. This equation is detailed in Eq. 2-19. The pit size at which a crack initiated is known by using the stress intensity threshold criterion. Indeed, the authors stated that "the surface crack is assumed to nucleate from a hemispherical corrosion pit when the stress intensity factor range of the pit equivalent to a crack, $\Delta K_s$, increases to the threshold driving force for fatigue crack growth, $\Delta K_{th}$." [30]. Therefore, by equalling

the stress intensity factor range, detailed in Eq. 2-20, to the stress intensity threshold, the critical pit size is obtained, as shown in Eq. 2-21. Then, this critical pit size is substituted in Eq. 2-19, and $t_{ci}$ is known.

**Eq. 2-18**
$$\frac{dV}{dt} = 2\pi a^2 \frac{da}{dt} = \frac{MI_{p_0}}{nF\rho} \exp\left(-\frac{\Delta H}{RT}\right)$$

*where $a$ is the pit size, $M$ the molecular weight, $I_{p_0}$ the pitting current density, $n$ the valence, $F$ the Faraday's constant, $\rho$ the density, $\Delta H$ the activation energy, $T$ the absolute temperature and $R$ the universal gas constant.*

**Eq. 2-19**
$$t_{ci} = \frac{2\pi nF\rho}{3MI_{p_0}}\left(a_{ci}^3 - a_0^3\right)\exp\left(\frac{\Delta H}{RT}\right)$$

*where $a_{ci}$ is the pit size at which a crack initiated and $a_0$ the initial pit size*

**Eq. 2-20**
$$\Delta K_s = \frac{2.2}{\pi} k_t \Delta\sigma \sqrt{\pi \cdot a}$$

*where $a$ is the pit size, $k_t$ a stress concentration factor and $\Delta\sigma$ the stress range*

**Eq. 2-21**
$$a_{ci} = \pi\left(\frac{\Delta K_{th}}{2.2k_t\Delta\sigma}\right)^2$$

*2.4.2.1.4  Growth rate competition and stress intensity threshold criteria*

In their model, Chen et al. [31] used two criteria to describe the transition from a pit to a fatigue crack. Indeed, their experiments showed them that using the stress intensity threshold criterion alone was not sufficient. However, they showed that by using the stress intensity threshold criterion along with the growth rate competition criterion, the analytical results were consistent with the experimental results.

The expression of the stress intensity threshold is given in Eq. 2-22. The critical pit size, $c_{tr}$, is known by using the growth rate criterion. The pit growth rate, as detailed in Eq. 2-23, is obtained by assuming the pit volume rate as constant. The crack growth rate is obtained using the Paris' law and considering the stress intensity factor range as maximum. The rate in the Paris' law is expressed as a function of the number of cycles, N, whereas the pit growth rate is a function of the time. So, to be able to compare the rates, the authors have expressed the crack growth rate as a fun

ction of the time by using the relation $N = t \cdot f$ and by showing with their results that "the corrosion fatigue crack growth rate is independent of frequency" for the material used in their experiments (2024-T3 aluminium alloy). The crack growth rate is detailed in Eq. 2-24. The crack growth rate criterion provides the critical pits size, as shown in Eq. 2-25. Then this critical pit size is substituted in Eq. 2-22.

**Eq. 2-22**
$$\Delta K_{th} = \frac{1.12 k_t \Delta\sigma \sqrt{\pi c_{tr}}}{\Phi_{tr}}$$

*where $\Delta K_{th}$ is the stress intensity threshold, $k_t$ a stress concentration factor, $\Delta\sigma$ the stress range, $\Phi_{tr}$ a shape factor and $c_{tr}$ the critical pit size*

**Eq. 2-23**
$$\left(\frac{dc}{dt}\right)_{pit} = \frac{C_p}{2\pi} \beta^2 c^{-2}$$

*where $\left(\frac{dc}{dt}\right)_{pit}$ is the pit growth rate, $C_p$ a constant, $\beta$ the pit aspect ratio and $c$ the pit size*

**Eq. 2-24**
$$\left(\frac{dc}{dt}\right)_{crack} = C_F^* \left(1.12 \frac{k_t \Delta\sigma}{\Phi}\right)^n (\pi c)^{n/2} f$$

*where $\left(\frac{dc}{dt}\right)_{crack}$ is the crack growth rate, $C_F^*$ and $n$ are material constants, $f$ the frequency, $k_t$ a stress concentration factor, $\Delta\sigma$ the stress range, $\Phi$ a shape facto and $c$ the pit size.*

**Eq. 2-25**
$$c_{tr} = \left[\frac{C_P \beta_{tr}^2 \Phi^n}{2\pi C_F (k_t \Delta\sigma)^n}\right]^{\frac{2}{n+4}} \left(\frac{1}{f}\right)^{\frac{2}{n+4}}$$

Other authors, Shi and Mahadevan [32], have also used these two criteria to establish the time for a nucleated pit to initiate a fatigue crack. As Harlow and Wei [30], they have divided the corrosion fatigue life in different regimes. In this model, they have considered seven different stages:

    i. Pit nucleation

    ii. Pit growth

    iii. Transition from pitting to fatigue crack nucleation

    iv. Short crack growth

    v. Transition from short crack growth

    vi. Long crack growth

    vii. Fracture

Like in the previous models, they have also considered that the pit grows at a constant volumetric rate. From this assumption, they obtained the corrosion pit growth law and therefore the time for a pit of a given size to reach the critical pit size which will initiate a fatigue crack, as shown in Eq. 2-26. It can be noticed that this equation is identical to Harlow and Wei's equation (Eq. 2-19).

**Eq. 2-26**
$$t_{ci} = \frac{2\pi nF\rho}{3MI_{p_0}}\left(a_{ci}^3 - a_0^3\right)\exp\left(\frac{\Delta H}{RT}\right)$$

*where $a_{ci}$ is the pit size at which a crack initiated and $a_0$ the initial pit size*

In order to calculate the critical pit size, they used both the stress intensity threshold criterion, as shown in Eq. 2-27, and the growth rate competition criterion. The pit growth rate is given in Eq. 2-28 and the short crack growth rate in Eq. 2-29. However, the pit growth rate is a time based rate whereas the crack growth rate is a number of cycles based rate. Therefore, they need to express the crack growth rate as a function of the time to be able to compare the two rates. As the corrosion fatigue crack growth rate for the material used in their experiments (2024-T3 aluminium alloy) is independent of the frequency, it is possible to express the crack growth rate in a time base, as shown in Eq. 2-30.

Then by substituting in Eq. 2-30, the stress intensity factor by Eq. 2-27 and by applying the growth rate competition criterion, Shi and Mahadevan expressed the critical pit size, as detailed in Eq. 2-31. Finally, they substituted Eq. 2-31 in Eq. 2-26, and they have expressed the time for a nucleated pit to initiate a short fatigue crack.

**Eq. 2-27**
$$\left(\Delta K\right)_{pit} = \frac{1.12k_t\Delta\sigma\sqrt{\pi a_{ci}}}{\Phi} = \Delta K_{th}$$

**Eq. 2-28**
$$\frac{da}{dt} = \frac{C_p}{2\pi a^2}$$

*where $\frac{da}{dt}$ is the pit growth rate, $C_p$ a constant, and $a$ the pit size*

**Eq. 2-29**
$$\frac{da}{dN} = C_{sc}\left(\Delta K\right)^{m_{sc}}$$

*where $\frac{da}{dN}$ is the number of cycles based crack growth rate, $C_{sc}$ and $m_{sc}$ are materials*

*constant and $\Delta K$ the stress intensity factor.*

**Eq. 2-30**
$$\frac{da}{dt} = C_{sc}(\Delta K)^{m_{sc}} f$$

where $\dfrac{da}{dt}$ is the time base crack growth rate, $f$ is the frequency, $C_{sc}$ and $m_{sc}$ are materials constant and $\Delta K$ the stress intensity factor.

**Eq. 2-31**
$$a_{ci} = \left(\frac{C_p}{2\pi C_{sc} f}\right)^{\frac{2}{m_{sc}+4}} \left(\frac{\Phi}{1.12 k_t \Delta\sigma \sqrt{\pi}}\right)^{\frac{2m_{sc}}{m_{sc}+4}}$$

### 2.4.2.2 Models for fatigue with pre-existing corrosion

The only model for fatigue with pre-existing corrosion found in the literature was proposed by Wang et al. [33] but no detail is given regarding the origin of the equation used in the model. In their model, the authors distinguished two stages in the corrosion fatigue life: the initiation and the propagation. In the case of fatigue with pre-existing corrosion, they said that "the initiation life contribution from pit-growth may be ignored".

The fatigue life is expressed in Eq. 2-32, with the initiation stage detailed in Eq. 2-33 and the propagation stage shown in Eq. 2-34.

**Eq. 2-32**
$$N_f = N_i + N_P$$

**Eq. 2-33**
$$N_i = \frac{18 G \Delta K_{th}^2 (G + G_i) h^2}{(\Delta\sigma - \Delta\sigma_0^R) E G_i (h+l)^2 a_0}$$

**Eq. 2-34**
$$N_p = \frac{a_0^{(1-n/2)}}{C\Delta\sigma^n \beta_1^n k_t^n \pi^{n/2} \left(\dfrac{n}{2}-1\right)}$$

where $N$ is the number of cycles, $G$ the bulk shear modulus, $\Delta K_{th}$ the stress intensity threshold, $G_i$ the shear modulus of pitting, $E$ the elastic modulus, $h$ is the semi-minor length of the elliptical slip band area, $l$ the semi-length of slip band, $\Delta\sigma$ the stress range, $\Delta\sigma_0^R$ the fatigue limit at a stress range of ratio R, $a_0$ the initial pit size, $C$ and $n$ constants, $\beta_1$ the aspect ratio, and $k_t$ the stress concentration factor.

# 3 EXPERIMENTAL METHODS

## 3.1 Materials

### 3.1.1 15-5PH

The material investigated in this research was the 15-5PH (H1025) precipitation hardened stainless steel. The composition of 15-5PH, detailed in Table 3-1, as well as the H1025 heat treatment are said to ensure a δ-ferrite free martensitic microstructure and a high strength steel. In order to confirm that the batch of material used in this research met all the expected property requirements, microstructure and micro-hardness tests were carried out on 15-5PH samples.

| C | Si | Mn | Cr | Ni | Mo | Cu | P | S | Nb |
|---|---|---|---|---|---|---|---|---|---|
| 0.043 | 0.37 | 0.54 | 15.23 | 4.30 | 0.20 | 3.28 | 0.027 | 0.001 | 0.32 |

**Table 3-1: Chemical composition of 15-5PH stainless steel [47]**

Two different kinds of specimens were available for this project: 100x50x6mm rectangular panels and tension test specimens, as illustrated in Figure 3-1. The rectangular panels were mainly used for the corrosion testing, whereas the tension test specimens were used for fatigue testing.



**Figure 3-1: Specimen geometry**

## 3.1.2 Microstructure and δ-ferrite detection

Three sections of a 15-5PH panel were cut out following the three material directions (L: longitudinal, T: transverse and S: short transverse). These sections were mounted in Bakelite and polished with silicon carbide paper and diamond paste to give a 6μm finish. The samples in the T and S directions were swabbed for times between a few seconds to a minute in an etchant composed of 45ml of glycerol, 15ml of nitric acid and 30ml of hydrochloric acid in accordance with Petzow [48]. The sample in the L direction was electrolytically etched for a few seconds in a solution containing 20g of sodium hydroxide in 100ml of water according to the E407-99 ASTM standard [49]. The first etch reveals martensitic structure, whereas the second etch has the property of darkening δ-ferrite, notably in precipitation hardened stainless steels. Finally, the samples were observed with an optical microscope at different magnifications and pictures of the microstructure were taken.

### 3.1.2.1 Microstructure

Martensitic microstructures are characterised either by needles, laths or plates depending on the composition of the metal. The microstructure of the 15-5PH samples, displayed in Figure 3-2, exhibit needles throughout the whole surface, which confirm the matensitic structure of 15-5PH. The size of the needles was assessed and a maximum width of 5μm was found. At higher magnification, small particle-like features, which appeared black under the optical microscope, were noticed in the microstructure. The samples were then examined with a scanning electron microscope and two different types of features appeared under the electron beam, as illustrated in Figure 3-3: black features and small (<1μm) white ones. Element analyses were performed on these features on different areas of the sample. The large black features were found to be composed of around 35%wt of aluminium and 42%wt of oxygen. From this composition, it was suggested that the black features were alumina inclusions, which are thought to have resulted from the addition of aluminium to deoxidise the steel. When element analyses were performed on the small white features, the composition obtained was very close to the composition of 15-5PH stainless steel at the exception that it was slightly richer in niobium. It is important to notice that these white features were generally smaller than the diameter of the electron beam. Therefore not only the feature was analysed but also the metal surrounding. Moreover, the smaller the

feature was, the larger the part of the surrounding metal was included in the analysis. Although the small white features could not be properly identified, their high content of niobium could suggest that these features result from addition of niobium in 15-5PH. Indeed, it is understood that niobium is added to precipitation hardening stainless steels to act as a strengthener as it is a strong carbide former [51].
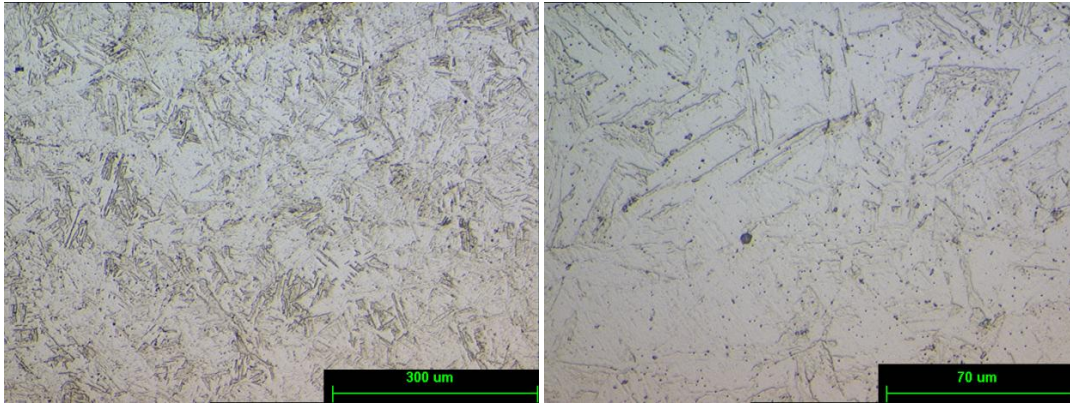


**Figure 3-2: Microstructure of 15-5PH ibserved with an optical microscope**



**Figure 3-3: Microstructure of 15-5PH observed with a scanning electron microscope**

### *3.1.2.2  δ-ferrite*

The microstructure of the 15-5PH sample after being etched in a solution darkening δ-ferrite is displayed in Figure 3-4. No dark areas were observed in the microstructure, which means that no δ-ferrite was present in the microstructure. However, the small particle-like features were also observed in that sample.
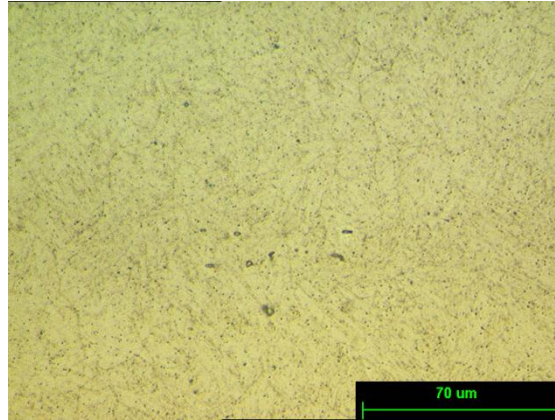


**Figure 3-4: Microstructure of 15-5PH after being etched to reveal δ-ferrite**

## 3.1.3  Micro-hardness testing

The micro-hardness was performed using a load of 1kgf for 15 seconds on the three samples (following the L, T and S directions) prepared for the microstructure and δ-ferrite detection. Four micro-hardness measurements were taken for each direction, as detailed in Table 3-2. Then the average of the four measurements for each sample was converted to an approximate ultimate tensile strength (UTS) value using a hardness conversion table [52]. The UTS estimated from the micro-hardness tests was found to be around 1300MPa in each material direction, which was higher than the typical UTS of 1200MPa reported by the manufacturer [47]. However, it is important to notice that micro-hardness measurements are not an accurate technique to measure the UTS of material, and have to be seen as an estimation only. Therefore, although the UTS assessed for this batch of material was different from the UTS reported by the manufacturer, the batch of 15-5PH used in that experiment was considered as meeting the mechanical property requirement since the estimated UTS was found to be higher than the typical UTS. Tensile testing would have had to be performed to obtain an

accurate value for the UTS, but due to the limited number of samples, the priority was given to fatigue testing.

| | Sample L | Sample T | Sample S |
|---|---|---|---|
| Hardness 1 (Hv) | 394 | 386 | 400 |
| Hardness 2 (Hv) | 406 | 412 | 450 |
| Hardness 3 (Hv) | 422 | 408 | 428 |
| Hardness 4 (Hv) | 407 | 407 | 417 |
| **Average hardness (Hv)** | **407** | **403** | **424** |
| **Estimated UTS (MPa)** | **1303** | **1291** | **1354** |

**Table 3-2: Vickers hardness measurement and estimated UTS**

Therefore, the batch of 15-5PH stainless steel under testing in this research met all the expected property requirements according to the material supplier. Indeed, the microstructure was found to be martensitic and δ-ferrite free and the estimated ultimate tensile strength reached the minimum of 1200MPa.

## 3.2 Pitting corrosion testing

The aim of these experiments was to assess the susceptibility to pitting corrosion of 15-5PH and investigate the size and distribution of corrosion pits developed after different periods of testing in neutral salt fog environment. The effect of the surface polishing of the panels in the initiation and propagation of pits in 15-5PH was also examined.

### 3.2.1 Specimen preparation

Three rectangular panels (100x50x6mm) were used for these experiments. One of the main surfaces of each panel was polished following the process below:

  i. Polish with a 15μm Kemet liquid diamond suspension and a DP-Plan polishing cloth.

  ii. Polish with a 9μm Metprep water based diamond solution and a Texmet polishing cloth.

  iii. Polish with a 6μm Metprep water based diamond solution and a DP-Dac polishing cloth.

The time of polishing required for each stage was different from one panel to another and was left to the discretion of the experimenter. Then the panels were cleaned and degreased with isopropanol. Finally the panels were coated with Lacomit lacquer on all the surfaces but the polished one, to prevent pitting initiation.

Once the samples were polished and coated, they were put in the salt spray cabinet.

## 3.2.2 Salt spray cabinet

A salt spray cabinet is an enclosure where fog is sprayed from an atomiser jet. The fog is made from a salt solution which is pumped from a water tank and then atomised by compressed air. In these experiments, the testing was made in a neutral salt fog environment using a 5%NaCl concentrated solution according to the B117-03 ASTM standard [50].

The polished rectangular panels were exposed for 18 days, 3 weeks and 4 weeks with a 45 degree angle. During the exposure time, all samples were regularly turned around and put in different places inside the cabinet for the same amount of time in order that they should receive similar fog deposition. Once their respective exposure time was completed, the samples were removed from the salt spray cabinet and gently cleaned with water to remove the salt deposits.

To measure the pit size distribution for each exposure time, the samples were then observed with an optical microscope fitted with an image analyser software.

## 3.2.3 Image analysis

In order to have a good representation of the pit size distribution over the whole area of each sample, the corroded surface of each panel was divided into twenty-four equal zones (6x4). In each zone, a particular area was considered by the experimenter and a picture of that area was taken. The pits contained in the area were then detected by the LEICA image analysis software by setting a grey level which was determined by the experimenter for each area. Once the pits were detected, the software measured the length and width of each detected pit in the considered area. Finally, the measurements were sorted by 0.5µm size intervals and the pit size distributions were plotted. For each pit size distribution, extreme value statistics were applied to predict the most probable size of the largest pit for a given exposure time. Extreme value statistics were chosen because it is known that the failure of a component by pitting is caused by the deepest pit, and that pit depth is dependent of the sample size [48].

## 3.2.4 Extreme value statistics

Extreme value statistics were founded by Gumbel [53, 54] and forecast an extreme value (e.g. depth, length, etc…) in a sample of a certain size from the observations of the extremes in a sample of a given size. Shibata [55] had shown how this theory could be applied to corrosion and particularly to the forecast of the maximum pit depth in a metallic part.

In this research, extreme value statistics were used to predict the most probable length and width of the largest pit for different exposure times. To obtain these values, the twenty highest values of each pit size distribution were ranked in decreasing order. Then the cumulative probability, F(y), of having a pit size (length or width) x and the reduced variable, y, were calculated for each value according to Eq. 3-1[55] and Eq. 3-2[55]. Finally a plot of the reduced variable, y, as a function of the pit size was drawn for each exposure time. Each plot was approximated by a best-fitting straight line of which the general expression is detailed in Eq. 3-3[55]. Then by knowing the slope coefficient and intercept point of the best-fitting line, the standard deviation, α, and the location parameter, λ, were identified and the most probable size of the largest pit, x, was calculated according to Eq. 3-4[55].

**Eq. 3-1**
$$F(y) = 1 - \frac{i}{1+n}$$

*where        i is the i th of the ordered value x in descending order*

*n is the total number of ordered values*

**Eq. 3-2**
$$y = -\ln(-\ln(F(y)))$$

**Eq. 3-3**
$$y = \frac{1}{\alpha} x - \frac{\lambda}{\alpha}$$

**Eq. 3-4**
$$x = \alpha \ln(n) + \lambda$$

## 3.3 Crevice corrosion testing

Areas of pit-like corrosion damage, best described as crevice corrosion (cf. Section 2.2 for details), were observed on several specimens in the salt spray cabinet and were thought to be the most significant cause of large pit-flaws in landing gear manufactured from high strength stainless steels, as shown in Figure 3-5. This damage could be expected to form in regions where the surface was contaminated by debris or covered by a seal and where water has penetrated. Therefore, it was decided to assess the susceptibility of 15-5PH stainless steel to crevice corrosion. For that rectangular panels and tension test specimens were fitted with crevice former and placed in a salt spray cabinet.
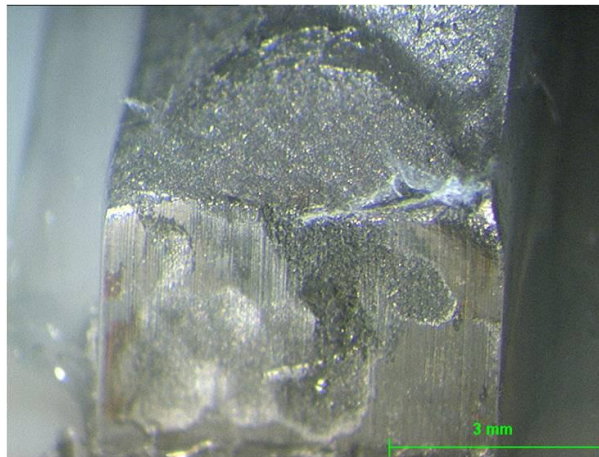


**Figure 3-5: Crevice corrosion flaw having caused failure of the specimen**

### 3.3.1 Specimen preparation

Nine rectangular panels with two M6 holes drilled in each specimen were used in two sets of experiments. In the first set, four panels were used in their initial condition. In the second set of experiments, five specimens were reground by the Cranfield University workshop to achieve different surface finish in order to examine the effect of the surface roughness on the initiation of crevice corrosion in 15-5PH. The surface roughness (Ra) of each specimen were measured using a Talysurf profilometer and is detailed in Table 3-3. Then the panels were cleaned, degreased with isopropanol and fitted with crevice formers.

| | Panel | Ra upper face (μm) | Ra lower face (μm) |
|---|---|---|---|
| 1st set of experiments | 24E | 0.8 | 0.4 |
| | 7D | 0.8 | 0.5 |
| | 5E | 0.8 | 0.5 |
| | 36F | 0.9 | 0.5 |
| 2nd set of experiments | 12D | 1.4 | 1.3 |
| | 1B | 0.8 | 0.7 |
| | 33F | 1.0 | 0.8 |
| | 34F | 1.9 | 1.7 |
| | 6E | 2.2 | 1.1 |

**Table 3-3: Surface roughness (Ra) of the rectangular panels**

## 3.3.2 Crevice former

The crevice formers were made of Perspex in order to be able to see the formation of crevice corrosion during the experiments. They were castellated and designed to give eighteen individual crevice corrosion sites, as shown in Figure 3-6, so that the severity of attack could be assessed by counting the number of sites that had become active.

Four crevice formers were assembled on each panel, as illustrated in Figure 3-7. The assembly of each side of a hole consisted of a M6 stainless steel bolt, a stainless steel washer, a crevice former, the 15-5PH stainless steel panel, another crevice former, another stainless steel washer and finally a stainless steel nut. The bolts tightening the crevice formers were wrapped in PTFE tape, as shown in Figure 3-8 to prevent any contact with the panel and thus any galvanic corrosion.



**Figure 3-6: Crevice former for rectangular panels**

## 3. EXPERIMENTAL METHODS
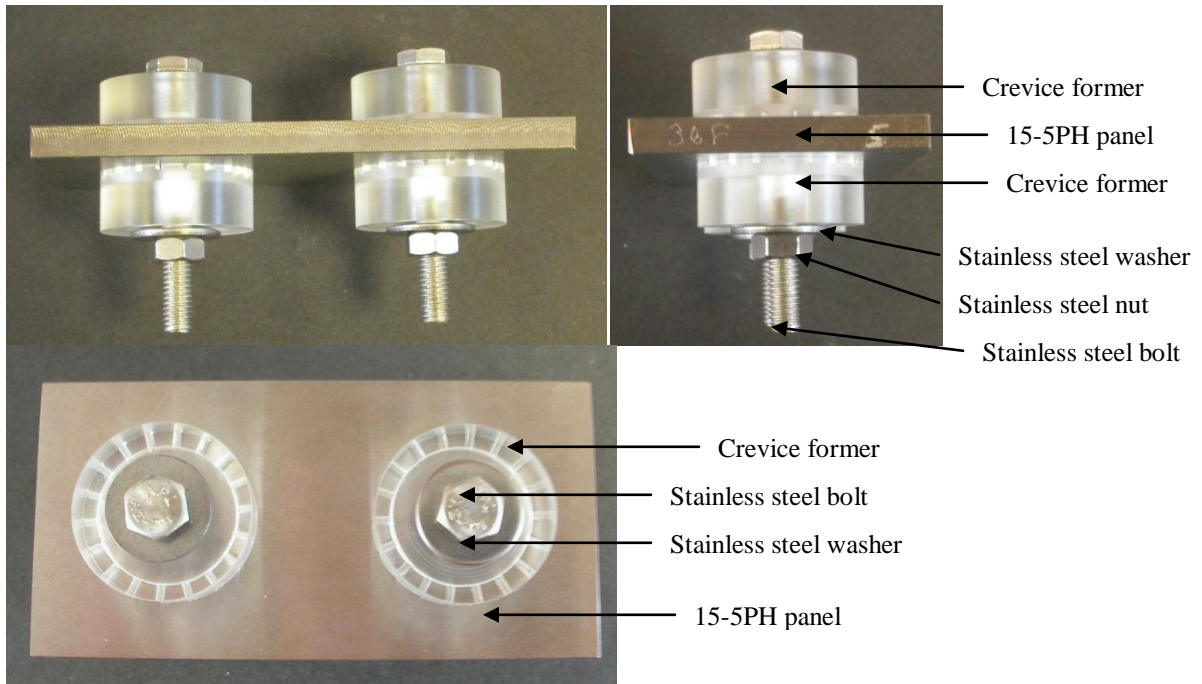


**Figure 3-7: Crevice formers assembled on 15-5PH stainless steel panels**



**Figure 3-8: Stainless steel bolts wrapped with PTFE tape to avoid galvanic corrosion**

In order to be consistent, the torque applied to the bolts had to be the same for each panel in a same set of experiments. Two arbitrary torques were applied: the torque applied to each bolt was 0.138 Nm in the first set of experiments, whereas in the second one the torque applied was 1 Nm. According to Oldfield [12] and Kain [13], the thightness between the crevice former and the material is a significant parameter, this is why the second experiment was performed with a higher torque.

Once the panels were fitted with the crevice formers, they were placed in the salt spray cabinet for various amounts of time.

### 3.3.3 Exposure conditions

The panels were left in the salt spray cabinet until a maximum of sites had initiated and propagated a corrosion flaw. The moment chosen to remove the panels was left at the experimenter discretion after 4 to 6 weeks of exposure. The four panels of the first set of experiments were left in the salt spray cabinet for 1941 hours, whereas for the second set of experiments the five panels were exposed for 768 hours. All the panels were set with an angle of 45 degree in the salt spray cabinet, leading to different conditions on each face of a panel, since one face (the upper face) was more exposed to the fog than the other (the lower face). Thus, at the end of the experiments, two sets of data were collected for each panel. During the exposure time, all samples were regularly put in different places inside the cabinet for the same amount of time in order that they should receive similar fog deposition. Once their respective exposure time was completed, the samples were removed from the salt spray cabinet and gently cleaned with water to remove the salt deposits. The samples were regularly taken out of the salt spray cabinet to record the crevice corrosion initiation and propagation through the crevice formers.

### 3.3.4 Image analysis

The Perspex allowed the detection of active crevice corrosion through the crevice former. Therefore, the number of active crevices on each face of each panel was noted regularly. In addition, pictures of the active crevices were taken at different times with a stereomicroscope fitted with a CCTV camera.

#### 3.3.4.1 Surface area measurement

The software VistaMetrix was used to measure the area of active crevices from the pictures of the panel surface taken through the crevice former during the experiments. A transparent overlay was placed above the considered picture, as illustrated in Figure 3-9. The scale was moved and adjusted to match the scale of the picture. Then a closed path was traced around the area of active crevice corrosion, and the area was automatically assessed by the software.

Therefore, it was possible to record the propagation of active crevice corrosion for each site of each panel at different times. The data were then sorted by interval sizes, and the distributions of the active crevice corrosion surface area for different times were plotted using histograms.

*a) Picture of the considered active crevice site*
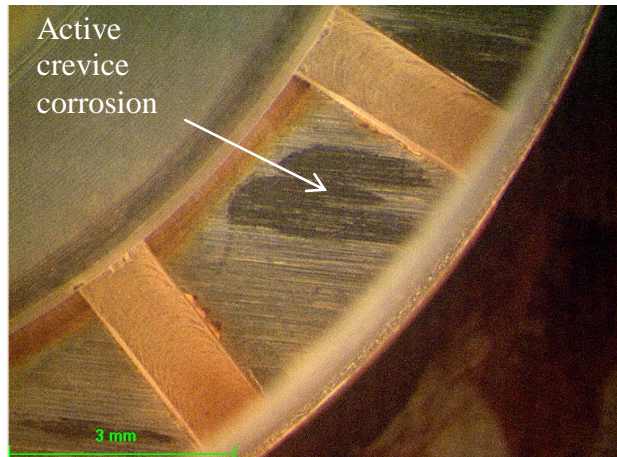


*b) The VistaMetrix scale is matched with the scale of the picture*
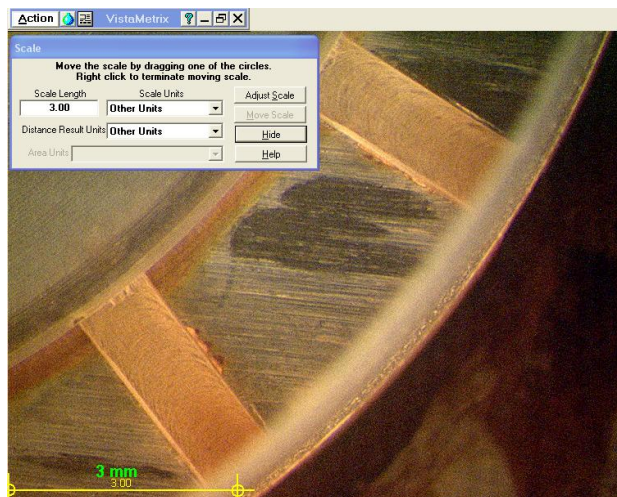


*c) A path is drawn around the area of active crevice corrosion, and the value of the area is measured*
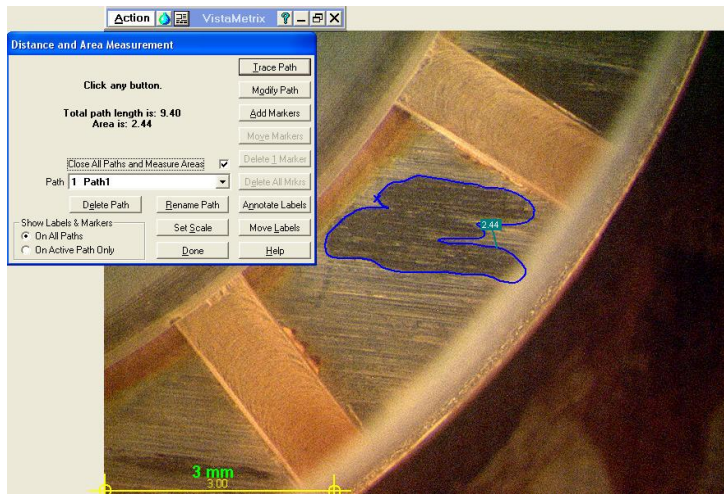


**Figure 3-9: Illustration of the steps carried out to measure the area of active crevice corrosion**

### *3.3.4.2 Depth measurement*

The active crevice corrosion depth was measured with a confocal laser scanning microscope. However, when the crevice formers were in place, the measurements were not possible, as the height of the crevice former prevented the confocal laser scanning microscope to reach its working distance. Moreover, the crevice formers could not be removed during the experiments to allow the measurement, because this would have changed the conditions into the crevices and therefore disrupted the corrosion process. Thus the measurement of the depth of active crevice corrosion through time was not possible. Hence, it was decided that the depth of the active crevice corrosion would only be measured at the end of the exposure time, once the experiment was finished and the crevice formers could be removed.

To measure the depth of the active crevice corrosion, the lowest and highest focal point had to be set by the experimenter, as well as the contrast and brightness for the different focal plans. Then the active corrosion area was scanned and 2D and 3D image of the active crevice corrosion was displayed, as illustrated in Figure 3-10. Then these images were scanned with a horizontal profile line cursor by the experimenter. From the profiles obtained, the depth of the deepest point and the average depth for the whole damage were recorded. The data were then sorted by interval sizes, and the distributions of the crevice corrosion deepest point and average area were plotted using histograms.

## 3.3.5   Extreme value statistics

The principle described in section 3.2.4 was applied to assess the most probable maximum area of active crevice corrosion for different exposure times. However, unlike section 3.2.4, the values considered were not the only twenty highest values for each distribution but all the values.

Regarding the most probable maximum depth of active crevice corrosion all the depth measurements were considered in the extreme value statistics. However the most probable maximum depth of active crevice corrosion was assessed for only two different exposure times for the reasons given in section 3.3.4.2: after 1941 hours for the panels used in the first set of crevice corrosion testing, and 768 hours for the panels of the second set of experiments.

Profile cursor
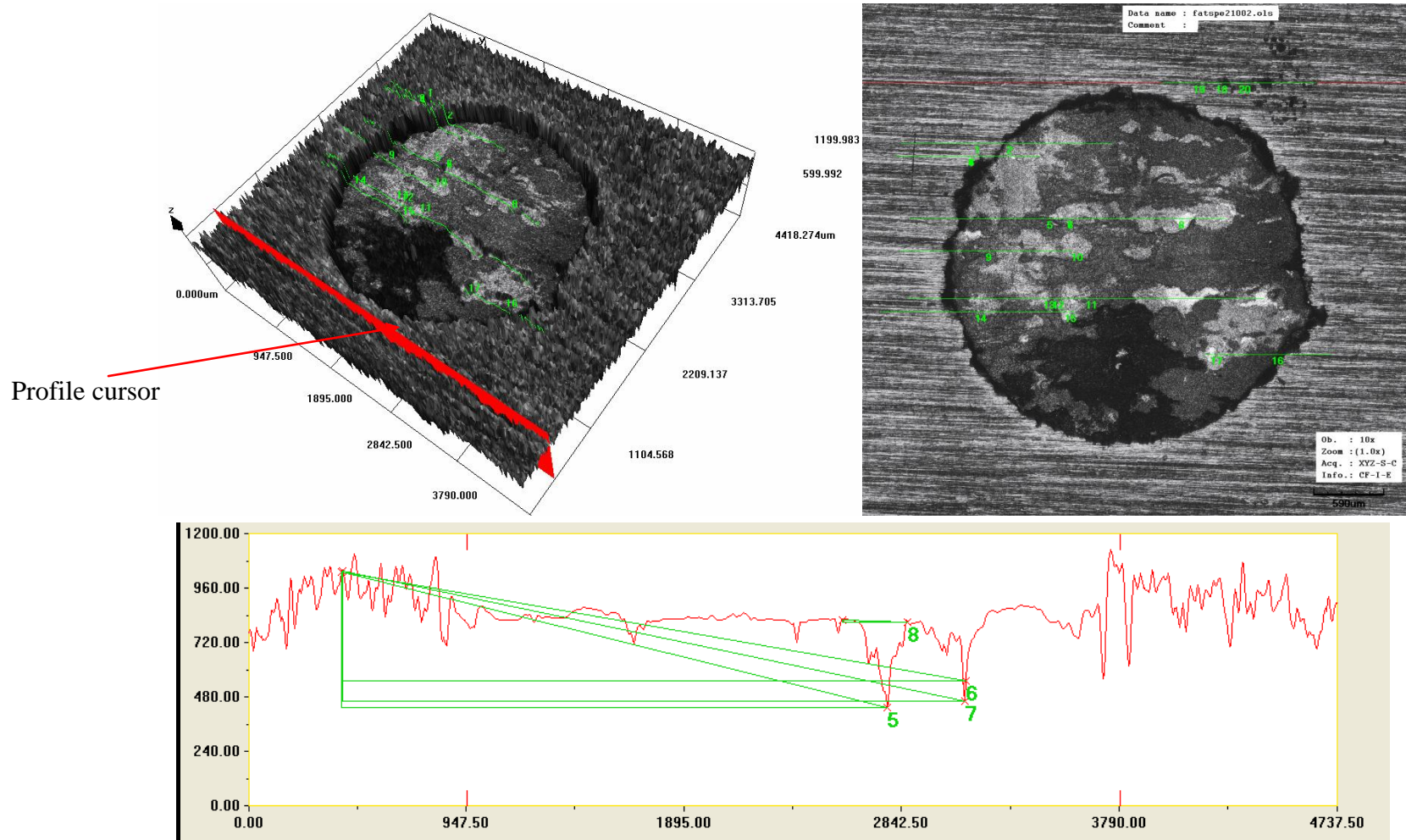
**Figure 3-10: 2D and 3D images of a corrosion damage and profile**

## 3.4 Fatigue testing

Tension test specimens, illustrated in Figure 3-11, with a 30x12x6mm gauge length, were used to carry out fatigue crack growth rate and corrosion fatigue testing. Tests were performed either in air or in corrosive environment, and different techniques were considered to monitor the fatigue crack development.



**Figure 3-11: Tension test specimen**

### 3.4.1 Cell design

In order to carry out fatigue testing in corrosive environment, a cell was designed to contain a 3.5% NaCl solution. The cell needed to be easy to remove and replace so that access to the crack for measurement can be possible during the fatigue test. A cell consisting of a fixed base and a removable supple tube was first designed. The base was composed of two identical semi PTFE circles which fitted the tension test specimens just under the gauge length, as shown in Figure 3-12. The semi circles were tightened around the specimen by two stainless bolts and then sealed with silicon sealant to prevent leakage of the salt solution. Finally, a removable rubber tube, long enough to cover the gauge length, was fitted around the base, as illustrated in Figure 3-12.

The main advantages of this first cell were that it was easy to produce, and access to the crack was possible by just peeling down the supple tube. However, because of the opacity of the rubber tube it was not possible to see the crack without removing the tube. Therefore, a second cell was designed where the crack was visible through the cell.
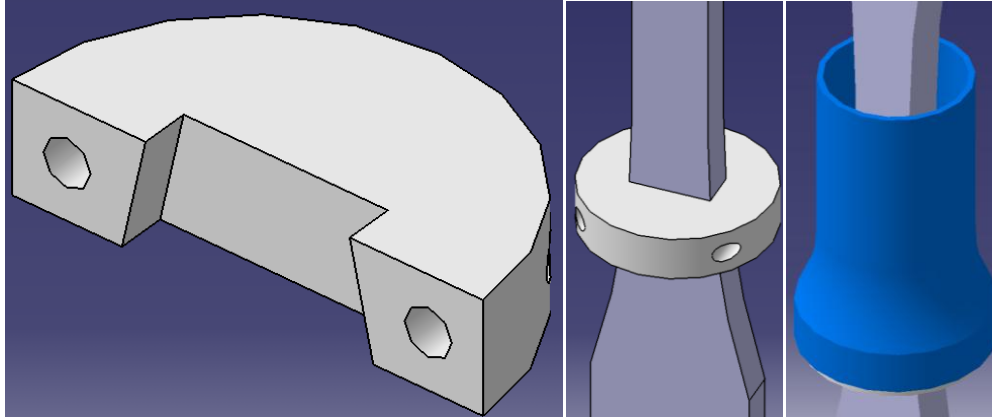
**Figure 3-12: Sketch of the first cell**
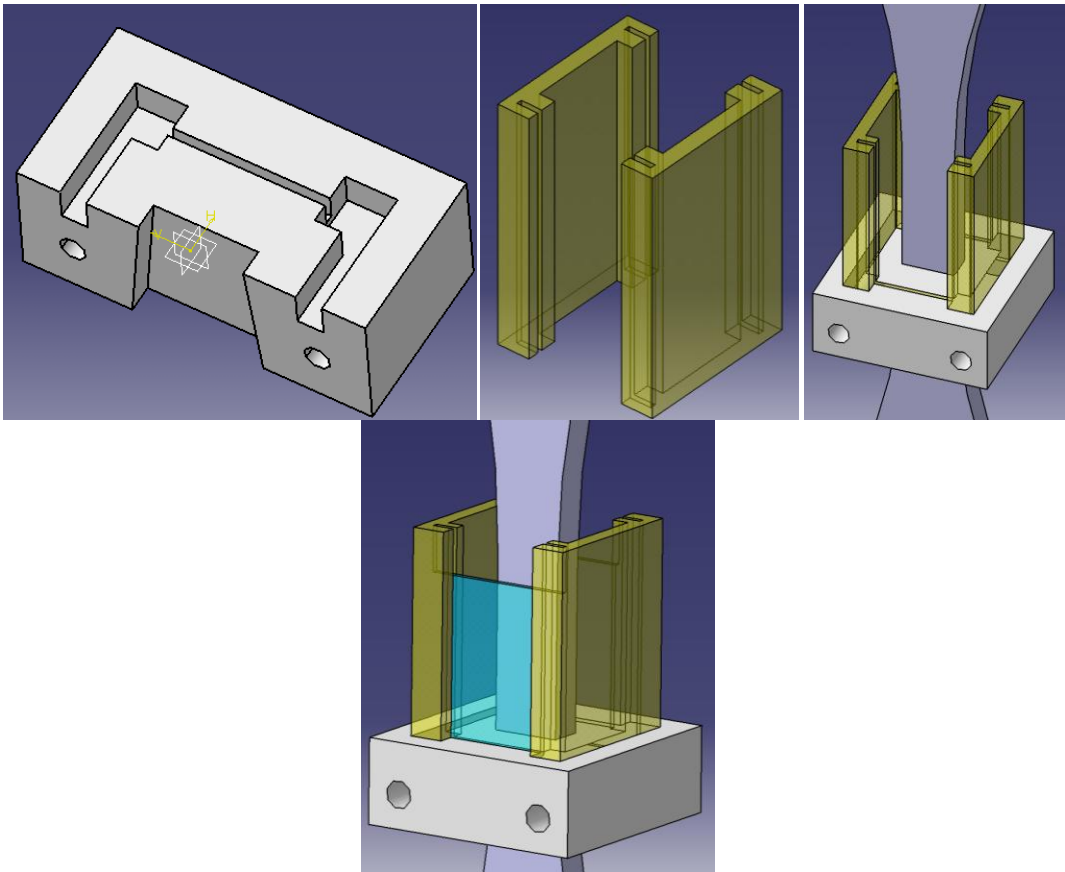


**Figure 3-13: Sketch of the second cell**

As in the first cell, a PTFE base composed of two identical parts was manufactured to fit the tension specimen under the gauge length, as shown in Figure 3-13. The two parts of the base were tightened around the specimen by two stainless bolts and then sealed with silicon sealant to prevent leakage of the salt solution. The base had been made with two different sets of grooves on the upper surface. The larger pair of grooves

was designed to slot two Perspex walls. The walls were in clear Perspex to let the light go through the cell. The finer grooves, which were also on the side of the walls, were designed to fit two removable glass slides. The location of the glass slides was designed to be in front of each side of the gauge length, thus the development of a crack on the specimen would be visible through the cell. However, the glass slide had to be removable to still have access to the crack for direct measurement. Finally, to avoid any leakage from the salt solution where two parts were slotted together, grease was applied in the grooves. In addition, each time that the glass slides were removed for measurement, the respective grooves were greased before the slides were put back in place.

## 3.4.2 Crack monitoring

To be able to identify the initiation of fatigue crack and record its propagation different methods were used in this research.

### 3.4.2.1 Replica technique

The replica technique was the most employed method during this project. The material used for the replica, produced by Microset [56], consists of liquid monomers, a base and a catalyst, which are supplied in a "twin-pack" cartridge. The material used in this research was the 101RT grade which is a "general purpose fast curing thixotropic material". To make a replica, the cartridge was mounted in a dispensing gun, which by pressure of the trigger leads the base and catalyst through a static mixing nozzle. At the end of the nozzle, the base and the catalyst were fully mixed and could be applied directly to the examined surface. The material cured in five minutes at room temperature. Once cured, the replica was peeled off and could be directly observed with a microscope. The crack length was either measured directly from the replica with the reticule of an optical microscope, or a stereo microscope fitted with a CCTV camera was used to take pictures of the replicas and the crack lengths were measured from the pictures, as shown in Figure 3-14. Replica of the crack were taken on both sides of the specimen, therefore for a particular number of cycles, the crack length was defined as the mean value between the crack lengths measured on the replicas of the front and back of the specimen.

Replicas were taken at different cycle intervals during the testing. For that, fatigue cycling was stopped and the salt solution contained in the cell was drained. Then the

surfaces of the tensile test specimen were gently wiped to remove the water from the specimen, and then the replica material was applied and let to cure for 5 minutes. Once the replicas were peeled off, the salt solution was replaced in the cell and the test was resumed.

The replica technique was an easy and reliable method to use but was disruptive and time consuming which therefore prevented to take a lot of measurement during the tests. Indeed, the tests had to be stopped for at least 10 minutes to take replicas. Hence, another quicker, automated and non-disruptive method was envisaged to monitor the fatigue crack during the tests using a digital camera.
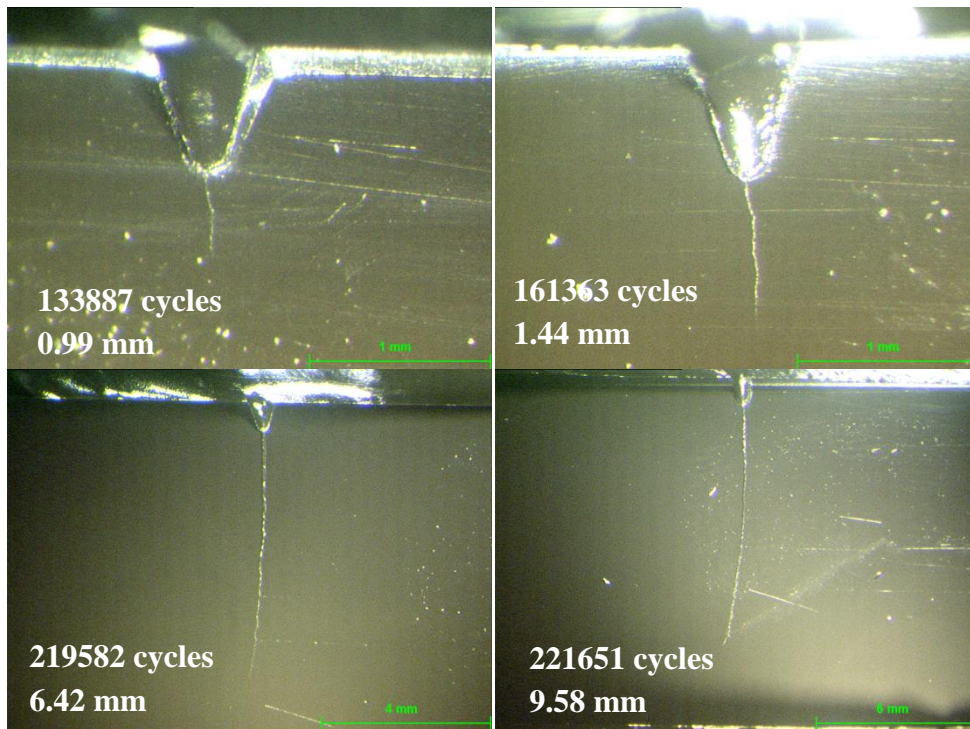


**Figure 3-14: Replicas of fatigue crack initiated at a notch (Specimen 7)**

### 3.4.2.2 Digital camera

A digital camera on a tripod was aimed at the area to watch on the gauge length of the tensile test specimen, as illustrated in Figure 3-15. The second cell was used in the experiments where the camera was used, so that the gauge length of the specimen was visible through the slide even when the cell was full. A cold light source was also placed near the specimen in order to get the optimum lighting to detect and follow the crack.

The camera was controlled by a piece of software where the experimenter could enter the number of cycles at which the camera had to take a picture. It was decided that pictures would be taken every 1000 cycles. Each picture was automatically stored in a folder and therefore it was possible to follow the fatigue crack development, as shown in Figure 3-16. Then, from the pictures the number of cycles to initiate a crack for a particular specimen and testing conditions could be identified and the crack length could be measured every thousand cycles using an image analyser software. In this case VistaMetrix was used.

The crack length measurements were made by tracking back the crack from just before failure, where the crack was clearly visible, to the earliest stage at which the crack could be distinguished. Measurements were taken only if the beginning and the tip of the crack were visible.
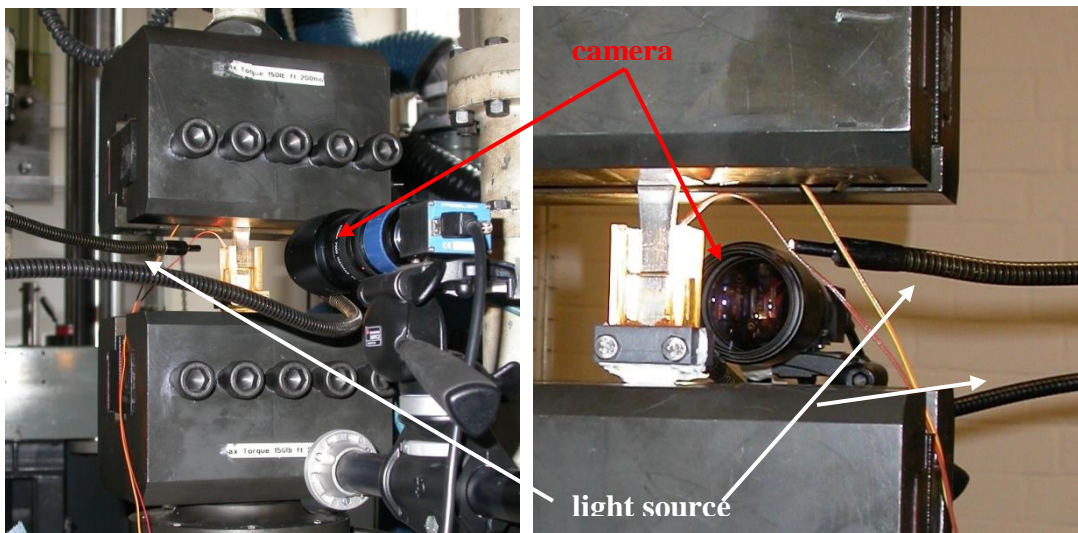


**Figure 3-15: Digital camera set up**

Although the replica technique and the camera allowed the record of fatigue crack progression, only the surface cracks were monitored. Therefore, electro potential monitoring was also used in parallel with the camera to gain information regarding the crack into the material.

### 3.4.2.3 Electro potential monitoring technique

The principle of this technique is that the resistance of the specimen would change as the crack grows. This change in resistance can be monitored by introducing at

different intervals, a constant current in the specimen and recording its potential. Indeed, if the current stays constant, any change in resistance will lead to a proportional change on the potential (Ohm's law). Finally, by calibrating the potential with the crack length, any change in potential can be linked with an increase in crack size.
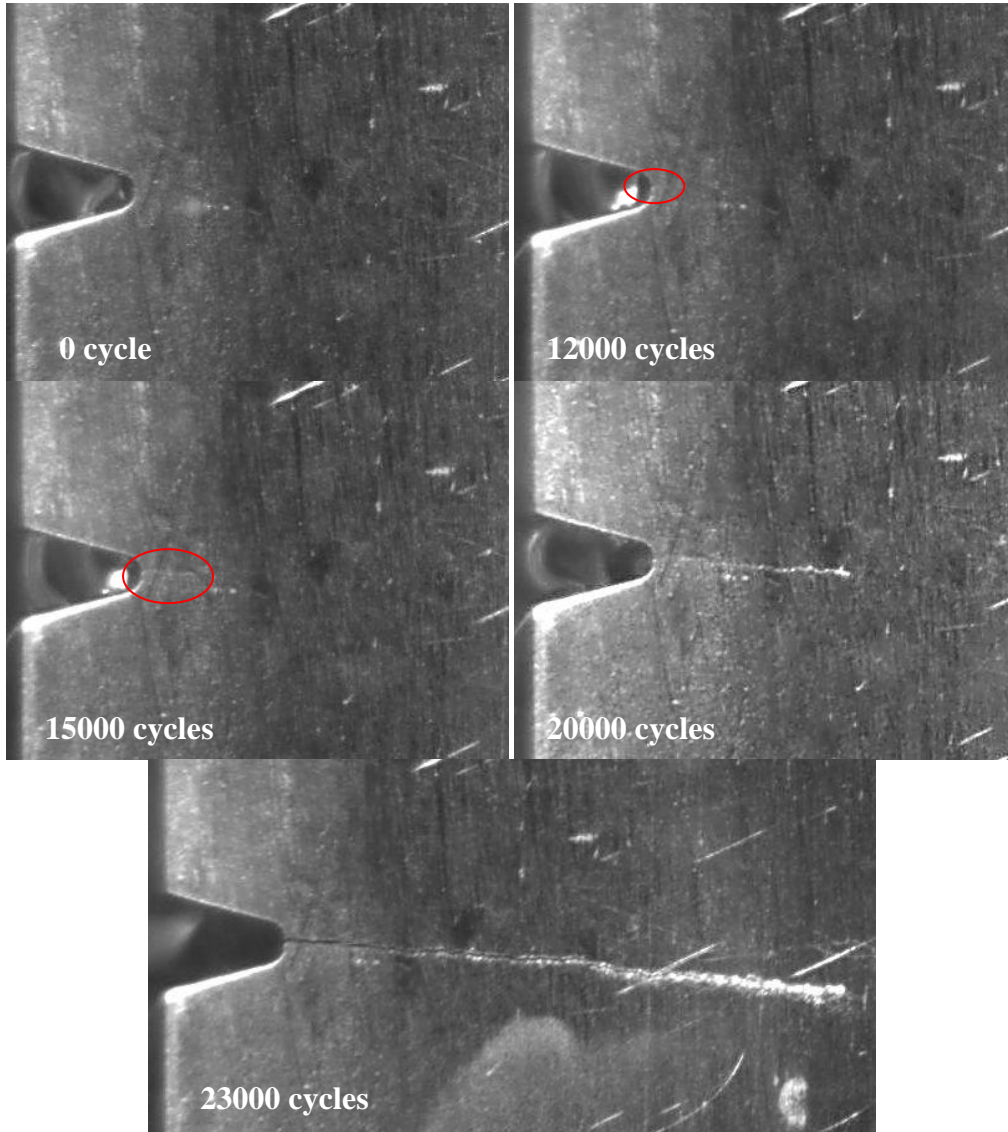


**Figure 3-16: Crack growth development monitored by digital camera**

In this project, that method was used on single edge notch (SEN) tension test specimens and on pre-corroded tension test specimens to record the progression of fatigue cracks from the notch and the corrosion flaw. Two pairs of probes were fitted on each specimen: a reference and an active pair. The actives probes will record any change in crack size, but also in temperature and electronic noise. If another pair of

probes is placed far enough from the crack, then it will also record the changes in temperature and electronic noise but will not be affected by the change in crack size. Therefore, by dividing any reading of the active probes by the respective reading of the reference probes, a normalized potential is obtained in which the electronic noise and temperature effects are not included [45].

The reference probes were placed on one lateral side of the specimen - for the SEN tension test specimens, the reference probes where on the same side than the notch. In both types of specimens, the first reference probe was placed at 12mm from the top edge and 3mm from the side edges of the specimen, whereas the second reference probe was at 30mm from the top edge and 3mm from the side edges of the specimen, as illustrated in Figure 3-17. On the other lateral side of the specimen, two 10mm deep M3 holes were drilled at 8mm from the top and bottom edges and at 3mm from the side edges, as shown in Figure 3-17. In these two holes, two threaded M3 bars were fitted and the cables from the current source were fixed at the other end so that the current could be introduced in the specimen. The threaded bars were chosen fine and long enough so that they would not hinder the specimen to be properly gripped in the fatigue machine. Regarding the actives probes, they were placed on either sides of the defect, as detailed in Figure 3-18. For the SEN tension test specimen, one probe was fixed on the top left hand side of the notch, whereas the second probe was placed on the bottom left hand side. Both probes were set at 1mm from the centre of the notch and 1mm from the respective edge of the specimen. For the pre-corroded specimen, the probes were placed above and below the corrosion flaw at 5mm from its centre. The probes were fixed at 6mm from the edges of the specimen in order to be in the middle of the specimen. All the probes were capacitive discharge spot welded to the specimen and then recovered by a drop of Araldite to protect the weld and avoid the wires to be inadvertently removed during testing.

Once the specimen was in place on the fatigue machine, the probes were plugged to a voltmeter and the specimen was linked to a current source by the threaded bars. The reading apparatus were plugged to a computer. Every 1000cycles (value set by the experimenter), a 15A current was sent to the specimen and a dozen potential readings were taken by the voltmeter. The software then recorded the mean reading for the

reference and active probes, as well as their respective standard deviation. Finally, a curve of the normalised potential as a function of the number of cycles was plotted.

The crack length measured from the pictures taken with the camera was then plotted against the normalised potential to extract the equation linking the potential to the crack length.
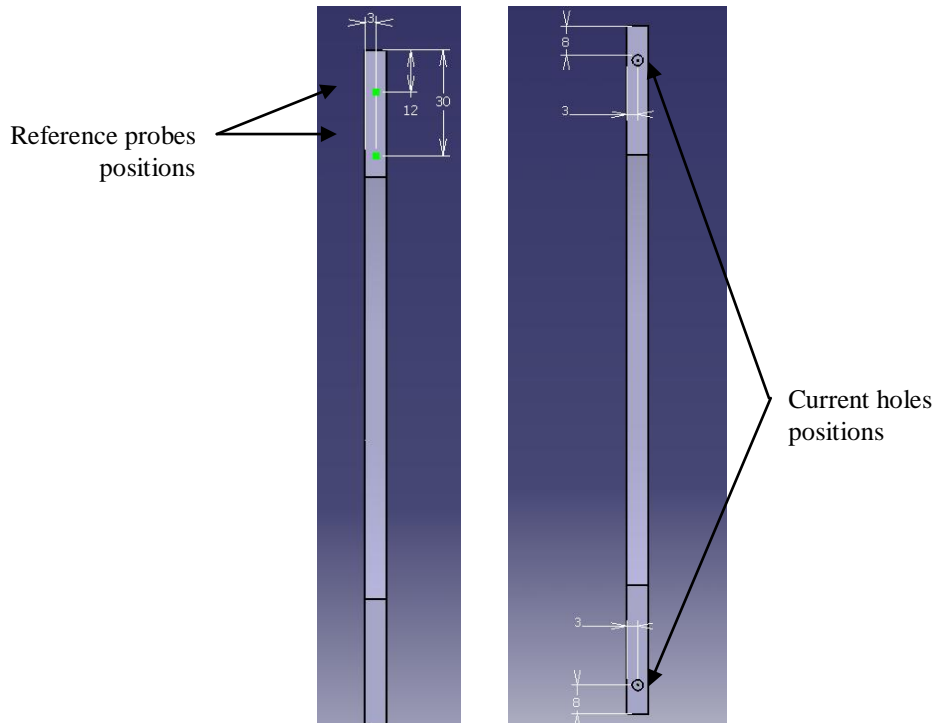


**Figure 3-17: Location of the reference probes and the current holes on one lateral sides of the tension test specimen**

Single edge notch specimen      Pre-corroded specimen
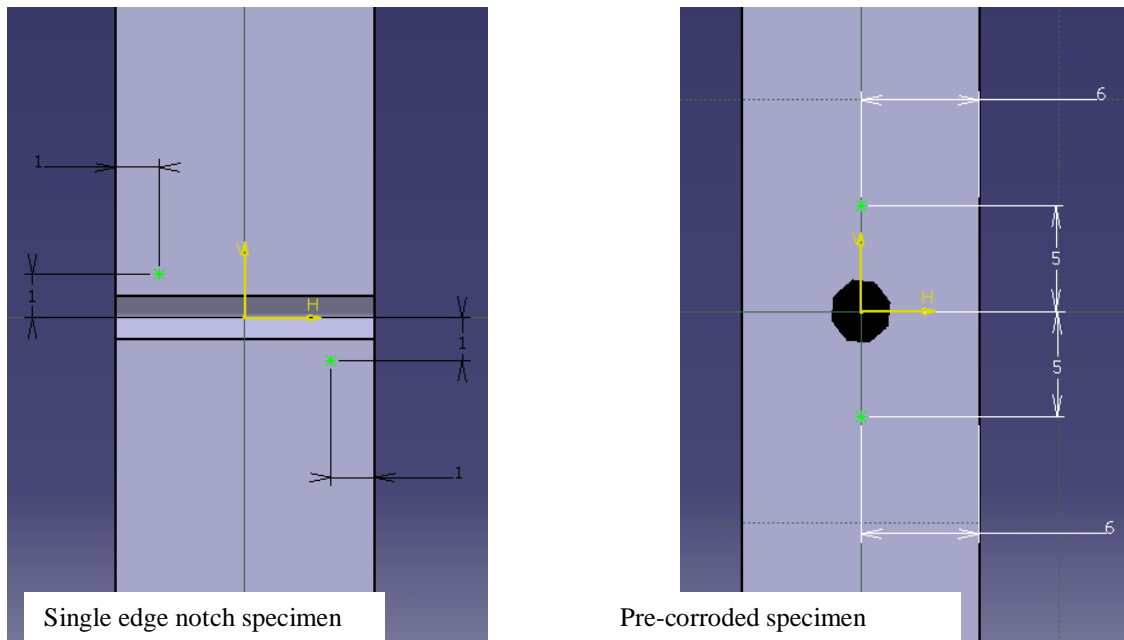
**Figure 3-18: Location of the active probes on SEN and pre-corroded tension test specimens**

All these crack length measurement methods were used to assess the crack growth rate in 15-5PH in air and in environment.

## 3.4.3 Crack growth rate testing

The aim of these tests was to obtain the crack growth rate curve for 15-5PH and establish an accurate value of stress intensity range threshold $\Delta K_{th}$ of this stainless steel. The tests were carried out both in air and in a 3.5% sodium chloride (NaCl) solution on tension test specimens with a single edge notch machined by electrical discharge machining (EDM). Before being tested, the gauge length of the specimen was hand polished by the experimenter to remove the grinding mark and scratches and allow the detection of the fatigue crack.

### 3.4.3.1 In air

The tests in air were performed on a 30kN Instron machine at a frequency of 10Hz. The crack propagation on the front and back of the specimen was recorded by the use of replicas. The length of the cracks (notch length included) on both sides of the specimen was measured from the replicas. Then the mean crack length was considered by taking the average of the two crack length measurements. The stress intensity range for each mean crack length was calculated using Eq. 3-5 where ā is the mean crack length, $\Delta\sigma$ is the applied stress range and $\beta$ is the geometrical factor. The appropriate geometrical

factor for the specimen geometry used in this research was calculated by finite element analysis and the process is described in section 0. The crack growth rate was assessed by dividing the difference of crack length by the difference of number of cycles between two measurements. Finally, the crack growth rate as a function of the stress intensity range was plotted in a logarithmic graph.

**Eq. 3-5**  $$\Delta K_{th} = \beta \Delta \sigma \sqrt{\pi \overline{a}}$$

### 3.4.3.2  In environment

The tests in environment were performed on a 250kN Instron machine at a frequency of 3Hz. The SEN tension test specimens were fitted with a cell containing a 3.5% NaCl solution and the crack development was monitored by digital camera and electro potential measurement. The same method as described in section 3.4.3.1 was used to plot the crack growth rate curve in environment.

The tests in environment were performed to assess whether or not the 3.5% NaCl solution has an effect on the propagation of the crack. Indeed, all the pre-corroded tension test specimens were fitted with a cell containing the salt solution when tested in fatigue in order to keep the corrosion flaw wet and thus active.

### 3.4.3.3  Striation counting

In order to verify the accuracy of the crack growth rate obtained by measuring the crack length with the different techniques detailed in section 3.4.3, specimen fracture surfaces had been observed with a SFEG scanning electron microscope to measure the spacing of the striations, as displayed in Figure 3-19. A reference point at the boundary between the notch and the fracture surface was taken. Then, striations spacing was measured at different lengths from the reference point. For each length, three different areas were examined and the distance between eleven striations, that is to say the distance for ten striation spacing, was measured. A mean distance was calculating by averaging the three measurements for each crack length.  Finally, the crack growth rate for a particular crack length was assessed by divided the mean distance for ten striation spacing for that crack length by ten.
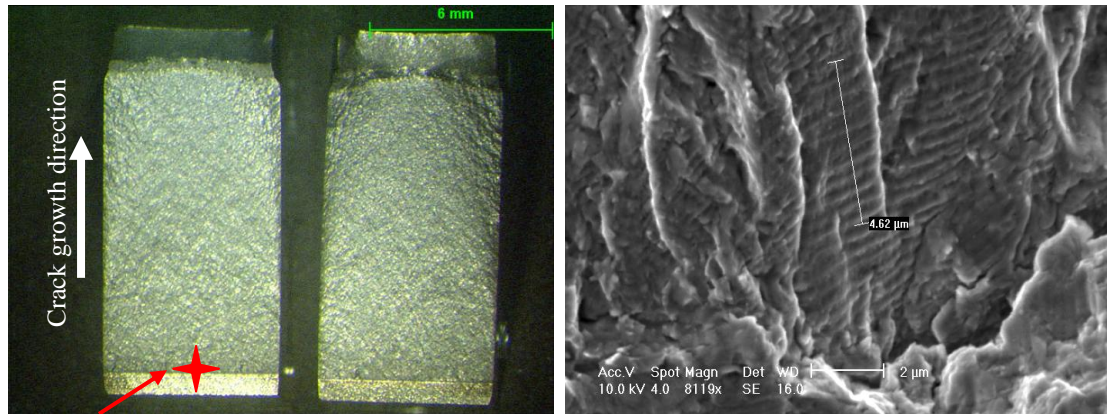
**Figure 3-19: Specimen fracture surfaces and fatigue striations**

## 3.4.4 Fatigue testing of pre-corroded specimens

Fatigue tests were carried out on pre-corroded tension test specimens in order to assess the influence of corrosion damage size on the initiation of fatigue cracks in 15-5PH stainless steel. The conditions of pre-corrosion were slightly different depending on whether pitting corrosion or crevice corrosion was wanted.

### 3.4.4.1 Pre-corrosion of the tension test specimens: pitting corrosion

Similarly to the pitting corrosion of the rectangular panels detailed in section 3.2.1, a tension test specimen was first hand polished with silicon carbide paper and diamond paste to give a 6μm finish. Then, the specimen was coated with Lacomit lacquer on all the surfaces except for the gauge length in order to prevent pit initiation in these areas. Finally, the specimen was left for 3 weeks in the salt spray cabinet.

Once the exposure time was reached, the specimen was removed from the salt spray cabinet and gently cleaned with water to removed salt deposits. Then, the gauge length of the specimen was divided in eighteen (6x3) areas and observed with a microscope to establish the pit size distribution, as described in section 3.2.3. Finally, like in section 3.2.4, extreme value statistics were used to predict the most probable size of the largest pit.

### 3.4.4.2 Pre-corrosion of the tension test specimens: crevice corrosion

Tension test specimens were fitted with a 3mm in diameter crevice formers made of Perspex which were designed to produce one crevice in the middle of the gauge length of the specimens, as illustrated in Figure 3-20. They were attached with two rubber bands at each extremity of the specimens, as shown in Figure 3-21. The two rubber

bands for a same specimen were chosen to have a similar thickness and size in order to have the same pressure at both ends of the specimen. The tension test specimens were not polished before being fitted with the crevice formers, but only degreased with isopropanol. The specimens were then put in the salt spray cabinet for various amounts of time up to two months.
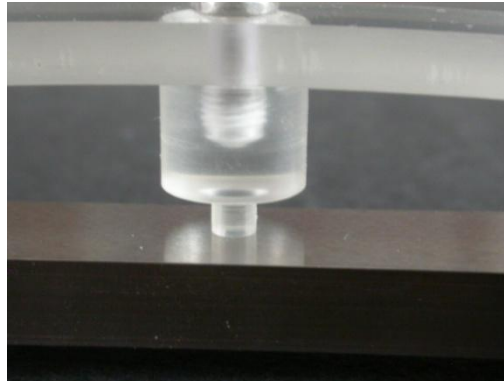


**Figure 3-20: Crevice former for tension test specimens**



**Figure 3-21: Crevice former attached to a tension test fatigue specimen**

Once the exposure time was reached, the specimens were removed from the salt spray cabinet and gently cleaned with water to remove salt deposits. Each corrosion flaw was then replicated or observed with a confocal laser scanning microscope, as detailed in section 0, and the shape and the depth of the flaws were examined to identify the areas were fatigue cracks were the most likely going to initiate.

When the corrosion flaws were assessed, the tension test specimens were fitted with a cell to contain the salt solution, and tested in fatigue.

### 3.4.4.3 Fatigue testing

Two different digitally controlled machines were used during the fatigue testing. A 100kN Instron machine was used to carry out the fatigue testing of the tension test specimen subjected to pitting corrosion, whereas the specimens with crevice corrosion

were tested with a 250kN Instron machine. This change of machine was not linked with the type of corrosion damage but with the availability of the testing machine at the time of the testing.

A pair of attachment was designed in order to provide additional restraint where sample was gripped and hold the specimen in the event that it began to slip, as well as avoid friction, as shown in Figure 3-22. The attachments were fitted over one top and one bottom grip, on the same side of the 100kN machine. The tension test specimen was held such a way that the contours of the attachments fit the shoulders of the specimen. Finally the grips were tightened to hold the specimen in place. No attachment was designed for the 250kN machine. The dimension of grips of the two machines being different, the previous attachment could not be used. Therefore, it was decided to decrease the stress at which the test were carried out to reduce the risk of the specimen slipping in the grips.

Each test was performed with a R ratio of 0.1, a frequency of 1Hz for the test carried out with the 100kN machine, and a frequency of 3Hz when using the 250kN machine. All the specimens were fitted with a cell containing the 3.5% NaCl solution in order to keep the corrosion flaws wet and thus active during the testing. The development of the fatigue crack from the corrosion flaw was monitored using the different techniques detailed in section 3.4.2. The stress at which the specimens were tested varied and is detailed with the results of these tests in section 5.
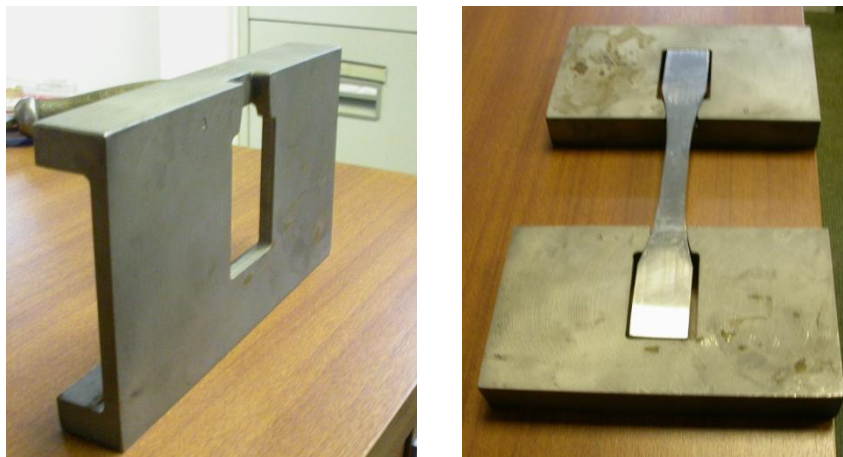


**Figure 3-22: Fatigue attachments**

## 3. EXPERIMENTAL METHODS

The stress, at which each specimen was testing, was decided accordingly to the severity of the corrosion flaws and the fatigue live wanted. The severity of a particular flaw was defined by the stress concentration factor associated with that flaw which was calculated using finite element analysis.

# 4 FINITE ELEMENT ANALYSIS

The software Abaqus was used in this research to conduct the finite element work. This method was used to assess the stress concentration factor, $k_t$, of different corrosion flaws, to produce the β factor curve for the single edge notch tension test specimens used in that project and also to design two larger scale tension test specimens, as detailed in section 7.1. The $k_t$ assessment was made by modelling the macroscopic gross shape of the corrosion flaw, the microscopic irregularities were not considered here.

## 4.1 Stress concentration factor assessment

The severity of a damage is represented by the value of the stress concentration factor, $k_t$. The higher the stress concentration factor, the more damaging is the flaw. $k_t$ can be calculated using finite element analysis (FEA) by calculating the ratio of the maximum stress due to the damage and the nominal stress in the sample.

The stress concentration factors of several damages were assessed. A first set of calculation was done with arbitrary dimensions for semi-elliptical damage to have the general trend of the effect of the damage geometry on the stress concentration factor. Then actual corrosion damage dimensions were used. The shape of actual damage was assumed to the closest regular geometry when it was modelled, as for instance a semi-ellipse.

### 4.1.1 Methods

The tension test specimen having two symmetry axes it was therefore possible to model only one quarter of the specimen. In addition, the ends of the specimen were not modelled because of the $S^t$ Venant principle. This principle states that the stress in an area of a structure remote from the point of application of the load will not be affected by the applied load. Practically, areas further than two or three diameters in length are considered as remote. The examined corrosion flaw profile was drawn in the top left corner of the cross section of the specimen, so that the flaw is located in the middle of the gauge length of the tension test specimen, as detailed in Figure 4-1.
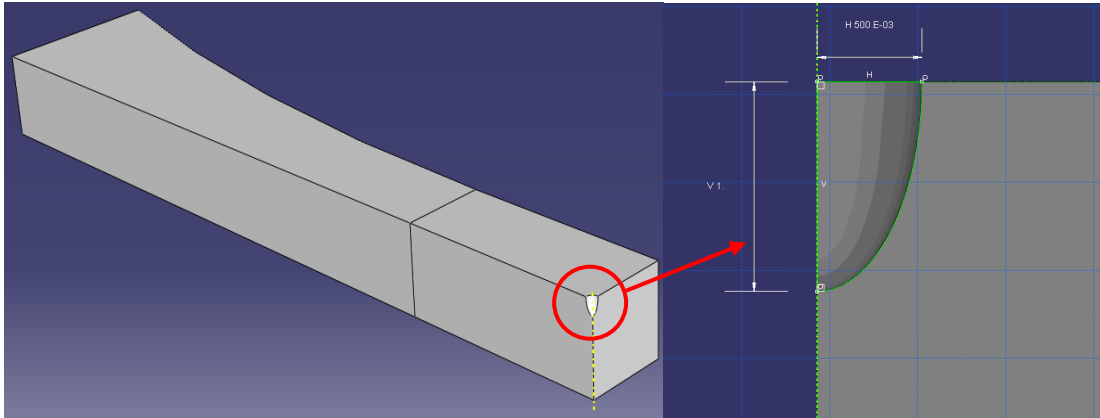
**Figure 4-1: Corrosion flaw geometry and location**

After having created the specimen and corrosion flaw geometry, the specimen was partitioned in different areas, and a mesh was applied to the different areas. The mesh in finite element analysis is extremely important, as the analysis is mesh dependant. Therefore, the area of interest, which is in that case where the corrosion flaw was, needed a fine and regular mesh in order to have the most accurate results for this region. However, this kind of mesh was not needed in the other parts of the specimen, which were less affected by the corrosion flaw, and such a mesh applied to the whole specimen would have been too much time consuming and used too much computer memory. Thus, a regular but larger mesh was applied to the rest of the specimen, and a transition mesh was linking the fine mesh of the gauge length to the larger mesh, as shown in Figure 4-2. For the two regular meshes, 8-node linear hexahedron reduced integration elements were used, whereas the transition mesh was composed of 4-node linear tetrahedron elements.

Once the mesh was completed, the boundary conditions for the symmetry and displacement were applied. Finally a tension load was applied to have a nominal longitudinal stress of 800MPa in the gauge length. This stress was arbitrarily chosen and the results were not dependent on the applied load as this was a purely elastic analysis. After the analysis was completed, the longitudinal stress field of the specimen was displayed. The location and value of the maximum longitudinal stress was shown on the specimen. Then, to obtain the stress concentration of the corrosion flaw, $k_t$, the maximum longitudinal stress was divided by the nominal longitudinal stress. The $k_t$ and location of the maximum longitudinal stress were recorded for each corrosion flaw and

this information was used for setting the stress at which the respective specimens would be tested, and locate the area where the fatigue crack would initiate.
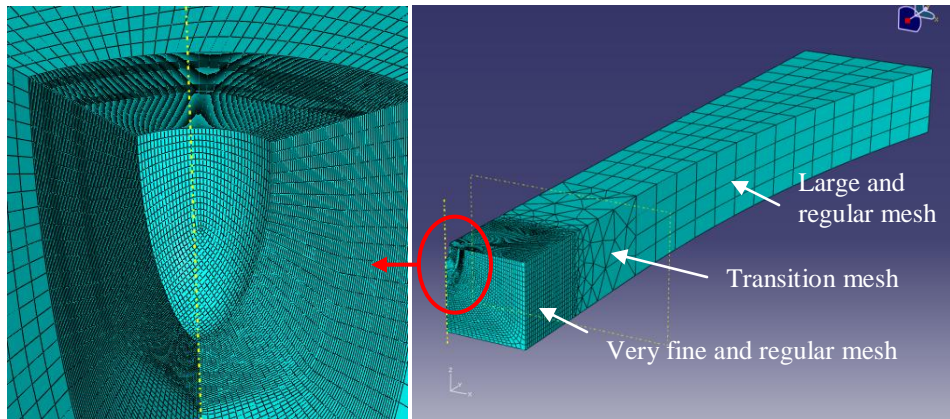


**Figure 4-2: Mesh**

## 4.1.2  Arbitrary geometries
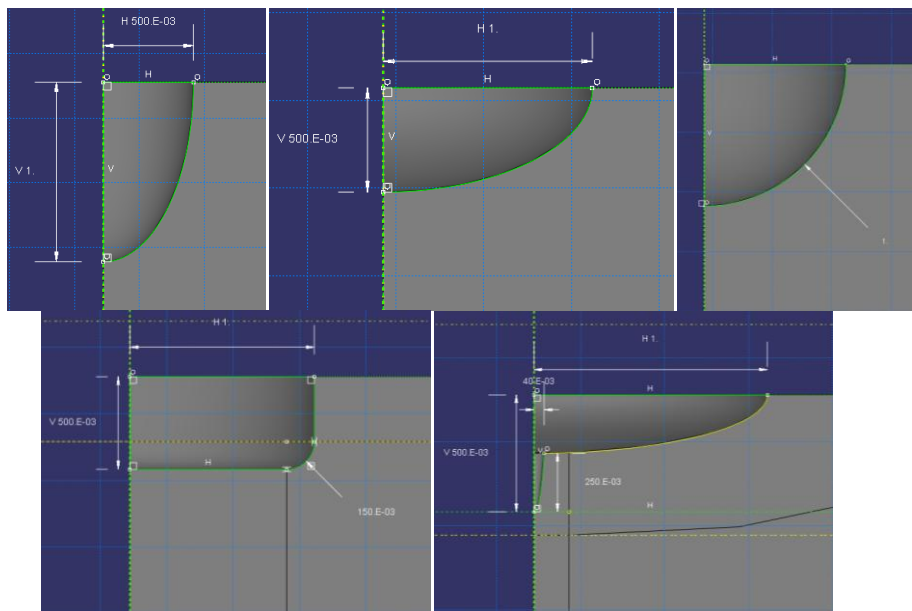


**Figure 4-3: Profile of the arbitrary geometry corrosion flaws**

Five arbitrary geometries of corrosion flaw were modelled, as detailed in Figure 4-3. The first geometry considered was a semi-elliptical deep and narrow flaw, of which the dimensions were 1mm deep and 0.5mm wide. The second geometry represented a semi-elliptical shallow with a 1mm width and a 0.5mm depth. A third geometry was modelled as a 1mm radius hemispherical flaw. The fourth considered geometry was a

flat bottom flaw, with a 1mm width, 0.5mm depth and a bottom corner radius of 0.15mm. Finally, a fifth geometry represented a shallow flaw combined with a deep and narrow flaw at the centre.

For each geometry, the contours of the longitudinal stress are displayed in Figure 4-4. The location of the maximum longitudinal stress was indicated by a white arrow on the picture, and its value as well as the corresponding stress concentration factor, were detailed in Table 4-1. From these results, it appears that for 15-5PH stainless steel, deep and narrow flaws are more damaging than shallow flaws. In addition, shallow flaw with a deeper part at the bottom represents the most severe damage from these five cases.
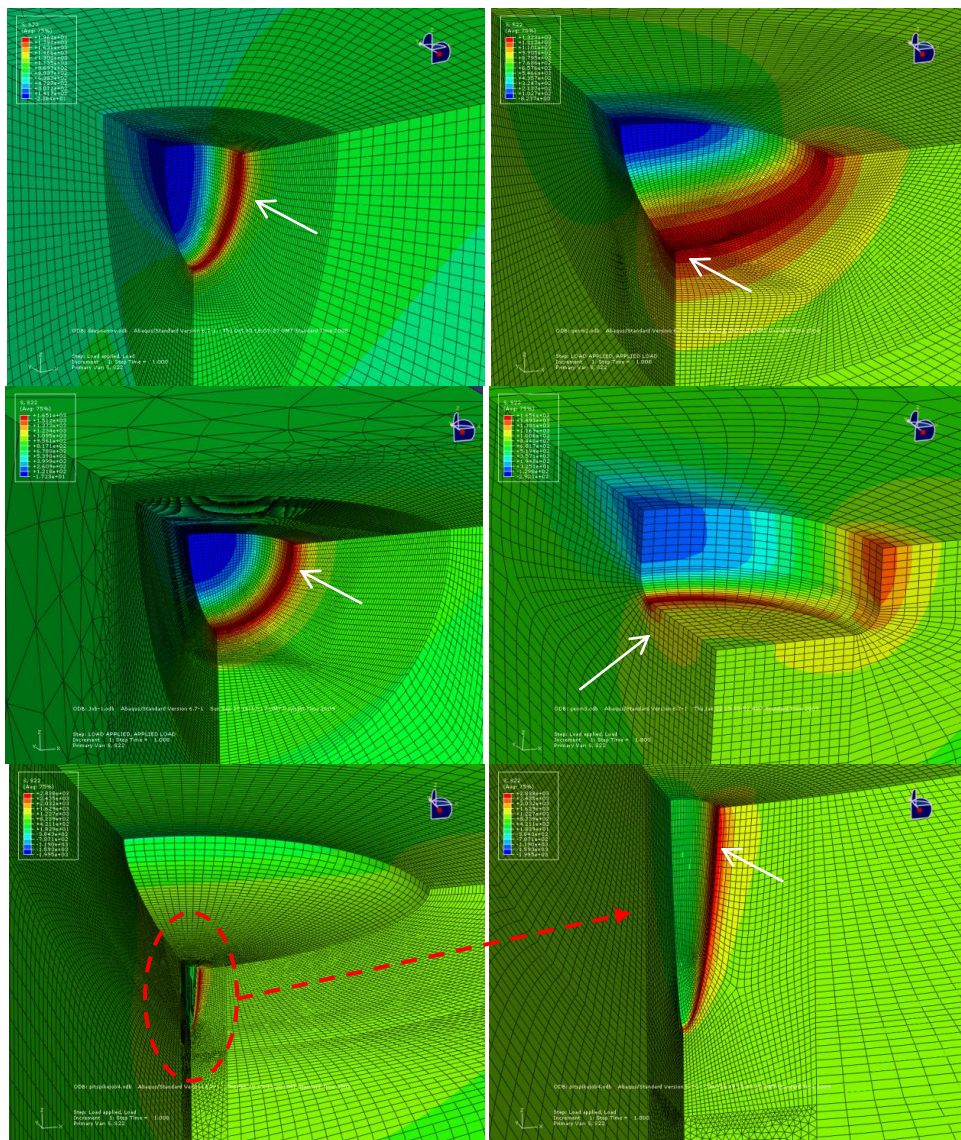


**Figure 4-4: Longitudinal stress contours for each flaw geometry**

| Geometry | | | Maximum Longitudinal stress | | $k_t$ |
|---|---|---|---|---|---|
| Shape | Half width (mm) | Depth (mm) | Value (MPa) | Location | |
| deep and narrow | 0.5 | 1 | 1962 | 30 deg from the surface | 2.45 |
| shallow | 1 | 0.5 | 1323 | point of maximum depth | 1.65 |
| circular | 1 | 1 | 1651 | 30 deg from the surface | 2.06 |
| flat bottom | 0.5 Corner radius 0.15mm | 0.5 | 1656 | corner radius | 2.07 |
| Shallow + deep and narrow | 0.5 0.05 | 0.25 0.25 | 2838 | deeper part − 30 deg | 3.55 |

**Table 4-1: Stress concentration factors for arbitrary geometries**

The stress concentration factor assessment for actual geometries is presented in section 5.4.3.

### 4.1.3  Larger scale fatigue specimen

The larger scale fatigue specimens having a much larger section than the small fatigue specimens, as detailed in section 7.1, more elements would be needed to mesh the specimen, which would considerably increase the computational time. Therefore, in order to save time, it was decided to use the small fatigue specimen geometry to assess the stress concentration factor of a flaw. However, because the larger scale fatigue specimen section is circular and that the section of the small specimens is rectangular, a preliminary finite element analysis with an identical corrosion flaw was carried out in both type of specimens to examine the effect of the specimen section geometry on the stress concentration factor value.

The considered flaw was 1mm deep and 0.5mm wide, and was placed in the middle of the gauge length of the specimens. A load was applied in each specimen such as the stress in the gauge length of the specimens was 800MPa. The longitudinal stress contours for both specimens are displayed in Figure 4-5. The maximum longitudinal stress was 1962MPa in the small fatigue specimen, which corresponded to a stress concentration factor of 2.45, whereas the maximum longitudinal stress was 1982MPa in the larger scale fatigue specimen, which was equivalent to a stress concentration factor

of 2.47. In both cases, the maximum longitudinal stress was located at approximately 30 degrees from the surface.

Despite the slight difference (0.8%) between the stress concentration factors due to the slight difference of mesh between the two specimens, it was concluded that the specimen geometry did not have a significant effect on the stress concentration factor value. Therefore, the finite element analyses to assess the stress concentration factor of the corrosion flaws found in the larger scale fatigue specimens were carried out with the small fatigue specimen geometry to keep to the minimum the number of elements used, hence the computational time.
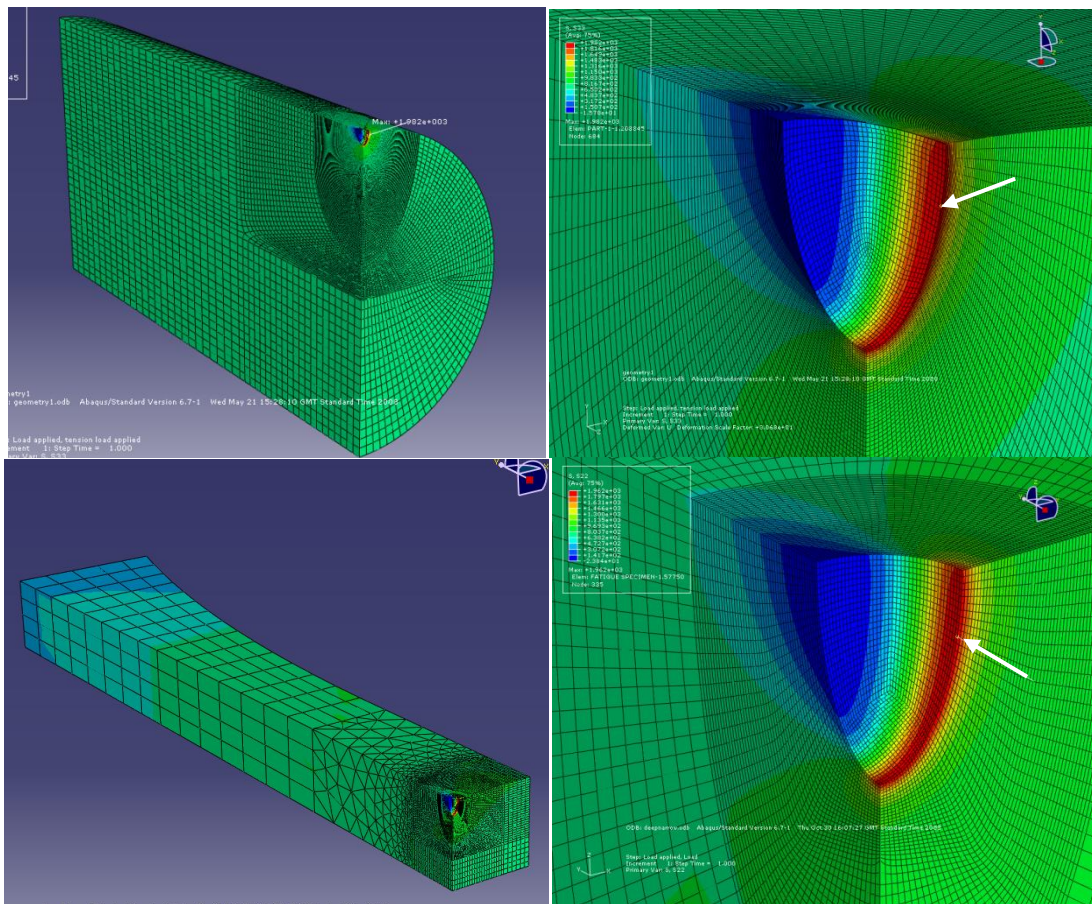


**Figure 4-5: Longitudinal stress contours in the larger scale and small fatigue specimens with an identical corrosion damage**

59

## 4.2 β factor assessment
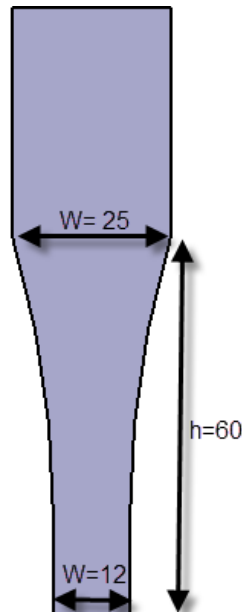


**Figure 4-6: Half specimen geometry**

The β factor is a geometrical factor used in the stress intensity factor calculation, detailed in Eq. 2-2. It is function of the specimen height and width ratio, h/W, and crack length and specimen width ratio, a/W. β factor curves as a function of a/W, are available in the compendium of stress intensity factors [46] for standard geometries, that is to say for rectangular plates with h/W ratio equals to 1 or 2 for instance. However, the geometry of the specimen used in that research project, exhibited in Figure 4-6, does not have a rectangular shape, and has a h/W ratio variable over its length. Therefore the geometrical factor β curve for the tension test specimen used in this research was not available in the literature, and it was decided to calculate the β factor for this specimen geometry in order to get the most accurate results as possible. Indeed, the β factor which is used in the expression of the stress intensity K, as detailed in Eq. 4-1 can be linked with the J integral at the crack tip which can be obtained by finite element analysis. In LEFM (Linear Elastic Fracture Mechanics) conditions, the energy release rate, G, and the J integral are equals. In addition, the energy release rate G and the stress intensity factor K are linked by Eq. 4-2 where E is the Young's modulus of the material. Therefore, by substituting the expression of the stress intensity factor into the

expression of the energy release rate, it is possible to express β as a function of the energy release rate or the J-integral, as shown in Eq. 4-3. Therefore, finite element analysis was carried out to produce the J integral at the crack tip of a fatigue crack growing from a single edge notch with the tension test specimen geometry used in this project.

**Eq. 4-1** $$K = \beta\sigma\sqrt{\pi a}$$

**Eq. 4-2** $$G = J = \frac{K^2}{E}$$

**Eq. 4-3** $$\beta = \frac{1}{\sigma}\sqrt{\frac{JE}{\pi a}}$$

## 4.2.1 Crack propagation program

The first stage of the process was to create a program to propagate a crack and calculate the J integral at each interval of crack propagation. All the steps carried out to create the program are summarised in the flow chart in Figure 4-8.

A 12x50mm single edge notch specimen was modelled; 12mm being the width of the tension test specimen used in this project. Only one half of the specimen was considered because of the symmetry axes in the whole specimen. An analytical rigid surface had to be defined in the plan of the crack path to allow the crack propagation modelling, as shown in Figure 4-7. Then, the assembly was assigned material properties and meshed. Afterwards, boundary conditions were set for the symmetry and the displacements. Similarly, between the specimen and the analytical rigid surface, a frictionless contact was set and all the nodes were set in contact for the initial conditions.

Two steps were required to run the analysis: first apply the load, and then untie, node by node, the contact between the specimen and the analytical rigid surface. This second step was set to take place only when the stress reached an arbitrary value of 500MPa. Moreover, each time a node was untied, that is to say, each time that the crack grew, the J integral at the crack tip was calculated. This sequence was repeated until the crack reached a length of 10mm. Then the β factor for different crack lengths, a, was

calculated from the respective J integral values, and the β factor curve was plot as a function of the ratio a/W (where W is the width of the specimen).

The aim of this first analysis was not to have exploitable results but to create a program to model the crack propagation and also to have the J integral value at the crack tip at each step of propagation for different times of the analysis. The pictures displayed in Figure 4-9 show the crack propagation for different times of the analysis. The specimen seems more and more tilted as the time increased, but this is only due to the high factor of magnification.
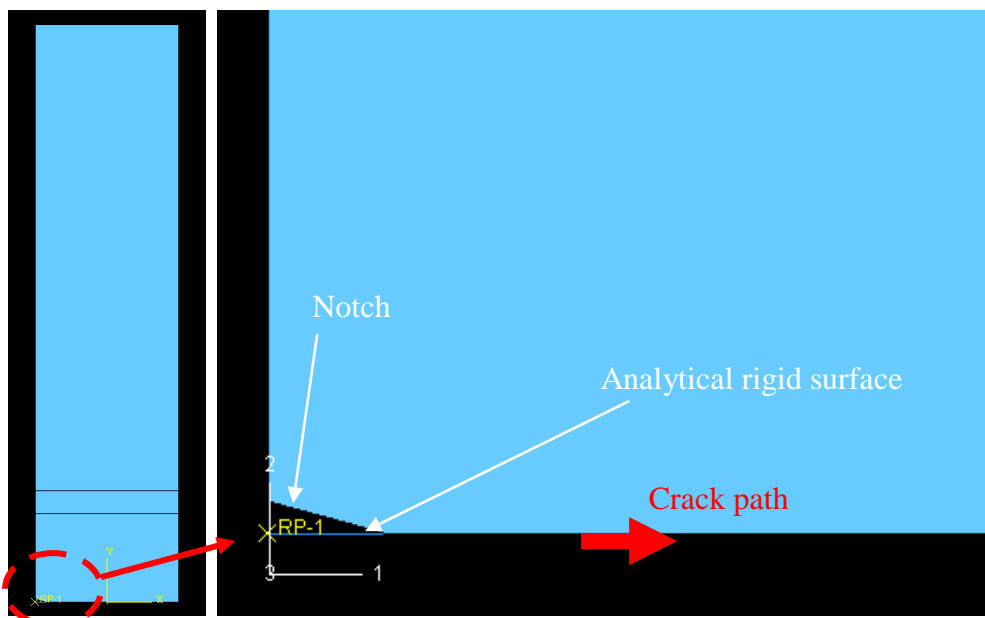


**Figure 4-7: SEN specimen and analytical rigid surface**

```
                    ┌──────────────┐
                    │    Start     │
                    └──────────────┘
                           │
                           ▼
                 ┌────────────────────┐
                 │     Geometry       │
                 │  Fatigue specimen  │
                 │  Analytical surface│
                 └────────────────────┘
                           │
                           ▼
                 ┌────────────────────┐
                 │       Mesh         │
                 └────────────────────┘
                           │
                           ▼
                 ┌────────────────────┐
                 │     Material       │
                 └────────────────────┘
                           │
                           ▼
                 ┌────────────────────┐
                 │       BC's         │
                 │     Symmetry       │
                 │    Displacement    │
                 └────────────────────┘
                           │
                           ▼
                 ┌────────────────────┐
                 │    Interactions    │
                 │ Frictionless contact│
                 │ specimen/analy surf │
                 └────────────────────┘
                           │
                           ▼
                 ┌────────────────────┐
                 │ Initial conditions │
                 │ specimen/analy surf│
                 │    in contact      │
                 │   (all the nodes)  │
                 └────────────────────┘
                           │
                           ▼
                 ┌────────────────────┐
                 │      Step 1        │
                 │   Load applied     │
                 └────────────────────┘
```

Step n, n≥2
Debond
Node by node

J-integral
For step n-1
20 contours

$\beta = f(a/w)$

$\sigma \geq 500 \text{MPa}$   n   y

n ≤ 100   y   n

End
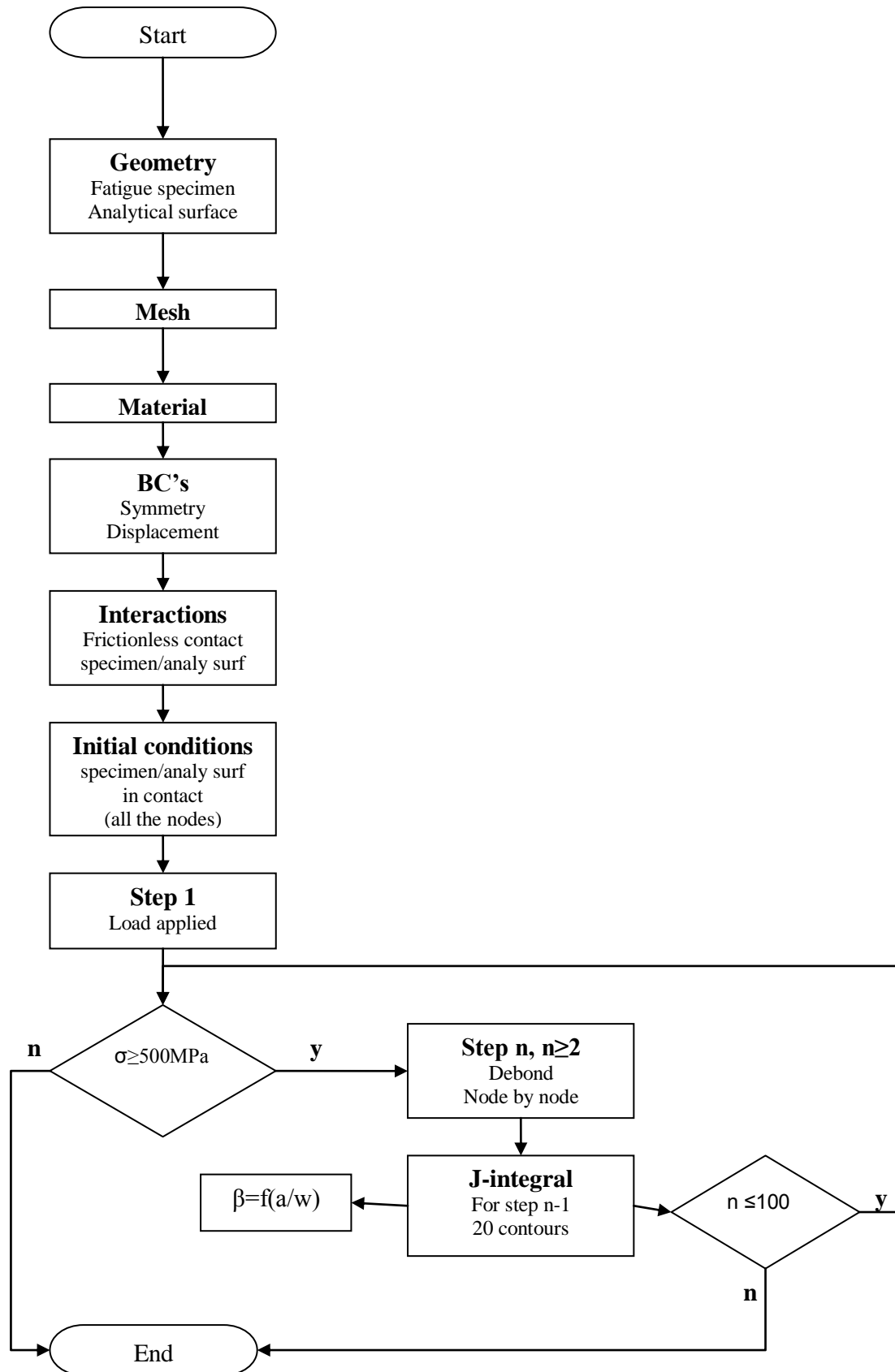
**Figure 4-8: Flow chart for the crack propagation and J integral calculation program by FEA**
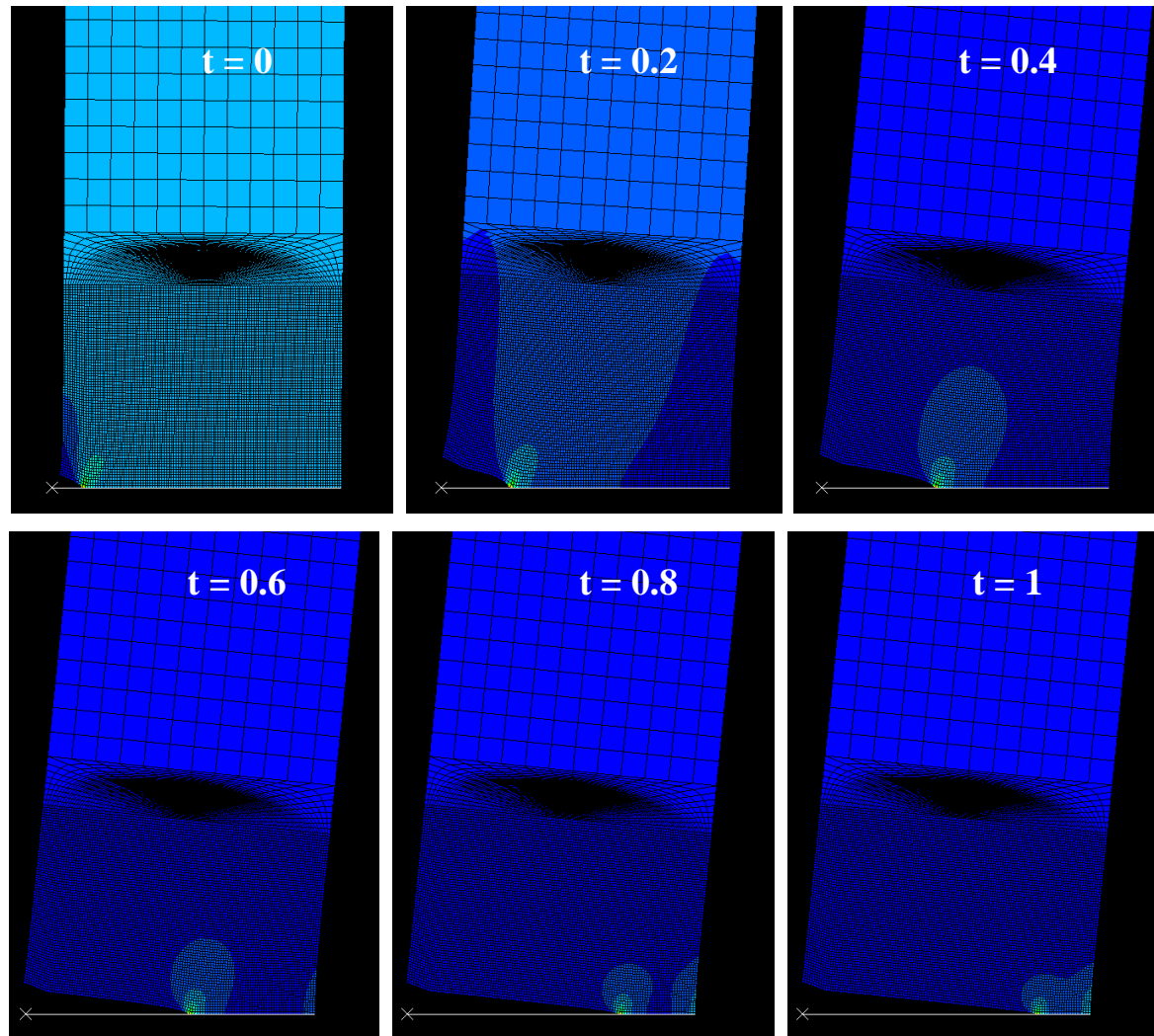
**Figure 4-9: Crack propagation at different steps of the analysis**

## 4.2.2  Crack propagation program validation

To validate the program, a β factor curve from the literature was chosen as reference and compared with the β factor curve found with the finite element analysis. The β factor curve for an edge crack in a finite width sheet with uniaxial tensile stress and h/W equals 1 [46] (h being the height of the specimen and W its width), was chosen as the reference curve.

The program described in section 4.2.1 was applied to a 12x12mm specimen with a crack of 1mm in length. The dimensions were chosen to have the same width as the tension test specimen used in this project and a ratio h/W equalled to 1. The J integral values were recorded at each step of the crack propagation.  Then the β factor was calculated from the J integral values for different crack lengths, and plotted as a function of the ratio a/W. The reference and the FE curves are displayed in Figure 4-11. An offset of 0.1 had to be applied to the FE curve to match the reference curve, due to the fact that the program gives at step n the J integral for step n-1.

Despite that offset, the error between the two curves was assessed to be less than 2%, hence the program was validated and applied to the tension test specimen geometry used in that research.

## 4.2.3  Application to the specimen geometry used in this project

The crack propagation program was run with the geometry of the specimens used in that research, illustrated in Figure 4-10, and the J-integral values for each crack propagation step were recorded. The β factor curve was then drawn as a function of the a/W ratio, as shown in Figure 4-12, with a being the crack length and W the width of the specimen (12mm). The effect of the notch on the β factor can be seen in the small, steep part of the beginning of the curve (before a/W=0.1). The β factor for any particular a/W ratio was then extrapolated from this curve.



**Figure 4-10: Fatigue specimen used in this research program**

## 4. FINITE ELEMENT ANALYSIS
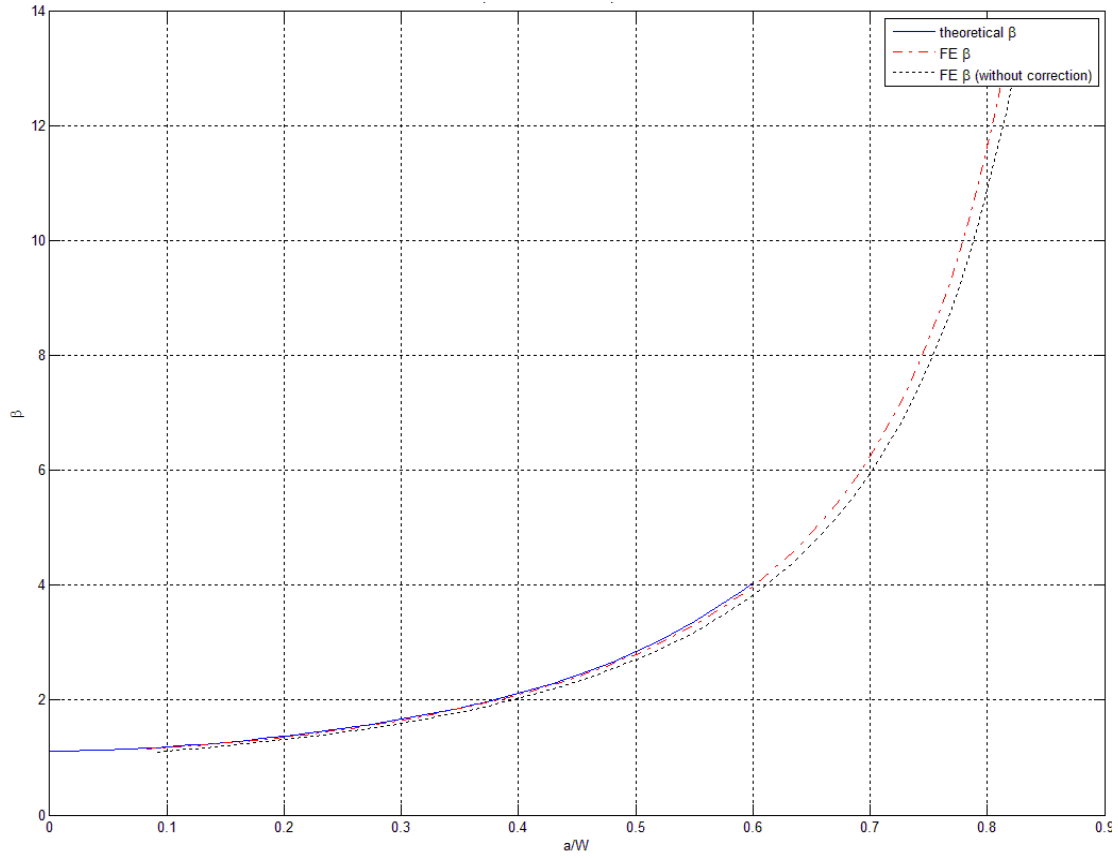


**Figure 4-11: Comparison of the reference and FE β factor curves**
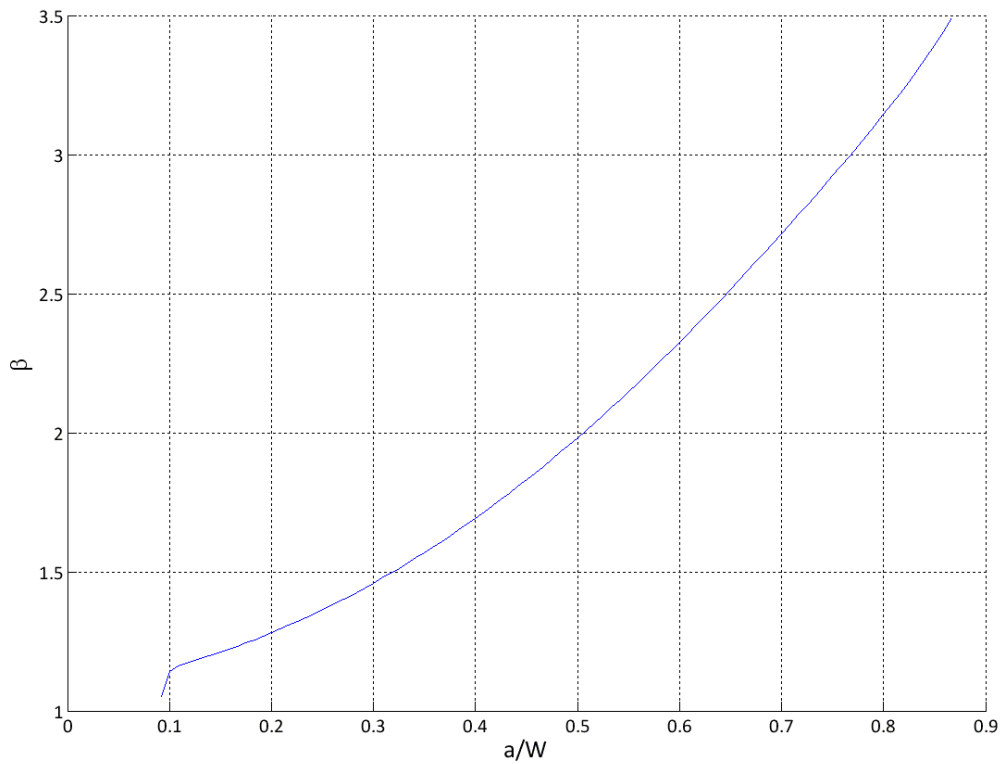


**Figure 4-12: Geometrical factor curve for the specimen used in that research project**

66

# 5 RESULTS AND DISCUSSION

## 5.1 Pitting corrosion testing

The three polished panels exposed in the salt spray cabinet for respectively 18 days, 3 weeks and 4 weeks, exhibited corrosion product mainly located near the longitudinal edges of the panels, and corrosion product running marks, as illustrated in Figure 5-1.
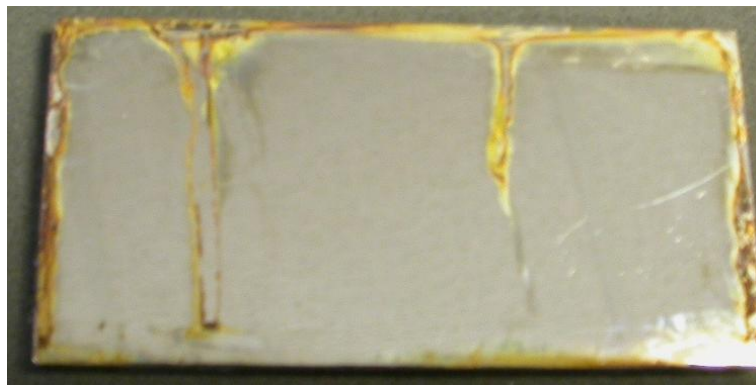


**Figure 5-1: Corrosion product on a 15-5PH panel after 3 weeks in the salt spray cabinet**

Most of the corrosion product was found on the longitudinal edges of the panels, which is where the salt solution had collected during the exposure, as the panels were inclined at 45 degrees in the salt spray cabinet. The corrosion product running marks were the result of the panels regularly turned around during the experiment. The amount of corrosion product observed on the panels was found to be increasing with the exposure period. A reference indent was made near an area covered by corrosion product on the three panels. Then, the corrosion product was removed with a fine grade of silicon carbide paper and the area located near the reference indent was examined with an optical microscope, as shown in Figure 5-2. It appeared that pits were underneath the corrosion product. Therefore, the corrosion product on the three panels was carefully removed and then the panels were observed with an optical microscope fitted with an image analyser software in order to measure the pit size distributions for each exposure time, as detailed in section 3.2.3.
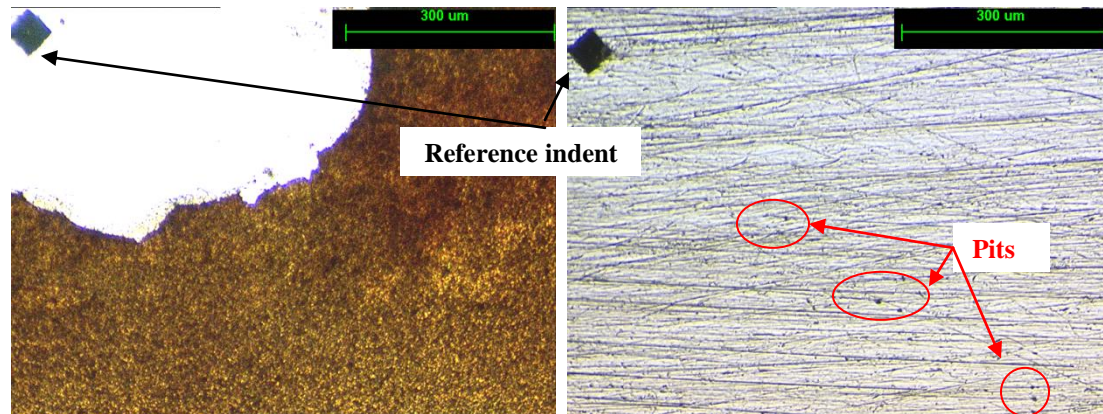
**Figure 5-2: Pits observed underneath the corrosion product**

In addition to corrosion pits, larger flaws due to crevice corrosion were present on the panel. They originated at sites where solution had penetrated beneath the protective lacquer

## 5.1.1 Image analysis

- ### *Panel exposed for 18 days*

870 pits were detected on the examined area of the panel exposed for 18 days in the salt spray cabinet. Both pit size distributions, shown in Figure 5-3, exhibited a peak located in the 0.5-1μm interval followed by steep decrease. However, for the length distribution, most of the detected pits (74%) were in the 0.5-1.5μm range, whereas for the width distribution, 84% of the detected pits were in the 0-1μm interval. In addition, the length distribution was more scattered than the width distribution. Indeed, the maximum length was included between 20 and 20.5μm and two detected pits were in this interval, whereas the maximum measured width was in the 13-13.5μm range and was reached by only one pit.
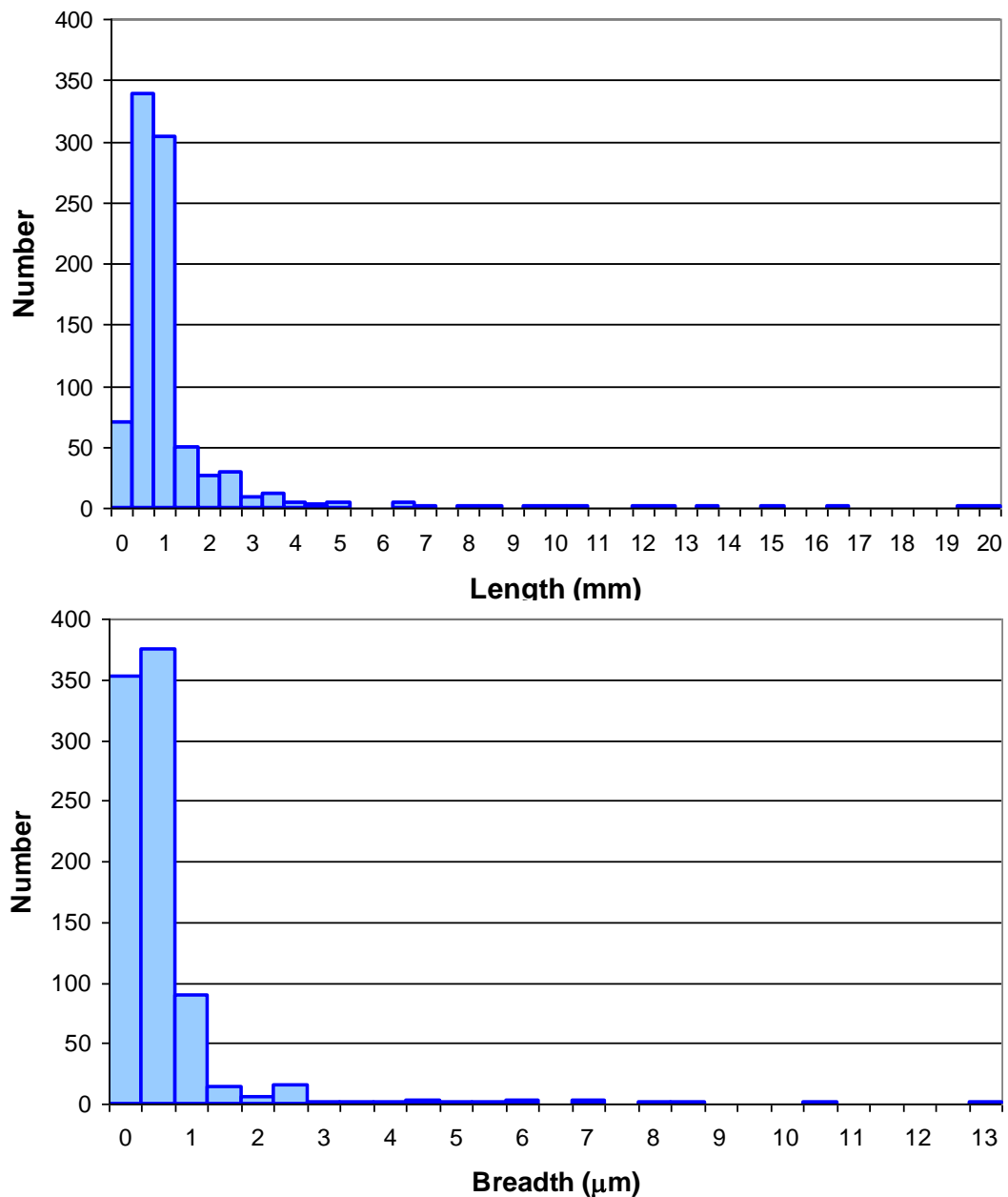
**Figure 5-3: Pit length and width distributions after 18 days in the salt spray cabinet**

- *Panel exposed for 3weeks*

879 pits were detected on the examined area of the panel exposed for 3 weeks in the salt spray cabinet. Both pit size distributions, shown in Figure 5-4, exhibited a peak followed by a steep decrease, but their respective peak was located in different ranges: 1-1.5μm for the length distribution and 0.5-1μm for the width peak. However, for each distribution, most of the detected pits (73% for the length and 93% for the width) were in the 0-1.5 μm range. Moreover, the length distribution was much wider than the width

distribution. Indeed, the maximum length was included between 38.5 and 39μm whereas the maximum measured width was in the 17-17.5μm range. For each distribution, only one detected pit was in these intervals.
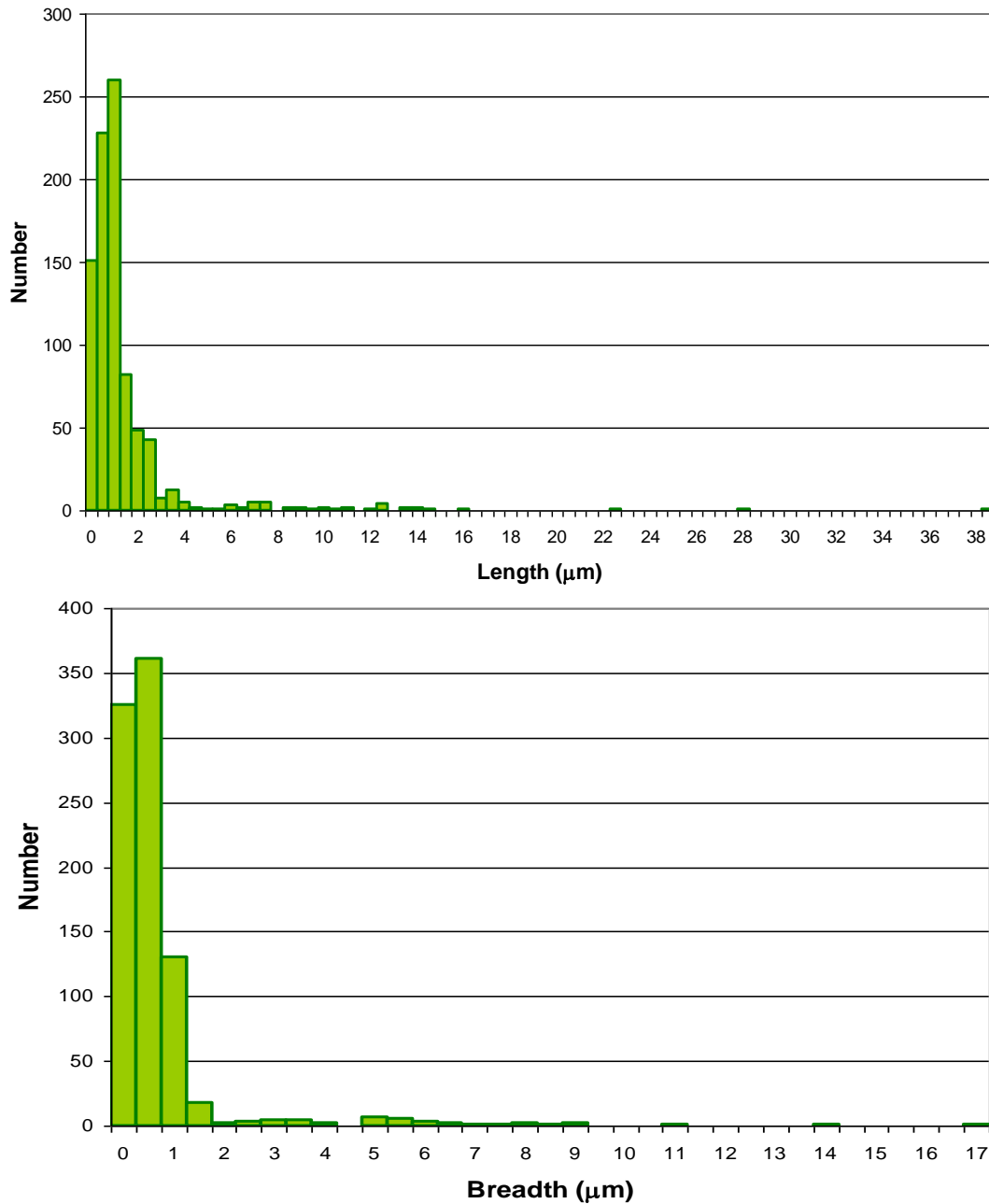


**Figure 5-4: Pit length and width distribution after 3 weeks in the salt spray cabinet**

- *__Panel exposed for 4 weeks__*

1535 pits were detected on the panel exposed for 4 weeks in the salt spray cabinet. Both distributions, shown in Figure 5-5, exhibited a peak located in the 0.5-1μm interval

followed by a steep decrease. However, for the length distribution, most of the detected pits (78%) were in the 0.5-1.5µm range, whereas for the width distribution, 89% of the detected pits were in the 0-1µm interval. In addition, the length distribution was slightly more scattered than the width distribution. Indeed, the maximum length was included between 13 and 14µm and only one detected pits was in this interval, whereas the maximum measured width, which was also reached by only one pit, was in the 10.5-11µm range.
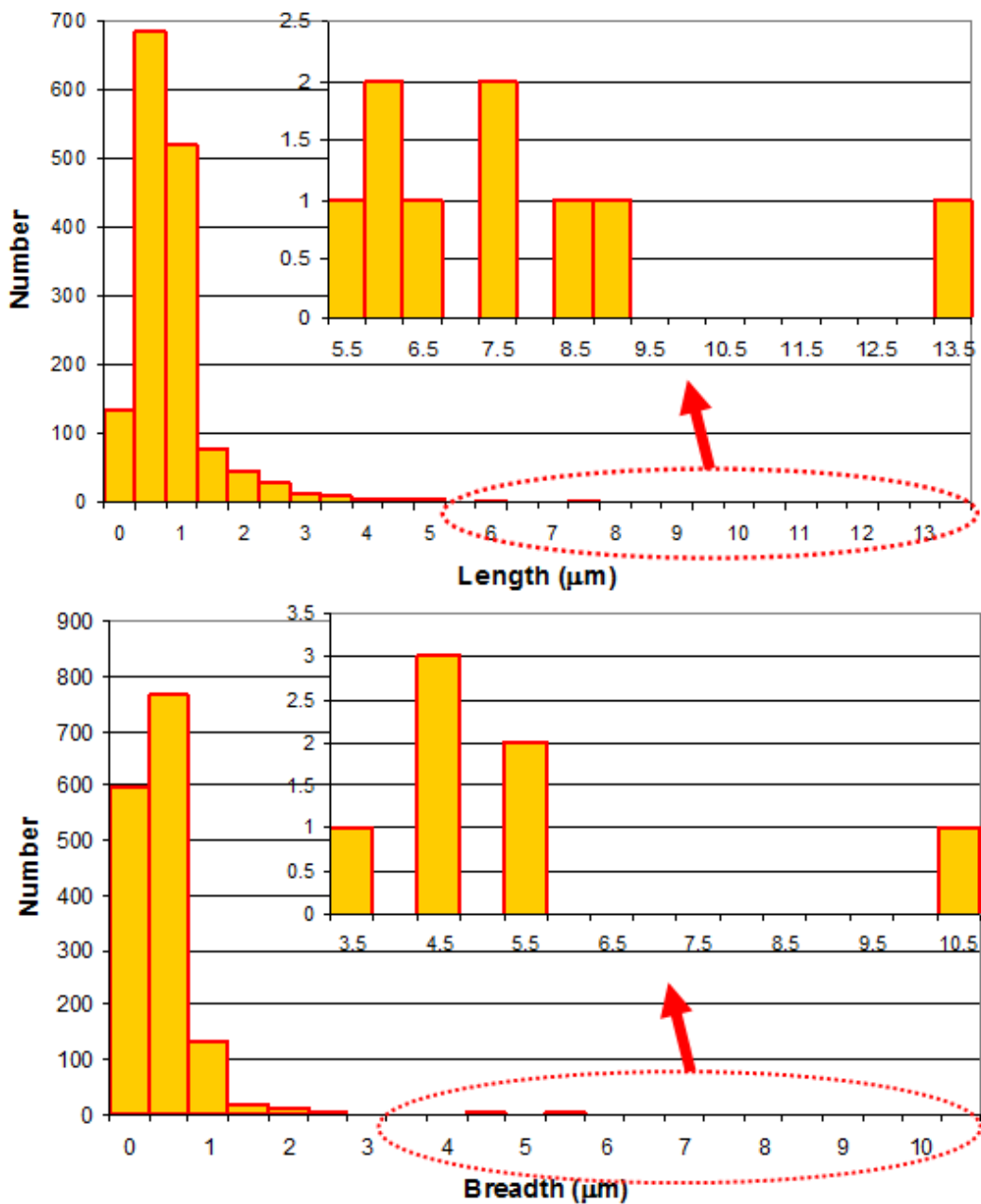


**Figure 5-5: Pit length and width distribution after 4 weeks in the salt spray cabinet**

## 5.1.2 Extreme value statistics

For each pit size distribution, extreme value statistics was applied, as detailed in section 3.2.4, to predict the most probable size of the largest pit for a given exposure time. The extreme value graphs for each distribution are displayed in Figure 5-6. The graphs for the 18 days panel exhibited a reasonably straight line, whereas the graphs for the 3weeks and 4 weeks panels were composed of two segments, of which the first one had a steeper slope compared to the second. The most probable sizes of the largest pit for a given exposure time, given in Table 5-1, were calculated using the whole graph for the 18days panel, and the second segment of the graphs for the 3 weeks and 4weeks panels. The most probable size of the largest pit for a panel of 15-5PH tested for 3 weeks in the salt spray cabinet was bigger in length and width than the most probable size of the largest pit for a panel of 15-5PH exposed for 18days. Surprisingly, however, the most probable size of the largest pit for the 4 weeks panel was smaller in length and width than that of the 18 days panel. This particularity might be explained by the fact that the specimens, as explained in section 3.2.1, although being all polished following the same procedure, they did not all "react" the same and demanded different time of polishing, which have may impacted the properties of the specimens on the surface.

| | | $1/\alpha$ | $\lambda/\alpha$ | $\alpha$ | $\lambda$ | n | x (µm) |
|---|---|---|---|---|---|---|---|
| **18 days** | length | 0.29 | 2.81 | 3.48 | 9.78 | 20 | 20.2 |
| | breadth | 0.42 | 2.13 | 2.35 | 5.01 | 20 | 12.1 |
| **3 weeks** | length | 0.08 | 0.01 | 12.41 | 0.15 | 20 | 37.3 |
| | breadth | 0.29 | 1.75 | 3.49 | 6.12 | 20 | 16.6 |
| **4 weeks** | length | 0.37 | 1.59 | 2.70 | 4.30 | 20 | 12.39 |
| | breadth | 0.30 | 0.07 | 3.31 | 0.23 | 20 | 10.2 |

**Table 5-1: Calculated values of the most probable size of the largest pit x for the three exposure times**
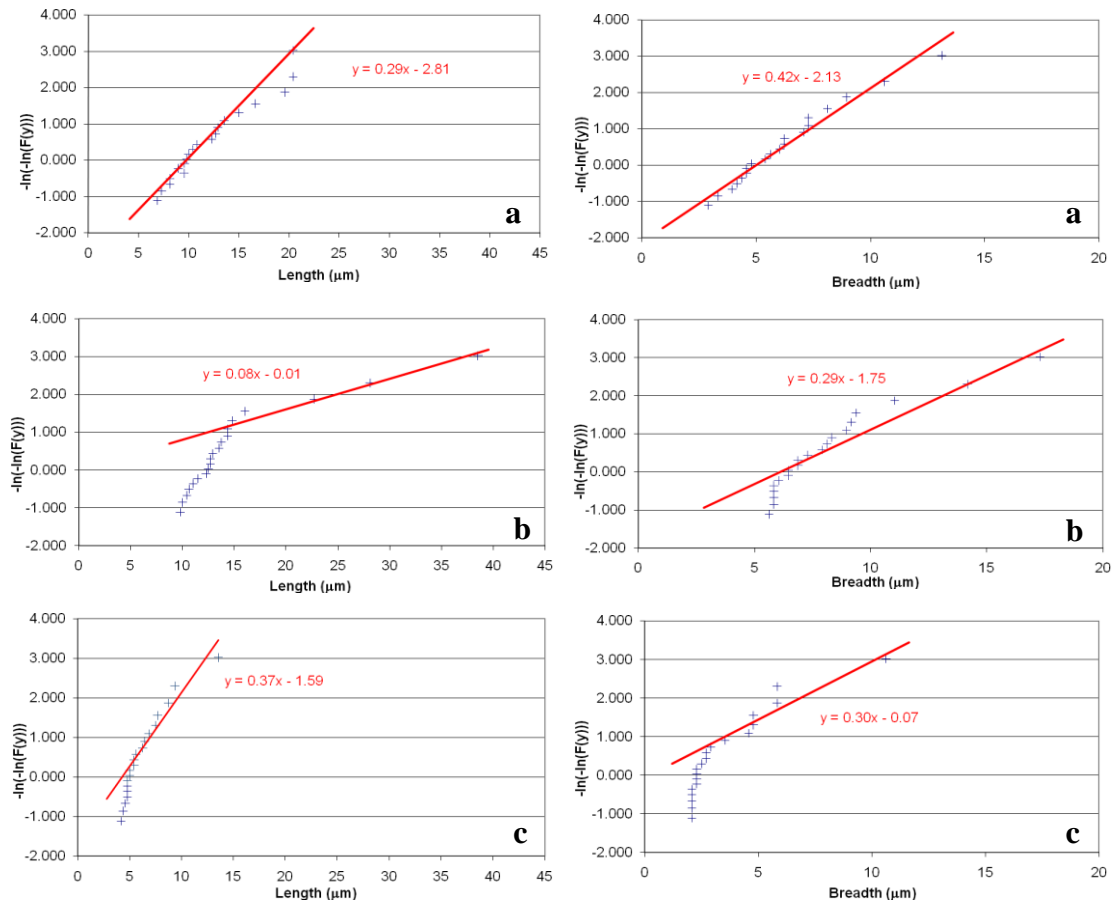
**Figure 5-6: Extreme value graphs for 18 days (a), 3weeks (b) and 4 weeks (c) exposure**

## 5.2 Crevice corrosion testing

Two sets of crevice corrosion testing were carried out. The first set had the aim of assessing the susceptibility of 15-5PH to crevice corrosion, whereas the second aim was to examine the effect of surface roughness on the initiation of crevice corrosion.

### 5.2.1 Susceptibility to crevice corrosion

The number of active crevices on each face of four panels (marked 24E, 7D, 5E and 36F) was recorded as exposure time increased, as illustrated in Figure 5-7 and Figure 5-8. Considering the upper, more exposed surface, panel 24E was the panel which had the most active crevices. Indeed, 26 active crevices out of the 36 crevice corrosion sites developed after 1941 hours in the salt spray cabinet. The second panel with the most active crevices was panel 5E with 16 active crevices out of the 36. Although the number of active crevices was different for these two panels, their curve showing the evolution of the number of active crevices followed a similar pattern, as displayed in Figure 5-7.

In the same way, the curves for the development of active crevices for panels 7D and 36F have a similar trend. However, panel 7D had 12 active crevices out of a possible 36, whereas panel 36F had only 7 active crevices.

Regarding the lower, less exposed surface, the number of actives crevices recorded was much lower than on the upper surface. Indeed, panel 24E, which had the most active crevices, had only developed 3 active crevices out of the possible 36. Panels 7D and 5E developed respectively 2 and 1 active crevices, whereas none was developed on panel 36F.

Weibull statistics [57] were used to calculate the probabilities of having no active crevice corrosion ($P_{nc}$) as a function of the exposure time, as displayed in Figure 5-9. The percentage of crevices that had not become active in any given time can be read from the right hand axis. These probabilities were calculated using the results for panel 24E alone (blue line) and the combined results from the four panels (green line). This graph showed that after an initiation period of 24 hours, the probability of having no active crevice is no longer zero, which means that a panel of 15-5PH stainless steel have very strong chances of developing active crevice corrosion under these conditions.

When the crevice formers were removed at the end of the experiment, it was noticed that the bolt holding one of the crevice former of panel 24E was much tighter that the other one. It was under that crevice former that the greater number of crevice sites had become active. Indeed all eighteen sites had initiated crevice corrosion. The tightness ( i.e the gap between the metal and the crevice former) of a crevice is said to have an effect on the severity of crevice corrosion and the surface finish [13, 15, 16]. In this experiment, all the panels tested had approximately the same surface roughness, as detailed in section 3.3.1. Therefore, it was decided to carry out a second set of experiment with panels of different surface roughness to assess the effect of surface finish on the initiation of crevice corrosion in 15-5PH.

**Figure 5-7: Number of active crevices as a function of the exposure time on the upper, more exposed face**

**Figure 5-8: Number of active crevices as a function of the exposure time on the lower, less exposed face**
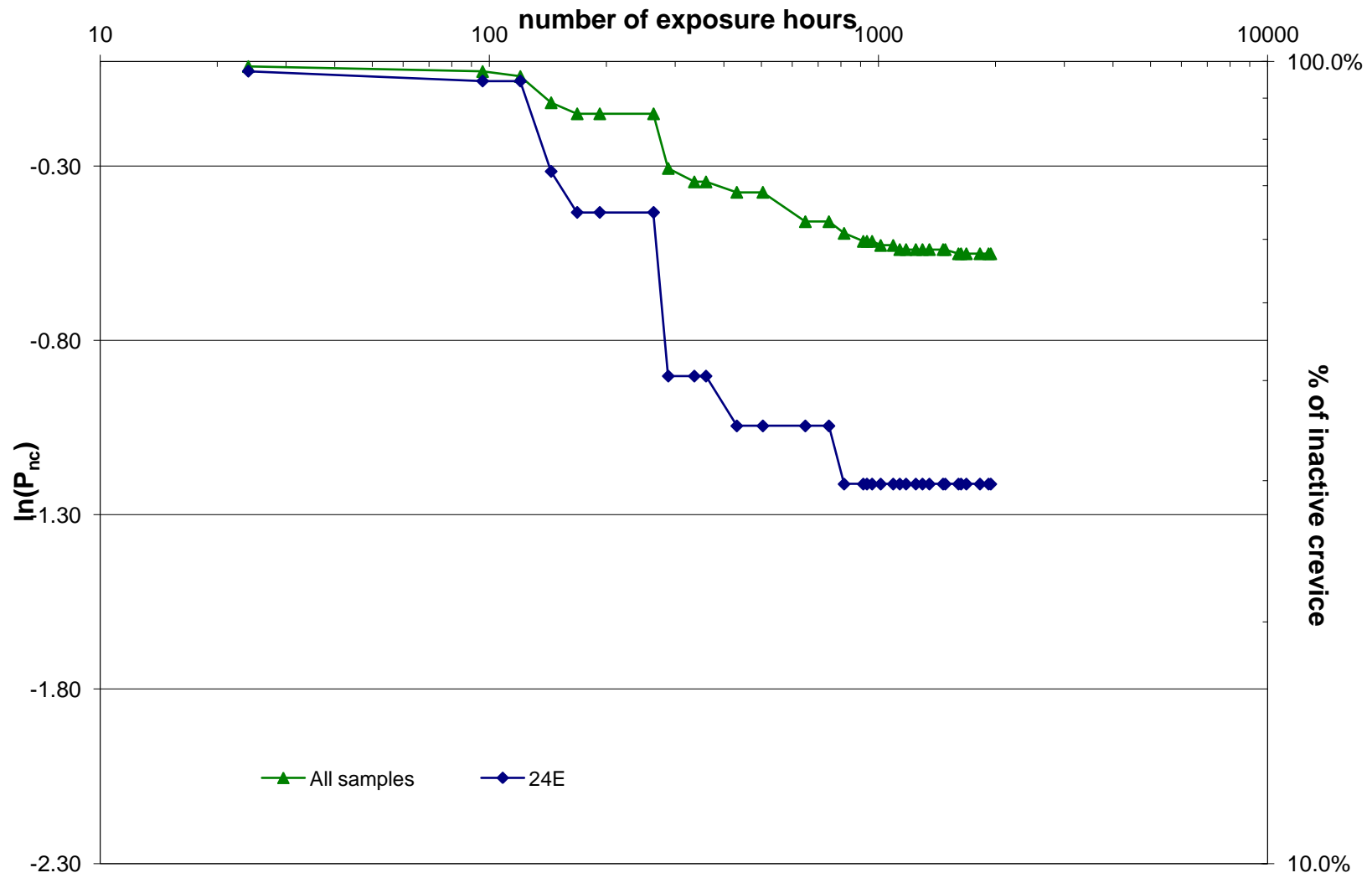
**Figure 5-9: Probability of having no active crevice corrosion as a function of time**

## 5.2.2 Effect of surface finish

Five panels marked 12D, 1B, 33F, 34F and 6E, and of which the respective surface roughnesses are detailed in Table 5-2, were used to examine the effect of the surface finish on the initiation of crevice corrosion.

| Panels | Ra face A (μm) | Ra face B (μm) |
|--------|----------------|----------------|
| 12D | 1.4 | 1.3 |
| 1B | 0.8 | 0.7 |
| 33F | 1.0 | 0.8 |
| 34F | 1.9 | 1.7 |
| 6E | 2.2 | 1.1 |

**Table 5-2: Surface roughness (Ra) measurements on the crevice corrosion panels used in the second set of experiments**

Similarly to the first set of experiments, the number of active crevices on each face of the panels was recorded at different times, as illustrated in Figure 5-10 and Figure 5-11. According to the work of Oldfield [15] and Kain [16], it was anticipated that a narrower crevice gap, that is to say a finer surface finish, would lead to a more rapid onset of active crevice corrosion, as the smaller volume of crevice solution would acidify more quickly. However, no clear pattern relating the surface roughness to the number of active crevices had been observed during these experiments. Nevertheless, variable effects of crevice gap on the initiation of active crevices had been noticed on both surfaces.

Regarding the upper, more exposed surface of the panels, shown in Figure 5-10, panel 12D, which had a surface roughness of 1.4μm, had initiated 25 crevices out of the possible 36 by the end of the experiment, whereas panel 1B, which had a finer surface finish (0.8μm), developed only 7 crevices. However, panel 6E, which had the roughest surface (2.2μm), did not initiate more active crevices than panel 12D, since at the end of the experiment only 12 active crevices were counted.

Considering the lower, less exposed surface of the panels, shown in Figure 5-11, a clearer trend was observed with the exception of the panel with the finest finish (1B, 0.7μm). Indeed, at the end of the experiment, the number of active crevices on each panel, except panel 1B, increased systematically in the order of increasing crevice gaps. The panel 34F, 12D, 6E and 33F, which are in order of the roughest panel to the

finest, have respectively developed 26, 24, 15 and 9 active crevices. If this order had been respected for all the panels, panel 1B, which had the finest surface finish among the lower surface of the five panels, would have developed less than 9 active crevices. However, 16 active crevices had been counted on that panel at the end of the experiment.

For both the upper and lower surfaces, although no clear patter had been observed, it seems that the rougher panels develop more active crevices, which is the reverse of what was expected. It appears that in these experiments, the onset of crevice corrosion had been controlled not by the volume of electrolyte contained in the crevice but by the access of that electrolyte contained into the crevice gap; access being easier in the case of the rougher surface with the wider gap.
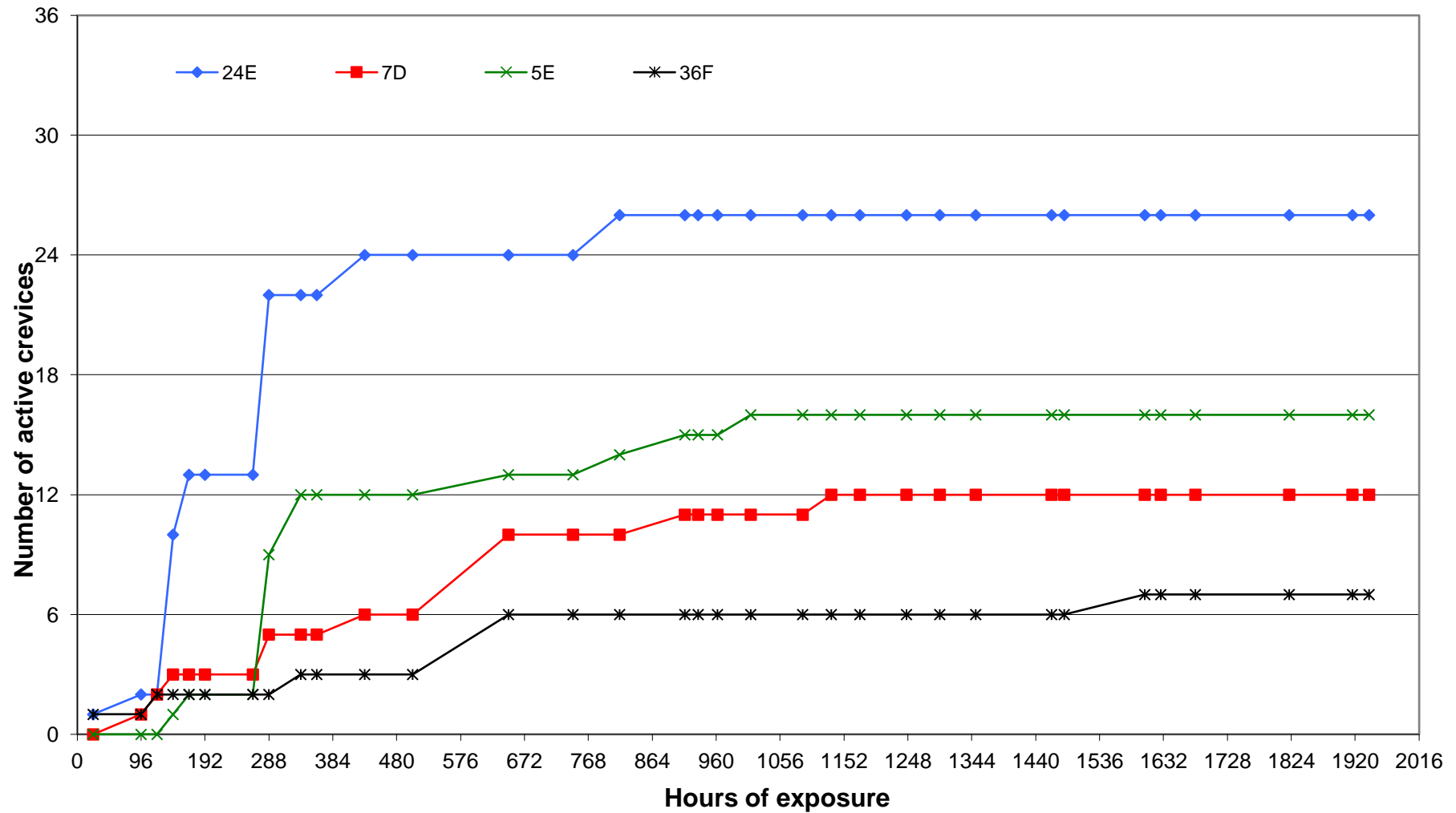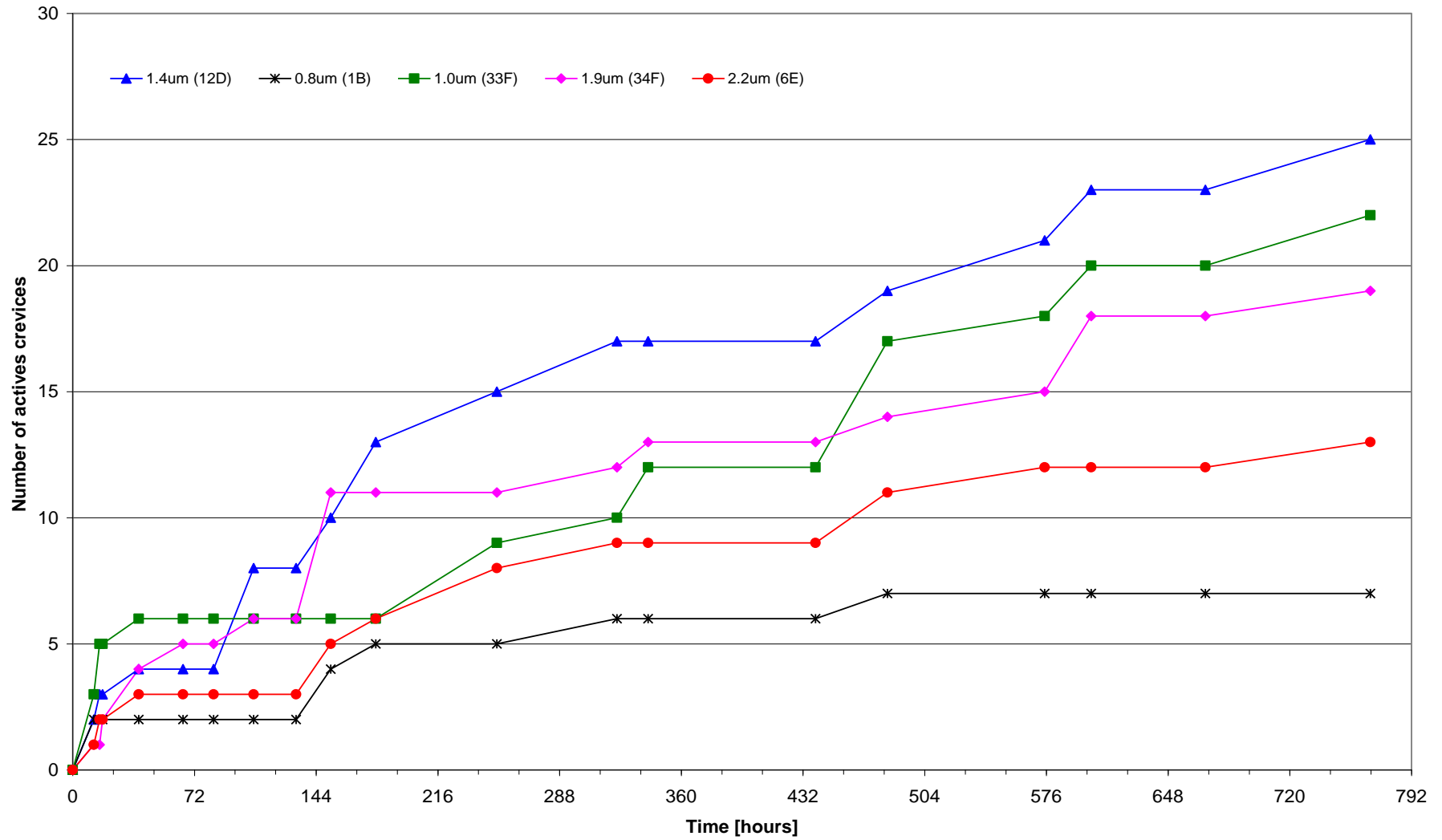
**Figure 5-10: Number of active crevices as a function of the exposure time on the upper, more exposed face**

# 5. RESULTS AND DISCUSSION



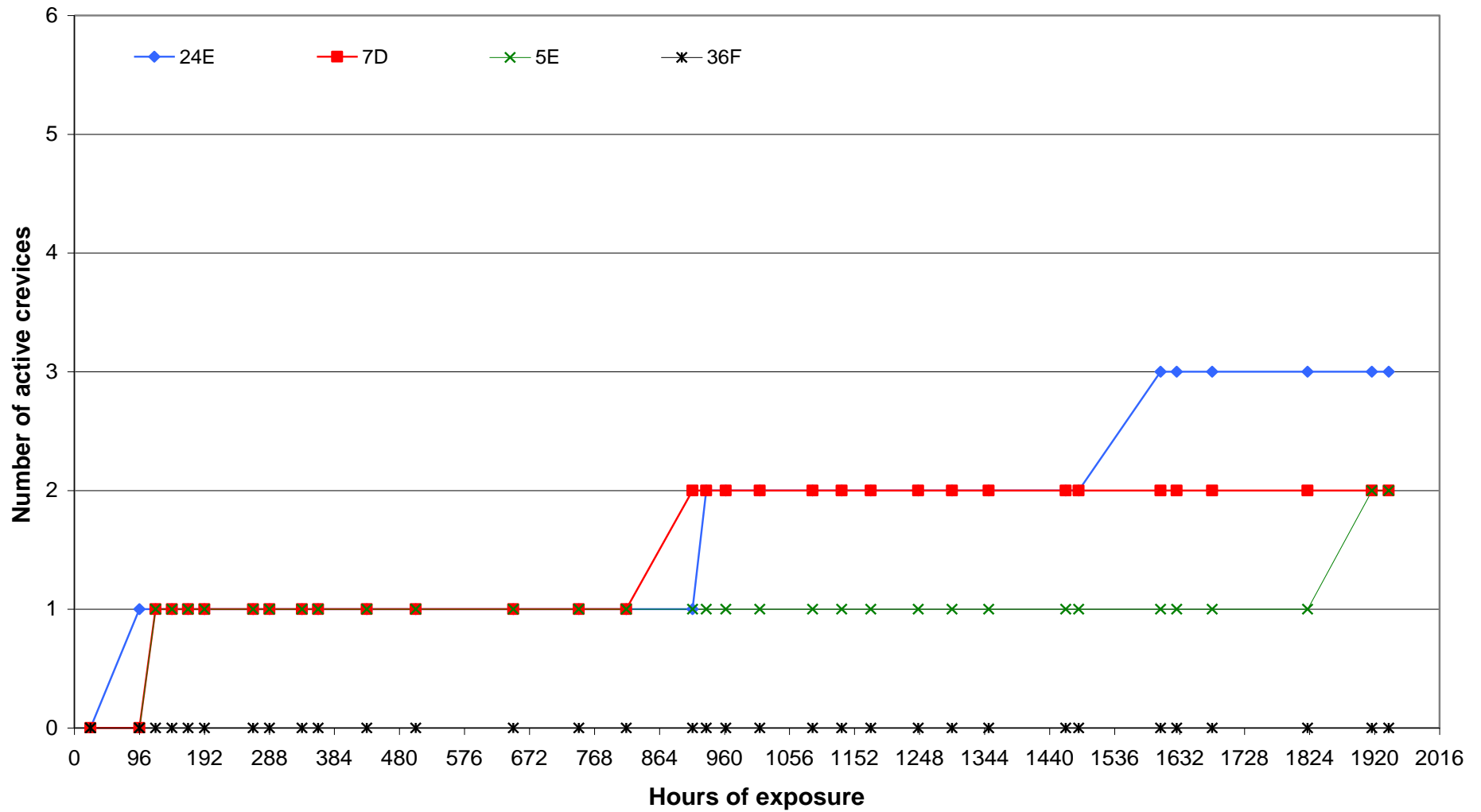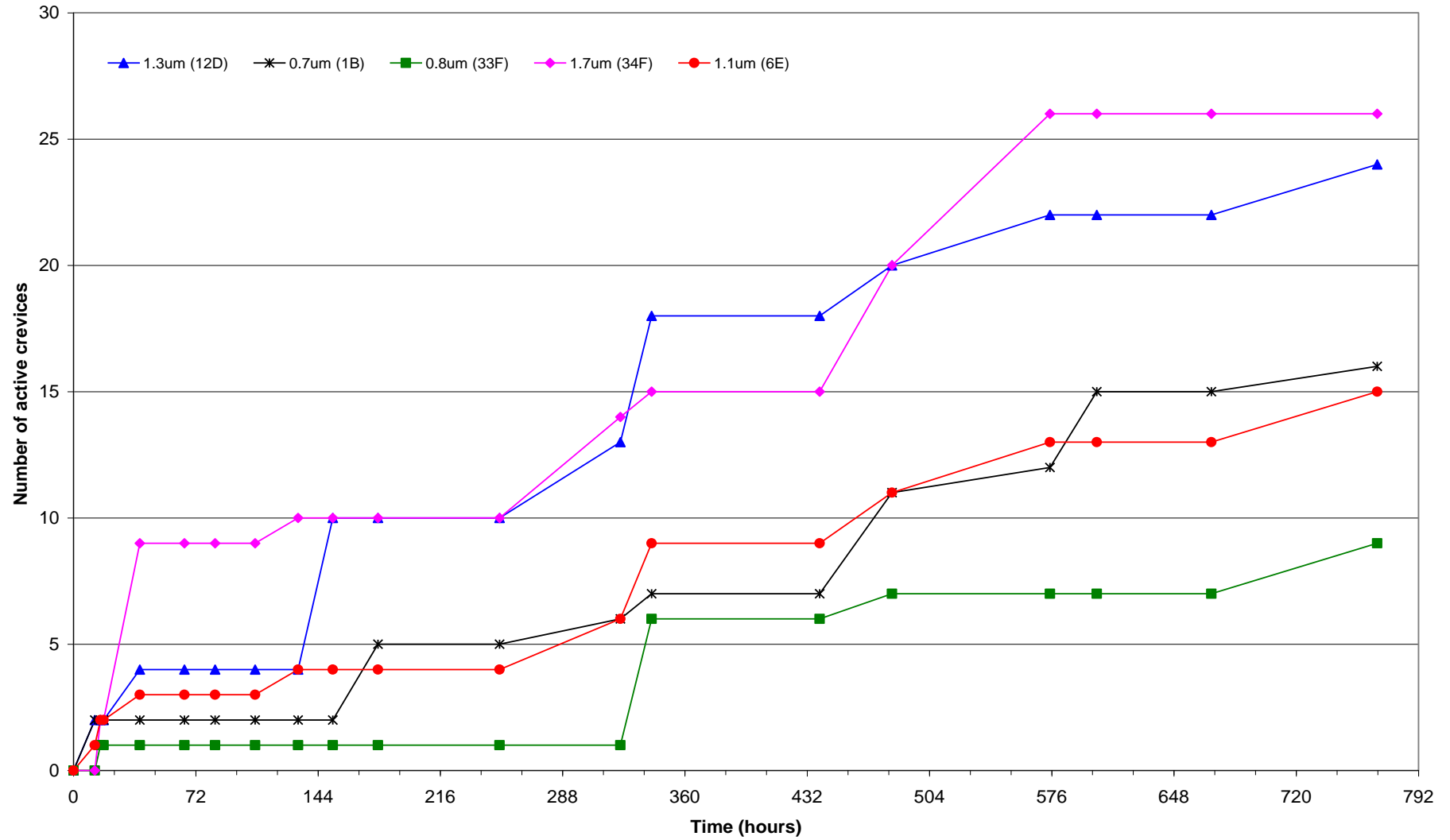**Figure 5-11: Number of active crevices as a function of the exposure time on the lower, less exposed face**

## 5.2.3 Crevice corrosion propagation pattern

In both set of experiments, it was observed that the crevice corrosion propagated along the grinding marks of the panel, as illustrated in Figure 5-12. It was also noticed that in general, the crevice corrosion first spread across the area of the crevice former, until the whole area has become active. When the entire area of the crevice former had become active, no further growth across the surface took place and the corrosion then developed into the materials. This was observed in most of the experiments, although in some cases the entire area had not become active before the corrosion propagated into the material. Figure 5-13 shows the propagation of crevice corrosion for the same site at different times. After a 12 hours exposure to the salt spray, a dark area of active corrosion following the grinding marks, occupied around one quarter of the area of the crevice former. Then after 83 hours, that active area had spread to approximately one half of the area of the crevice former, still following the grinding marks. At 439 hours, the active area had stopped propagating across the surface and started to develop into the material. Finally, after 768 hours, the active corrosion was still developing into the material and a deeper zone (circled in red in Figure 5-13) could clearly be noticed.
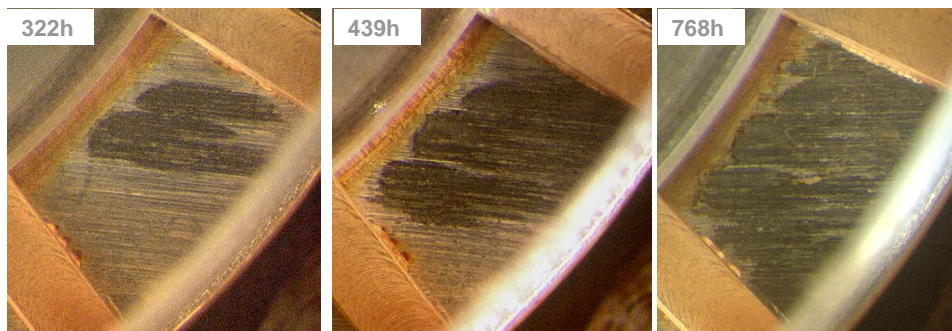


**Figure 5-12: Crevice corrosion propagation along the grinding marks**
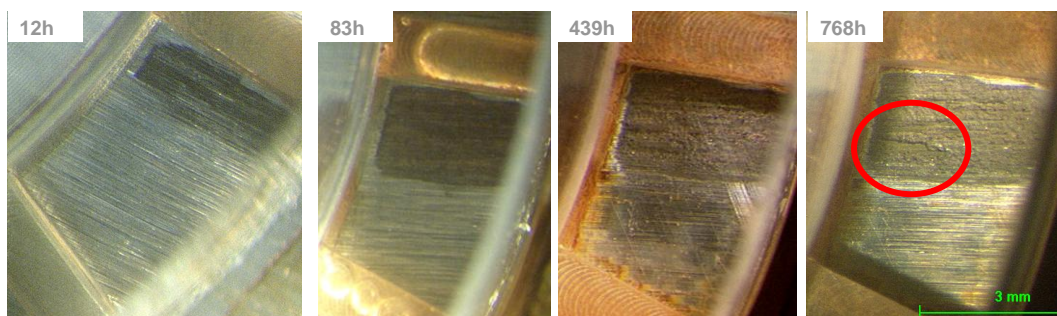


**Figure 5-13: Crevice corrosion propagation first across the surface and then into the material**

## 5. RESULTS AND DISCUSSION

The active corrosion spreading along the grinding marks can be explained by the fact that it would be easier for acidic solution accumulating in the crevice to run along the grooves, formed by the grinding marks, rather that crossing from a groove to another, as sketched in Figure 5-14. The level of acid in a particular groove would need to be high enough to go over the ridge of that groove to the next one.

At time $t_1$                                    At time $t_2 > t_1$
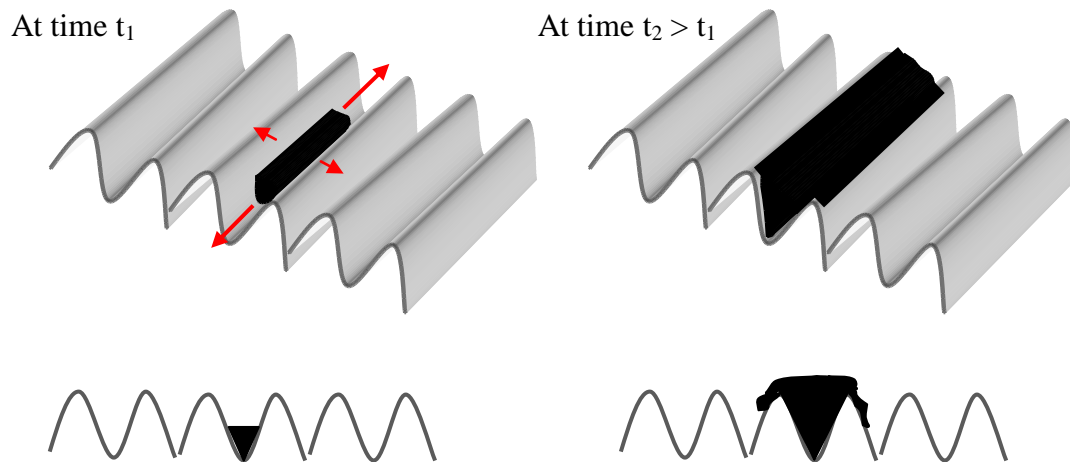
**Figure 5-14: Sketch of the propagation of the acidic solution in the crevice**

### 5.2.4 Crevice corrosion surface area

Each crevice corrosion site of each panel had been measured using the methodology described in section 3.3.4.1 for different exposure times. The distributions of the active crevice corrosion surface area for the two sets of experiments are displayed in Figure 5-15 and Figure 5-16. Although measurements were made for ten and twelve different exposure times respectively for the first and second set of experiments, only six distributions per set were displayed.
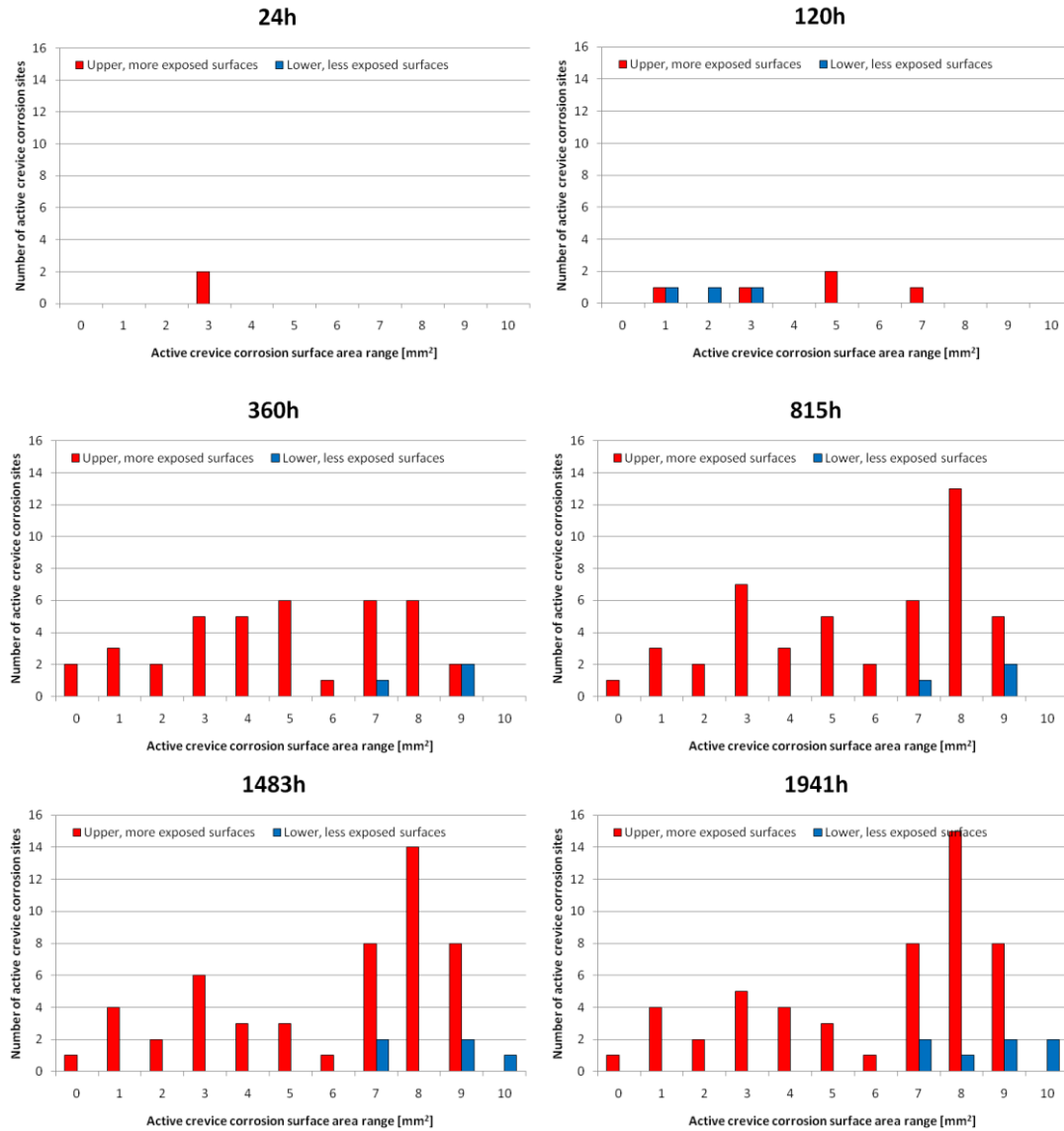
**Figure 5-15: First set of experiment - Active crevice corrosion surface area distributions at different exposure times**

### 5.2.4.1  Active crevice corrosion surface area distributions

Considering the upper, more exposed surfaces in both set of experiments, illustrated in red in Figure 5-15 and Figure 5-16, it was observed that the distributions are first restrained to few ranges and then spread over more and more ranges with time. For instance, for the second set of experiments, the distribution for the upper, more exposed surfaces first lay between 0-3mm$^2$ at 12.5h and then spread over more ranges with time, to finally lie between 0-11mm$^2$ at the end of the experiment.

84
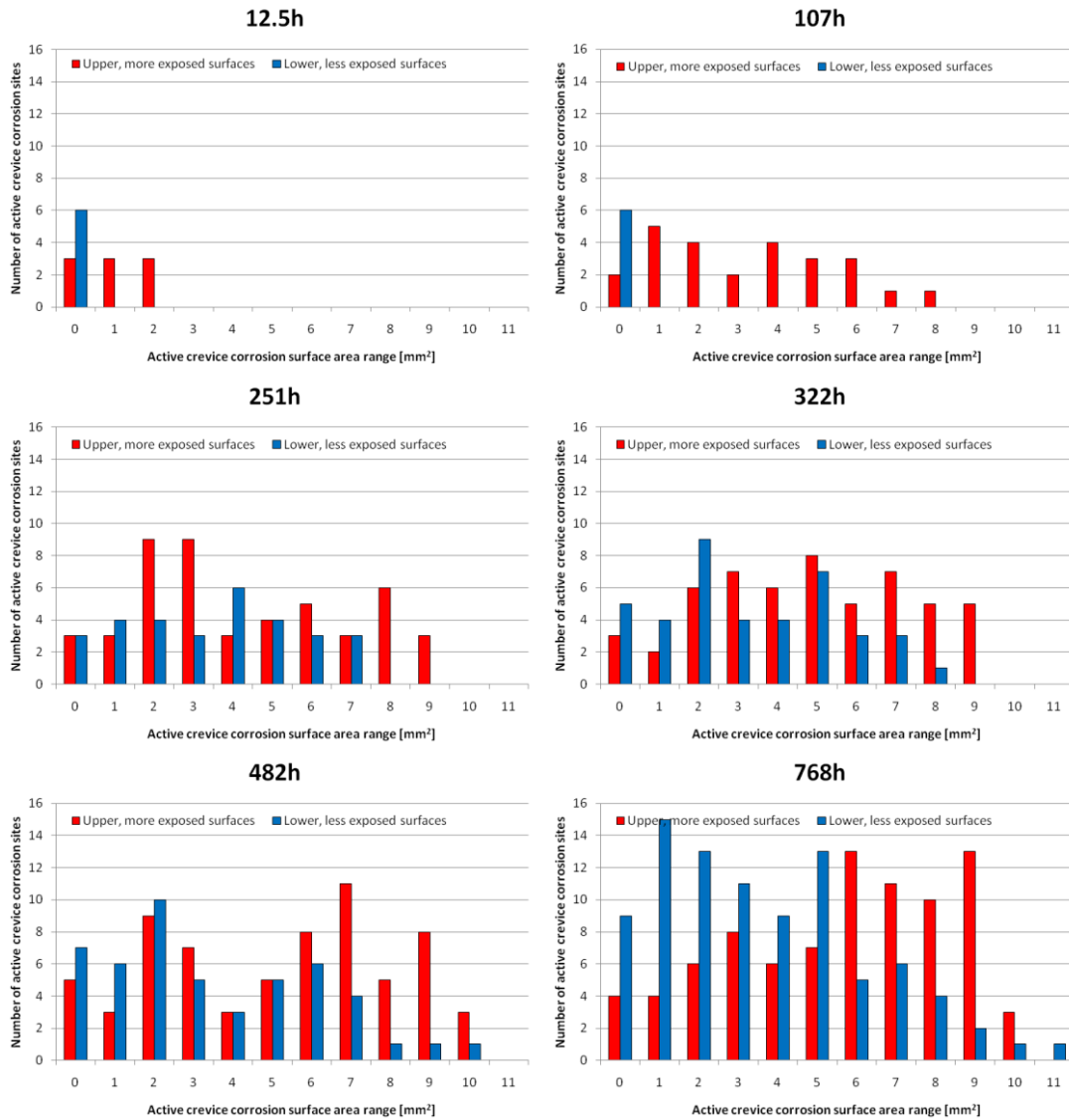
**Figure 5-16: Second set of experiment - Active crevice corrosion surface area distributions at different exposure times**

However it was noticed that, in both set of experiments, the distributions stopped spreading over more ranges after a certain amount of exposure. Indeed, no area of active crevice corrosion site larger than 10mm2 was detected after 264h in the first set of experiments, whereas no site larger than $11mm^2$ was measured after 439h in the second set. In addition, in both set of experiments, it can be seen that the peak of the distributions shifted to the right with increasing exposure time. Indeed, in the first set for instance, at 120h the peak was in the $5-6mm^2$, whereas from 815h, the peak of the distribution was between 8 and $9mm^2$. Nevertheless, in the first set of experiments, it was noticed that after 815h, the peak range did not shift to the right anymore, but the number of active crevice corrosion sites being in that peak range did increased with time. Indeed at 815h, the number of active sites being in the $8-9mm^2$ peak range was

85

13, it then contains 14 active sites at 1483h and 15 after 1941h. In contrast, the maximum range reached by active crevice corrosion sites on the upper, more exposed surfaces, 9-10mm$^2$, included 5 active sites at 815h and 8 at 1483h and 1941h.

Regarding the lower, less exposed surfaces, displayed in blue in Figure 5-15 and Figure 5-16, it was noticed that in the first set of experiments, the number of ranges over which the distribution lay was limited of few ranges, whereas in the second set the distributions spread over more ranges with time. In addition, in the second set, the peak of the distribution shifted to the right with increasing time. Regarding, the first set, although the distribution did not display any obvious peak, the whole distribution moved to the right with exposure time.

### 5.2.4.2 Most probable maximum active site area

Extreme value statistics was applied to these distributions in order to get the most probable maximum area of active crevice corrosion site at different exposure time for both set of experiments and both surfaces and thus assess the crevice corrosion growth rate across the surface. Figure 5-17 displayed the extreme value graph corresponding to the distributions shown in Figure 5-16. At short exposure times (e.g. 107h), the graphs had a reasonable straight line fit for data smaller that 9mm$^2$, from which the most probable maximum area of active crevice corrosion can be calculated. At longer exposure times (e.g. 322h), the graphs deviated from a straight line and levelled off as the area of active crevice corrosion approached 9mm$^2$. These observations were made for both set of experiments and both surfaces. As the aim of these measurements was to examine the crevice corrosion growth rate across the surface, the most probable maximum areas of active crevice corrosion were calculated by applying extremes value statistics to the data less than 9mm$^2$ since from that point the growth significantly slow down. Indeed, each castellated crevice sites on the crevice former had an area of 11.3mm$^2$ and the maximum possible area of active crevice corrosion was defined by the size of the crevice former. According to the extreme value graphs, 9mm$^2$ seemed to be the point where the growth rate of the active crevice corrosion area was influenced by the restricted size of the crevice former.

## 5. RESULTS AND DISCUSSION
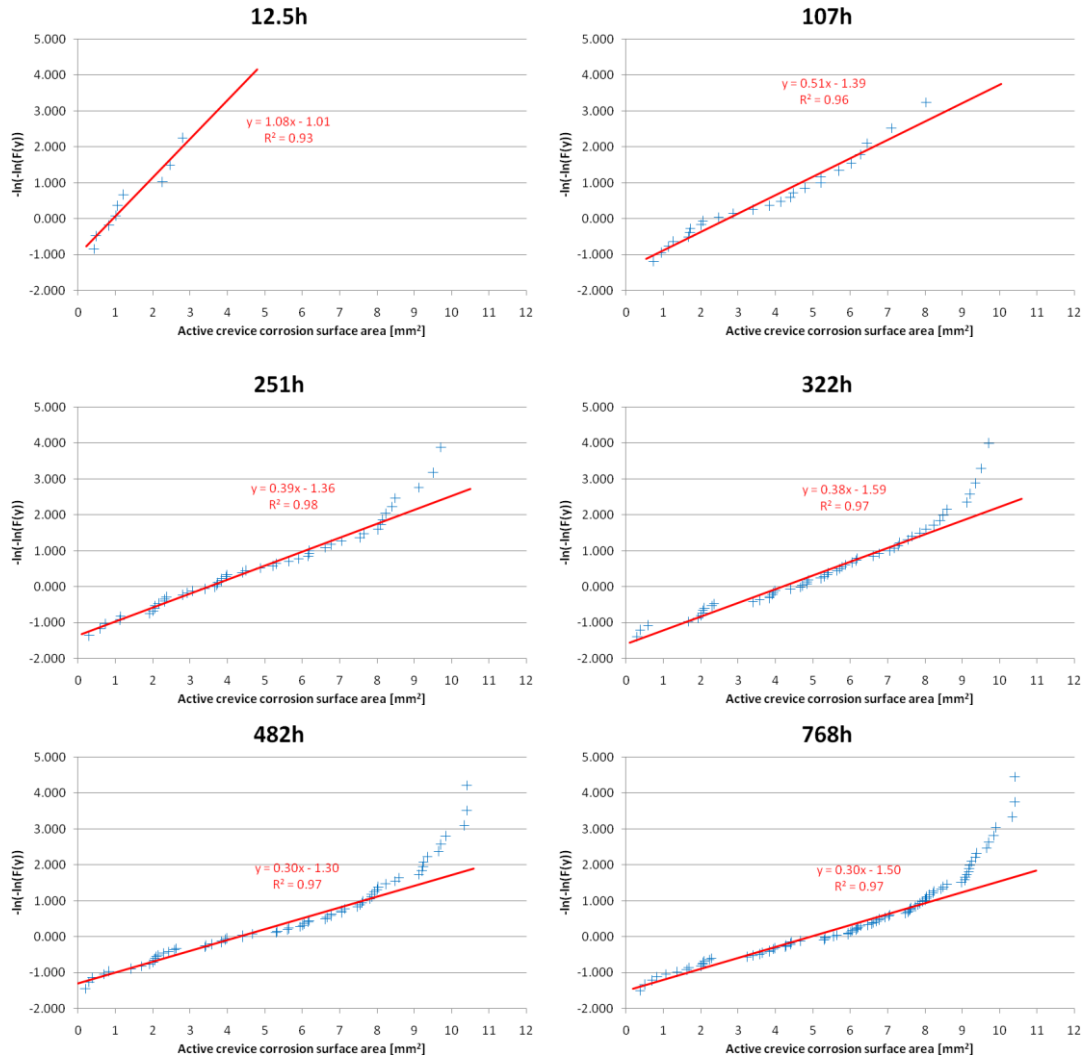


**Figure 5-17: Extreme value graph of active crevice corrosion surface area**

In Figure 5-18 are displayed the most probable maximum area of active crevice corrosion sites at different exposure times for both experiments and both surfaces. Considering the upper, more exposed surfaces, the area growth rates for both set of experiments followed a similar trend with a high initial growth rate until approximately 300 hours, followed by a slowdown.

Regarding the lower, less exposed surface curves, the area growth rate curve for the second experiment followed a pattern closed to the one followed by the upper, more exposed surface curves but with lower amplitude. However, the curve for the first experiment had a high initial rate until 300 hours and then seemed to flatten around 10mm$^2$.
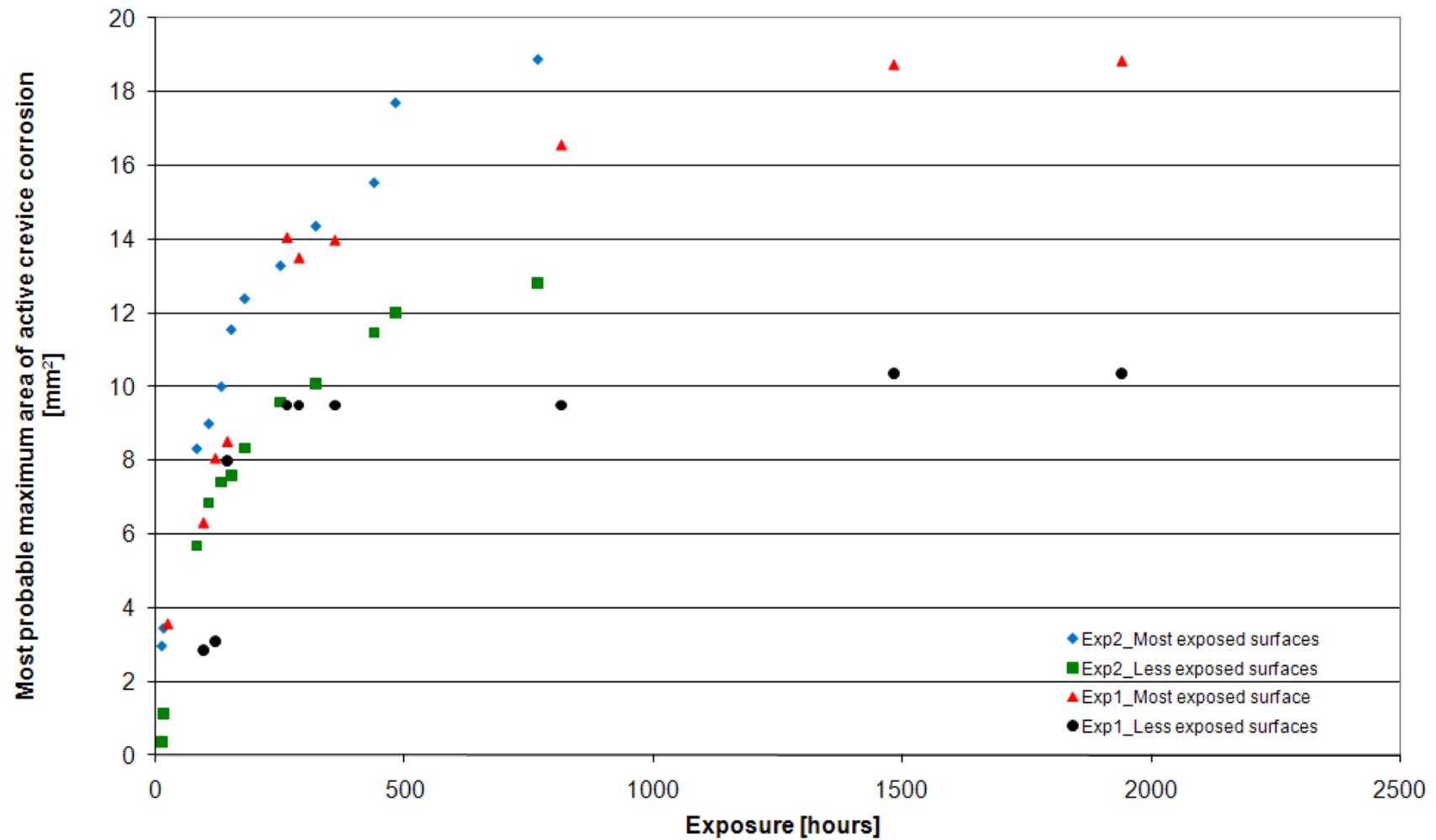
**Figure 5-18: Most probable maximum area of active crevice corrosion as a function of the exposure time**

## 5.2.5  Crevice corrosion depth

The maximum and average depth of each crevice corrosion site had been measured with a confocal laser scanning microscope at the end of the exposure time (1941h for the first set of experiments and 768h for the second set) for the upper, more exposed surface, as explained in section 0.

The maximum and average depth distributions for the active crevice sites of each set of experiments are shown in Figure 5-19. 34 sites were measured for the first set of experiments, whereas 85 sites were measured for the second set. The distributions for the first set of experiments appeared more scattered than the distributions for the second set. Indeed, the maximum depth distribution was included between 0 and 1000µm for the first batch of experiments, whereas it lay between 0 and 250µm for the second batch. Likewise, the average depth distribution range was 0-500µm for the first set of experiments, whereas it was 0-100µm for the second set.

Considering the first batch of experiments, the peak of the curve for the maximum depth lay between 50 and 100µm with 41% of the active crevice corrosion sites being in this interval, whereas the peak for the average depth (56% of the sites) was included in the 0-50µm range. The deepest active crevice corrosion site was 987µm and the maximum average depth was 472.5µm.

Regarding the second batch of experiment, the peak of the curve for the maximum depth lay between 100 and 150µm with 40% of the active crevice corrosion sites being in this interval, whereas the peak for the average depth (88% of the sites) was included in the 0-50µm range. The deepest active crevice corrosion site was 249µm and the maximum average depth was 97µm.

Extreme value statistics was applied to the top twenty values of each distribution in order to assess the most probable maximum size of the deepest active site and the most probable maximum average depth for both set of experiments. The extreme value graphs for the second set of experiments, displayed in Figure 5-20, had a reasonably straight line, whereas the graphs for the first set of experiments were composed of two segments, of which the first one had a steeper slope compared to the second segment. The whole graphs were used in the second set of experiments to calculate the extreme values, whereas only the second segment was used for the first set of experiments. The extreme values for the maximum depth and the average depth,

given in Table 5-3, were significantly higher for the panel of the first experiment compared to those of the second experiment, which is in agreement with the fact that the exposure was longer in the first set of experiments.
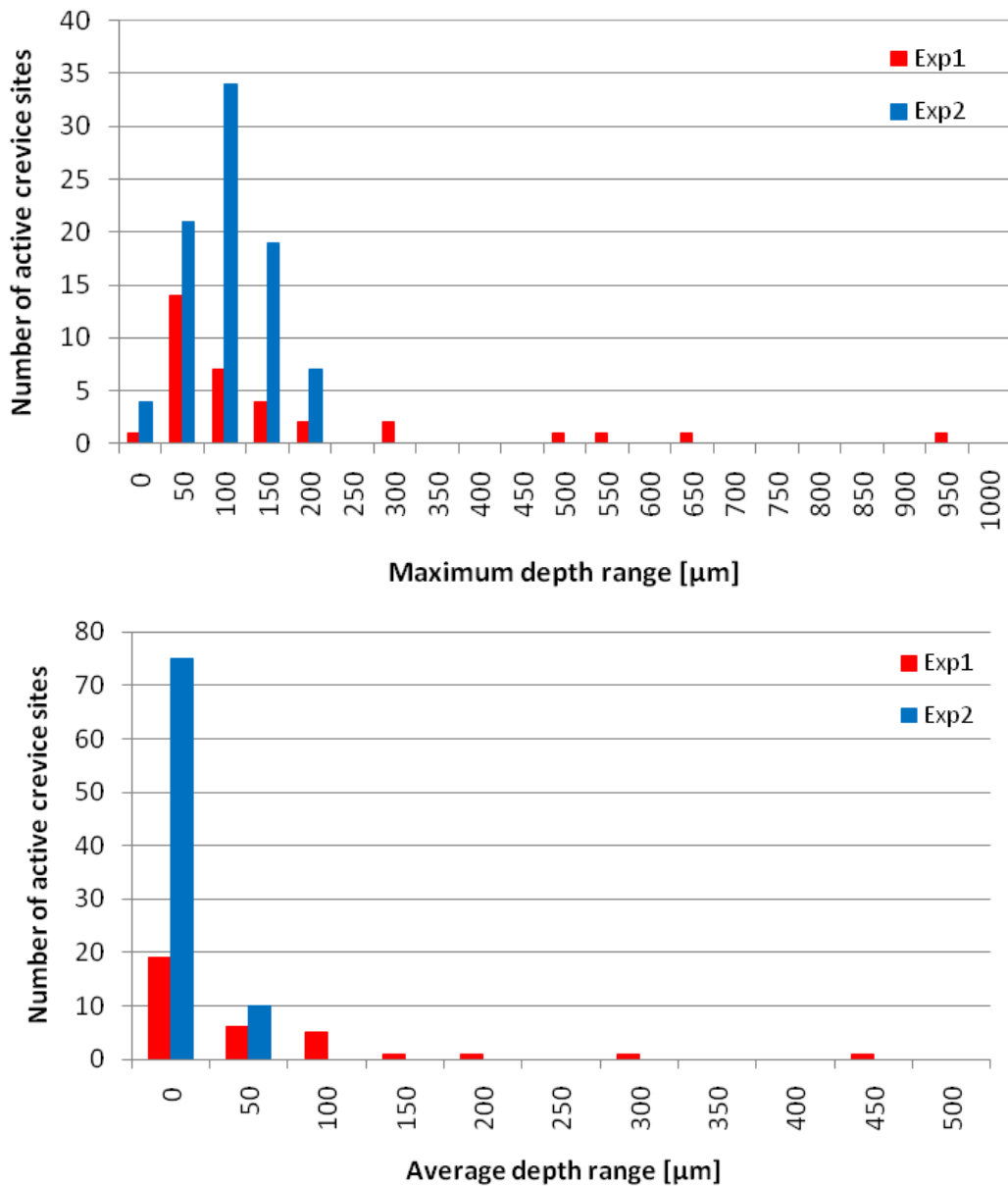


**Figure 5-19: Maximum depth distribution**

|  | Exp1 | Exp2 |
|---|---|---|
| The most probable deepest active crevice corrosion site [μm] | 950 | 251.5 |
| The most probable average depth of active crevice corrosion site [μm] | 439 | 92 |

**Table 5-3: Most probable maximum values for the depth of active crevice corrosion site**

## 5. RESULTS AND DISCUSSION
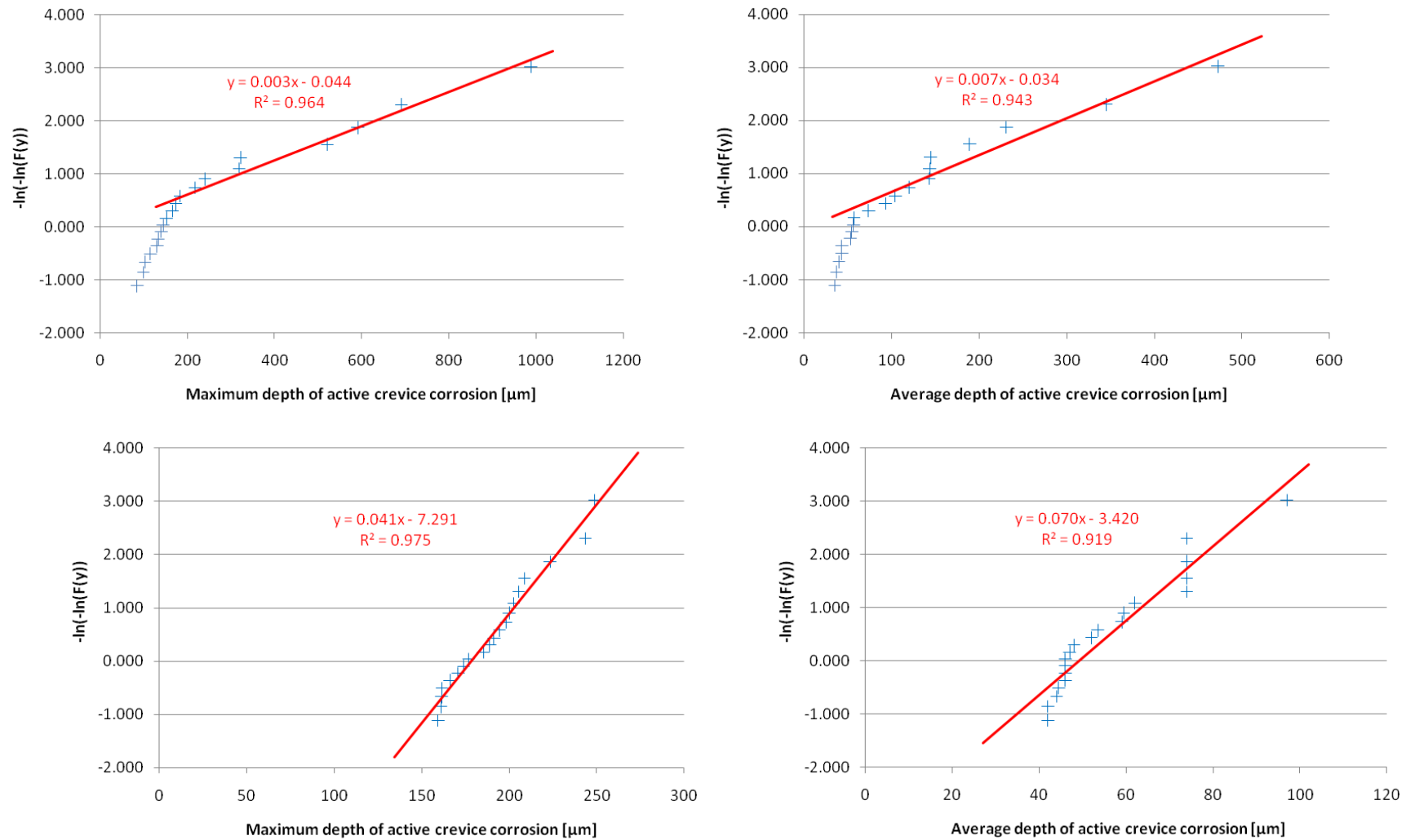


**Figure 5-20: Extreme value graph of active crevice corrosion depth for the first and second set of experiments (respectively top and bottom graph)**

## 5.3  Crack growth rate testing

Single edge notched specimen had been tested in fatigue in air and in 3.5% NaCl solution in order to assess the fatigue crack growth rate in 15-5PH in both environments, as explained in section 3.4.3.

### 5.3.1  Fatigue crack growth rate in air

In this set of experiments, four single edge notched specimens were tested in fatigue and the length of the crack was recorded using replica, as detailed in section 3.4.2.1. For each specimen, the stress range used to start the test and its evolution during the test is detailed in Table 5-4. The corresponding plot of the crack length as a function of the number of cycles is displayed in Figure 5-21. The graphs for specimens 16 and 7 exhibit an exponential curve, whereas the plots of specimens 12 and 3 displayed a step curve pattern.

The crack growth rate was derived from the data of the crack length as a function of the number of cycles, and the corresponding stress intensity factor range was calculated, as detailed in section 2.3.4. The stress intensity range as function of the crack growth rate for the four specimens was gathered in the same log-log plot, as shown in Figure 5-22. The testing conditions for specimen 16 and specimen 7 led to a stress intensity range increasing with the crack length, whereas the testing conditions for specimen 12 and specimen 3 were set to have a stress intensity range decreasing with the crack length in order to reach the stress intensity range threshold $\Delta K_{th}$. The crack growth rate curve had a reasonable straight line fit, as displayed in Figure 5-22 from which the Paris equation, $\frac{da}{dN} = 10^{-11}(\Delta K)^{2.62}$ , was obtained. In addition, it was possible to assess the stress intensity range threshold, $\Delta K_{th}$ =5MPa.$\sqrt{m}$, since, as explained in section 2.3.4, experimentally $\Delta K_{th}$ corresponds to a maximum crack growth rate of $10^{-8}$ mm/cycle.

| Specimen | $\Delta\sigma$ start | $\Delta\sigma$ during test |
|----------|----------|--------------------------|
| 16 | 350 MPa | decreased progressively |
| 7 | 180 MPa | constant |
| 12 | 180 MPa | decreased to 79MPa after 235 000 cycles |
| 3 | 180 MPa | Decreased progressively |

**Table 5-4: Stress ranges applied for the fatigue crack growth rate testing in air**
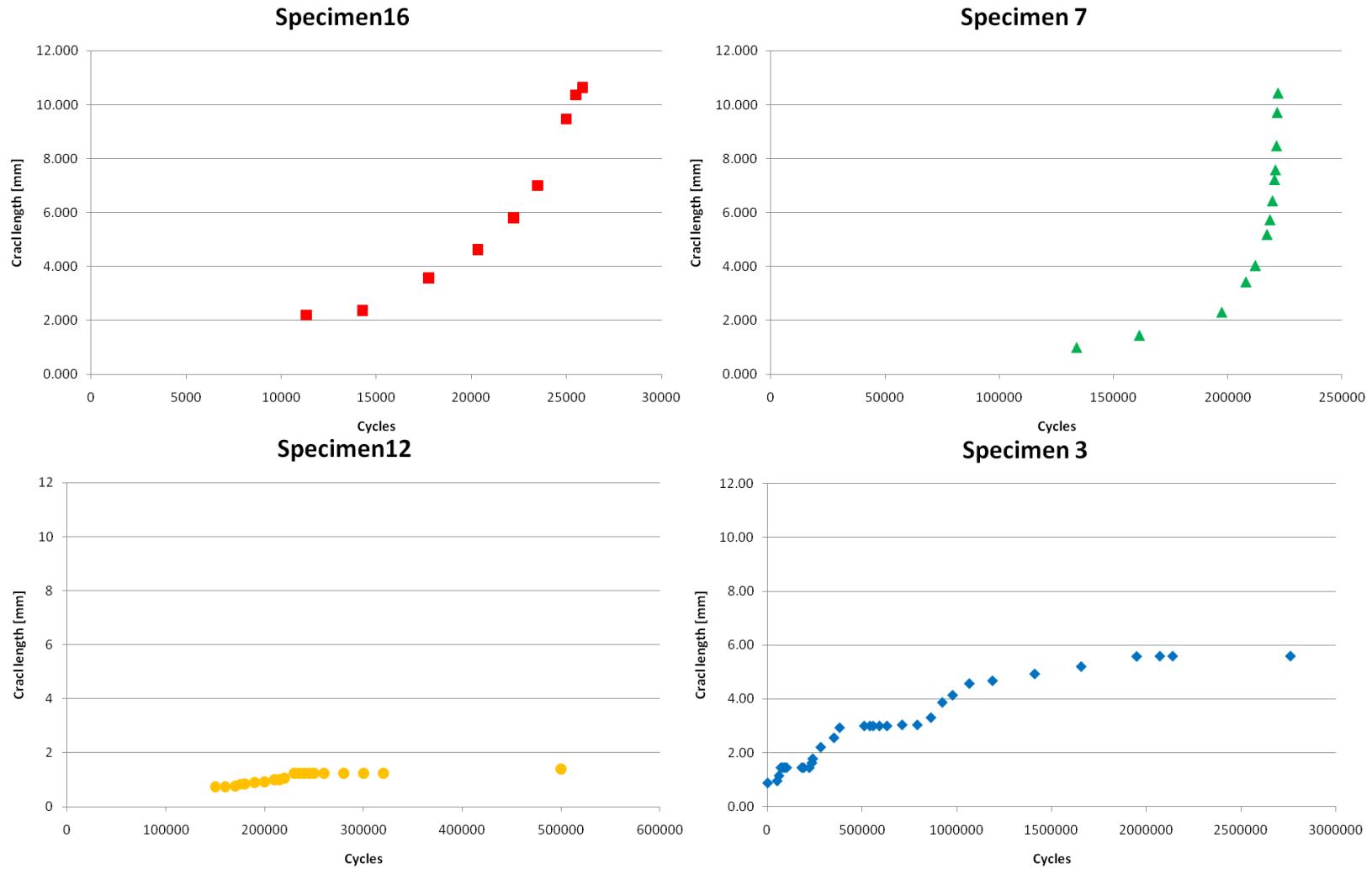
**Figure 5-21: Fatigue crack length as a function of the number of cycles, R=0.1, f=10Hz**

# 5. RESULTS AND DISCUSSION
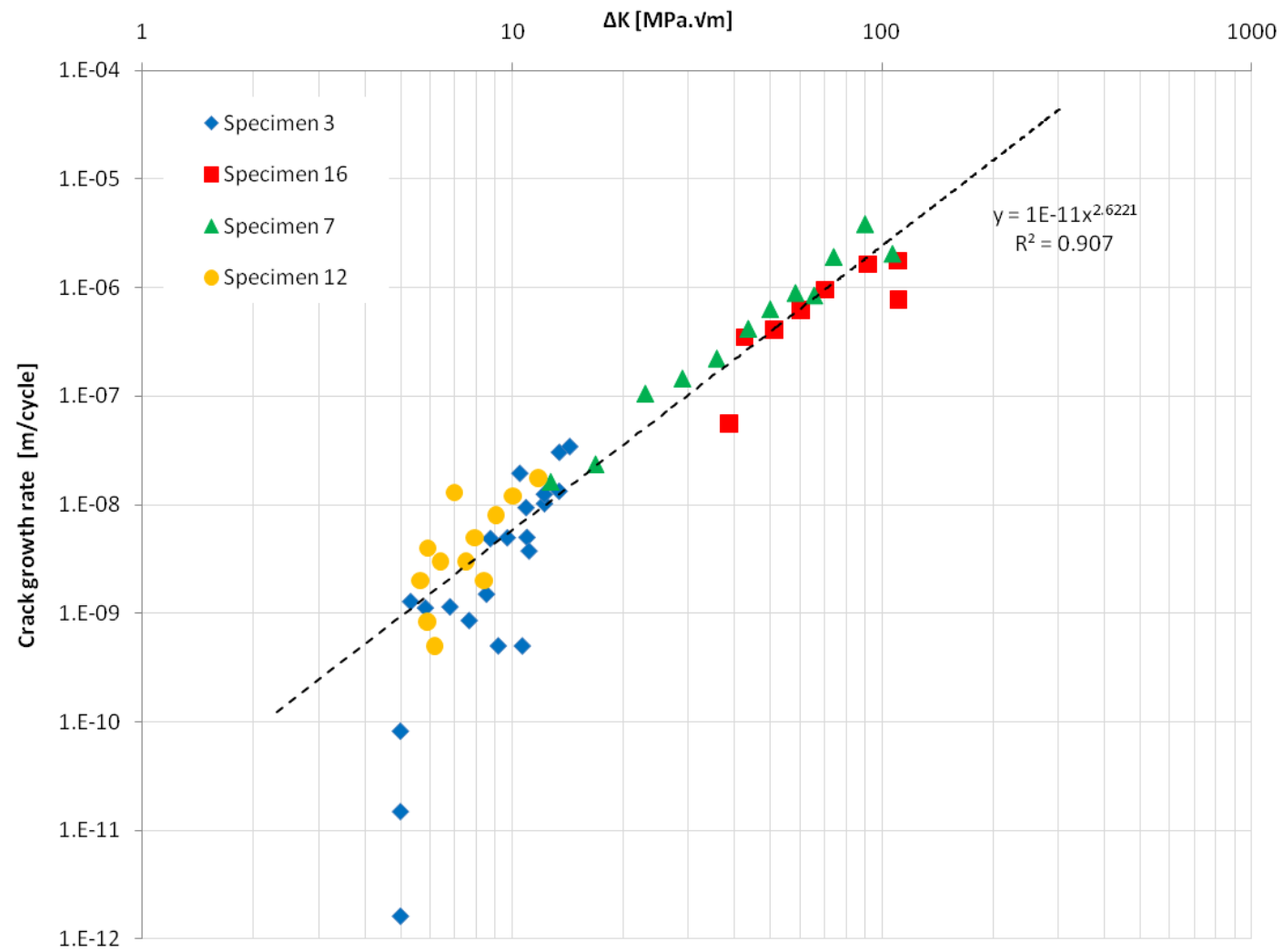


**Figure 5-22: 15-5PH fatigue crack growth rate in air, R=0.1, f=10Hz**

## 5.3.2 Striation spacing measurement
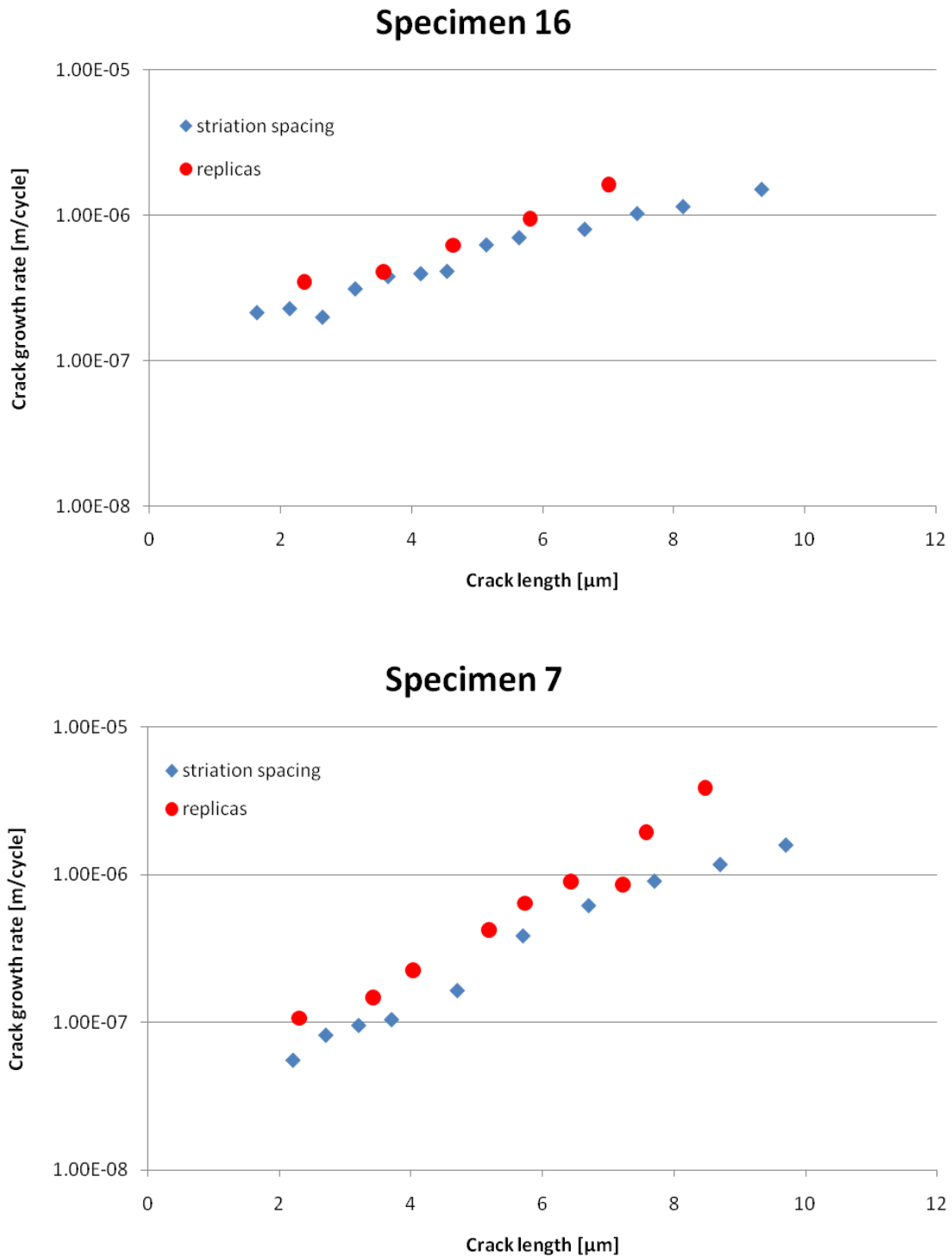




**Figure 5-23: Crack growth rate comparison: replica and striation spacing measurements**

In order to verify the accuracy of the crack growth rate obtained by measuring the crack length with replica material, striation spacing measurement was performed for specimen 7 and specimen 16.

The crack growth rate obtained from the striation spacing was compared to the crack growth rate obtained with replicas measurement, as detailed in Figure 5-23. For both specimens, the crack growth rate from the replica was slightly higher than the crack growth rate assessed from the striation spacing measurement, and the gap between the two rates increased with the crack length. However, in spite of the slight offset, the crack growth rates obtained by the two methods were in close agreement and it was concluded that the replica method was a reliable method for crack length measurement.

### 5.3.3  Crack growth rate in aqueous NaCl environment

In this set of experiments, four single edge notched specimens were tested in fatigue in a 3.5% NaCl solution. For each specimen, the stress range used to start the test and its evolution during the test is detailed in Table 5-5. The length of the crack was recorded using a digital camera and electro-potential monitoring, as detailed in section 3.4.2, except for specimen 18. The corresponding plot of the crack length as a function of the number of cycles is displayed in Figure 5-24. The fracture surface of specimen 18 was observed with a scanning electron microscope and striation spacing measurement, as explained in section 3.4.3.3, was carried out. The plot of the crack growth rate as a function of the crack length is displayed in Figure 5-25.

| Specimen | $\Delta\sigma$ start | $\Delta\sigma$ during test | Failure after |
|---|---|---|---|
| 18 | 235 MPa | constant | 52 262 cycles |
| 13 | 280 MPa | constant | 23 972 cycles |
| 5 | 200 MPa | Progressively decreased | test stopped after 148 000 cycles |
| 9 | 150 MPa | Progressively decreased, then increased again due to crack arrest and finally decreased | 888 841 cycles |

**Table 5-5: Stress ranges applied for the fatigue crack growth rate testing in environment**
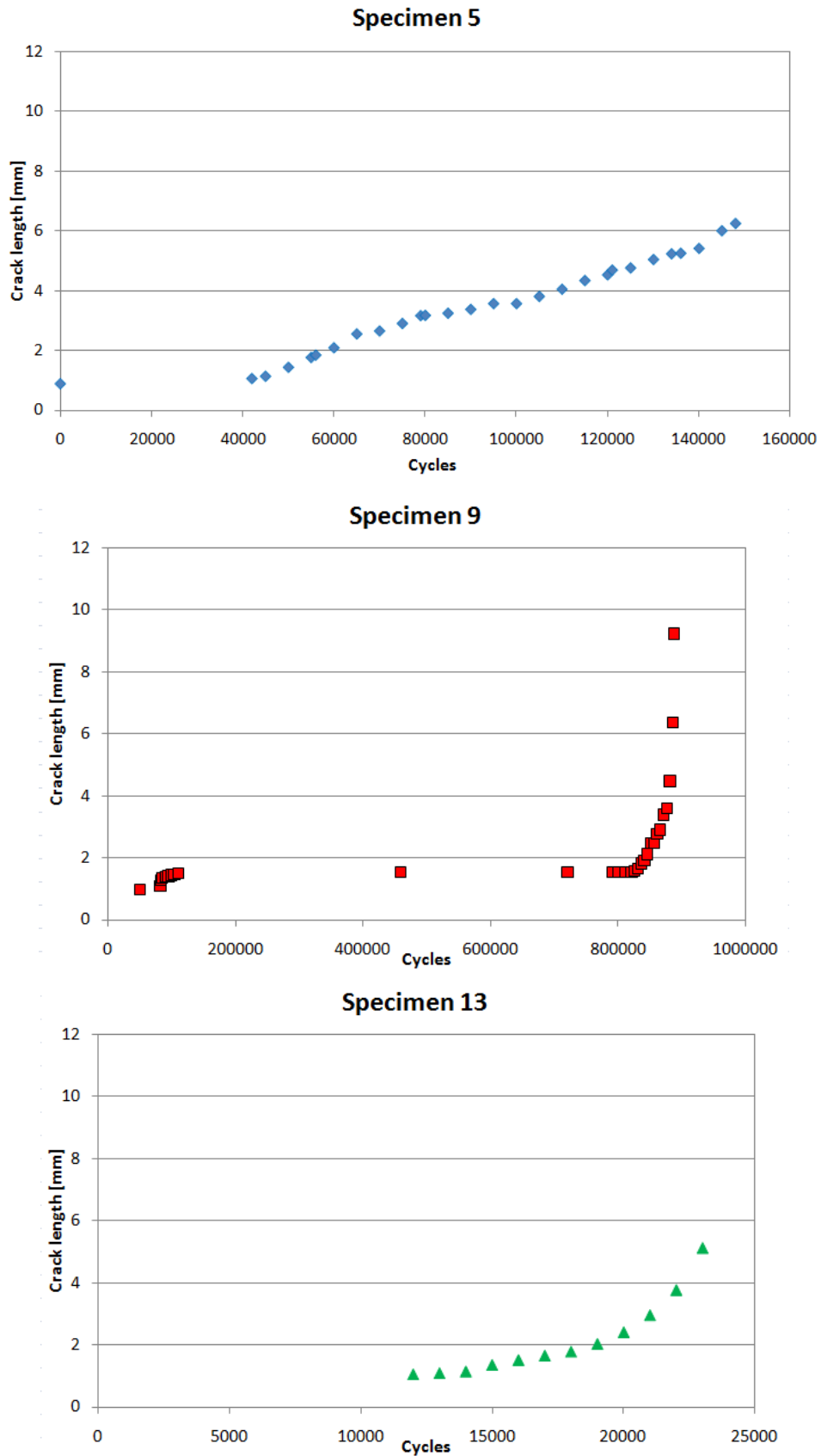
**Figure 5-24: Fatigue crack length as a function of the number of cycle in a 3.5% NaCl solution, R=0.1, f=3Hz**
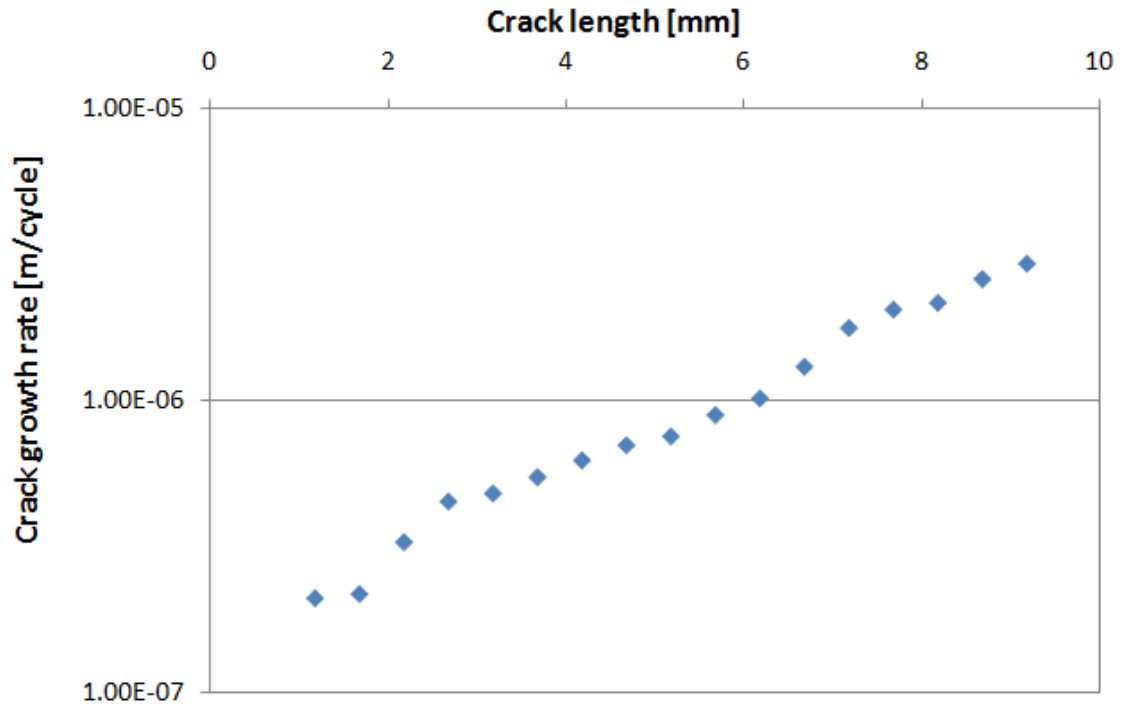
**Figure 5-25: Specimen 18 – Crack growth rate as a function of the crack length in 3.5% NaCl solution, R=0.1, f=3Hz**

The data for the four specimens were processed to produce the crack growth rate as a function of the stress intensity range at the crack tip, $\Delta K$, as displayed in Figure 5-26. The testing conditions for specimen 18 and specimen 13 led to high crack growth rates and high stress intensity ranges, whereas the testing conditions for specimen 5 and specimen 9 produced lower crack growth rates and stress intensity ranges. The stress intensity threshold was not reached for 15-5PH in 3.5% NaCl. The data for specimen 9 showed a lot of scatter due to the crack arrests observed during the test. The data for medium stress intensity ranges (10-30 MPa.$\sqrt{m}$) for the four specimens were in good agreement. However, the data for specimen 18 at higher stress intensity ranges ( $\geq 50$ MPa.$\sqrt{m}$) seemed to diverge from the data obtained from specimen 13 and specimen 9.
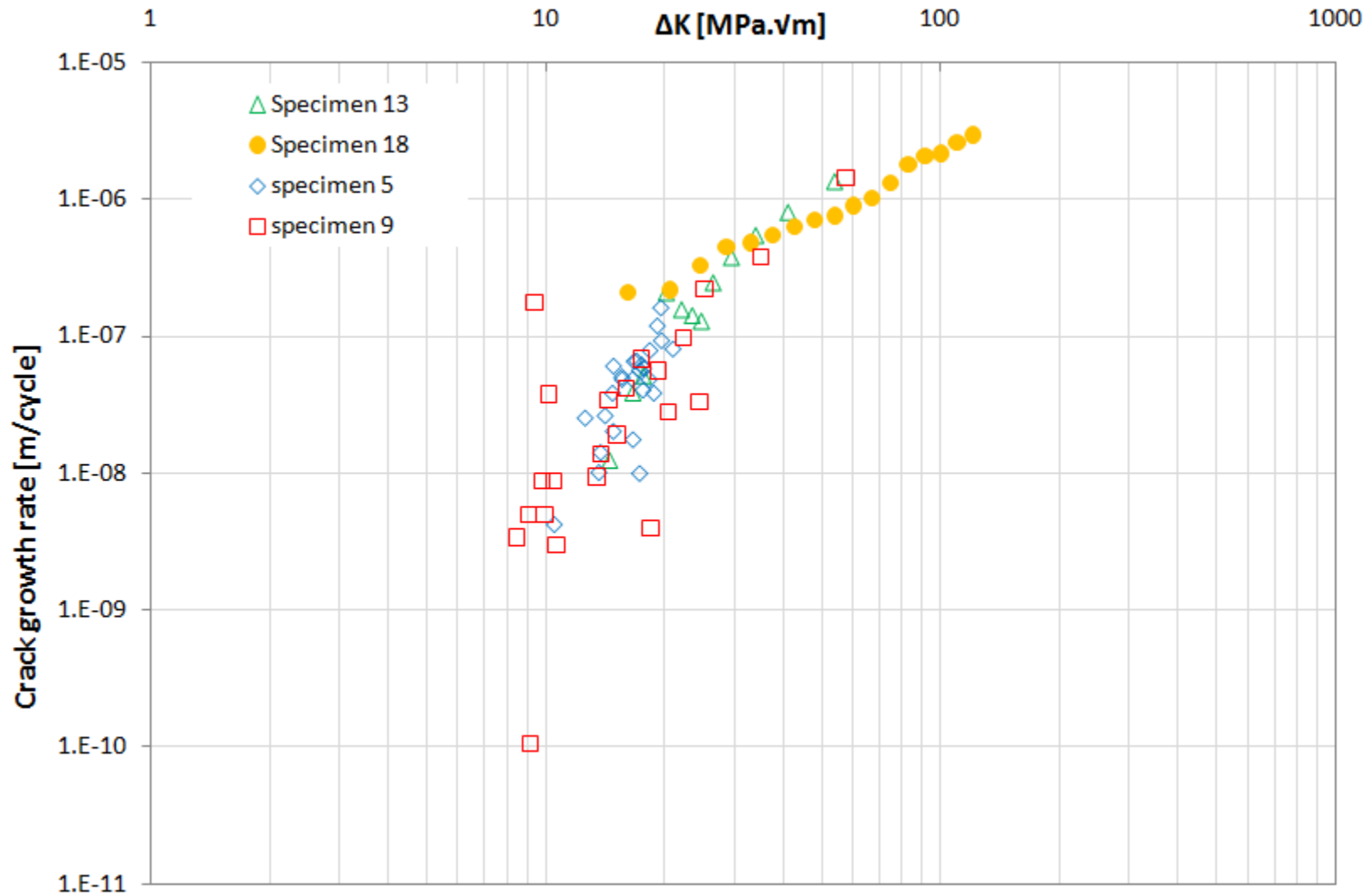
**Figure 5-26: Fatigue crack growth rate in 3.5% NaCl solution, R=0.1, f=3 Hz**

## 5.4  Fatigue testing of pre-corroded specimens

Seven 15-5PH fatigue specimens had been corroded in the salt spray cabinet before being tested in fatigue, as described in section 3.4.4. Prior to carry out the fatigue testing, the corrosion flaws were assessed by image analysis.

### 5.4.1  Corrosion flaw assessment

Specimen 10 had been prepared in order to have pitting corrosion in the gauge length of the specimen, whereas the seven other specimens (specimens 2, 6, 17, 20, 21, 24) were fitted with single crevice formers to produce crevice corrosion in the centre of the gauge length of the specimen.

- ***Specimen 10***

After being exposed for 3 weeks in the salt spray cabinet, specimen 10 displayed corrosion product on the gauge length, underneath which corrosion pits were detected. From the pit size distributions, shown in Figure 5-27, it has been noticed that most of the pits had a size which did not exceed 2μm (69% for the length distribution and 88% for the width distribution). In addition, although the specimen was prepared to initiate pitting corrosion, several areas of damage due to crevice corrosion were present on the specimen. They originated at sites where solution had penetrated beneath the protective lacquer. Replica of the largest damage was taken before testing to examine the flaw, as shown in Figure 5-28 . The damage occupied an area of approximately 5mm by 5mm and was globally shallow. Indeed, the grinding marks were still visible in the corroded area, which meant was the metal was only superficially attacked. However, a deeper area was noticed on the damage, as illustrated in Figure 5-28. This damage was expected to initiate a fatigue crack which would ultimately cause the failure of the specimen, and was monitored by replica during the fatigue test.

# 5. RESULTS AND DISCUSSION
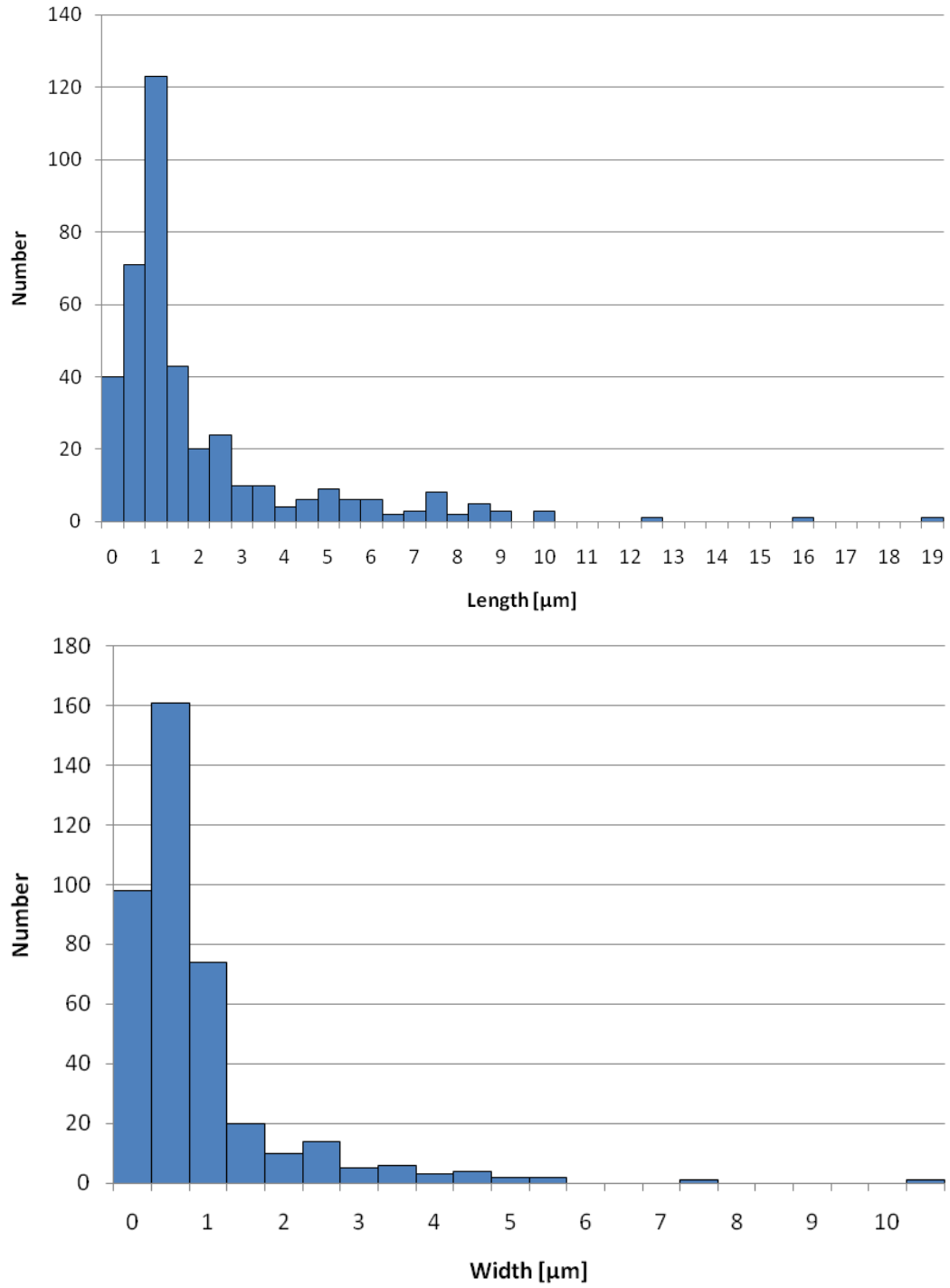


**Figure 5-27: Pit size distribution in specimen 10**

**Figure 5-28: Replica of the crevice corrosion damage in specimen 10**

- ***Specimens 2, 6, 17, 20, 21 and 24***

With the exception of specimen 17, which exhibited several small pits on several areas of the specimen and three distinct large areas of crevice corrosion on the gauge length of the specimen, each of the other specimens displayed only one circular flaw after being removed from the salt spray cabinet. Small corrosion flaws also developed independently on the samples at site remote from the crevice former.

The circular damage on specimen 6 was measured has having a diameter of 3mm, as shown in Figure 5-29, which was exactly the shape of the crevice former. In addition, different areas were observed in the corrosion damage zone: a dark area in the centre, surrounded by a zone of "clean" metal, surrounded by corrosion product. The dark area corresponded to an acidic zone under the crevice former, which resulted from the process of crevice corrosion, and therefore a zone of active crevice corrosion had developed. Around that zone, the conditions were less acidic and no active crevice corrosion initiated. However, the low pH did not favour the precipitation of corrosion product and the metal stayed in its initial condition. Finally, in the third zone, the conditions were slightly alkaline from the cathodic reaction, which are the necessary conditions for the precipitations of corrosion product.
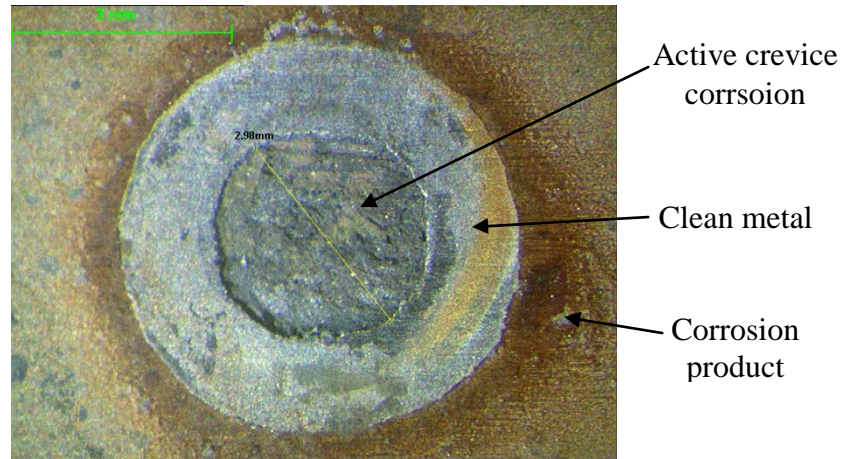
**Figure 5-29: Crevice corrosion damage in specimen 6**

The shape of the flaws was assessed using a confocal laser scanning microscope, as explained in section 0. The size of the each flaw was approximately 3mm in diameter (i.e. the diameter of the crevice former) and the bottom surface was not regular with the presence of significantly deeper local area than the rest of the damage, as illustrated in Figure 5-30. The maximum depth of each flaw was measured, as detailed in Table 5-6.
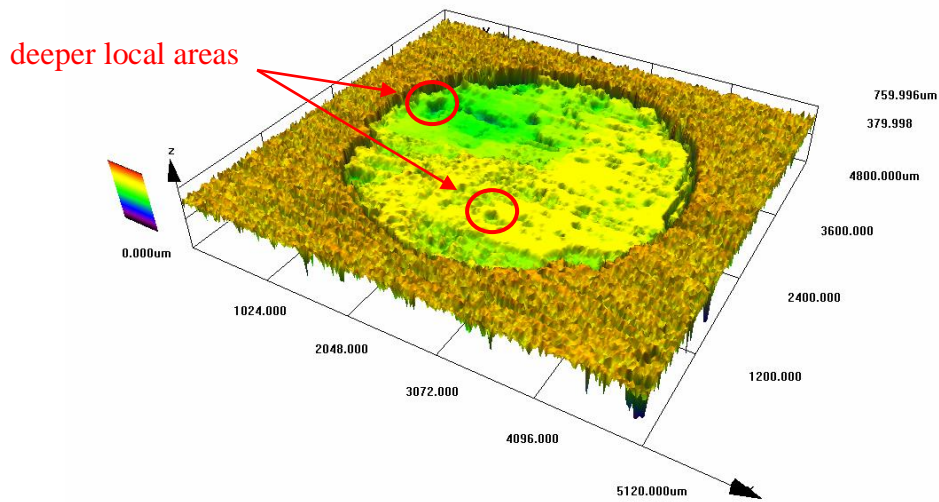


**Figure 5-30: Specimen 2 - 3D image of the crevice corrosion damage**

| specimen | 6 | 2 | 20 | 21 | 24 |
|---|---|---|---|---|---|
| **Maximum depth [μm]** | 250 | 338 | 291 | 631 | 1023 |

**Table 5-6: Maximum measured depth of crevice corrosion flaw on fatigue specimens**

103

## 5.4.2 Fatigue testing

Specimens 2, 6, 20, 21 and 21 were monitored by a digital camera, which was focused on the large circular corrosion flaw, whereas replica technique was used for specimen 10 and 17. The large area of corrosion induced by crevice corrosion on the side of specimen 10 was expected to initiate a fatigue crack which could ultimately cause the failure specimen, compared to the small pits present in the gauge length. Therefore, it was the damage side of specimen 10 which was monitored by replica.

Every specimen was tested in fatigue in a 3.5% NaCl solution, as explained in section 3.4.4.3. The testing parameters, as well as the number of cycles at which the specimen failed, are given in Table 5-7.

| Specimen | $\sigma_{max}$ [MPa] | R | f [Hz] | $N_{failure}$ [cycles] |
|----------|---------------------|-----|--------|------------------------|
| 10 | 1110 | 0.1 | 1 | 6 526 |
| 17 | 970 | 0.1 | 3 | 8 196 |
| 6 | 350 | 0.1 | 3 | 167 806 |
| 2 | 350 | 0.1 | 3 | 158 485 |
| 20 | 350 | 0.1 | 3 | 211 393 |
| 21 | 350 | 0.1 | 3 | 208 679 |
| 24 | 350 | 0.1 | 3 | 91 572 |

**Table 5-7: Fatigue testing parameters and fatigue life**

Failure crack initiated from the large crevice corrosion as expected for specimens 6, 2, 21 and 24, therefore the complete crack development was monitored. Likewise, the failure of specimen 10 was due to a fatigue crack having initiated at the large area of corrosion on the side of the specimen, as illustrated in Figure 5-31, and replica of the crack could be taken. However, specimen 20 failed from a crack, which initiated from a smaller corrosion flaw near the edge of the specimen and was not in the monitored area. Regarding specimen 17, although fatigue cracks initiated from the three large areas of crevice corrosion in the gauge length (marked A, B and C in, the crack which caused the failure of the specimen initiated from a small but deep flaw (marked D) located near the edge of the specimen. Yet, the first replica of the monitored zone taken after 5000

cycles being larger than the monitored zone, it was possible to observe cracks having initiated from that flaw D.

Excluding specimens 10 and 17, which were tested at higher stresses, fatigue lives of the five other pre-corroded fatigue specimens tested at 350MPa varied from $9.1 \times 10^4$ to $2.1 \times 10^5$ cycles, as detailed in Table 5-7, which is approximately a factor of 3 between the shortest and longest fatigue lives.
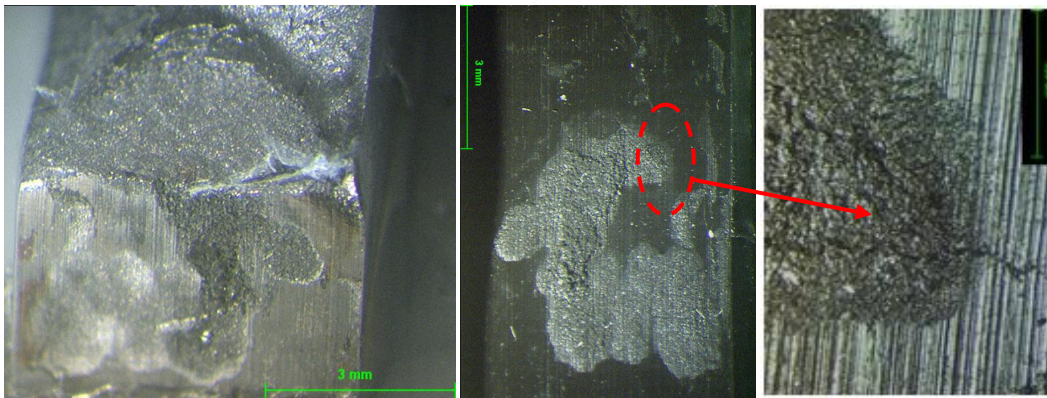


**Figure 5-31: Specimen 10 – Fracture surface and replica of the fatigue crack initiating from the large crevice corrosion flaw after 6000 cycles**
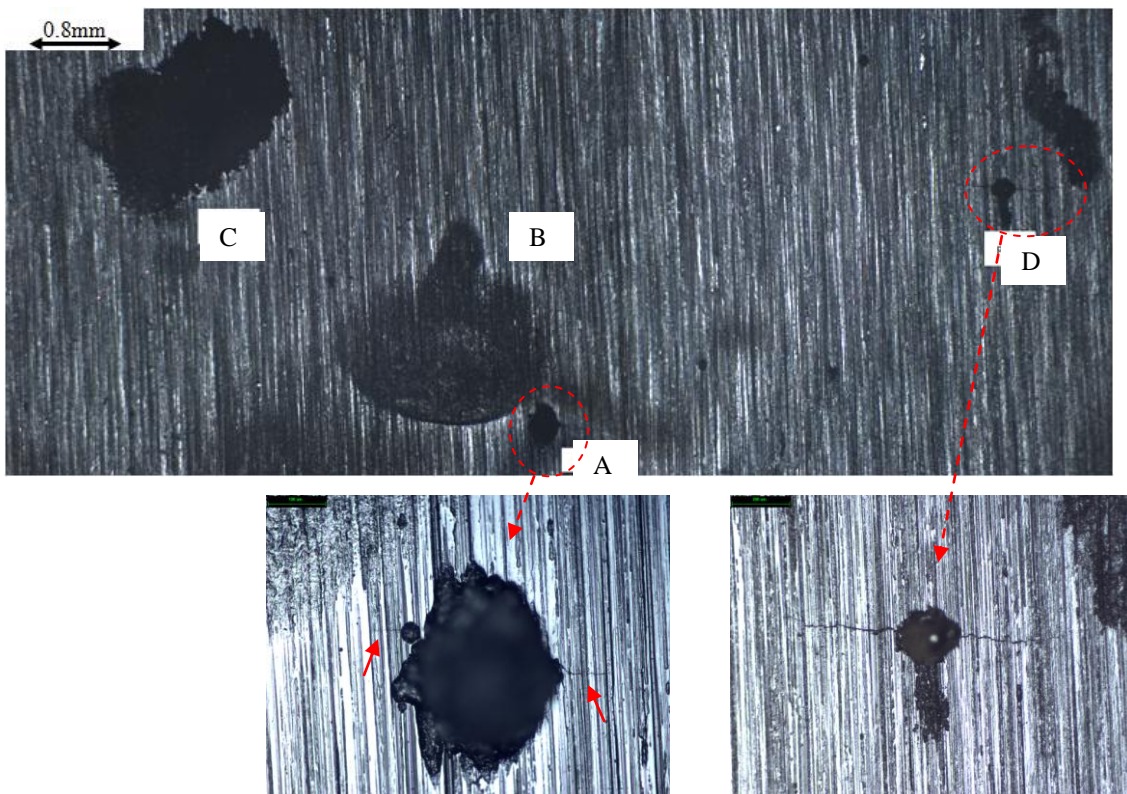


**Figure 5-32: Specimen 17 – Replica taken after 5000 cycles, cracks initiating from flaws A and D**

An estimation of the fatigue crack initiation was enable from the different monitoring technique, as detailed in Table 5-8, with more or less precision depending on the technique used, the frequency of the monitoring, as well as other parameters such as the lighting, the surface finish of the specimen (i.e. presence of scratches) which could hinder small crack detection.

| Specimen | $\sigma_{max}$ [MPa] | estimated $N_{initiation}$ [cycles] | $N_{failure}$ [cycles] |
|----------|----------------------|-------------------------------------|------------------------|
| 10 | 1110 | between 5 000 and 6 000 | 6 526 |
| 17 | 970 | < 5 000 | 8 196 |
| 6 | 350 | < 5 000 | 167 806 |
| 2 | 350 | between 115 000 and 116 000 | 158 485 |
| 20 | 350 | n/a | 211 393 |
| 21 | 350 | < 140 000 | 208 679 |
| 24 | 350 | < 30 000 | 91 572 |

**Table 5-8: Estimation of the fatigue crack initiation from the monitoring of the cracks**

## 5.4.3  Stress concentration factor

From the facture surfaces of each specimen, it was possible to accurately measure using a SFEG scanning electron microscope, the width and depth of flaws in which the fatigue crack had initiated, as illustrated in Figure 5-33. As previously said, the bottom surface of the flaw was very irregular, therefore only the maximum depth was recorded. In addition, it was noticed that the crack development within the flaw was never across the largest diameter, but was a chord of the roughly circular defect displaced from the diameter, as show in Figure 5-34, therefore the width of the flaw was less than the 3mm width of the crevice former.
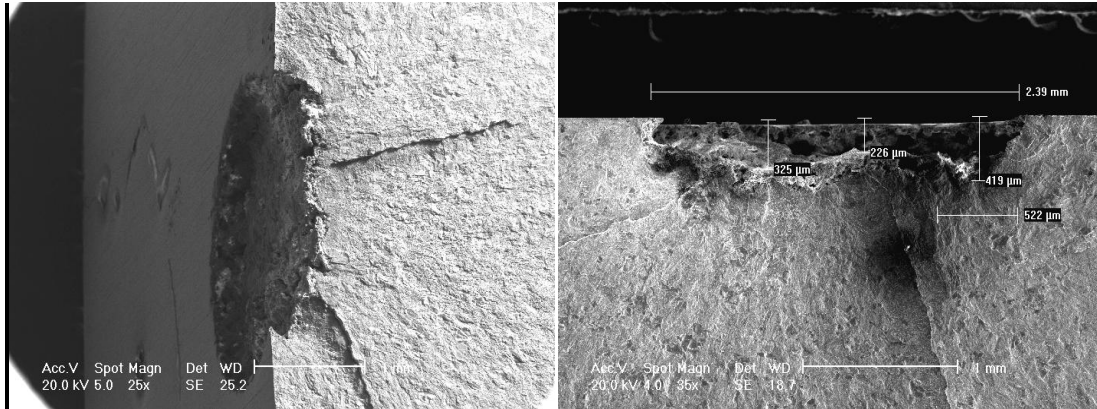
**Figure 5-33: Specimen 21 – Different views of the fracture surface of the flaw where the fatigue crack initiated**
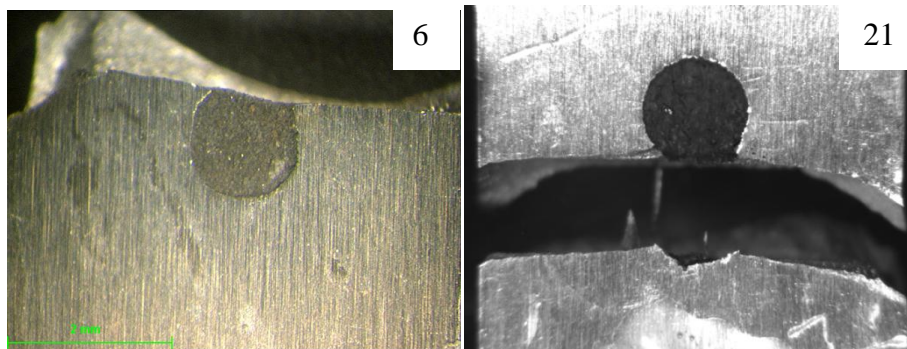


**Figure 5-34: Specimens 6 and 21 - Fatigue crack development displaced from the largest diameter of the flaw**

Knowing the macroscopic dimensions of the flaws, it was then possible to assess the stress concentration factor Kt of each flaw using the finite element analysis method described in section 4.1.1. The dimensions, as well as the associated Kt of each flaw, are detailed in Table 5-9.

| Specimen | Width 2a [mm] | Depth b [mm] | Kt$_{FEA}$ |
|----------|---------------|--------------|------------|
| 10 | 0.146 | 0.097 | 1.16 |
| 17 | 0.200 | 0.174 | 2.29 |
| 6 | 2.000 | 0.320 | 1.55 |
| 2 | 2.880 | 0.276 | 1.30 |
| 20 | 0.330 | 0.110 | 1.78 |
| 21 | 2.400 | 0.470 | 1.50 |
| 24 | 2.600 | 0.720 | 1.72 |

**Table 5-9: Dimensions of initiating flaws and FE calculated Kt**

# 6 MLX17

A second precipitation hardened stainless steel, MLX17, of which the chemical composition is detailed in Table 6-1, was examined at the end of the project to compare its performances in terms of corrosion susceptibility and corrosion fatigue life with those of 15-5PH established as the benchmark material.

| C | Si | Mn | Cr | Ni | Mo | Al | P | S | Ti |
|------|------|------|------|------|------|------|------|-------|------|
| <0.01 | <0.05 | <0.03 | 11.94 | 10.67 | 2.16 | 1.55 | <0.01 | <0.003 | 0.30 |

**Table 6-1: Chemical composition of MLX17 stainless steel [58]**

## 6.1 Crevice corrosion

### 6.1.1 Testing results

The susceptibility to crevice corrosion of MLX17 stainless steel was assessed following the method explained in section 0. After being exposed for 1393h in the salt spray cabinet, only 15 crevice corrosion sites had become active over the 48 possible. In most cases, different levels of corroded areas were noticed on the active sites with a shallow corroded area in the centre and a deeper corroded area towards the edges, as illustrated in Figure 6-1. In some particular cases, the site was not active in the centre and no corrosion took place there.
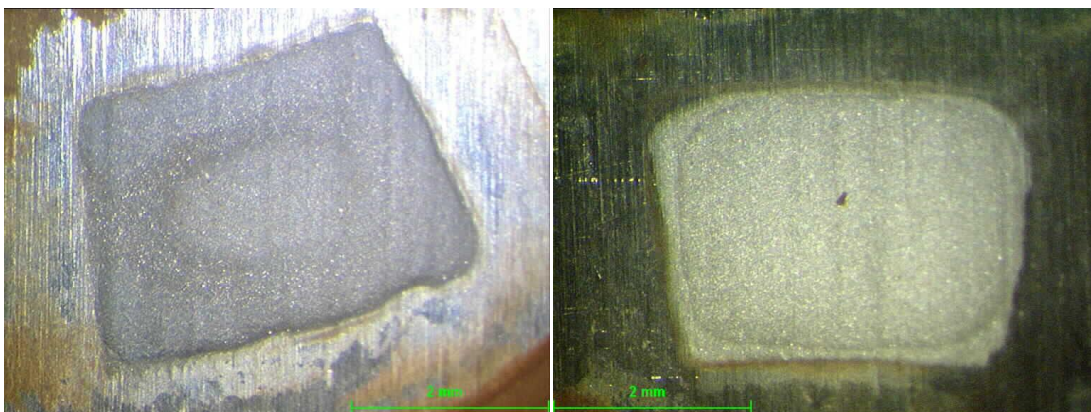


**Figure 6-1: MLX17 active crevice corrosion sites**

The surface area, as well as the maximum and average depth of each crevice corrosion site had been measured at the end of the exposure time (1393h) using the methodology described in section 3.3.4. The distribution of the active crevice corrosion surface area and the maximum along with the average depth distributions are displayed in Figure 6-2 and Figure 6-3. The surface area distribution appeared quite narrow. Indeed, it spread between 6 and 11mm$^2$ and 80% of the active sites were in the 9-11mm$^2$ range. However the depth distributions were more scattered. The average depth distribution lay between 0 and 140µm but 60% of the active sites had an average depth included in the 20-60µm range. The maximum depth distribution spread over 40 and 200µm but 53% of the active sites had a maximum depth between 40 and 80µm. Only two active sites had been found to have a maximum depth being in the 180-200µm.
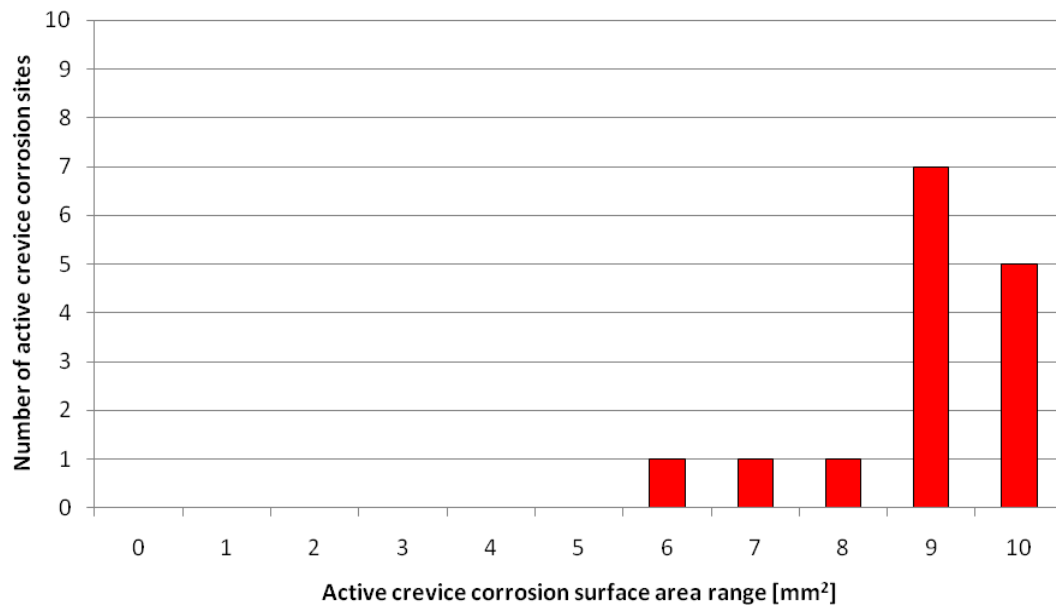


**Figure 6-2: Active crevice corrosion surface area distribution after 1393h**
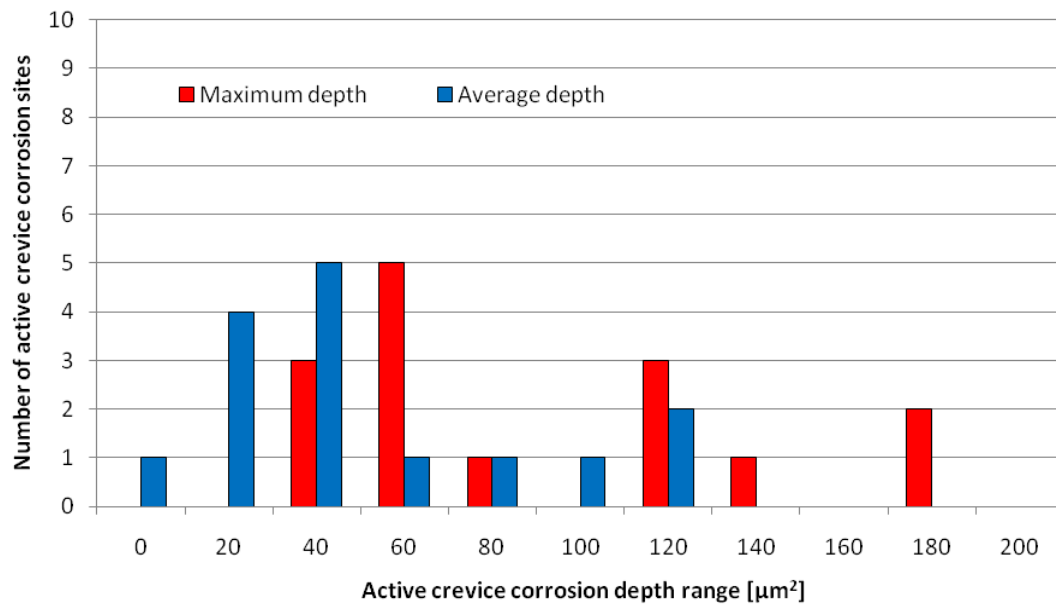
**Figure 6-3: Active crevice corrosion depth distribution after 1393h**

Extreme value statistics was applied to these distributions. The extreme value graphs are shown in Figure 6-4. Each of the three graphs showed a reasonably straight line from which the extreme value had been calculated. The most probable maximum surface area of active crevice corrosion in MLX17 after 1393h was assessed to be 14,8mm$^2$, while the most probable maximum average depth of active crevice corrosion site and the most probable maximum size of the deepest active site were found to be respectively 146.7μm and 199.9μm.

## 6.1.2 Comparison with 15-5PH

MLX17 appeared to be less susceptible to crevice corrosion than 15-5PH. Indeed, MLX17 developed active corrosion in 30% of the possible crevice corrosion sites, whereas in both set of experiments conducted with 15-5PH, more than 40% of the possible site initiated active crevice corrosion, as detailed in Table 6-2. In addition, it was noticed that the crevice corrosion damage in MLX17 were shallow, with a maximum depth range being 180-200μm for only 2 active sites, while 15-5PH deepest active crevice corrosion site was 950μm. It was also observed that in most of the sites which had developed active corrosion in MLX17, the centre of the site was nearly pristine, which was not the case for any of the active site in 15-5PH.

| | MLX 17 | 15-5PH | |
|---|---|---|---|
| | | set 1 | set 2 |
| Number of crevice corrosion sites | 48 | 144 | 180 |
| Number of active crevice site | 15 | 61 | 86 |
| % of active crevice site | 31.25 | 42.36 | 47.78 |

**Table 6-2: Percentage of active crevice corrosion site for MLX17 and 15-5PH**

## 6.2 Fatigue testing of pre-corroded specimen

### 6.2.1 Corrosion flaw assessment

A MLX17 fatigue specimen was pre-corroded following the method described in 3.4.4.2. A circular corrosion flaw was detected under the crevice former after removing the specimen from the salt spray cabinet. A 3D picture of the corrosion flaw was obtained using a confocal laser scanning microscope, as displayed in Figure 6-5, from which the depth of the damage was assessed. The damage had the same diameter than the crevice former and appeared very shallow. Indeed, the average depth was 17.5μm and the centre of the damage was not corroded, as shown in Figure 6-6.

### 6.2.2 Fatigue testing

The MLX17 specimen was tested at a maximum stress of 350MPa, a R ratio of 0.1 and a frequency f of 3Hz in a 3.5% NaCl solution. The crevice corrosion damage was expected to initiate the fatigue crack, which would ultimately cause the failure of the specimen, hence that area was therefore monitored using a digital camera which was taking pictures every thousand cycles

The failure of the specimen occurred after 583 659 cycles. However, the fatigue crack did not initiate from the large corrosion damage but from a smaller flaw, as shown in Figure 6-7. That flaw was located behind the paper scale placed on the specimen, and initiated during the test. Indeed, it was noted that the evaporation of the 3.5% NaCl solution led to salt deposits on the paper scale and also in the thin gap between the paper scale and the specimen. All the conditions for crevice corrosion to happen were met: lack of oxygen and chloride concentrations, hence the initiation of that flaw.
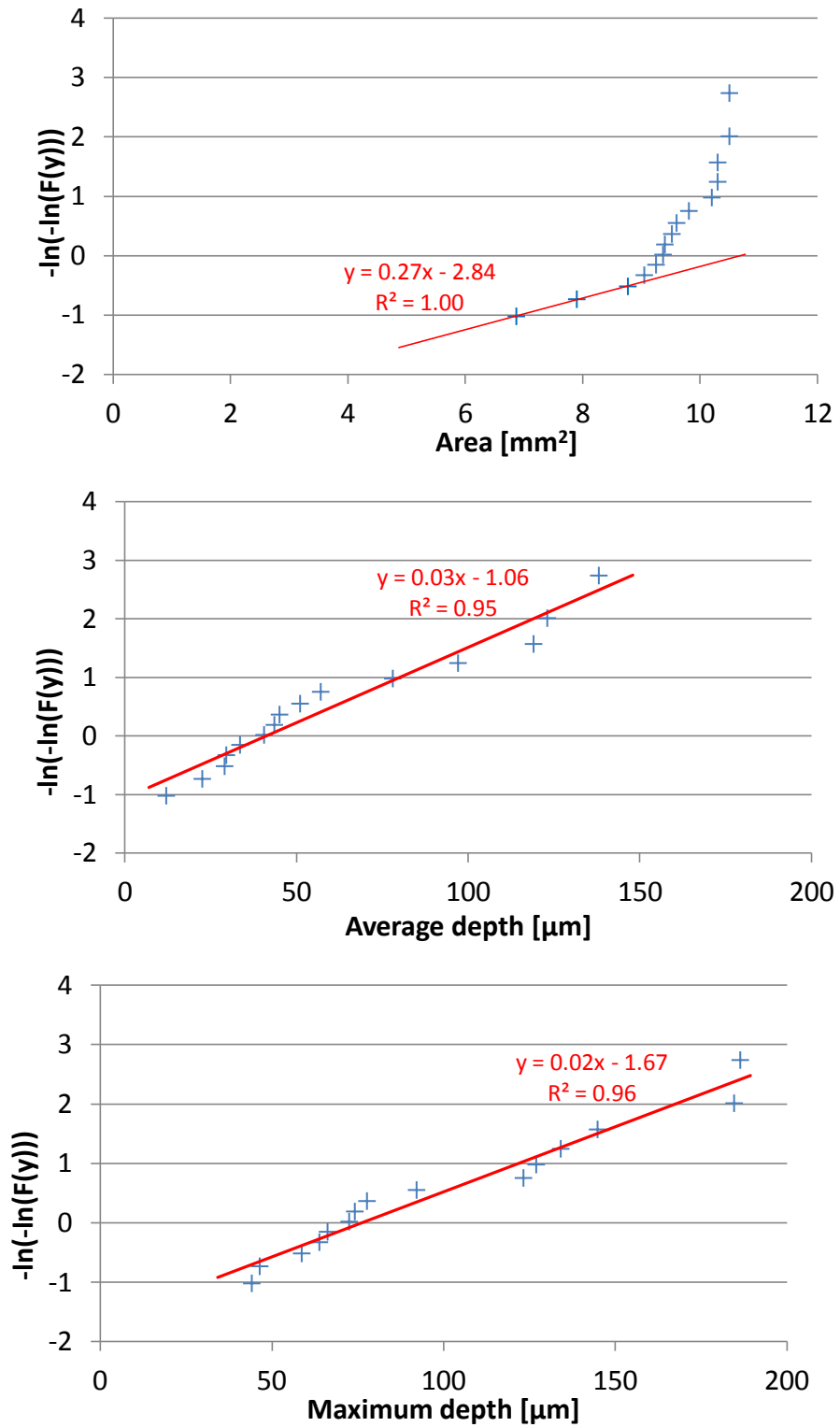
**Figure 6-4: Extreme value graph for MLX17 surface area and depth distributions**
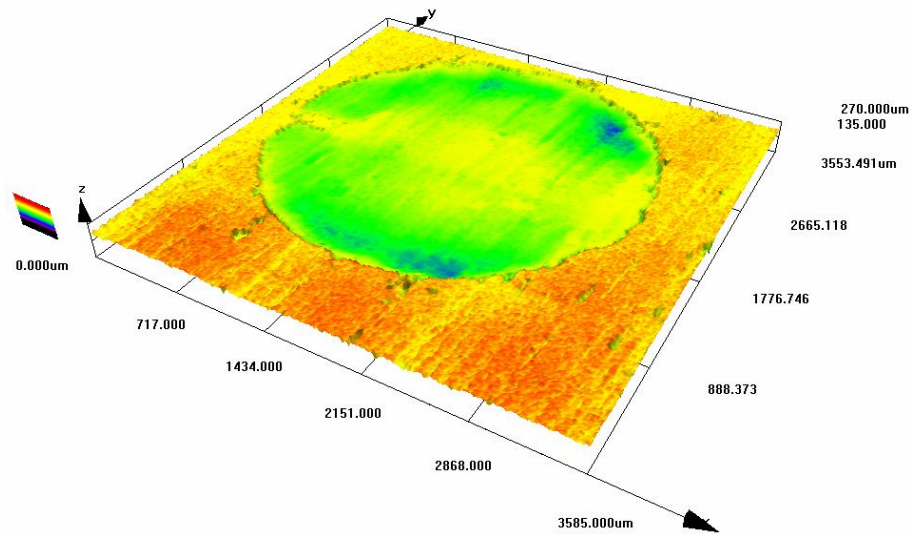
**Figure 6-5: 3D image of the corrosion damage in MLX7 specimen**
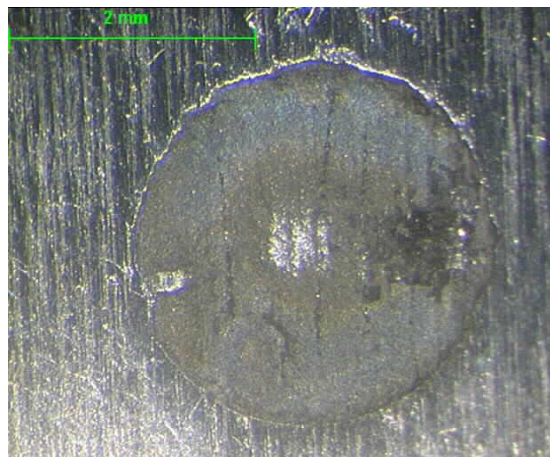


**Figure 6-6: Corrosion damage in MLX17 specimen with an uncorroded area in the centre**
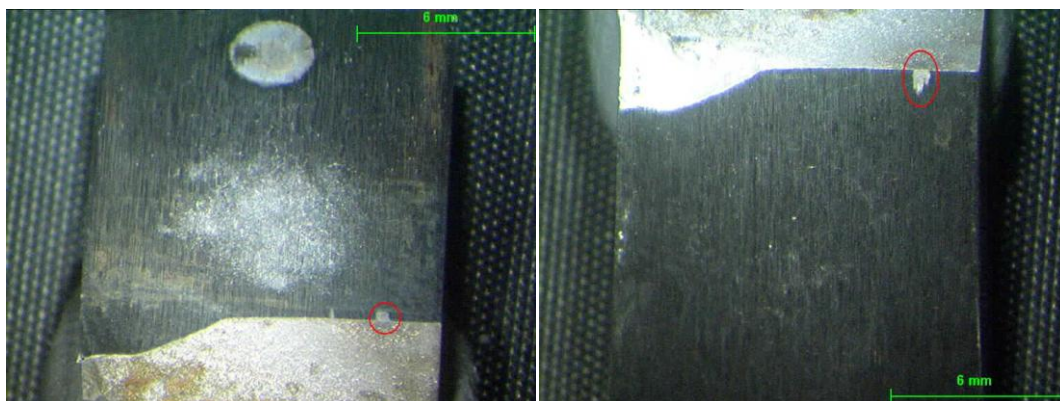


**Figure 6-7: MLX17 specimen - Corrosion flaw which initiated fatigue crack**

113

## 6.2.3 Stress concentration factor

The shape and dimensions of the flaw having caused the failure of the specimen were obtained by observing the fracture surface with a SFEG scanning electron microscope, as illustrated in Figure 6-8. The damage was very shallow (between 5 and 10µm deep), except at one place, where the flaw had a semi-elliptical shape with a width of 100µm and a depth of 34µm. It was decided to only consider the semi-elliptical part of the flaw in the FE model, as it was thought to be the more damaging part. The centre of the semi-ellipse was measured to be at 2mm from the lateral edge of the specimen. Therefore, a semi-ellipse with a major axis of 50µm and a minor axis of 34µm, of which the centre was located at 2mm from the lateral edge of the specimen, was sketched in the FE model to represent the damage. The methodology of the FE analysis is described in section 4.1.A stress concentration factor of 1.83 was assessed for that flaw.
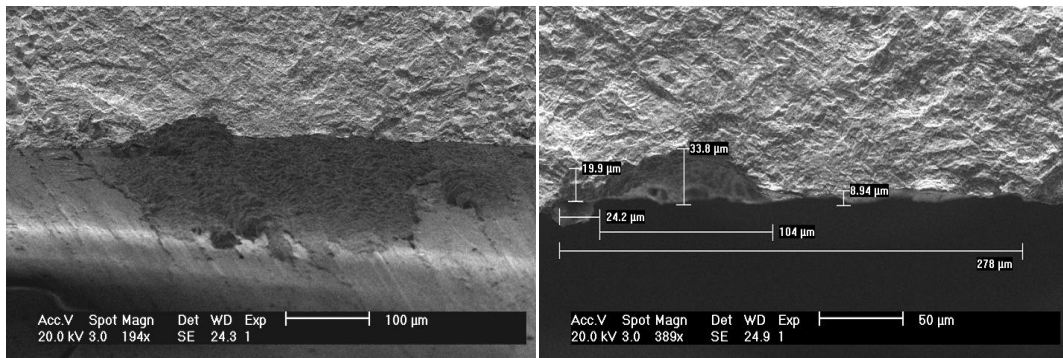


**Figure 6-8: Different views of the fracture surface of the flaw where the fatigue crack initiated**

# 7  LARGER SCALE FATIGUE SPECIMEN

The main aim of this research was to provide a model to establish the critical corrosion flaw size to initiate a fatigue crack and use this as a criterion for selecting the best material. In order to test the validity of the model, fatigue tests on larger scale tension test specimens were performed to more closely resemble the geometry of a landing gear component.  These larger specimens were designed using the software package CATIA V5.

## 7.1  Design

The requirements of the design were:

- A circular gauge length of 25mm in diameter in order to represent an actuator at a scale 1:2.
- A specimen of maximum length 476mm so that two specimens could be manufactured from a 15-5PH bar of 953mm in length and 114mm in diameter.
- A thickness of 64mm at the ends of the specimen to fit in the existing grips of the 1000kN test machine displayed in Figure 7-1.



**Figure 7-1: Grips of the 1000kN test machine**

In addition to these requirements, the change of section between the gauge length (25mm in diameter) and the ends of the specimen (114mm in diameter) had to be smooth so as not to induce stress concentration. Indeed, if the change of section had a

high stress concentration factor, the failure would be likely to take place in this area instead of the gauge length.

The general shape of the specimen is given in Figure 7-2. Two designs were studied, as displayed in Figure 7-3. The first design had a radius of 95 mm for the change of section, whereas the second design had a radius of 110mm. The other parameters were identical in both designs.
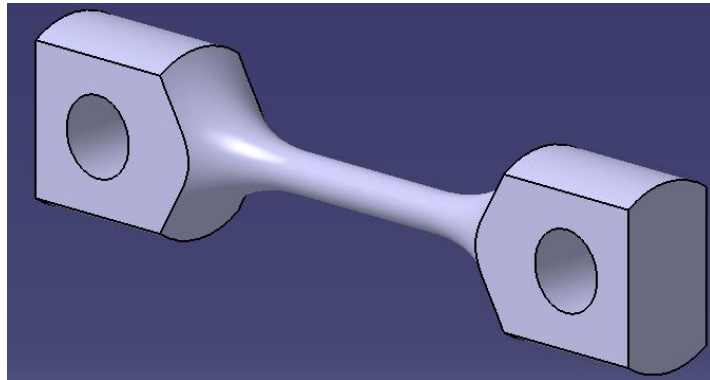


**Figure 7-2: Larger scale tension test specimen sketch**
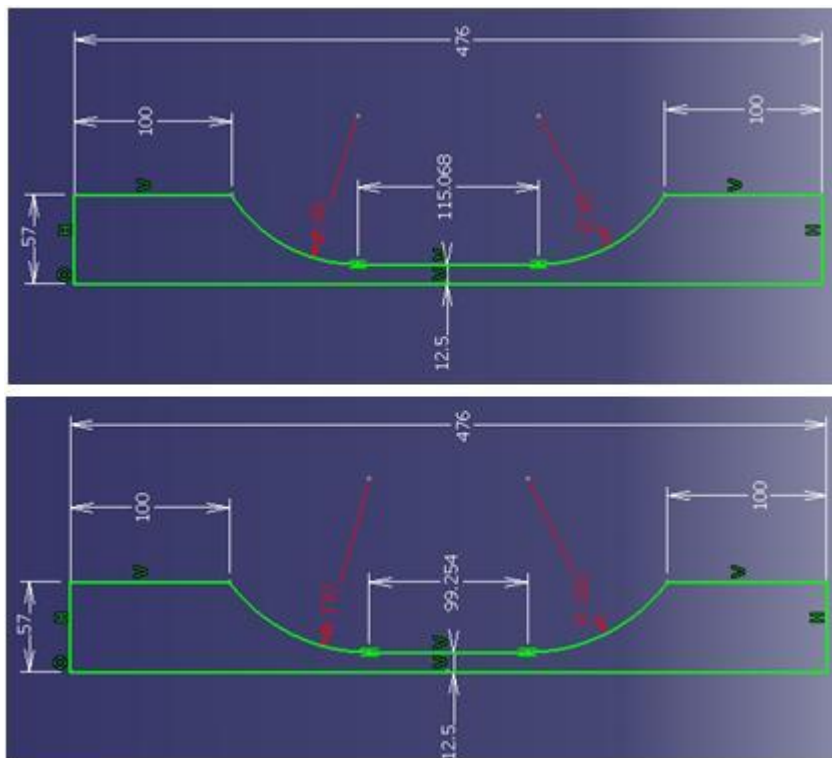


**Figure 7-3: Larger scale tension test specimen profiles**

## 7. LARGER SCALE FATIGUE SPECIMEN

A procedure similar to the methodology described in section 4.1 was followed to assess the stress concentration factor of the change of section. Only one quarter of the specimen was modelled because of the two symmetry axes of the specimen. In addition, the pin from the grips was added in order to have an analysis of the contact between the pin and the specimen, to be sure that the specimen would not fail around the pin hole. The specimen and the pin were meshed, as illustrated in Figure 7-4, with a regular mesh everywhere except at the junction between the end of the change of section and the ends of the specimen where a transition mesh had to be employed. In addition, a finer regular mesh was used where the change of section and the gauge length intercept. Then, the boundary conditions were set according to the symmetry of the specimen and its degree of freedom. Finally, a load, such as the stress in the gauge length of the specimen was 800MPa, was applied.
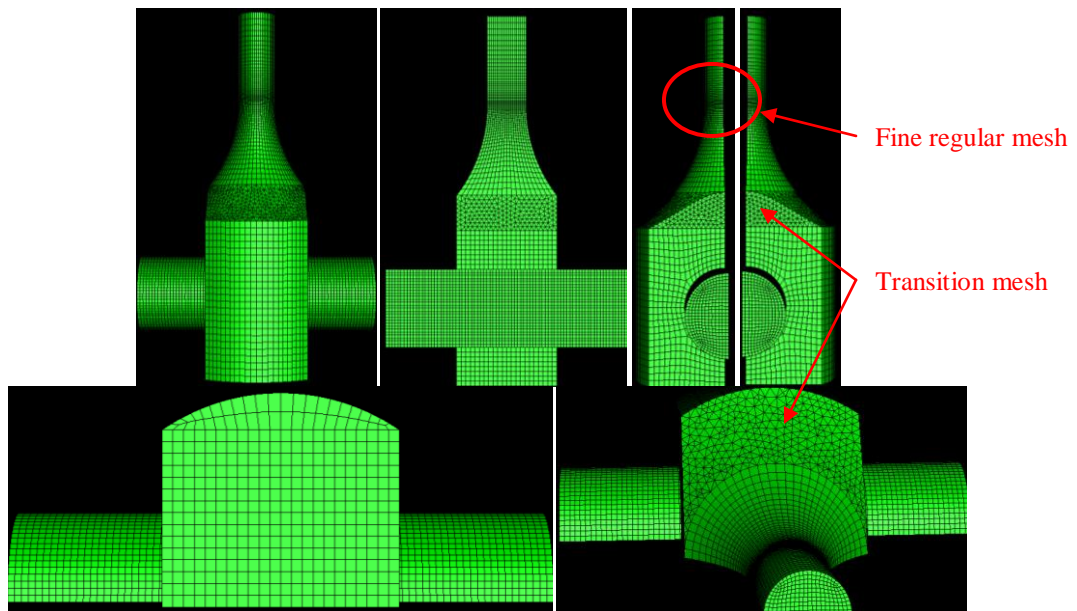


**Figure 7-4: Mesh of the larger scale tension specimen and pin**

The longitudinal stress contours for both designs were very similar and Figure 7-5 illustrated the case of the 95mm radius design. In both cases, the gauge length and the beginning of the change of section were the most stressed parts of the specimen. The longitudinal stress along a line starting from the top of the gauge length to the middle of the change of section was plotted for the two designs, as shown in Figure 7-6, in order to assess and locate the maximum longitudinal stress, and therefore assess and locate

the highest stress concentration factor in the specimen. The change of section with a radius of 95mm was equivalent to a stress concentration factor of 1.05, whereas with a radius of 110mm, it was equivalent to a stress concentration factor of 1.04. Therefore the chosen design was the 110mm radius design as it has a slightly lower stress concentration factor.
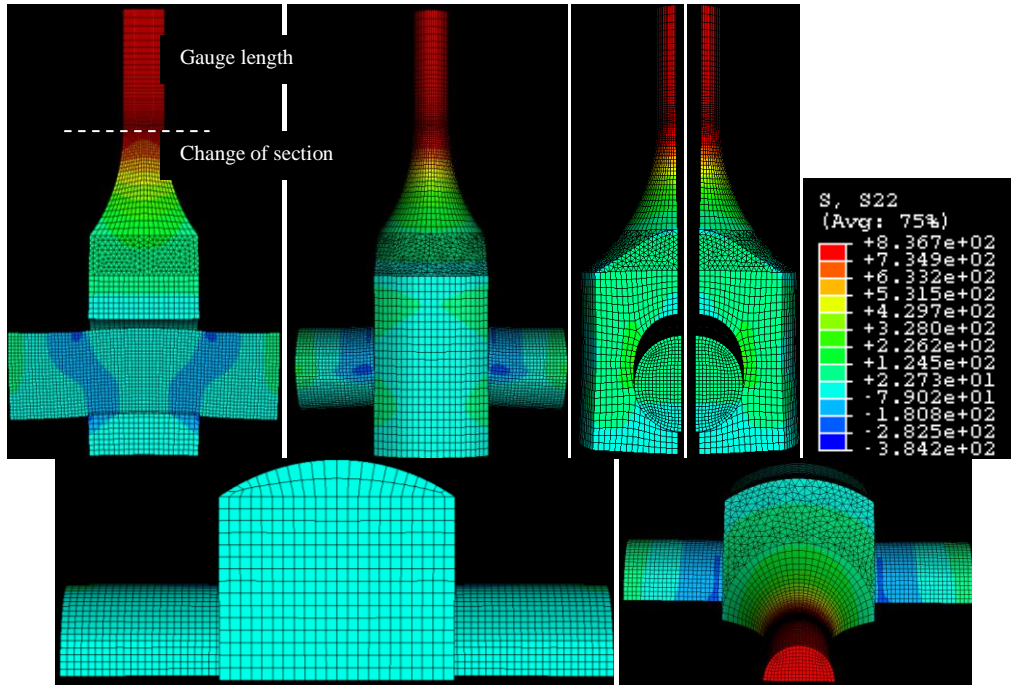


**Figure 7-5: R=95mm - Longitudinal stress contours**

In order to ensure that the specimen would not fail around the pinhole, the stresses at that location were also examined. The longitudinal stress around the pinhole was plotted as a function of the angle, so that the value and location of the maximum longitudinal stress in that area could be identified, as displayed in Figure 7-7. The maximum stress was located at 90 degrees and the stress concentration factor associated with the pinhole was 5.7. Clearly, the stress concentration around the pinhole was high and much higher than the one for the change of section (5.7 against 1.04). However, the longitudinal stress contours showed that the most stressed part of the specimen was the gauge length and the change of section (maximum longitudinal stress was 831MPa) which was much higher than the maximum longitudinal stress reached around the pinhole (350MPa). Therefore, it was expected that the specimen would fail in the gauge length.
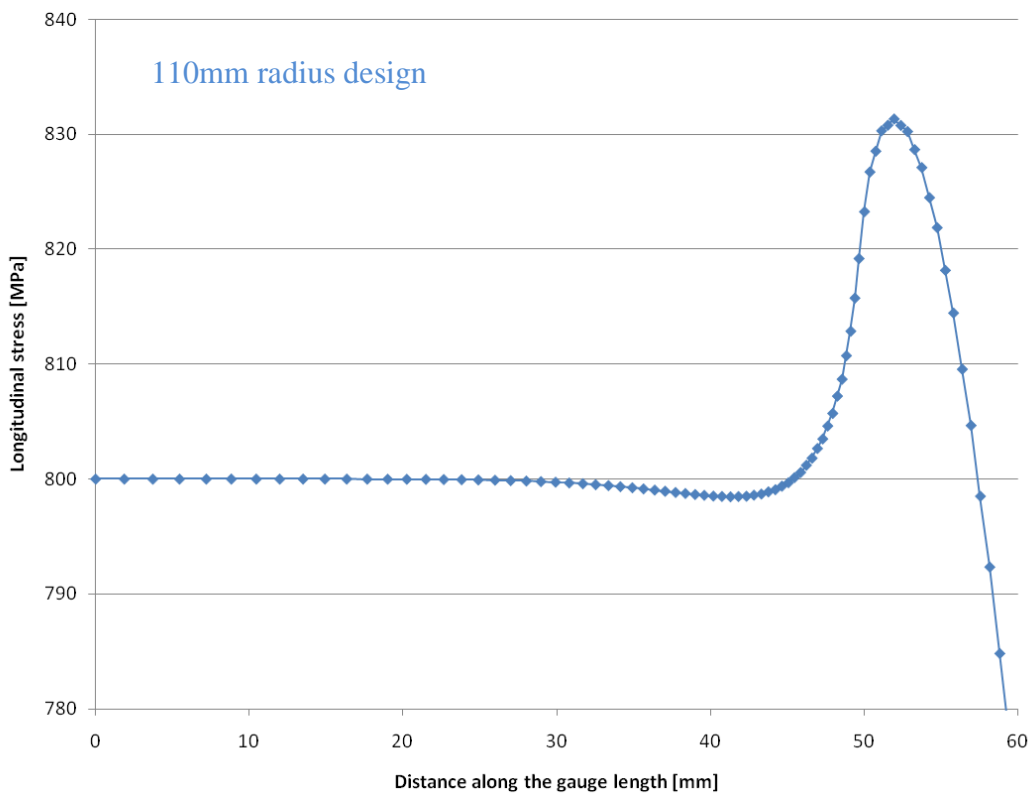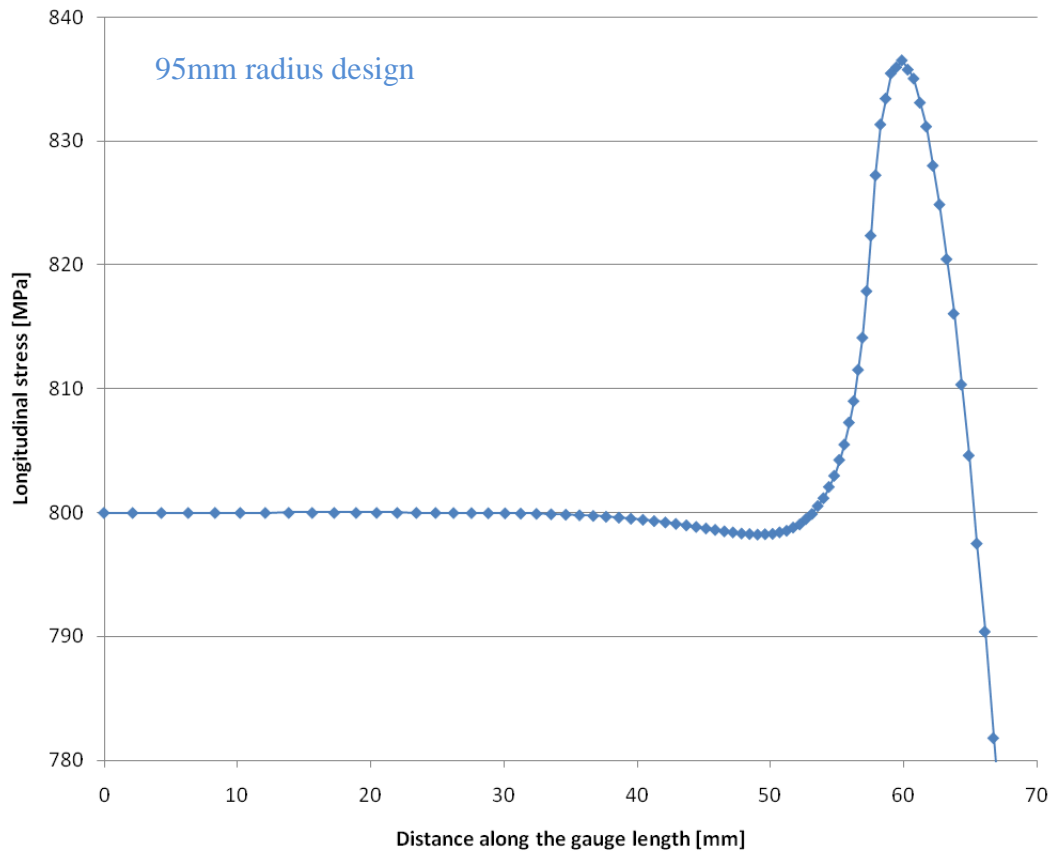
**Figure 7-6: Longitudinal stress along the gauge length and the change of section**
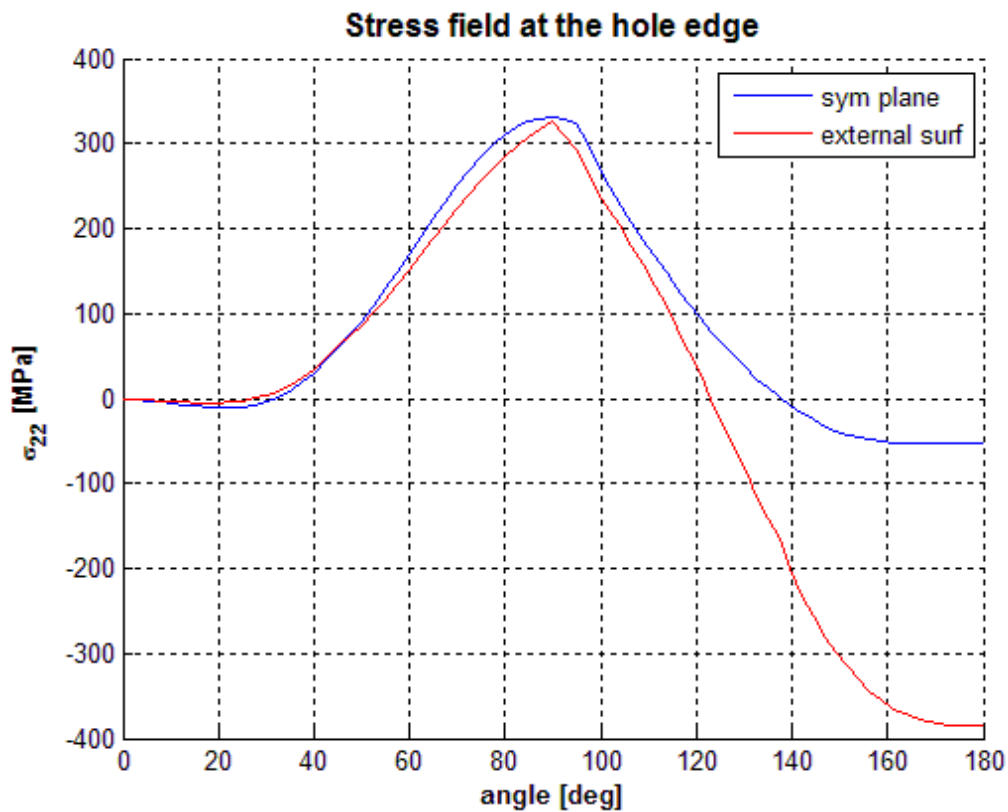
**Figure 7-7: R=110mm - Longitudinal stress around the pinhole**

Two 15-5PH stainless steel larger scale tension test specimens had been manufactured following the 110mm radius design.

## 7.2 Pre-corrosion

### 7.2.1 Crevice former geometry

All the corrosion tests which had been carried out previously were performed with flat specimens and a flat crevice former. If the crevice formers used for the smaller tension test specimens were used for the larger scale specimen, then the conditions would be different. Indeed, the larger scale tension test specimen had a circular section hence the crevice former flat surface would not fit the curve. It was therefore decided to carry out corrosion testing on 15-5PH stainless steel flat rectangular specimens with cylindrical crevice formers made of Perspex in order to assess the influence of the geometry of the crevice former-specimen assembly on the corrosion, and decide of the best design for the crevice former for the circular gauge length of the larger scale tension test specimen.

## 7. LARGER SCALE FATIGUE SPECIMEN

To examine the effect of the crevice former-specimen assembly geometry, four 25mm in diameter Perspex cylinders were set on each face of a flat rectangular 15-5PH stainless steel flat rectangular panel, as illustrated in Figure 7-8, to reproduce the contact of a flat crevice former on the 25mm circular section of the larger scale specimen. The cylinders were held with rubber bands in order to keep them in contact with the specimen and then put in the salt spray cabinet for several weeks. The specimen was placed with a 45 degree angle and was regularly turn around and put in different places inside the cabinet.
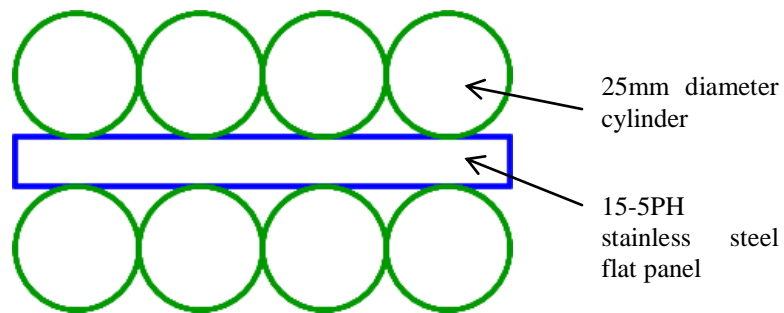


**Figure 7-8: Sketch of a flat rectangular specimen fitted with cylindrical crevice formers**

After several weeks of exposition, the crevice formers were removed and the corrosion damage examined. Different zones were observed on the panel where the crevice former was: a dark area in the centre, surrounded by a zone of "clean" metal, surrounded by corrosion product. The dark area corresponded to an acidic zone under the crevice former, which resulted from the process of crevice corrosion, and therefore a zone of active crevice corrosion had developed. It was noticed that the active crevice corrosion had only developed along the axis of the cylindrical crevice former, that is to say, where the crevice former and the panel were in contact, as illustrated in Figure 7-9. Around that zone, the conditions were less acidic and no active crevice corrosion initiated. However, the low pH did not favour the precipitation of corrosion product and the metal stayed in its initial condition. Finally, in the third zone, the conditions were slightly alkaline from the cathodic reaction, which were the necessary conditions for the precipitation of corrosion product. According to the results of that experience, it was concluded that the most suitable crevice former geometry for the larger scale fatigue specimen would be a crevice former which would fit the curve of the specimen circular

section or a small flat surface, such that the contact between the flat surface and the circular section was maximum.



**Figure 7-9: Crevice corrosion due to cylindrical crevice formers on a flat panel**
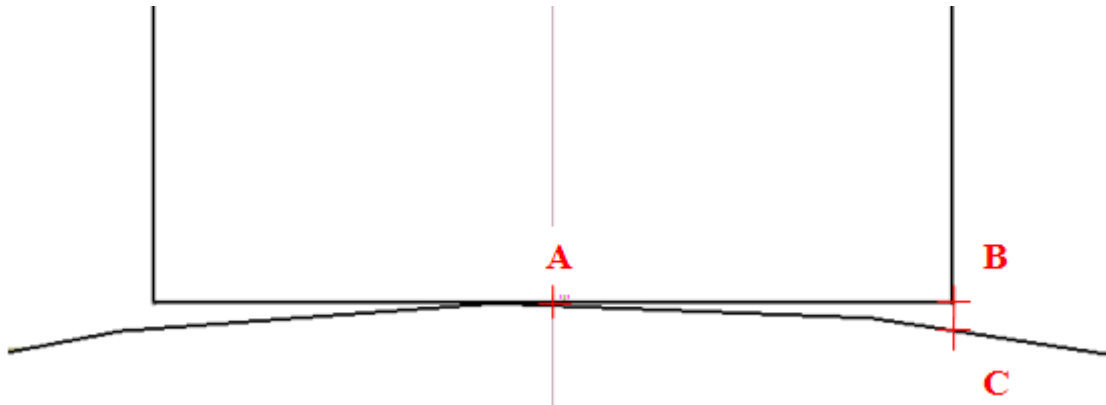


**Figure 7-10: Sketch of the contact between the flat crevice former and the circular section of the larger scale fatigue specimen**

The crevice former geometry used for the small fatigue specimen was considered. Indeed, that crevice former produced corrosion damage with reasonable sizes, and its dimensions (3mm in diameter) were small compared to the 25mm diameter of the larger scale fatigue specimen. Therefore, although being flat, the crevice former would reasonably fit the curvature of the fatigue specimen, as illustrated in Figure 7-10.

The distance [BC] between the tip of the crevice former and the specimen was assessed by trigonometry. Indeed, the distances [AO] and [AB], where O was the centre of the specimen circular section, were known since [AO] was the radius of the circular section (25mm) and [AB] was the radius of the crevice former (1.5mm). Hence, the angle α between [AO] and [AB] was also know, since $= \tan^{-1}\frac{[AB]}{[AO]}$ . Knowing α, the

chord between the points A and C was calculated using the equation $[AC] = 2[AO] \sin\left(\frac{\alpha}{2}\right)$. Finally, using the Pythagorean theorem in the $\widehat{ABC}$ triangle, the distance [BC] was estimated.

The gap between the tip of the crevice former and the specimen, distance [BC], was assessed to be 30µm, hence the contact between the crevice former and the specimen would be maximum. Therefore, it was decided to design and manufacture a 3mm in diameter crevice former, similar to the crevice former used with the smaller fatigue specimen, which would be fitting the large scale fatigue specimens. The crevice former, displayed in Figure 7-11, was hold to the specimen by using nylons screws, of which the tip would be placed into the centres made to manufacture the specimen. In addition, wooden wedges were also used to prevent the crevice former from moving. The specimens fitted with the crevice former were then placed in the salt spray cabinet until a crevice corrosion flaw with a reasonable size was formed.
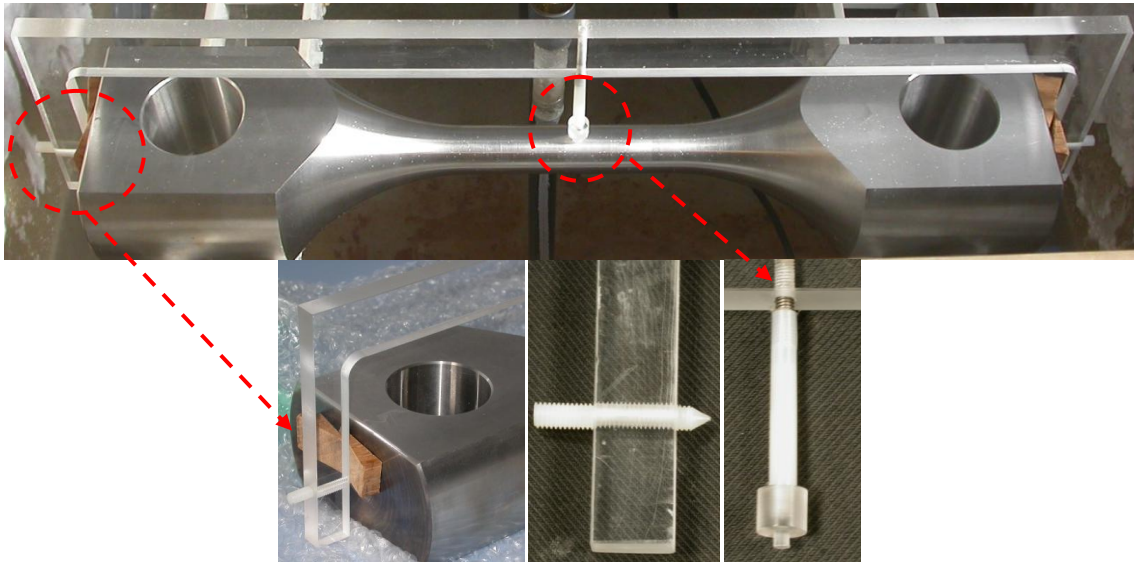


**Figure 7-11: Crevice former for the larger scale fatigue specimen**

## 7.2.2 Corrosion flaw assessment

When the specimens were removed from the salt spray cabinet, corrosion product around and running from the crevice former was noticed, as well as some patches of dry salt, as displayed in Figure 7-12. The surface of the specimens was gently wiped and the product corrosion was removed with a fine grade a silicon carbide paper. Corrosion

damage was noticed on the end of both specimens, where they were resting during the exposure, but they were not expected to initiate any fatigue crack during the fatigue test due to the lower stress in that part of the specimen.

The surface of the gauge length of both specimens was examined and replicas of detected corrosion flaws were taken.



**Figure 7-12: Larger scale fatigue specimen 1 after being removed from the salt spray cabinet**

> ### *Larger scale fatigue specimen 1*

A large corrosion flaw under the crevice former was detected, along with smaller corrosion flaws under the dry salt patches and corrosion product, as shown in Figure 7-13. Replicas of the flaws were taken and examined with an optical microscope to assess their severity, as shown in Figure 7-14. The damage found under the corrosion product and dry salt patches appeared neither very large nor very deep compared to the flaw produced by the crevice former. Therefore, it was expected that the first flaw to initiate a fatigue crack would be the flaw produced by the crevice former.
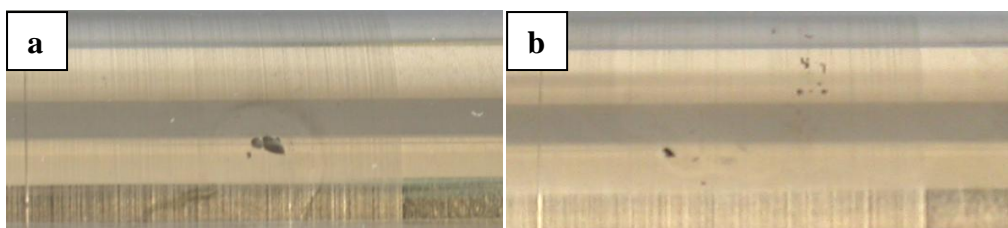


**Figure 7-13: Corrosion flaws under the crevice former (a) and dry salt patches (b)**
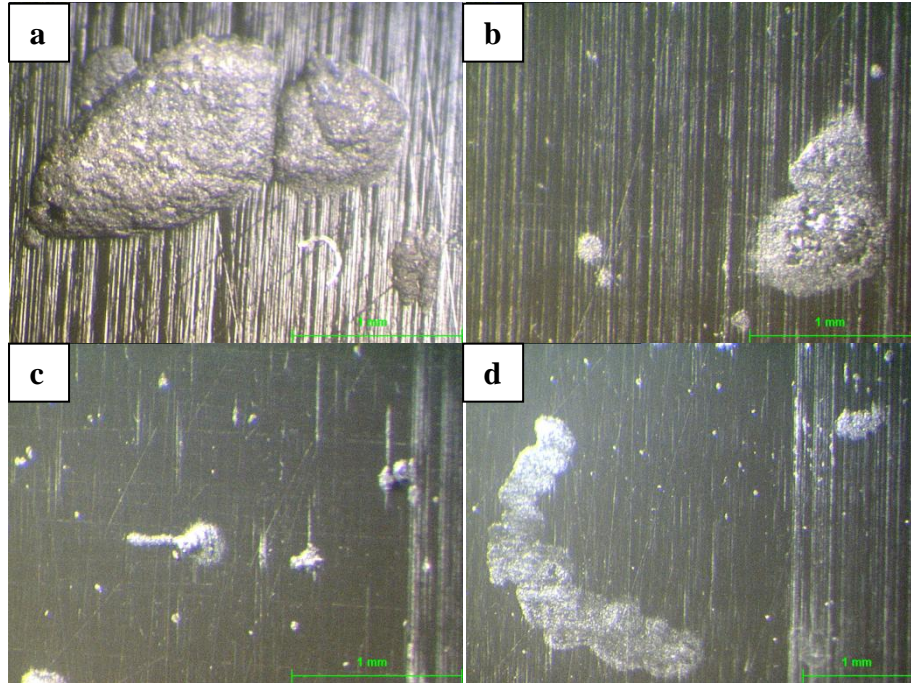
**Figure 7-14: Replicas of the corrosion under the crevice former (a) and dry salt patches (b, c and d) on larger scale fatigue specimen 1**

> ➤ *Large scale fatigue specimen 2*

A large corrosion flaw under the crevice former was detected, along with smaller corrosion flaws under the dry salt patches and corrosion product. Replicas of the flaws were taken and examined with an optical microscope to assess their severity, as shown in Figure 7-15. It was noticed that the corrosion flaw produced by the crevice former had a rectangular shape, which corresponded perfectly to the area where the crevice former and the specimen section were in contact or very close. The damage found under the corrosion product and dry salt patches appeared neither very large nor very deep compared to the flaw produced by the crevice former. The replica of the flaw found under the crevice former was also observed with a confocal laser scanning microscope in order to locate and assess the deepest point of the flaw, as displayed in Figure 7-16. The deepest point was found on the rounded slightly offset part of the damage, and was assessed to 350µm. It was expected that this part of the flaw would be first to initiate a fatigue crack.
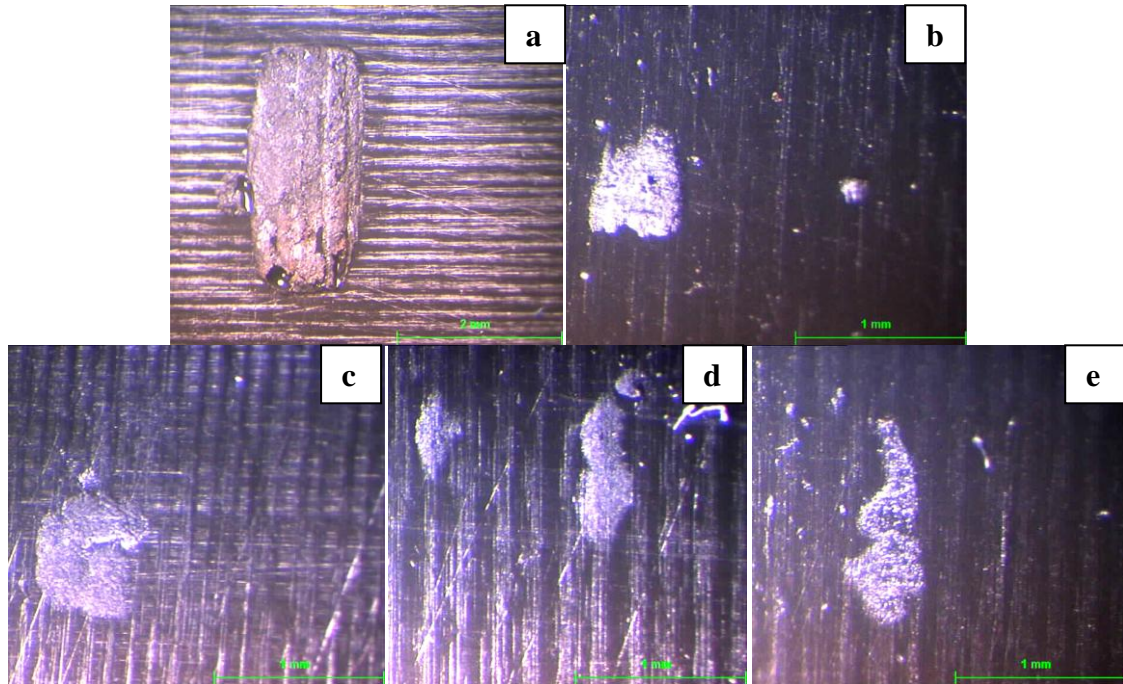
**Figure 7-15: Replicas of the corrosion under the crevice former (a) and dry salt patches (b, c, d, and e) on larger scale fatigue specimen 2**
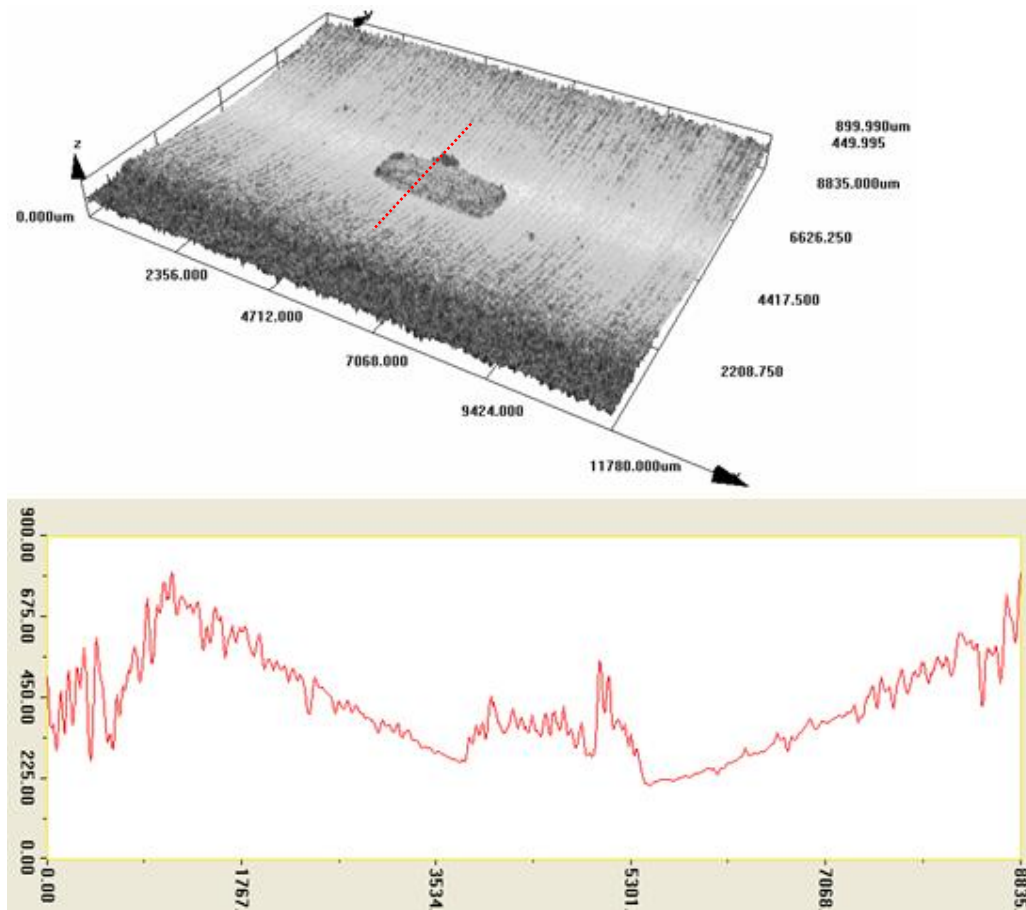


**Figure 7-16: 3D image and section profile of the large corrosion flaw replica**

126

## 7.3 Fatigue testing

In order to keep the corrosion damage active during the fatigue testing, a cell composed of a large fixed Perspex circular base and a large removable supple rubber containing a 3.5% NaCl solution, was fitted on the larger scale tension test specimens. Then the specimen was set up in the lugs of the 1000kN fatigue machine.

The fatigue testing was performed at an applied stress range $\Delta\sigma$ of 315MPa, a R ratio of 0.1 and a frequency of 3Hz. The stress was set accordingly to the corrosion damage present on the specimen by using the results obtained from the fatigue testing of the smaller pre-corroded tension test specimens.

Replicas of the corrosion damage were taken before and at regular intervals during the test to record the initiation and propagation of fatigue cracks.

> ➤ *__Larger scale fatigue specimen 1__*

Replicas of the large corrosion flaw produced by the crevice former were regularly taken, as that flaw was expected to first initiate a fatigue crack. However, after 185000 cycles, a crack initiating from a smaller flaw was detected, while no crack was observed from the large corrosion flaw. The crack was assessed from the replica and was already measuring approximately 1.5mm on each side of the flaw at that stage, as illustrated in Figure 7-17. The flaw from which the crack initiated, was noticed when the specimen was removed from the salt spray cabinet, as displayed in Figure 7-14d, but was thought to be less damaging than the damage produced by the crevice former.
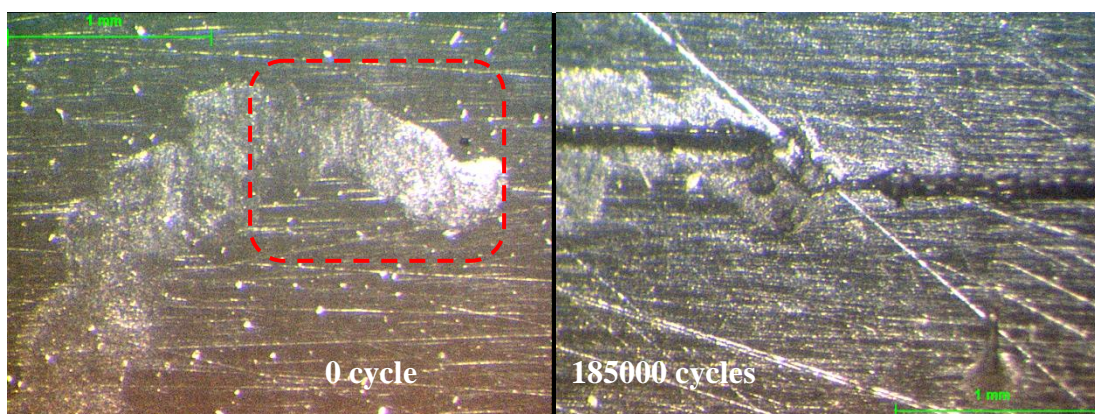


**Figure 7-17: Larger scale fatigue specimen 1 – Fatigue crack initiating from a corrosion flaw at 185000 cycles.**

The fatigue crack quickly propagated, as illustrated in Figure 7-18. Indeed, 28000 cycles were necessary to grow the left hand side of the crack from 1.5mm to 15mm, of

which 6000 cycles to propagate the crack from 6mm to 15mm. The specimen failed after 213597 cycles.

The examination of the fracture surface with an optical microscope showed that the corrosion flaw, which initiated the fatigue crack, had an intricate shape, as displayed in Figure 7-19. The fracture surface was then examined with a SFEG scanning electron microscope to have a more detailed view of the flaw. On the plan on the fracture surface, the flaw appeared to have a fairly regular semi-elliptical shape with a local deeper zone, as shown in Figure 7-20. At the bottom of that flaw, a subsurface flaw could also be distinguished. The fact that the damage had an intricate shape might explain why the depth of the flaw was not assessed properly with the replica, as it is very probable that the replica compound could not have reached the actual maximum depth of the flaw.

During the examination of the specimen with the SFEG scanning electron microscope, a fatigue crack initiating from a flaw produced by the crevice former was also noticed on the surface of the specimen, as illustrated in Figure 7-21.
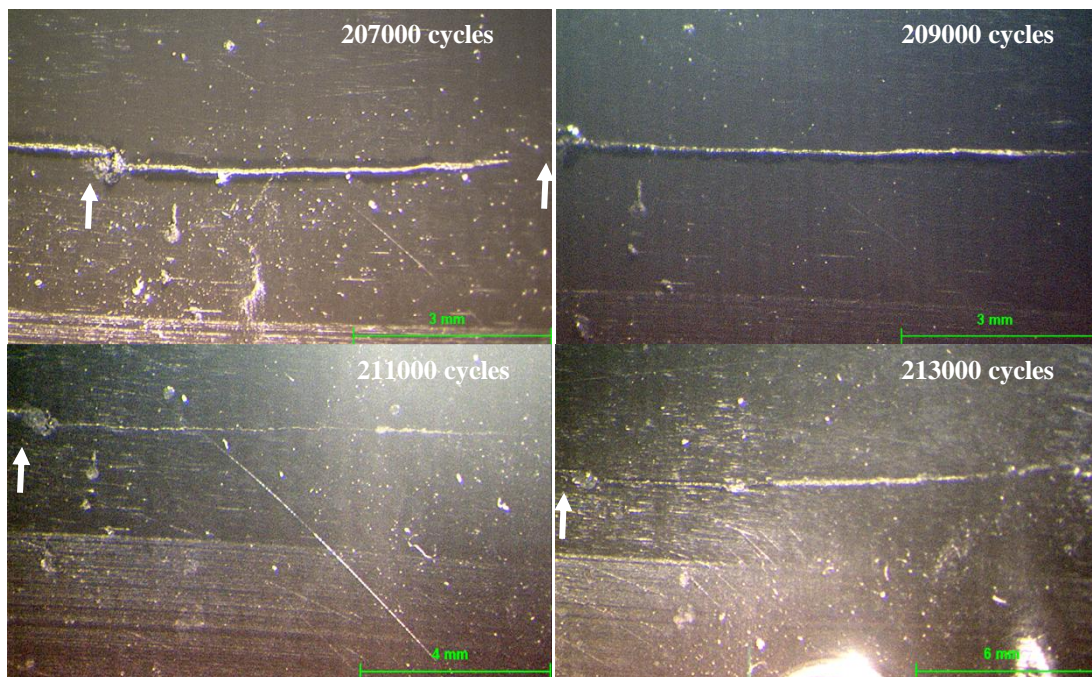


**Figure 7-18: Larger scale fatigue specimen 1 - Fatigue crack propagation**
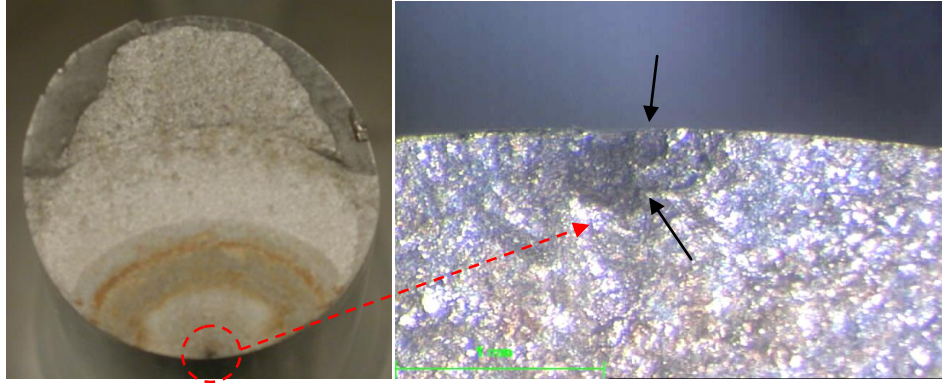
**Figure 7-19: Larger scale fatigue specimen 1 - Fracture surface and flaw having caused the failure**
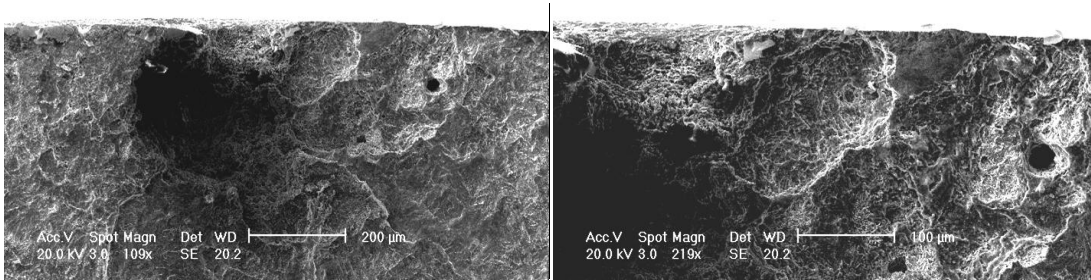


**Figure 7-20: Larger scale fatigue specimen 1 - Flaw having caused the failure**
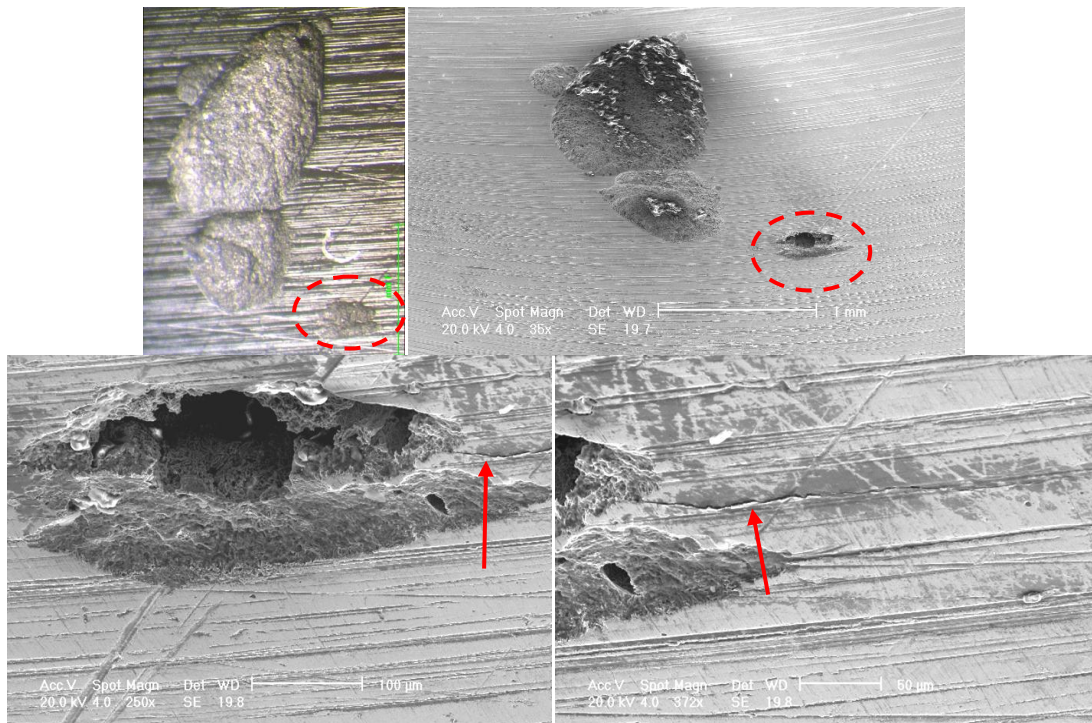


**Figure 7-21: Larger scale fatigue specimen 1 - Replica of the damage produced by the crevice former before testing (a) and fatigue crack initiating from the damage observed after failure (b)**

> ### *Larger scale fatigue specimen 2*

Replicas of the large corrosion flaw produced by the crevice former were regularly taken, as that flaw was expected to first initiate a fatigue crack. A 1.8mm fatigue crack initiating on the right hand side of the damage was noticed after 292700 cycles, as illustrated in Figure 7-22. A smaller crack, which was measuring 100μm, was also observed on the left hand side of the damage. The crack initiated in the deepest zone of the corrosion flaw, which was identified with the confocal laser scanning microscope, as detailed in section 7.2.2.

The crack quickly propagated, as displayed in Figure 7-23, and reached a length of 6.2mm and 7.5mm respectively on the left and right hand side of the damage after 313200 cycles. The specimen failed after 313200 cycles from the crack initiating from the corrosion flaw produced by the crevice former, as shown in Figure 7-24.



**Figure 7-22: Larger scale fatigue specimen 2 - Fatigue crack initiating after 292700 cycles**
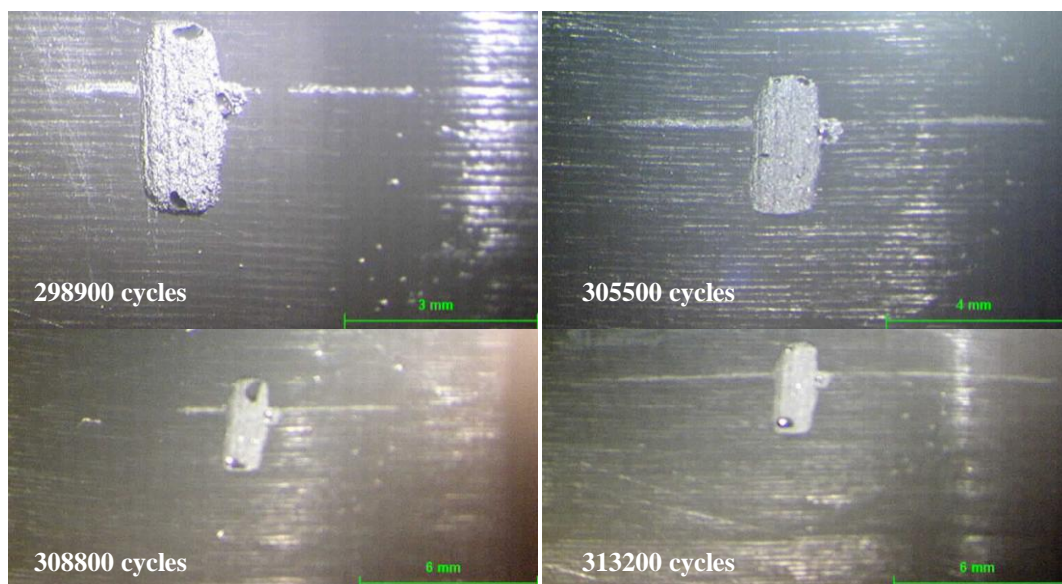


**Figure 7-23: Larger scale fatigue specimen 2 - Fatigue crack propagation**
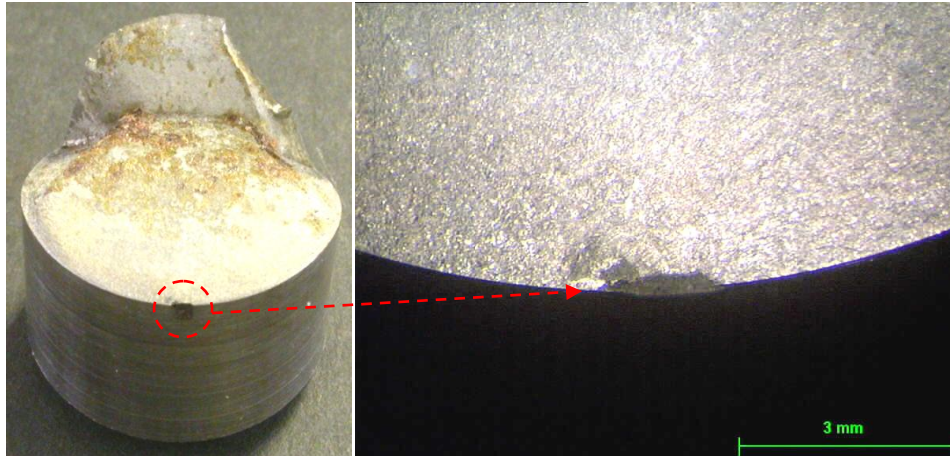
**Figure 7-24: Large scale fatigue specimen 2 - Fracture surface and corrosion flaw having caused the failure**

## 7.4 Stress concentration factor

The fracture surfaces of the two larger scale fatigue specimens were examined with a SFEG scanning electron microscope in order to get the dimensions of the flaws having initiated the fatigue cracks and to model them with finite element to assess their stress concentration factor.

- *__Large scale fatigue specimen 1__*

Two different analyses were carried out for the damage found in larger scale fatigue specimen 1, due to its intricate shape. The first analysis was performed with the flaw observed in the plan of the fracture surface, and the second analysis with the subsurface flaw. The dimensions of the flaws were obtained by observing them with a SFEG scanning electron microscope, as displayed in Figure 7-25.
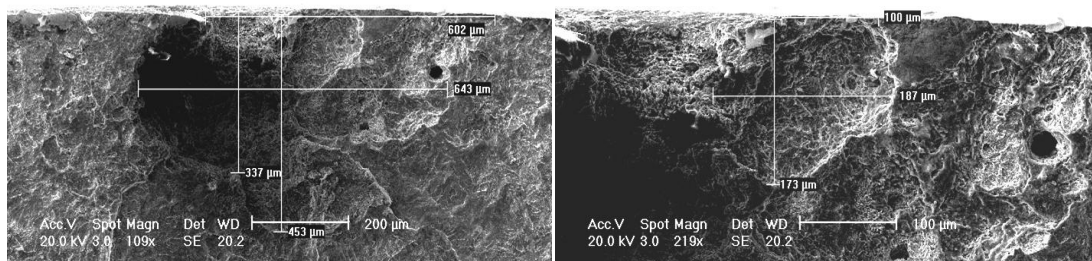


**Figure 7-25: Larger scale fatigue specimen 1 - Dimension of the corrosion flaw in the fracture surface plan (left) and the subsurface flaw (right)**

Different levels of depths and width were observed on the flaw found in the plan of the fracture surface. For the finite element model, the average depth of 395µm and the average width of 620µm were considered. The flaw was therefore modelled as a quarter of an ellipse with a major semi-axis of 395µm and a minor semi-axis of 320µm. The subsurface flaw was also modelled as a quarter of an ellipse. The maximum depth of the flaw, 170µm was considered as the major-semi axis and half of the surface width, 50µm, as the minor semi-axis. The damage corresponded respectively to a stress concentration factor of 2.18 and 2.7.

- ***Larger scale fatigue specimen 2***

Larger scale fatigue specimen 2 failed from a fatigue crack, which initiated form the corrosion damage produced by the crevice former. The examination of the fracture surface with a SFEG scanning electron microscope revealed that the dimensions of the flaw where the crack initiated were1.24mm in width and 175µm in depth, as illustrated in Figure 7-26. The damage was sketched in the finite element model as a quarter of an ellipse with a major semi-axis of 620µm and a minor axis of 175µm in the centre of the gauge length of the specimen. The stress concentration factor for that damage calculated by FE was 1.4.
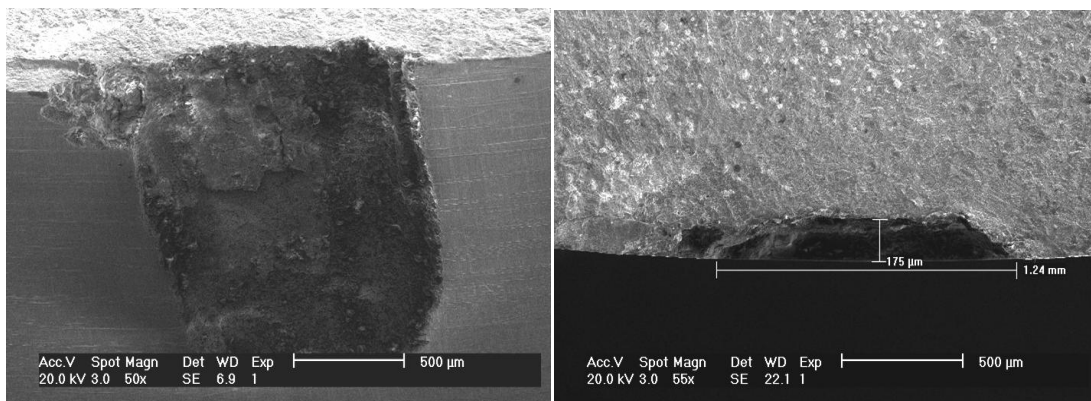


**Figure 7-26: Larger scale fatigue specimen 2 – Dimensions of the flaw where the fatigue crack initiated**

# 8 GENERAL DISCUSSION

## 8.1 Corrosion susceptibility

### 8.1.1 Pitting corrosion

#### *8.1.1.1 Comparison with MSc results*

The results of the 15-5PH pitting corrosion testing were compared to those found in a similar batch of tests carried out by the author during her MSc project [42]. The exposure times in the MSc project were 4 days, 10 days and 14days, compared with 18 days, 3 weeks and 4 weeks in that research.

Results show that the pit size distributions have similar shape whatever the exposure time, as displayed in Figure 8-1 and Figure 8-2, with a peak in the 0-1.5µm range followed by a rapid decrease of the number of pits as the size range increases. However, the heights of the peaks, that is to say the number of pits in the peak range, differ from one exposure period to another and they appear to be no relationship between the exposure time and the height of the peak. Indeed, the peak for a 14 days exposure was higher than the one for a 4 weeks exposure. Nevertheless, as the number of pits detected for each exposure time was different, a comparison of the percentage of pits within the peak range for each distribution was more appropriate to establish a comparison. No apparent link between the exposure period and the number of pits in the peak range were found, as shown in Figure 8-3.

In the same way, no particular tendency was displayed between the maximum pit size and the exposure time, as illustrated in Figure 8-4. Indeed, the longest pit was found for the 3 weeks exposure period, whereas the widest pit was detected in the 14 days distribution. In addition, the largest pit measured after a 4 weeks exposition in the salt spray cabinet, was smaller than the largest pit formed after 14 and 18 days exposure. However, it was noticed that the plot of the maximum pit size as a function of the exposure time for both the length and width distributions followed a very similar pattern, as exhibited in Figure 8-4. Similar observations were made regarding the probable size of the largest pit as a function of the exposure time. Indeed, as displayed

in Figure 8-5, the probable size of the largest pit does not increase with the exposure time, but the pattern followed for the length and the width distribution are similar.
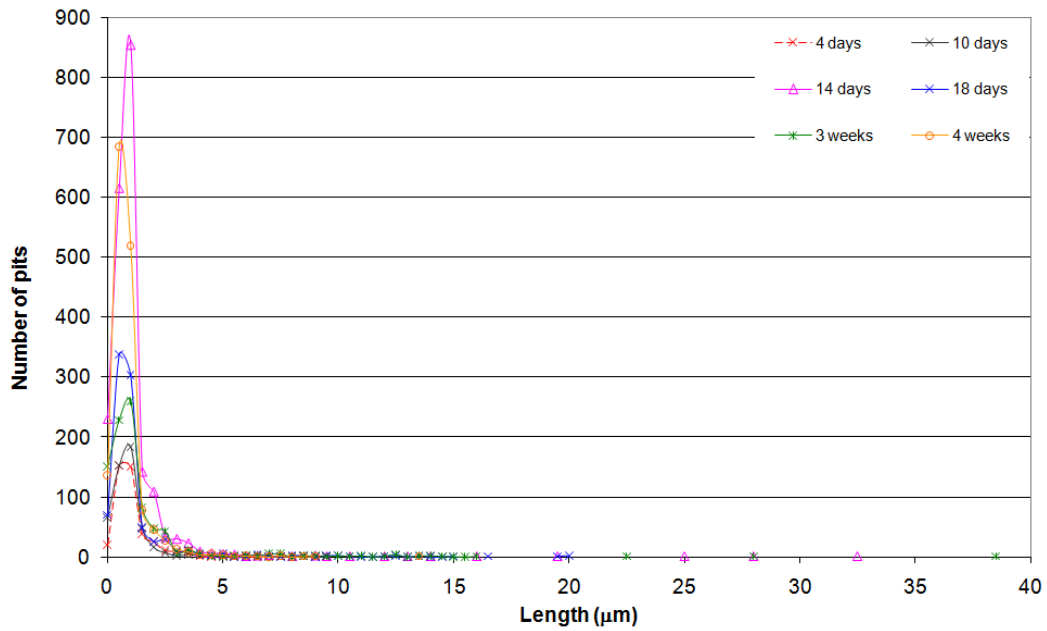


**Figure 8-1: Pit length distribution gathering MSc and MPhil testing results**
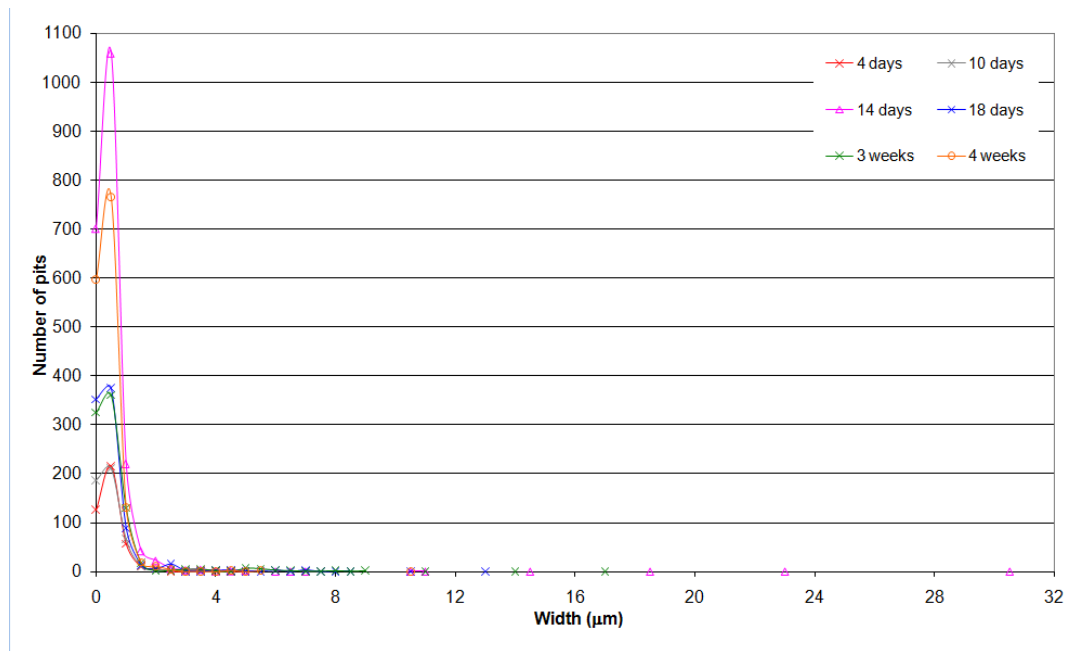


**Figure 8-2: Pit length distribution gathering MSc and MPhil testing results**

134
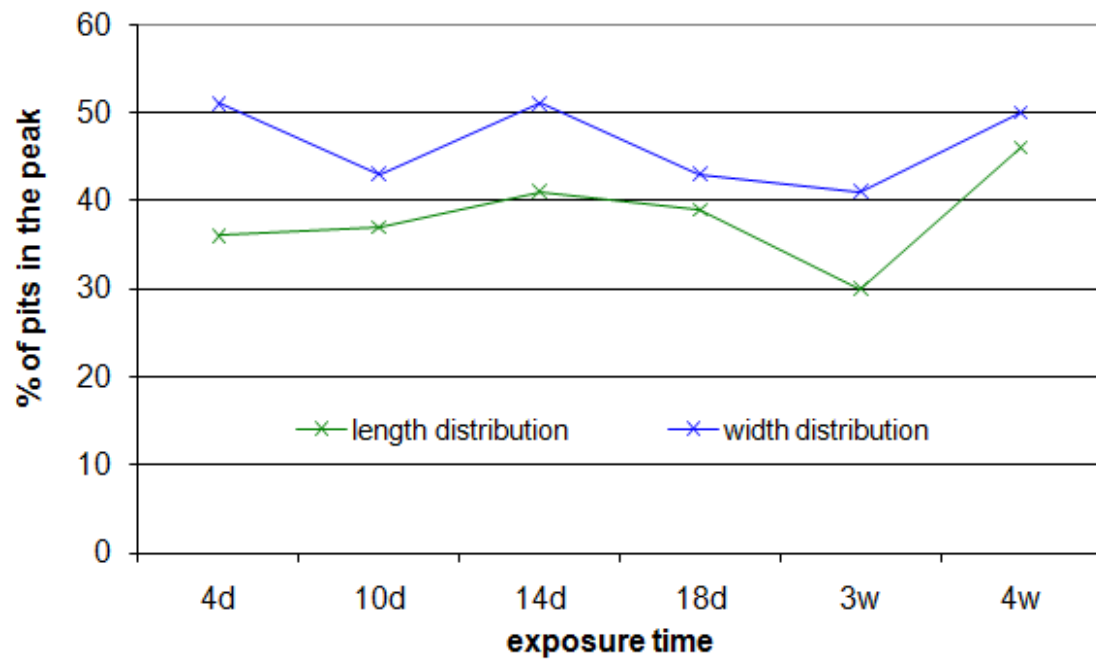
**Figure 8-3: Percentage of pits in the peak range as a function of the exposure time**
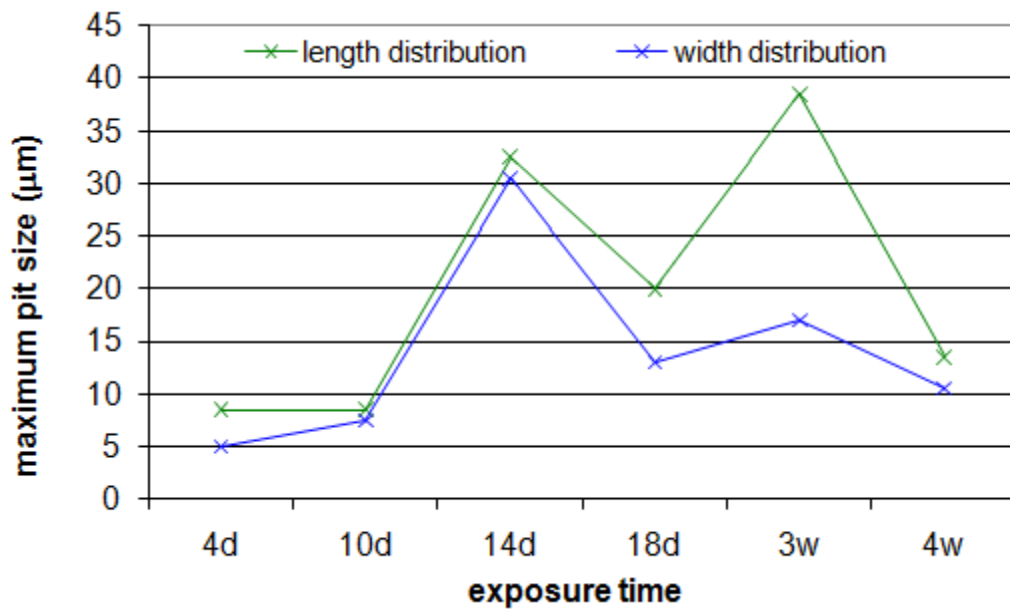


**Figure 8-4: Maximum pit size as a function of the exposure time**
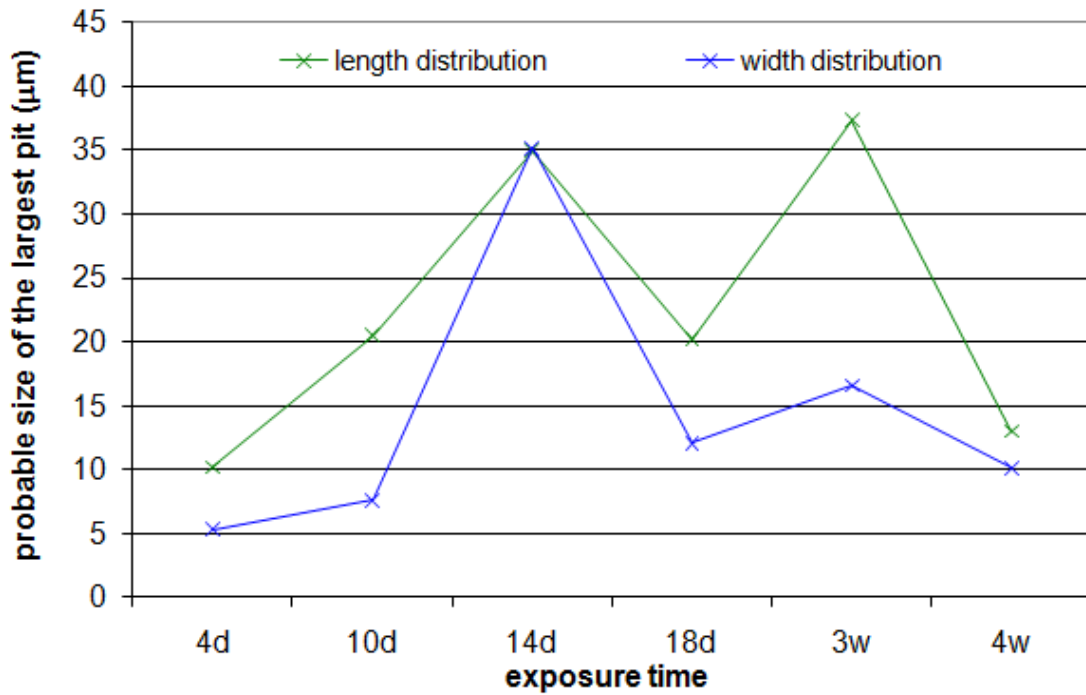
**Figure 8-5: Most probable size of the largest pit as a function of the exposure time**

Although no particular trend was highlighted over the 6 exposure times, the results obtained during the author MSc project [42] for the 4 days, 10 days and 14days exposure period, showed that the largest pit size, as well as the most probable size of the largest pit, increased with the corrosion exposure time. This tendency was not found when comparing only the results obtained for that project (18 days, 3 and 4 weeks exposure time).

Several parameters could be the cause of these differences between the two sets of testing. Indeed, as detailed in section 2.1, pitting corrosion initiation and propagation depends on many factors, and pitting corrosion is described, notably by Burstein [10], as "one of the most difficult forms of corrosion to manage reliably". Some of the parameters which could have induced these differences might be due to a slight change of conditions inside the salt spray cabinet, or due to the difference of polishing technique used between the two sets (silicon carbide paper and diamond paste in the first set of testing, and diamond liquid suspension and paste in the second), or to the size of non-metallic present in the microstructure. Indeed, several authors [2,8,9,10,15] considered non-metallic inclusions as the common site for pitting initiation. Each 15-5PH stainless steels panels having being tested, contained several non-metallic

inclusions of different sizes, and during the polishing process these inclusions had been cut in different sections, leading to a large panel of sizes for pitting ignition size. For instance, if on one hand, three inclusions of different sizes are considered and that during the polishing of the panel, the inclusions have been cut in their middle, as shown in Figure 8-6 case 1, then these inclusions would initiate three corrosion pits and the size of these pits detected by the image analyser software would be the diameter of the inclusion where they initiated. On the other hand, if three inclusions of the same size are considered and that the polishing had cut each inclusion in a different place, as illustrated in Figure 8-6 case 2, then these inclusions would initiate three corrosion pits with a size corresponding to the chord of the respective inclusions.
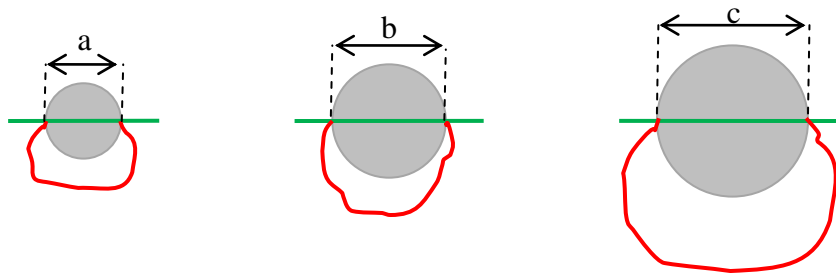
Case 1: Three inclusions of different size cut in their middle section
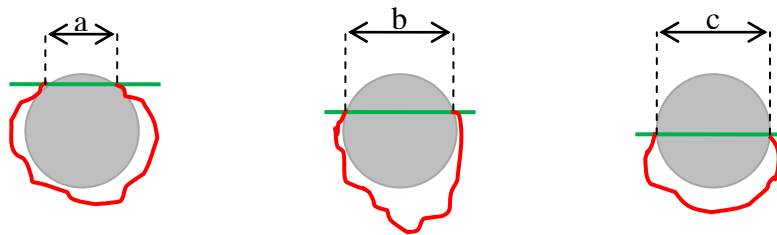
Case 2: Three inclusions of same size cut in different sections

**Figure 8-6: Influence of non-metallic inclusion sizes and polishing section cut on sizes of initiating pit detected by image analyser software**

### 8.1.1.2 Pre-corrosion of fatigue specimen 10

Fatigue specimen 10 had been exposed in the salt spray cabinet for 3 weeks. The corrosion flaws on that specimen were compared to those found on the panels also exposed during 3 weeks in the salt spray cabinet. In both specimens, most of the detected pits have a size comprised in the 0-2µm range. However the percentage of pits being in that range is higher for the 3 weeks panels than for the fatigue specimen, as detailed in Table 8-1, which means that the pit size distributions for the fatigue

specimen are more spread than the panel distributions. Yet, the maximum detected pit size is larger, nearly twice bigger, for the panel than for the fatigue specimen.

It is important to notice that only the gauge length surface of the fatigue specimen was exposed to the salt spray, which is a much smaller area than the surface of the 3 weeks panels. Therefore the probability of having a large non-metallic inclusion present in the gauge length area, and which could initiate a large corrosion pit, was smaller than for the panel.

| | | Fatigue specimen 10 | 3 weeks panel |
|---|---|---|---|
| **Number of detected pits** | | 401 | 879 |
| **% of pits in the 0-2μm range** | *length* | 69% | 82% |
| | *width* | 88% | 95.90% |
| **Maximum detected pit size range** | *length* | 19-19.5 μm | 38.5-39 μm |
| | *width* | 10.5-11 μm | 17-17.5 μm |

**Table 8-1: Comparison of corrosion flaws in a fatigue specimen and a paned exposed for 3 weeks in the salt spray cabinet**

## 8.1.2 Crevice corrosion

From crevice corrosion experiments, it can be concluded that 15-5PH stainless steel is very likely to corrode if a crevice is created on its surface. Indeed, according to the test results, the probability of having no active crevice corrosion was calculated, as displayed in Figure 5-9, and it shows that this probability is already less than 100% after only 12 hours; in other words, it means that in the presence of a crevice, active corrosion will already have developed after only 12 hours. In addition, corrosion damage due to crevice corrosion also developed in specimens, which were tested for pitting corrosion, and in the case of fatigue specimens, these crevice corrosion flaws were the origin of the fatigue crack which ultimately caused the failure of the specimens. Furthermore, it is known that the critical temperature to initiate crevice corrosion is lower than the pitting critical temperature, which eases the occurrence of crevice corrosion compared to pitting. Therefore, it can be said that 15-5PH is more prone to crevice corrosion than pitting and that crevice corrosion is thought to be the most likely cause of any pit-like flaws in this material.

## 8.2 Crack growth rate and stress intensity threshold

According to fatigue crack growth rate curves found in the Atlas of fatigue curves [43], the crack growth rate of 15-5PH is faster in 3.5%NaCl than in air, as shown in Figure 8-7 comparing the curves labelled "H1100 R=0.05 1min hold Salt soln" and "H1100 R=0.05 1min hold RT air". Although the testing conditions were not exactly the same, it was expected that the results of the tests performed in air and in 3.5%NaCl in that research project would show the same tendency. However, as illustrated in Figure 8-8, the corrosive environment did not seem to have an effect on the crack growth rate. Indeed, the data from both tests are very similar, they belong in the same ranges of crack growth rates for a given stress intensity range.

The crack growth rate obtained experimentally in air was then compared to the crack growth rate in air of 15-5PH provided in the AFGROW software [44], as displayed in Figure 8-8. At high values of stress intensity ranges, the curve inferred from the test is lower than the AFGROW curve, which means that for a given stress intensity range, the crack growth rate according to AFGROW is faster than the one found experimentally in that project. In contrast, at low stress intensity ranges and for the stress intensity threshold, the two curves are in good agreement. One of the causes of the difference between the two curves might come from the $\beta$ factor used to calculate the stress intensity range, which was extrapolated from the FE model described in section 0. Indeed, although the FE model was validated by comparing the results to a reference curve, as shown in Figure 4-11, the results above the ratio *a/W=0.6* could not be compared with the reference. Therefore, at high stress intensity ranges, that is to say with a significant crack length *a,* the $\beta$ factor might be slightly erroneous, leading to a offset in the value of the experimental stress intensity range. However, not knowing the source of the AFGROW data, that curve should only be viewed as a guide and not a reference.
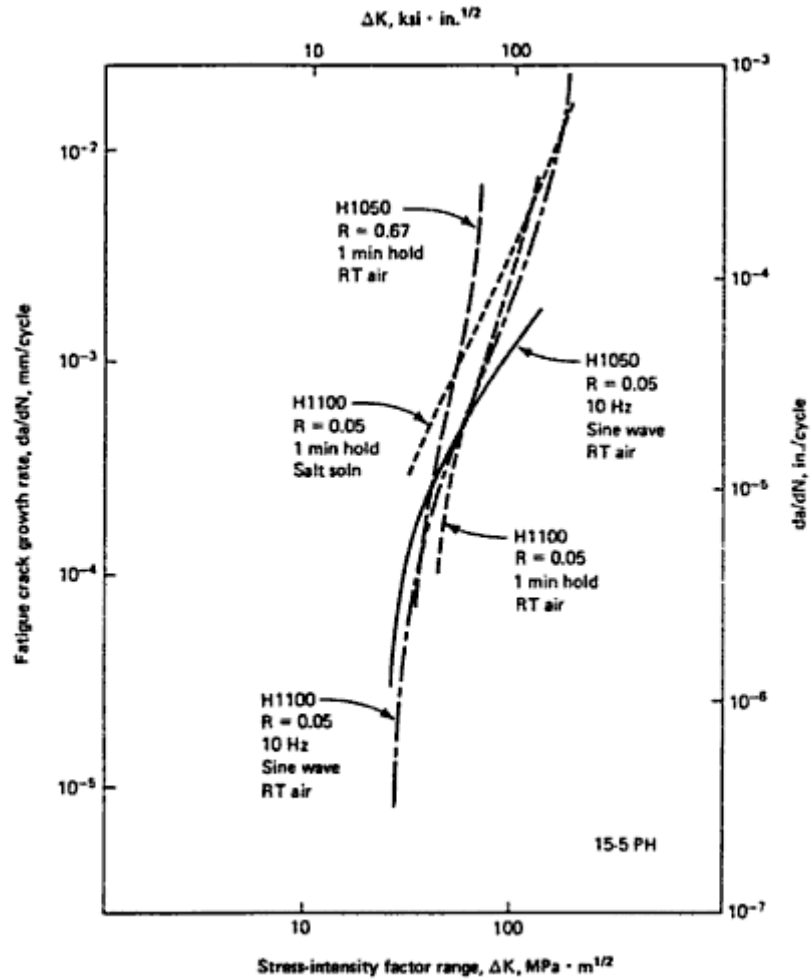
Fatigue crack growth rates in WOL specimens of 15-5 PH stainless steel in the H1050 and H1100 conditions in room temperature air and in a 3.5% NaCl solution.

**Figure 8-7: Fatigue crack growth rate in air and 3.5%NaCl** [43]
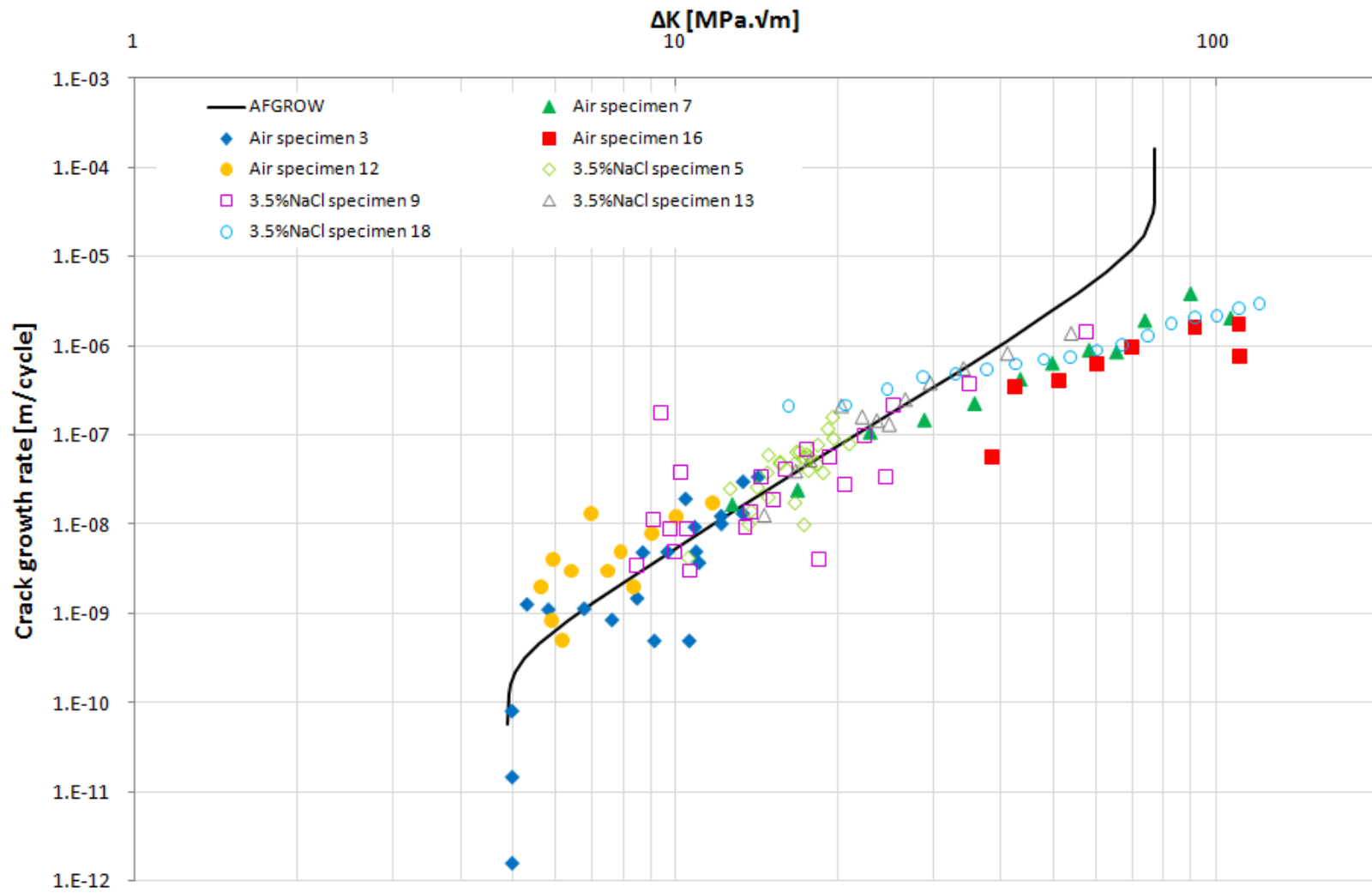
**Figure 8-8: Comparison between the AFGROW and the experimental crack growth rate**

# 8.3 Development of a model for fatigue initiated at a corrosion flaw

From the review of the models found in the literature, summarised in section 2.4.2, it was decided to use the corrosion fatigue model of Harlow and Wei [30] as the basis for the model coming from this research. In their model, the author expressed the critical size $a_c$ for which a corrosion flaw would initiate a surface crack, as detailed in Eq. 8-1. To complete and fit the model with the practical observations made during this research project, the growth of flaws generated by crevice corrosion and the growth of fatigue crack initiated by crevice corrosions flaw need to be modelled in order to assess the total life of a specimen subjected to fatigue initiated at a corrosion flaw.

**Eq. 8-1**
$$a_c = \frac{1}{\pi}\left(\frac{\Delta K_{th}}{k_t \Delta\sigma}\right)^2$$

## 8.3.1 Critical corrosion flaw size

Figure 8-9 displays the variation of the critical flaw size $a_c$, detailed in Eq. 8-1, as a function of the stress range $\Delta\sigma$. The stress intensity range threshold $\Delta K_{th}$ and the stress concentration factor $K_t$ were modified for each curve to examine the influence of these two parameters on the critical corrosion flaw size. Two different values of stress intensity range threshold were chosen:

- $\Delta K_{th} = 5\ MPa.m^{1/2}$, corresponding to the stress intensity range threshold of 15-5PH stainless steel as detailed in sections 5.3 and 8.2,
- and $\Delta K_{th} = 3.5\ MPa.m^{1/2}$, expected stress intensity range threshold for 300M steel.

Similarly, two different values of stress concentration factor were chosen corresponding to arbitrary corrosion flaw geometries, as detailed in section 4.1.2:

- $K_t = 1.65$ corresponding to a shallow corrosion flaw
- $K_t = 2.45$ corresponding to a deep and narrow corrosion flaw.
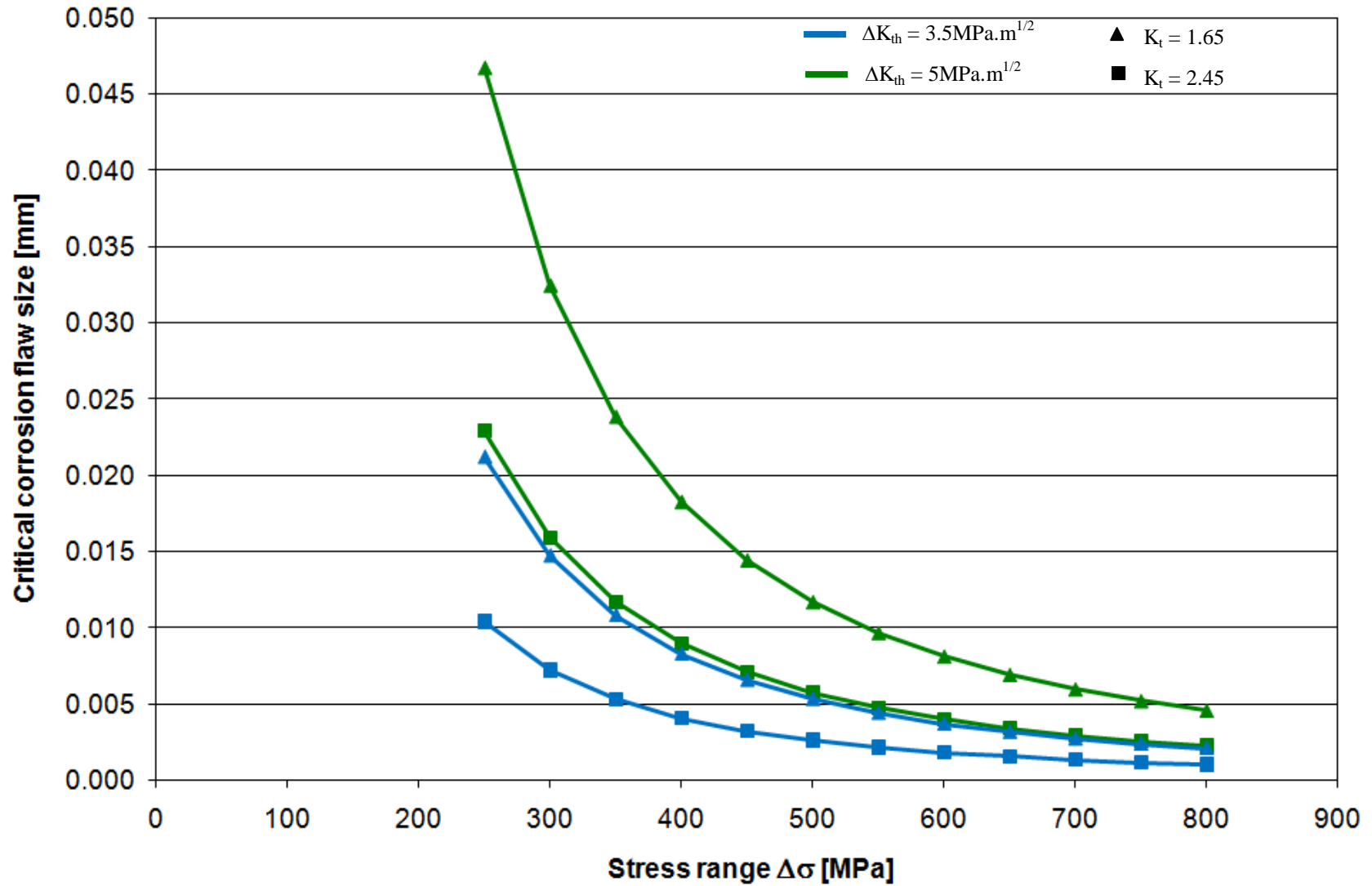
**Figure 8-9: Critical corrosion flaw size as a function of the stress range, stress intensity range threshold and stress concentration factor**

Figure 8-9 shows that the critical corrosion flaw size decreases as the stress intensity range threshold decreases. However, the critical flaw size decreases as the stress concentration factor increases.

The modelling results displayed in Figure 8-9 are used to compare 15-5PH stainless steel and 300M and predict the behaviour that would be expected in two different situations.

### 8.3.1.1 *Corrosion damage with constant stress concentration factor*

Considering a stress range of 250MPa and a stress concentration factor of 2.45 (deep and narrow flaw) for both materials, it appears that the critical flaw size for initiate a fatigue crack would be around 10μm for 300M and 21μm for 15-5PH. This means that to initiate a fatigue crack from a deep and narrow flaw with a $K_t$ of 2.45 in 15-5PH, the flaw has to grow twice as large as in 300M.

### 8.3.1.2 *Corrosion damage with differing stress concentration factor*

Salt spray testing has shown that 300M is prone to form large shallow surface irregularities during corrosion, whereas stainless steels usually form smaller but deeper corrosion flaws.

Considering a stress range of 250MPa, with a stress concentration factor of 1.65 corresponding to a shallow corrosion flaw for 300M and a stress concentration factor of 2.45 corresponding to a deep and narrow corrosion flaw for 15-5PH, the critical flaw size to initiate a fatigue crack would be 23μm for 300M and 21μm for 15-5PH. This means that a small but deep flaw in the more corrosion resistant stainless steel (15-5PH) could be as damaging as a more extensive but shallow corrosion damage in 300M.

## 8.3.2 Crevice corrosion modelling

Many models of crevice corrosion have been developed but they are mainly based on electrochemical parameters [11, 12, 61, 62, 63], which were not considered in that project research. Therefore, based on the observations made during the corrosion testing of 15-5PH stainless steel detailed in section 5.2, several assumptions were made to develop a crevice corrosion propagation model. The results of the experiments were used to test the validity of these hypotheses.

# 8. GENERAL DISCUSSION

> ## Assumptions

a) The volume rate of removal of metal by crevice corrosion is constant. This is because of the rate is controlled by the rate of the cathodic reaction, which is the reduction of dissolved $O_2$ on the exposed surfaces. The process is under cathodic control and the rate of cathodic reaction is expected to be constant; in the salt spray cabinet, at least. It follows that the volume of metal removed is given by Eq. 8-2.

**Eq. 8-2**
$$V = A \cdot t$$
*where V is the volume, t the time and A a constant*

b) The crevice corrosion first spreads across the area of the crevice former, until the whole area has become active. This has been observed in most of the experiments, although the entire area has not become active in some cases, as detailed in section 5.2.3.

c) The aspect ratio of the crevice corrosion remains constant during this stage, as shown in Figure 8-10. That is to say that the growth rate across the surface exceeds the growth rate into the material



**Figure 8-10: Profile of the crevice corrosion remaining constant**

Following assumptions a), b) and c), the equation of the area growth rate should be given by Eq. 8-3. It follows that if the area growth rate is proportional to $t^{2/3}$ and the volume growth rate is proportional to t, then the depth growth rate in the initial phase is proportional to $t^{1/3}$ and should be expressed by Eq. 8-4.

**Eq. 8-3**
$$Area = D \cdot t^{2/3}$$
*where Area is the area growth rate, D a constant and t the time*

$$\textbf{Eq. 8-4} \qquad d = F \cdot t^{\frac{1}{3}}$$

*where $d$ is the depth growth rate, $F$ a constant and $t$ the time*

d) When the entire area of the crevice former has become active, no further growth across the surface takes place. This means that in the case of a seal or debris on the surface, the maximum area of the crevice corrosion would be defined, as illustrated in Figure 8-11.
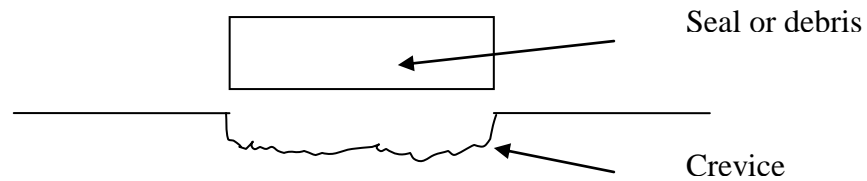


**Figure 8-11: Maximum area of crevice corrosion defined by the area of a seal or debris**

e) As the volume rate of metal removal is unchanged (cathodic control), the corrosion now develops into the material at an increased rate. This means that the depth of attack is now proportional to the time.

f) An overall depth growth rate equation of the following form is anticipated:

$$\textbf{Eq. 8-5} \qquad d = A \cdot t_1^{\frac{1}{3}} + B \cdot (t_2 - t_1)$$

*where $t_1$ is the time within initial phase, $t_2$ the total exposure time and A and B are constants*

> **Testing the hypotheses**

*Area growth rate*

From the crevice corrosion surface area measurements and assessment of the most probable maximum active site area, detailed in section 5.2.4, the area growth rate was assessed by plotting the four curves of the most probable maximum active site area as a function of the exposure time in a log-log scale graph, fitted with straight lines of the form $Area = C. t^k$ , where C is a constant, k an exposant and t is the time as shown in Figure 8-12.

The area growth rate for the upper, more exposed surfaces was found to be proportional to $t^{0.39}$ for the first set of experiments and to $t^{0.38}$ for the second batch, where t is the exposure time. For the lower, less exposed surfaces, the area growth rate

was found to be proportional to $t^{0.36}$ for the second set of experiments, and to $t^{0.34}$ for the first batch. However, the coefficient of determination, R, being much less than 0.9, for the area growth rate of the lower, less exposed surfaces for the first set of experiments, this value was not considered as being reliable. Indeed, the coefficient of determination or R-squared value, R, which is a number between 0 and 1, represents the reliability of the trend line compared to the set of data, with 1 being a perfect fit. The constant C was found to be different for every area growth rate, but for each set of experiments, it was noticed that the constant C for the most exposed surface was higher than C for the less exposed surface.

Therefore, by taking the average of the three reliable growth rates, it was found that the area growth rate was not proportional to $t^{2/3}$ as expected but seems to be rather proportional to $t^{3/8}$.

### *Depth growth rate*

As detailed in section 5.2.5, the depth of each crevice corrosion site was measured at the end of the experiment, once the crevice former was removed. As the first set of experiment ended after 1941h and the second after 768h, it was possible to assess the most probable deepest active crevice corrosion site for these two exposure times, respectively 950µm and 251.5µm. Two values are not sufficient to assess with confidence the depth growth rate. In addition, as the depth of the crevice site could not be monitored at different times during the experiment, it was not possible to assess the the time $t_1$ at which the transition from the initial to the second growth phase occurs according to the assumptions made.

The first assumption stated that the volume of metal removal was constant due to the cathodic control, with cathodic and anodic currents constant. This assumption was also considering a cathode/anode surface ratio constant. However, at the beginning of the crevice corrosion process, there are few small active regions. As corrosion progresses, the active regions grow and get larger and new active regions appear. Therefore, if the number of active site and their size increase and that the anodic current is constant, the current density on each active site will decrease. Hence, the volume of metal removal would not be constant on each site, and it would be less than expected, explaining that an area growth rate proportional to $t^{3/8}$ instead of $t^{3/8}$ was found.
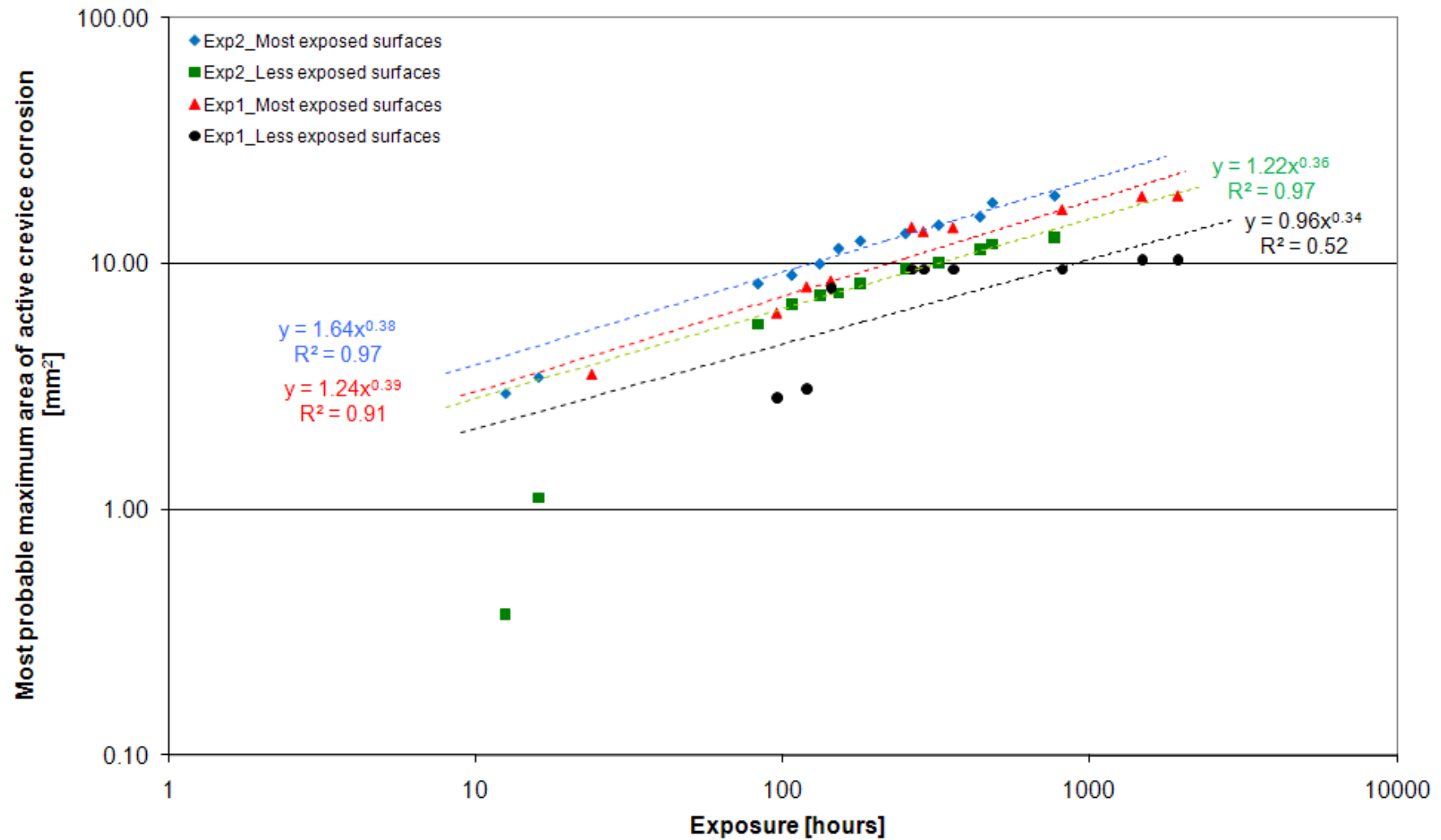
**Figure 8-12: Most probable maximum area of active crevice corrosion and area growth rate**

> ## ➤ **Further development of the model**

i. Further area measurements need to be made on other panels to increase the size of the data set and to confirm the proportionality to $t^{3/8}$. In addition, the constant C needs to be identified and the difference in C value between the most exposed surface and the less exposed surface needs to be confirmed.

ii. Measurements of the active crevice sites need to be done throughout the duration of the experiment, without removing the crevice former to avoid changing the conditions. These measurements as a function of the exposure time should enable to identify the transition time and the depth growth rate of each phase, and ultimately provide an overall depth growth rate. Still considering assumptions a), b) and c) as correct, and the area growth rate proportional to $t^{3/8}$, the depth growth rate in the initial phase should therefore be proportional to either $t^{5/8}$.

## 8.3.3  Fatigue life

### 8.3.3.1  *Stress concentrations factor and fatigue life*

Fatigue life consists of an initiation phase and a crack growth phase. It might be expected that the stress concentration factor $K_t$ will have an influence on the initiation of fatigue crack, as well as the early growth of the crack, but that the influence will fade as the crack grows until totally disappear. To examine the influence of $K_t$, the lives to achieve failure of 15-5PH pre-corroded fatigue and large scale fatigue specimens, as well as a MLX17 fatigue specimens, all tested at a maximum stress of 350MPa are plotted as a function of the stress concentration factor of the corrosion flaw which initiated the fatigue crack causing the ultimate failure of each specimen, as displayed in Figure 8-13.

MLX17 specimen shows a much longer total life than 15-5PH specimens. However, the corrosion damage which caused the ultimate failure of MLX17 specimen was not the damage formed in the salt spray cabinet, but a small crevice corrosion damage which developed during the fatigue testing, as explained in section 6.2.2. Therefore, the total fatigue life of that specimen includes a certain number of cycles during which the

corrosion flaw initiated and grew, without impacting on the fatigue life of the specimen, until that corrosion flaw reached a critical size causing the initiation of fatigue crack.

Regarding the two 15-5PH large scale specimens, the specimen with the highest $K_t$ is the specimen with the shorter life, as it would be expected. However, two points are not sufficient enough to prove that this behaviour is true in any case. Comparing the results of the large scale specimens with the smaller fatigue specimens, it appears that the lives of the larger scale fatigue specimens are longer than the lives of the smaller fatigue specimens for same ranges of $K_t$ values. Indeed, large scale specimen 2, with a $K_t$ value of 1.4 failed after 316 565 cycles, whereas fatigue specimen 21, with a $K_t$ value of 1.5 failed after 208 679 cycles. Likewise, the lives of large scale specimen 1 and fatigue specimen 20, which respectively failed after 213 597 and 211 393 cycles, are very close, whereas their respective Kt values are 2.18 and 1.78. However, it is important to notice that the section of the large scale specimen was much larger than the small fatigue specimen, hence a longer crack would be needed to cause the failure of the large scale fatigue.

As for the 15-5PH fatigue specimens, no general pattern appeared linking the total fatigue life to the stress concentration factor value.
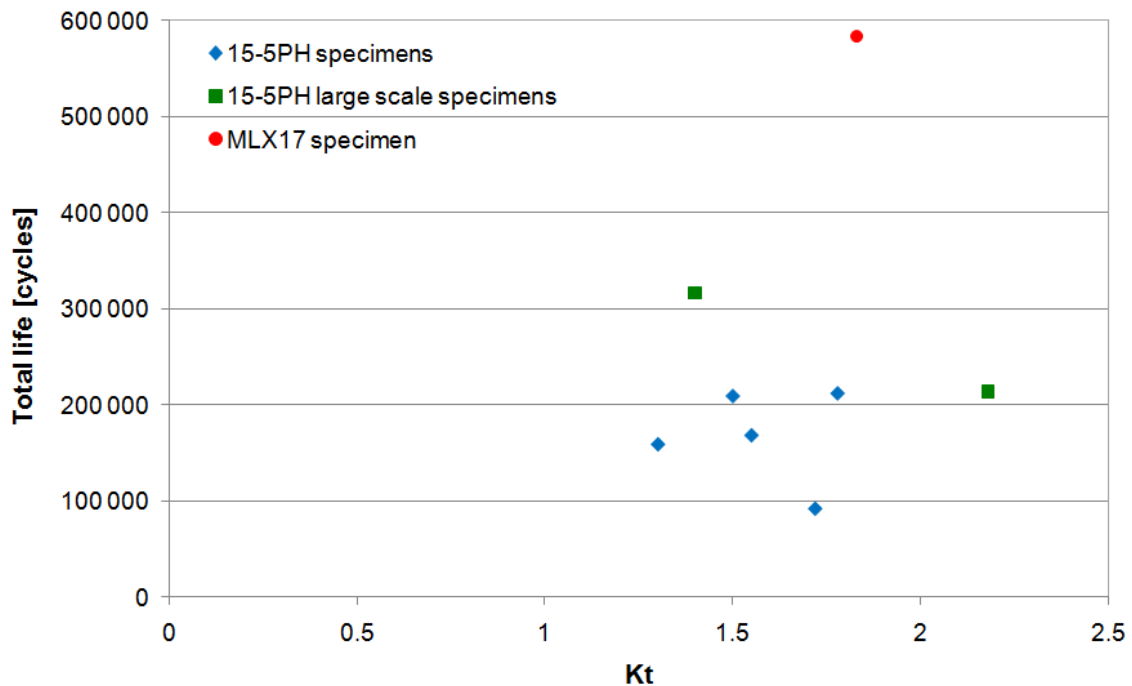


**Figure 8-13: Total fatigue life as a function of the stress concentration factor of the corrosion flaw**

## 8. GENERAL DISCUSSION

The fatigue life of specimens 2, 6, 21 and 24 was examined in more details as they were tested in the exact same conditions (maximum stress 350MPa, R=0.1 and 3.5%NaCl) and that the fatigue cracks which caused the ultimate failure of the specimens initiated from the corrosion flaw produced by the crevice former, contrary to specimen 20.

From the replica and pictures taken during the fatigue testing, it was possible to plot the surface crack development as measured from the centre of the corrosion flaws for the four specimens, as displayed in Figure 8-14. The point of intersection of the data with the vertical axis is the corrosion flaw half width.

The early crack growth behaviour from the corrosion damage shows significant variability, but the crack growth rate at surface crack length greater than about 1.5-2mm look similar. Using the data displayed in Figure 8-14, the lives to reach 0.2mm and 0.8mm crack length can be obtained for each specimen, as detailed in Table 8-2.
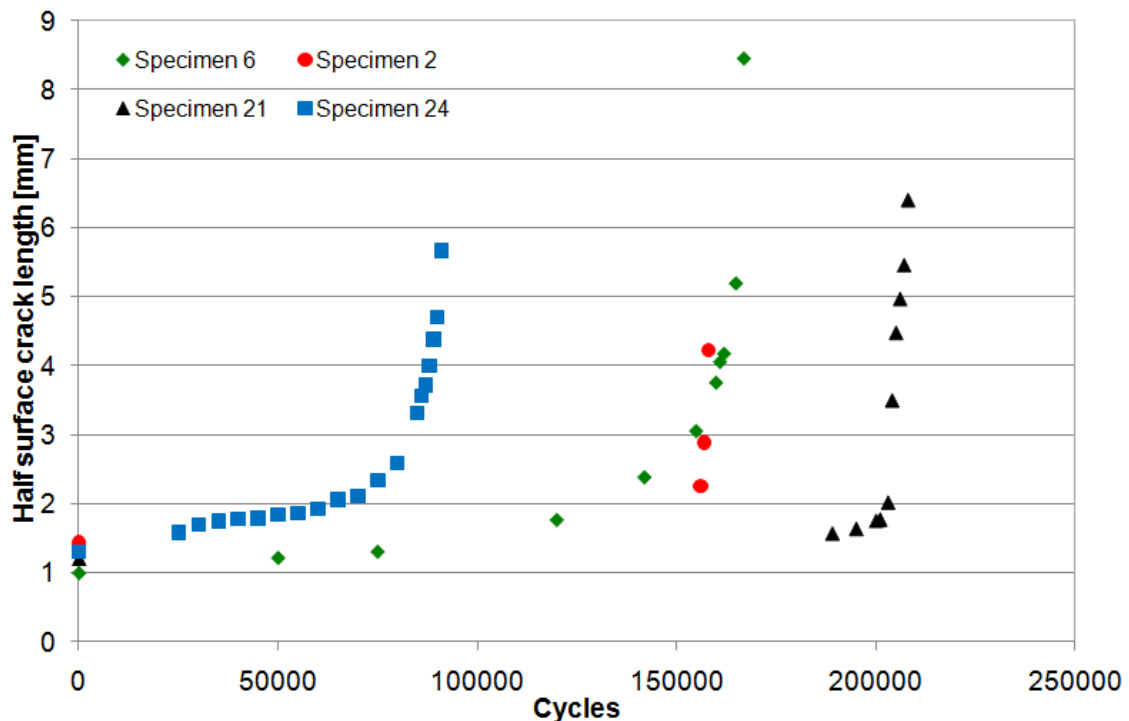


**Figure 8-14: Surface crack development from corrosion flaw for specimens 2, 6, 21 and 24**

Table 8-2 shows that the number of cycles to grow the fatigue crack to 0.2mm is between 26% and 51% of the total life, and that the life to grow a 0.8mm crack corresponds to 72% to 98% of the total fatigue life of the specimen. Regarding the crack

151

growth life between 0.8mm and failure of the specimen, it is always less than 30% of the total fatigue life, and for specimens 2 and 21 it is less than 2%. It can be seen that there is a significant variability in crack growth life for the four specimens, although they have been tested under nominally identical conditions.

| Specimen | Kt | $N_{tot}$ | N to $_{0.2mm}$ | N to $_{0.8mm}$ |
|----------|------|-----------|-----------------|-----------------|
| 6 | 1.55 | 167 806 | 50 000 | 120 000 |
| 2 | 1.3 | 158 485 | 80 000 | 156 000 |
| 21 | 1.5 | 208 679 | 100 000 | 203 000 |
| 24 | 1.72 | 91 572 | 18 000 | 70 000 |

**Table 8-2: Cycles to achieve 0.2mm, 0.8mm and failure crack length and $K_t$ value**
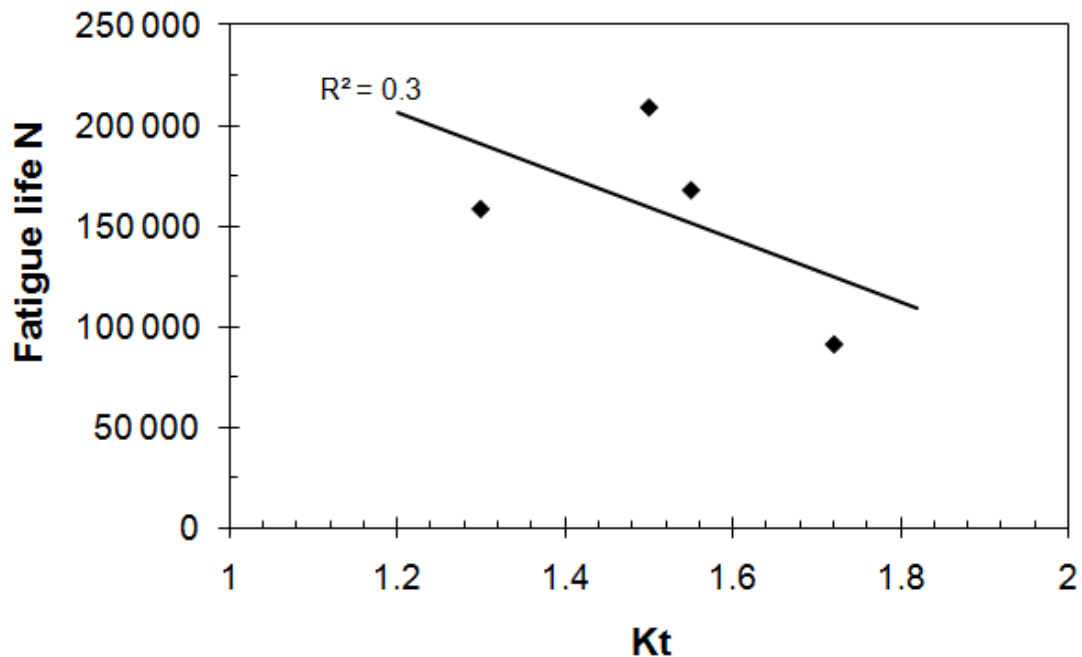


**Figure 8-15: Total fatigue life as a function of the stress concentration factor values for specimens 2, 6, 21 and 24**

The total fatigue life and the fatigue lives to grow the crack to 0.2mm and 0.8mm for specimens 2, 6, 21 and 24 are plotted as a function of the stress concentration factor $K_t$, as displayed in Figure 8-15 and Figure 8-16. Best fit lines to the data using a least square fit are also plotted. It can be noticed that the correlation between total fatigue life and $K_t$ is very poor ($R^2=0.3$), as displayed in Figure 8-15. However, the correlation improves when considering the life to reach a crack extension of 0.8mm ($R^2=0.4$) and it is even better when a 0.2mm crack extension is considered ($R^2=0.6$). This means that

the initiation and early crack growth behaviour are indeed influenced by the value of the stress concentration factor $K_t$. From the life to reach a 0.2mm crack extension, it can be noticed that the higher the $K_t$ value, the shorter the life.
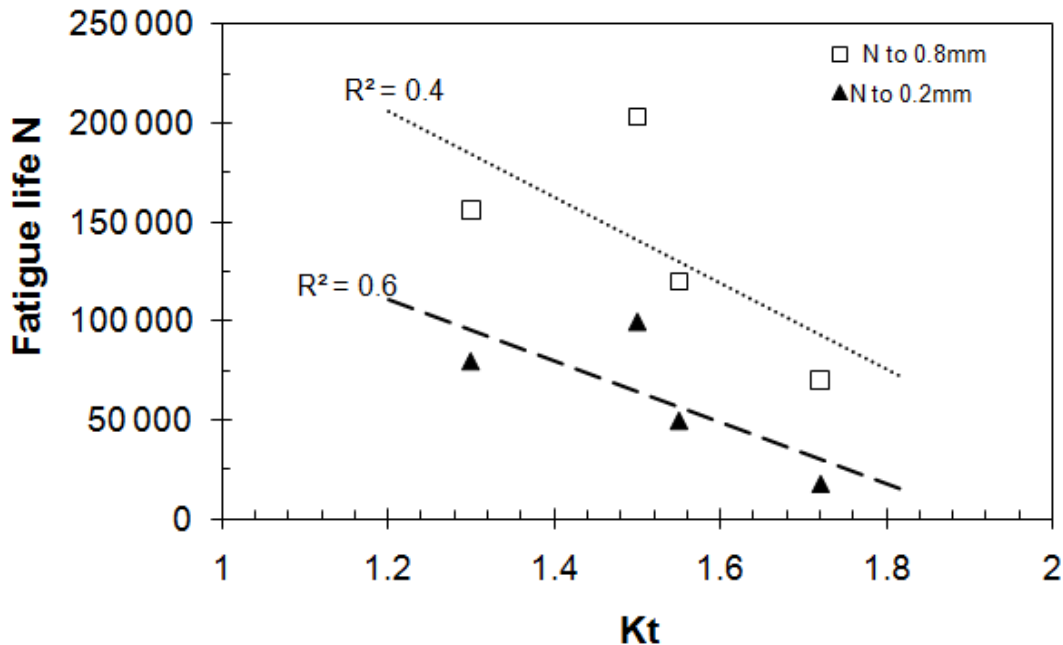


**Figure 8-16: Fatigue lives to reach a crack extension of 0.2 and 0.8mm as a function of the stress concentration factor values for specimens 2, 6, 21 and 24**

### 8.3.3.2  Initiation and crack growth behaviours

Section 8.3.3.1 showed that the stress concentration factor $K_t$ has an influence on the initiation and early crack growth behaviours, but has no effect on the life of longer cracks. Differences between initiation and crack growth behaviour was also highlighted by calculating the fatigue crack growth lives of specimens 2, 6, 21 and 24, using the corrosion flaw as a starting crack rather than a flaw. Then by comparing the experimental fatigue lives of these specimens with the calculated lives, the initiation stage during which the corrosion flaws are transformed into cracks can be assessed.

The AFGROW software package [44] was used to model the growth of an elliptical surface defect using the dimensions of the corrosion damage measured with the SFEG microscope for specimens 2, 6, 21 and 24, as detailed in section 5.4.3 and Table 8-3. The crack growth data for 15-5PH at a similar strength level to that used in this project research was used as the input material data.

## 8. GENERAL DISCUSSION

| Specimen | Elliptical surface defect width [mm] | Elliptical surface defect depth [mm] | Experiemental fatigue life [cycles] | Calculated fatigue life [cycles] | Initiation life [cycles] | Kt |
|---|---|---|---|---|---|---|
| 6 | 2.000 | 0.320 | 167 806 | 142 000 | 25 806 | 1.55 |
| 2 | 2.880 | 0.276 | 158 485 | 123 800 | 34 685 | 1.30 |
| 21 | 2.400 | 0.470 | 208 679 | 109 000 | 99 679 | 1.50 |
| 24 | 2.600 | 0.720 | 91 572 | 84 700 | 6 872 | 1.72 |

**Table 8-3: Experimental and calculated fatigue lives for specimens 2, 6, 21 and 24**
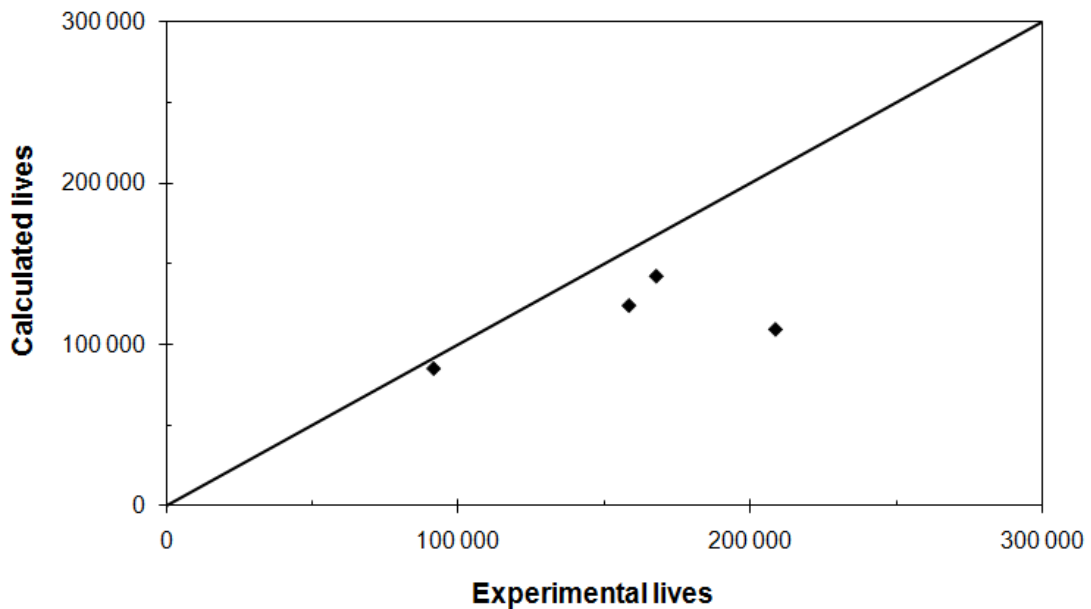


**Figure 8-17: Comparison of the experimental and calculated fatigue lives for specimens 2, 6, 21 and 24**

The agreement between the calculated life and the experimental life is very good for specimen 24 which has the shortest life and largest Kt ( Kt=1.72), as shown in Figure 8-17 and detailed in Table 8-3.

However, for specimens 2, 6 and 21 which have longer lives, it is inaccurate and conservative. This comparison shows that for shortest lives, as for specimen 24, most of the life is occupied by the fatigue crack growth, whereas for longest lives (specimens 2, 6 and 21), a significant part of the life is occupied by the transformation of the corrosion flaw into a growing crack.

154
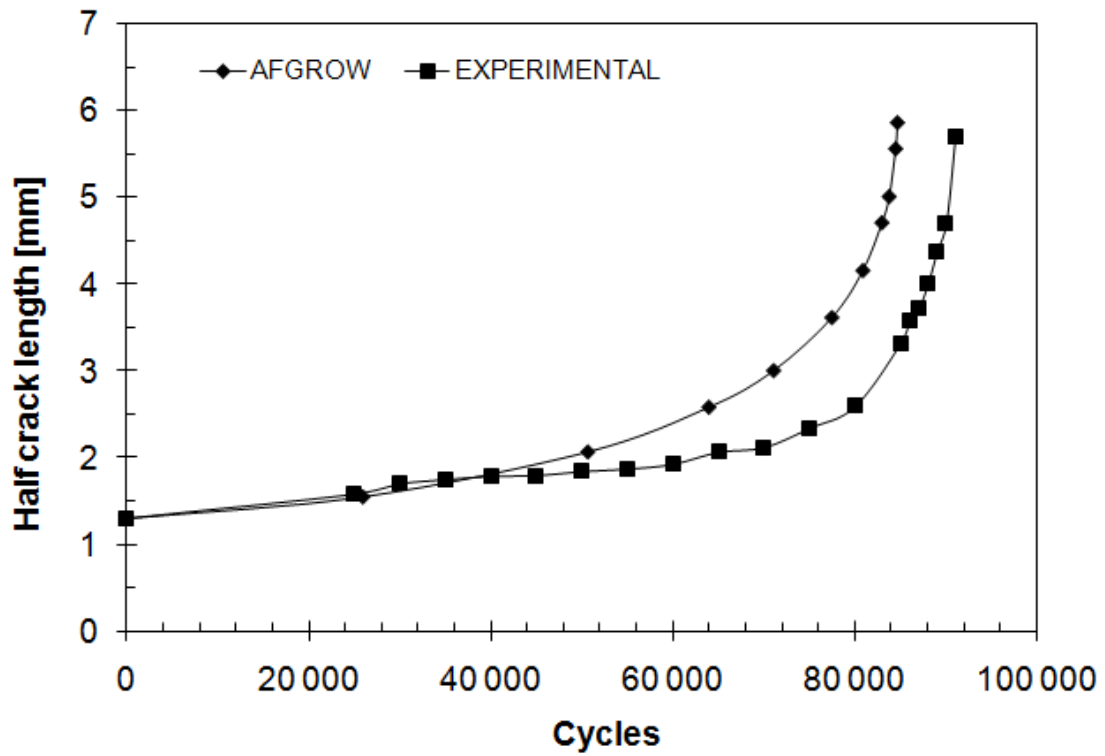
**Figure 8-18: Specimen 24 - Crack length as a function of the number of cycles measured experimentally and using AFGROW**
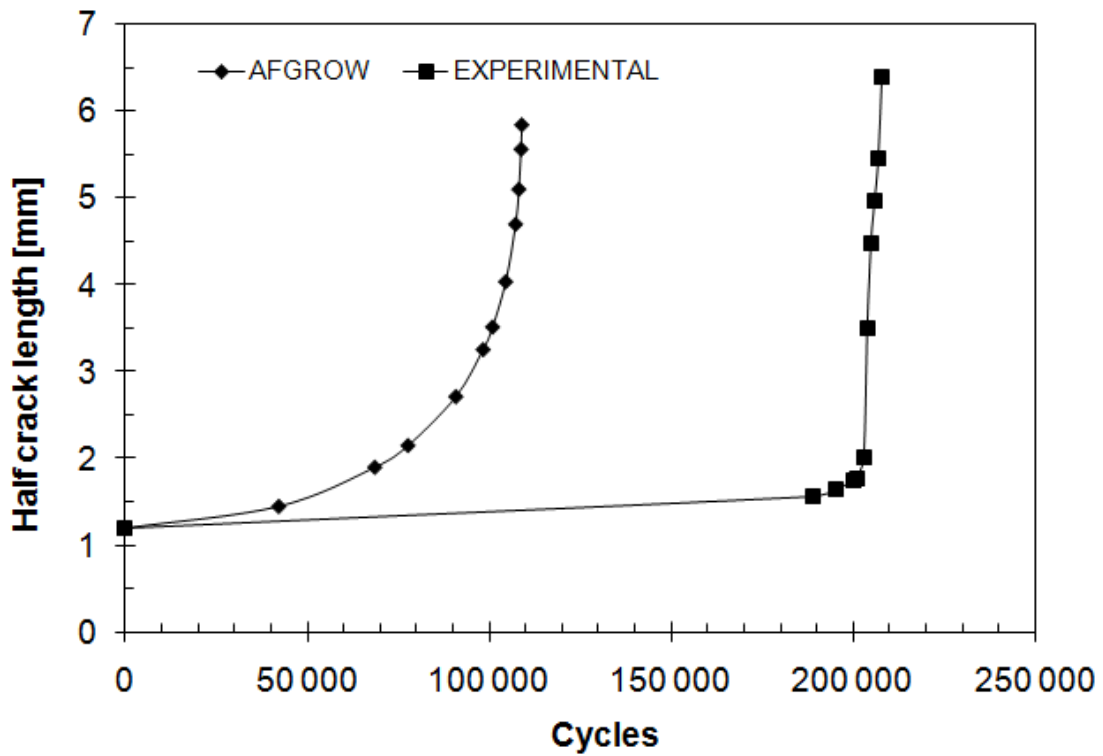


**Figure 8-19: Specimen 21- Crack length as a function of the number of cycles measured experimentally and using AFGROW**

Comparison of the crack length as a function of the number of cycles for the total experimentally measured life and the calculated crack growth life confirms that total life for specimen 24 is mainly crack growth life, as shown in Figure 8-18, whereas nearly 50% of total fatigue life of specimen 21 is dedicated to the transition from the corrosion flaw to the growing crack, as displayed in Figure 8-19.

The difference between the cycles required to initiate the growing crack in these and the other samples must be related to geometrical differences in their detailed morphology despite the similarities in their gross shapes.

### 8.3.4 Influence of the modelled flaw shape on the Kt value

Literature [59] gives a fatigue strength, $\sigma_{max}$, of 1050MPa (153ksi) at R=0.1 for pristine 15-5PH specimens. Therefore, for a specimen tested at 350MPa, a stress concentration in fatigue $K_f$ of 3 would be needed to reach the fatigue strength ( i.e. $K_f$= 1050/350). Yet, the stress concentration factors calculated using FE from the gross shapes of the defects having caused the failure of the fatigue specimens varies between 1.3 and 2.18 for the specimens tested at 350MPa. It shows that taking the gross shape of the defects underestimates the severity of the corrosion flaw, and that the excursions at the bottom of the crevice corrosion should be modelled as they enhance the nominal Kt values.

| Specimen | FE calculated Kt | Total life | $\sigma_{max}$ (MPa) |
|---|---|---|---|
| 6 | 1.55 | 167 806 | 350 |
| 2 | 1.3 | 158 485 | 350 |
| 20 | 1.78 | 211 383 | 350 |
| 21 | 1.5 | 208 679 | 350 |
| 24 | 1.72 | 91 572 | 350 |
| Larger 1 | 2.18 | 213 597 | 350 |
| Larger 2 | 1.4 | 316 565 | 350 |

**Table 8-4: FE calculated stress concentration factors and total fatigue life**

This conclusion is confirmed by the study performed by Cerit et. al [60], which demonstrates that "secondary small pits" located at the bottom of the corrosion cavity are stress concentrators and that the stress concentration factor value for a corrosion flaw with "secondary small pits" is higher than the $K_t$ value for the corrosion flaw

alone. For instance they found that a hemispherical pit of diameter $2c = 100\mu m$ and depth $a=50 \ \mu m$ has a $K_t$ value of 2.15, and that if a secondary hemispherical pit of diameter $2c = 10\mu m$ and depth $a=1 \ \mu m$ is considered at the bottom of the main pit, the $K_t$ value increases to 3.1.

These authors [60] also showed that the stress concentration factor value and the corrosion flaw aspect ratio ($a/2c$) were correlated. They found that the relationship between $K_t$ and the aspect ratio could be described by Eq. 8-6. Note that this relationship does not consider "secondary small pits".

**Eq. 8-6**
$$K_t = \frac{[1+6.6(a/2c)]}{[1+2(a/2c)]} \qquad [60]$$

The FE calculated values of $K_t$ of the corrosion flaws observed in the specimens tested in that project are plotted as a function of the aspect ratio of the flaws, as shown in Figure 8-20. The curve described by Eq. 8-6 is also plotted in that graph. It appears, that although the FE $K_t$ values globally follow the shape of the curve from the formula, the FE $K_t$ are always lower than the $K_t$ values given by the formula, as detailed in  , with more than 5% of difference at the exception of $K_t$ value for specimen 6 which shows very good agreement (0.5%).

| Specimen | a/2c | $K_t$ FE | $K_t$ formula | $\varepsilon$ |
|---|---|---|---|---|
| 6 | 0.160 | 1.55 | 1.56 | 0.5% |
| 2 | 0.096 | 1.30 | 1.37 | 5.1% |
| 20 | 0.333 | 1.78 | 1.92 | 7.3% |
| 21 | 0.196 | 1.50 | 1.65 | 8.9% |
| 24 | 0.277 | 1.72 | 1.82 | 5.5% |
| Larger 1 | 0.637 | 2.18 | 2.29 | 4.7% |
| Larger 1 | 1.700 | 2.70 | 2.78 | 2.8% |
| Larger 2 | 0.141 | 1.40 | 1.51 | 7.1% |

**Table 8-5: Kt values from FEA and formula**
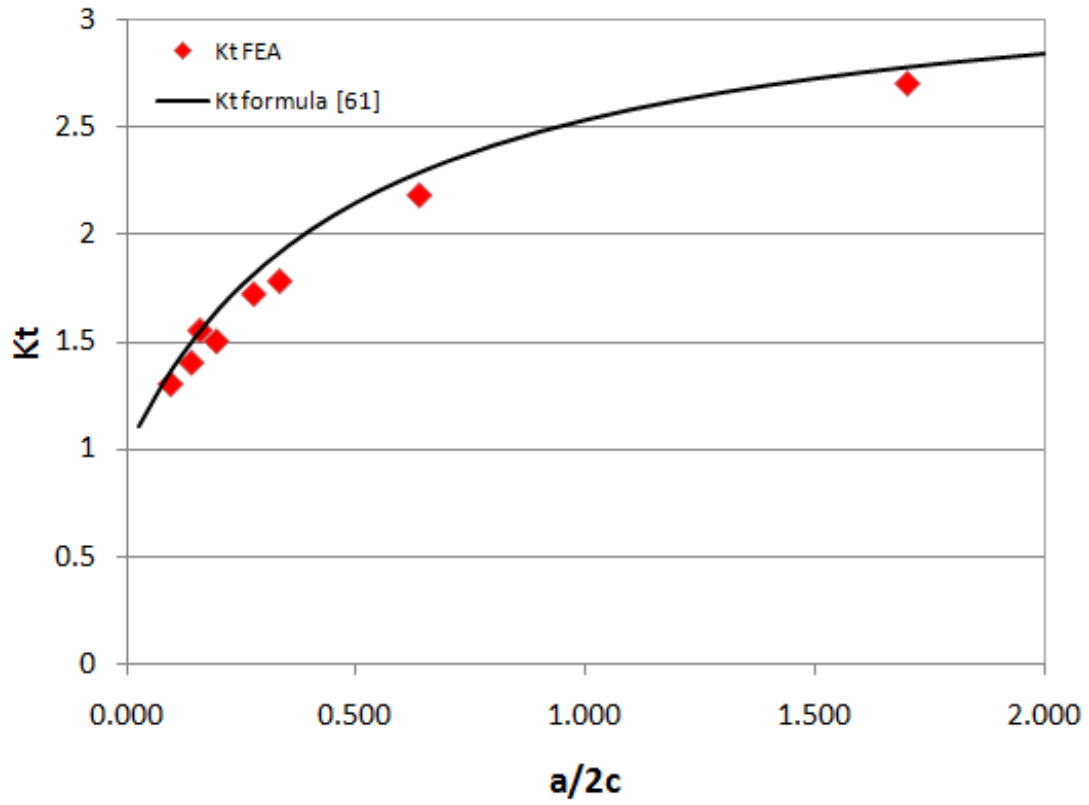
**Figure 8-20: Stress concentration factor as a function of the aspect ratio** *a/2c*

# 9 CONCLUSIONS

The work carried out during this research project has revealed that:

- When 15-5PH panels are subjected to pitting corrosion, the numbers of corrosion flaws that developed on the panels tended to increase with the exposure time in the neutral salt fog test. However, there did not appear to be a systematic increase in the measured maximum pit size or the most probable size of the largest flaw, which is believed to depend on the size of non-metallic inclusions present in the microstructure.

- 15-5 precipitation hardening stainless steel is more prone to crevice corrosion than pitting, and crevice corrosion is thought to be the most likely cause of any pit-like flaws in this material.

- The results of crevice corrosion tests also showed that the 15-5PH stainless steel panels with the rough surfaces seem to initiate the highest number of crevices, and that active crevice corrosion tends to spread following the grinding marks.

- The 15-5PH stainless steel stress intensity threshold was found to be 5 MPa.m$^{1/2}$ in air.

- At the frequencies and exposure times used in that project, the fatigue crack growth rate of 15-5PH stainless steel does not seem to be affected by the environment, according to the results obtained both in air and in 3.5%NaCl solution

- The critical corrosion flaw size criterion showed that a small but deep corrosion flaw in the more corrosion resistant stainless steel (15-5PH) could be as damaging in terms of corrosion fatigue as the more extensive but shallow corrosion damage in 300M

# 9. CONCLUSIONS

- MLX17 stainless steel appeared to be less susceptible to crevice corrosion than 15-5PH stainless steel, and developed shallower crevice corrosion flaws. The pre-corroded MLX17 specimen tested in fatigue did not failed from the corrosion flaw initiated in the salt spray cabinet, but from a smaller and deeper crevice corrosion flaw initiated during the fatigue test.

- The results of the modelling of the propagation of crevice corrosion in 15-5PH stainless steel showed that the initial growth across the metal surface was proportional $t^{3/8}$. It follows that the depth growth rate in that initial stage was proportional $t^{5/8}$.

- All pre-corroded fatigue specimens failed from fatigue cracks which initiated from crevice corrosion flaws.

- No general pattern linking total fatigue life and stress concentration factor value was found. However, it was shown that stress concentration factor Kt has an influence on the initiation and early crack growth behaviour, but has no effect on the life of longer cracks.

- Fatigue testing results showed that for a same range of Kt values, the lives of the larger scale fatigue specimens were longer than the lives of the smaller fatigue specimens. Therefore, it is possible to use the smaller fatigue specimens to predict conservative lives for the larger specimens.

- Not considering the small excursions found at the bottom of corrosion flaws in the assessment of the stress concentration factor, underestimates the values of Kt.

# 10 FURTHER WORK

1. The crevice corrosion propagation model should be refined by examining the corrosion growth rate into the material over time. Hence, the assumptions of the two stages propagation into the material, with an initial stage proportionality to $t^{5/8}$ according to surface area growth rate and constant volume assumption, and a second stage proportional to the time, after a transition time $t_1$ which needs to be identified, would be verified.

2. Finite element analysis considering excursions at the bottom of the corrosion flaws should be performed to assess more accurately the stress concentration factor Kt related to the corrosion flaw.

3. More fatigue tests with pre-corroded specimens should be carried out to investigate the transition between a corrosion flaw and a fatigue crack, and how to correlate the corrosion flaw Kt to a fatigue crack initiation time.

# REFERENCES

1. Cost of corrosion, *Corrosion Cost and Preventive Strategies in the United States*, available at: http://www.corrosioncost.com/pdf/main.pdf

2. Fontana, M.G. (1986), *Corrosion engineering* (3rd ed), McGraw-Hill, New-York.

3. Scully, J.C. (1990), *The fundamental of corrosion* (3rd ed), Pergamon press, U.K.

4. Shreir, L.L. (1976), *Corrosion*, The Butterworth Group, London.

5. Karlberg, G. and Wranglen, G. (1971), "On the mechanism of crevice corrosion of stainless Cr steels", *Corrosion Science*, Vol. 11, pp. 499-510.

6. France, W.D., Jr. (1972), "Crevice corrosion of metals", *Localized corrosion – Cause of metal failure*, ASTM STP 516, pp. 164-200.

7. Corrosion-doctors, *Corrosion pit shapes*, available at:
   http://corrosion-doctors.org/Forms-pitting/shapes.htm

8. Stewart, J. and Williams, D.E. (1992), "The initiation of pitting corrosion on austenitic stainless steel: on the role and importance of sulphide inclusions", *Corrosion Science,* Vol. 33, No. 3, pp. 457-474.

9. Frankel, G.S. (1998), "Pitting corrosion of metals. A review of the critical factors", *Journal of the Electrochemical Society,* Vol. 145, No. 6, pp. 2186-2198.

10. Burstein, G.T., Liu, C., Souto, R.M, and Vines, S.P (2004), "Origins of pitting corrosion", *Corrosion Engineering, Science and Technology*, Vol. 39, No. 1, pp. 25-30.

11. Sharland, S.M. (1987), "A review of the theoretical modelling of crevice and pitting corrosion", *Corrosion Science*, Vol. 27, No. 3, pp. 289-323.

12. Olfield, J.W. and Sutton, W.H. (1978), "Crevice corrosion of stainless steels – I.A Mathematical model", *British Corrosion Journal*, Vol. 13, No. 1, pp. 13-22.

13. Kain, R.M. (1984), "Crevice corrosion behaviour of stainless steel in seawater and related environments", *Corrosion*, Vol. 40, No. 6, pp. 313-321.

REFERENCES

14. Szklarska-Smialowska, Z. (1986), *Pitting Corrosion of Metals*, NACE, Houston, TX.

15. Newman, R.C. (2001), "Understanding the Corrosion of Stainless Steel", *Corrosion*, Vol. 57, No. 12, pp. 1030-1041.

16. Corrosion-doctors, Crevice corrosion, available at
http://corrosion-doctors.org/Forms-crevice/Crevice.htm

17. Wikipedia, De Havilland Comet, available at
http://fr.wikipedia.org/wiki/De_Havilland_Comet

18. Wikipedia, Aloha Airlines Flight 243, available at
http://en.wikipedia.org/wiki/Aloha_Airlines_Flight_243

19. Suresh, S. (1998), *Fatigue of Materials* (2nd ed), Cambridge University Press, U.K.

20. Anderson, T.L. (2005), *Fracture mechanics – Fundamentals and Applications* (3rd ed), Taylor&Francis, New-York

21. Ellyin, F. (1997), Fatigue Damage, Crack growth and life Prediction, Chapman and Hall, London.

22. Spurier, J. (2005), *Post-yield fracture mechanisms*, Advanced Materials MSc lecture notes, Cranfield University, U.K.

23. Irving, P.E. (2005), *Fatigue initiation in metals*, Advanced Materials MSc lecture notes, Cranfield University, U.K.

24. Irving, P.E. (2005), *Fracture mechanics in fatigue crack growth and stress corrosion cracking*, Advanced Materials MSc lecture notes, Cranfield University, U.K.

25. Irving, P.E. (2005), *Fatigue initiation in metals,* Advanced Materials MSc lecture notes, Cranfield University, U.K.

26. Congleton,J. and Craig, I.H. (1982), "Corrosion fatigue", *Corrosion process*, Applied Science Publishers Ltd., London.

27. McEvily, A.J. and Wei, R.P. (1972), *Fracture mechanics and corrosion fatigue*, University of Connecticut, Institute of Material Science.

28. Müller,M. (1982), "Theoretical considerations on corrosion fatigue crack initiation", *Metallurgical and Materials Transactions*, Vol. 13A, No. 4, pp 649-655

REFERENCES

29. Kondo,Y. (1989), "Prediction of fatigue crack initiation life based on pit growth", *The Journal of Science and Engineering corrosion*, Vol. 45, No.1, pp 7-11

30. Harlow, D.G. and Wei, R.P. (1994), "Probability approach for prediction of corrosion and corrosion fatigue life" , *AIAA Journal*, Vol. 32, No. 10, pp 2073-2079

31. Chen, G.S., Wan K.C., Gao M., Wei R.P., and Flournoy T.H. (1996), "Transition from pitting to fatigue crack growth − Modelling of corrosion fatigue crack nucleation in a 2024-T3 aluminium alloy", *Materials Science & Engineering A*, Vol. 219, pp 126-132

32. Shi, P. and Mahadevan, S. (2001), *"Damage tolerance approach for probabilistic pitting corrosion fatigue life prediction", Engineering fracture mechanics*, Vol. 68, No. 13, pp 1493-1507

33. WANG Qingyuan, Kawagoishi, N., Chen Q. and Pidaparti, R.M. (2003), "Evaluation of the probability distribution of pitting corrosion fatigue life in aircraft materials*", ACTA MECHANICA SINICA*, Vol. 19, No. 3, pp 247-252

34. Lindley, T.C, McIntyre, P. and Trant, P.J. (1982), "Fatigue-crack initiation at corrosion pits", *Metals Technology*, Vol. 9, pp 135-142

35. Harlow, D.G. and Wei, R.P. (1993), "A mechanistically based approach to probability modelling for corrosion fatigue crack growth", *Engineering Fracture Mechanics*, Vol. 45, No. 1, pp 79-88

36. Chen, G.S., Liao, C.M., Wan, K.C., Gao, M. and Wei, R.P. (1997), "Pitting corrosion and fatigue crack nucleation", *ASTM special technical publications*, No. 1298, pp 18-33

37. Goswami, T. and Hoeppner, D.W. (1999), "Transition criteria − From a pit to a crack", *Journal of the Mechanical Behavior of Materials,* Vol. 10, No.5-6, pp 261-278

38. Rokhlin, S.I., Kim, J.Y. and Nagy, B.Z. (1999), "Effect of pitting corrosion on fatigue crack initiation and fatigue life", *Engineering Fracture Mechanics*, Vol. 62, , pp 425-444

39. Medved, J.J., Breton, M. and Irving, P.E. (2004), "Corrosion pit size distributions and fatigue lives – a study of the EIFS technique for fatigue design

REFERENCES

in the presence of corrosion", *International Journal of Fatigue,* Vol. 26, pp 71-80

40. Kim, W., Paik, J. and Yajima, H. (2006), "Evaluation of corrosion fatigue crack initiation life of 13Cr steel", *Key Engineering Materials*, Vol. 326-328, pp 1007-1010

41. Ishihara, S., Saka, S., Nan, Z.Y., Goshima, T. and Sunada, S. (2006), "Prediction of corrosion fatigue lives of aluminium alloy on the basis of corrosion pit growth law", *Fatigue and Fracture of Engineering Materials and Structures,* Vol. 29, No. 6, pp 472-480

42. Rezig,E. (2006), "Influence of pitting corrosion on the initiation of fatigue cracks in 15-5PH stainless steel", MSc thesis, School of Industrial and Manufacturing Sciences, Cranfield University

43. Boyer, H.E (1986), *Atlas of fatigue curves*, American Society for Metals, Ohio.

44. Afgrow software available at: www.afgrow.net

45. Catlin,W.R., Lord, D.C., Prater, T.A. and Coffin, L.F. (1985), " The reversing DC electrical potential method", *Automated test methods for fracture and fatigue crack growth*, ASTM STP 877, pp 67-85.

46. Rooke,D.P., Cartwright, D.J. (1976), *Compendium of Stress Intensity Factors*, Procurement Executive, Ministry of Defence. H.M.S.O.

47. 15-5PH stainless steel product data bulletin UNS S15500 AK steel, available at www.aksteel.com/markets_products/stainless_precipitation.asp

48. Petzow, G., "Metallographic Etching. 2nd edition" ASM international 1999

49. Annual book of ASTM standards 2006, "Metals test methods and analytical procedures", Vol 03-01 Metals – Mechanical Testing; Elevated and low temperatures tests; Metallography, ASTM.

50. Annual book of ASTM standards 2005, "Metals test methods and analytical procedures", Vol 03-02 Wear and Erosion; Metal corrosion, ASTM.

51. General information on Niobium available at: www.en.wikipedia.org/wiki/Niobium#Steel_production

52. Hardness conversion table available at: www.gordonengland.co.uk/hardness

53. Gumbel, E.J. (1958), "Statistics of extremes", Columbia University Press, New York, USA, pp. 375.

REFERENCES

54. Gumbel, E.J. (1954), "Statistical theory of extreme values and some pratical applications", Vol. Applied Mathematics series 33, National Bureau of Standards.

55. Shibata, T. (1994), "Application of extreme value statistics to corrosion", Journal of Research of the National Institute of Standards and Technology, Vol.99, No.4, pp. 327-336.

56. Microset, "High resolution replication materials for engineering inspection" www.microset.co.uk

57. Application of Weibull statistics available at: http://www.weizmann.ac.il/wagner/Andras/chapters/ch43.html

58. MLX17 Statement of conformity (NF L 00-015) – G0107/RD-1A001-1/0/AD – Aubert&Duval

59. Military Handbook - MIL-HDBK-5H: Metallic Materials and Elements for Aerospace Vehicle Structures (Knovel Interactive Edition), (2003), p2-174, U.S. Department of Defense. Online version available at: http://knovel.com/web/portal/browse/display?_EXT_KNOVEL_DISPLAY_bookid=754&VerticalID=0

60. Cerit, M., Genel, K. And Eksi, S. (2009), "Numerical investigation on stress concentration of corrosion pit", Engineering failure analysis, Vol. 16, pp 2467-2472

61. Sharland,S.M. and Tasker,P.W. (1988), "A mathematical model of crevice and pitting corrosion –I. The physical model", *Corrosion Science*, Vol. 28, No.6, pp 603-620

62. Alkire,R., Tomasson,T. and Hebert,K. (1985), "The critical geometry for initiation of crevice corrosion", *Journal of The Electrochemical Society*, Vol. 132, No. 5, pp 1027-1031

63. Walton, J.C. (1990), "Mathematical modelling of mass transport and chemical reaction in crevice and pitting corrosion", Corrosion Science, Vol. 30, No. 8/9, pp 915-928